PhD Program in Bioengineering and Robotics

Curriculum: Bionanotechnology

Thesis title:

Functional and antioxidant bio-based polymer composites with potential applications in food packing

Student: Ana Isabel Quilez Molina
Cycle: XXXIII
Tutor(s): Ilker S. Bayer and Athanassia Athanassiou

Dedication page

To my parents, who have always believed in me and supported my untiring desire of staying abroad: you will always be my *home*.

To my uncle Francis who will remain in this thesis, as he does in our memory.

Acknowledgements

I would like to thank my supervisors Ilker S. Bayer and Athanassia Athanassiou for coordinating and tutoring my PhD degree and for giving me the opportunity to grow both scientifically and personally. Thanks to the lab technicians, Lara, Giorgio, and Riccardo, for your help and guidance, but also good rapport.

To Alejandro and Antonio for your support and kindness: you have always provided me the tools and advice that I needed to choose the right path. I am deeply grateful to my first Italian friends, Ari, Edo, Fede, Giulia M, Mery, Rush, and Yang, for these three years full of unforgettable moments and experiences. Everything I have achieved here would not have been possible without your patient and your friendship. Thanks to Gabri and Giorgia for your special warmth and Sicilian kindness. I would also like to thank Giacomo, Dag, Lia, Vale, and Marge, with whom I have spent wonderful times together. Sincere thanks to Giovanni, Danila, and Aurelio for your friendliness and encouragement during the last year of PhD. To my friends “of the fifth floor”, especially Lea, Dori, Giusy, Filippo, Giovanni, Ciccio e Simmo, for cheering me up every day from early morning.

A special thanks to my Spanish friends, Vale, Cris, Agus, Oscar, Elena, Anita, Celia, Clau, Isma, Jesus, Jorge, and Yoli, for reminding me where my roots are, and for your unconditional support. To my family for staying close to me every day, showing me that distance is just a number.

Table of Contents

List of Figures

Abstract

The inadequate management of plastic wastes, along with the low biodegradability of conventional petroleum-based polymers, has led to a global climatic crisis. A potential solution is the substitution of these ordinary polymers by bioplastics, which production or management present a low impact on the environment. Moreover, revalue agro-food wastes to create new biocomposites is a good strategy to improve waste disposal with economic benefits. Adding agro-food wastes into a polymer matrix can also provide several enhancements to the final biocomposite, such as the reduction of the percentage of oil derivatives and higher biodegradation rate. In addition, the final biocomposites can develop additional and innovative features such as antioxidant activity, better barrier properties against gases, or UV-light protection. These properties can be useful to prevent the damaging biochemical reactions occurring during food storage, like oxidation, loss of firmness, browning, off-odors, etc, increasing the shelf life of foods.

In this PhD-thesis, the development of eco-friendly materials with promising properties for food-packaging applications has been performed using a low-environmental impact approach. All projects were based on the use of food by-products or naturally derived molecules, and different processing techniques, like casting, extrusion, and hot-pressing, were employed.

In the first part of the thesis, caffeic acid, as a natural derivative, was used to provide antioxidant and UV-blocking responses to a transparent polymer blend form by poly(ethyl-cyanoacrylate) (PECA) and polypropylene carbonate (PPC). The morphological and barrier properties have been characterized and discussed.

Secondly, two food by-products, tealeaves extract and discarded balsamic vinegar, were used to modify the physicochemical properties of polyvinyl alcohol (PVA) films using one-pot method. Films showed tunable antioxidant and mechanical behaviors, varying respect to the concentration and the type of natural additive. The chemical composition of tea and tea waste extracts was analyzed, resulting in a wide variety of active polyphenols. Besides, films exhibited excellent oxygen barrier properties.

In the third project, versatile biocomposites (40 wt.% of cellulose and 60 wt.% of petroleum-based bioplastic) were fabricated using free-solvent and industry-scalable methods, like extrusion and hot-press. The content of the petroleum-based polymer, polycaprolactone (PCL), was reduced by incorporating an inorganic filler at high concentrations (10 and 25 wt.%). In addition, biocomposites were functionalized with two different natural derivatives: aqueous extract of pomegranate peel and curcumin, separately. Pomegranate peel extract provided a strong antioxidant response, while curcumin-composites displayed colorimetric-changes with pH. Finally, the pH-sensing properties of the curcumin biocomposites were tested during the storage of commercial shrimps.

The last part of the thesis describes the development of edible and bio-based materials using the orange peel and orange essential oil. The gelation conditions of the orange peel pectin were modified to create bioactive and edible materials with different functional characteristics. The properties of three sets of samples were evaluated in the view of acting as a suitable edible packaging as coating/film, such as the transparency, solubility, and water barrier properties. In the end, the revalorization of edible vegetable waste through the fabrication of valuable and bioactive packaging using a facile sustainable water-based process was performed with success.

Chapter 1: Introduction

1.1 State of the art of bio-based polymers

The production of plastic for packaging represents almost 40% of the total global plastic usage, 23 million tons of plastic packaging annually (Chandran et al., 2020; Varžinskas & Markevičiūtė, 2020). The most common polymers used for food packaging are polyethylene terephthalate (PET), polyvinylchloride (PVC), and polyethylene (PE). These polymers are highly available, cheap, and offer properties that ensure the efficient protection and preservation of foods (Ajay et al., 2019; Rameshkumar et al., 2020; Tallentire & Steubing, 2020). However, they derive from petroleum resources and exhibit great resistance to biodegradation and low recyclability (Ajay et al., 2019; Siracusa et al., 2008). Additionally, most packaging products are single-use or very short usage and they usually end up disposed of in landfills or incinerated (Chandran et al., 2020; Varžinskas & Markevičiūtė, 2020).

The critical environmental situation has driven towards the search for alternative packaging materials with low environmental impact. Bioplastics represent a wide group composed of natural and chemical polymers derived from renewable or petroleum resources and designed to diminish the carbon footprint, enhance the recycling value, and offer biodegradability/composability (Rameshkumar et al., 2020). The sector of bioplastics is undergoing a noticeable growth, enhanced by the environmental sustainability and the economic feasibility of these materials, expecting to rise to 2.62 million tons by 2023, (Rameshkumar et al., 2020). The different types of bioplastics are classified on basis of their origin and biodegradability are exposed in **Figure 1.1.**

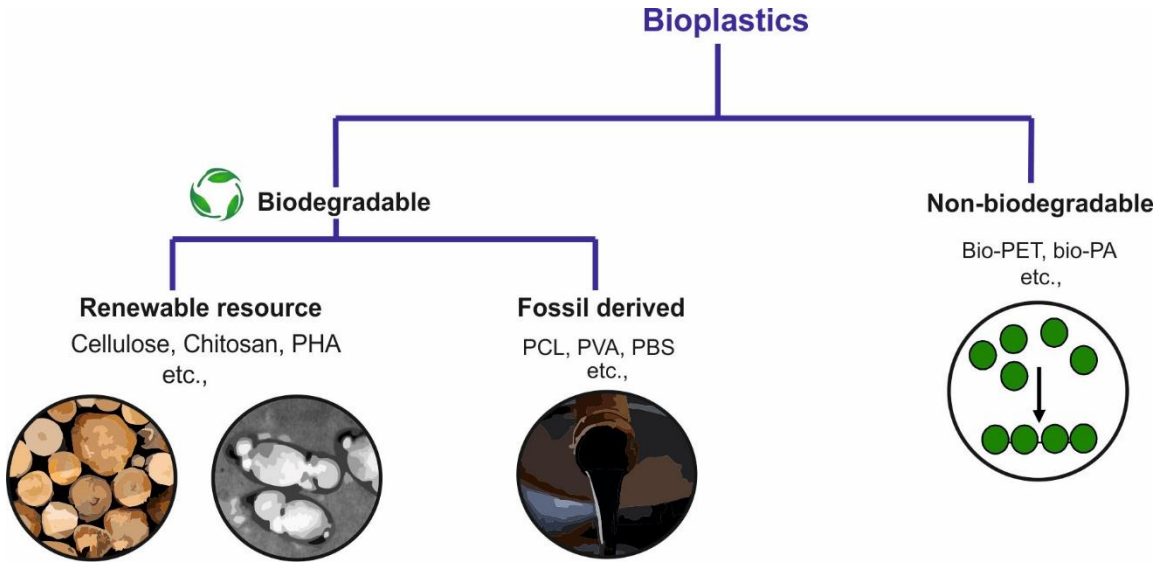

Figure 1.1 Schematic classification of bioplastics on basis of the origin and biodegradability

Among bioplastics, the first group belonged to non-biodegradable bioplastics collects polymers synthesized by naturally occurring monomers or building-blocks that reduced the carbon-footprint (Confente et al., 2020). For example, bio-derived from convectional petroleum polymers, such as bio-poly(ethylene terephthalate) (PET) and bio-polyamide (PA) denominated bio-PET and bio-PA, respectively. Most of which offer the same properties as the petroleum-based analogous (RameshKumar et al., 2020; Siracusa & Blanco, 2020). A great success is achieved with the production of polypropylene carbonate (PPC), resulting from the copolymerization of carbon dioxide and propylene oxide, in which a greenhouse gas is transformed into a valuable product (Luinstra & Borchardt, 2012; Mohanty et al., 2018). The second sub-group of bioplastics comprises petroleum-based polymers but with biodegradation features like Poly(vinyl alcohol) (PVA) and polycaprolactone (PCL) (RameshKumar et al., 2020). While the last group is represented by bio-based polymers, completely derived from natural resources and biodegradable. In addition to the environmental impact, the great advantage of bio-based polymers with respect to petrochemical polymers is the wide availability, biocompatibility, and low cost (Muller et al., 2017).

The next step is the valorization of urban or agro-food wastes to fabricate materials reducing the environmental impact of accumulated organic biomass in landfills (Confente et al., 2020). This idea supposes a revolution in the view of the management of plastic residues with significant effects in the economic and environmental sectors (Confente et al., 2020). Up to now, two different economic models have defined the plastics life cycle: linear economy or circular economy, schematically represented in **Figure 1.2(a-b)**. Linear economy describes the life cycle of the defined "black plastics", non-biodegradable and non-recyclable polymers, limited by the content of irremovable additives or polymer-blends, which avoid the possibility of these plastics to re-enter the economy (Turner, 2018). At the end of their life cycle, these polymers are conducted to landfills to be accumulated, or to incineration chambers to be burnt (Turner, 2018). In turn, the circular economy comprises the polymers and polymer-blends that can be converted into valuable products and re-entered in the economy chain (Confente et al., 2020). This concept contributes to improving the waste-management, providing substantial economical and sustainable benefits. However, only 2% of the generated plastics are recycled into the same or similar quality, and 32% is wasted in the ecosystem (Confente et al., 2020). The reincorporation of biodegradable and

organic urban and agro-food wastes in the economic circle would close the loop, limiting the production of wastes and consumption of natural resources (Confente et al., 2020). The scheme of the "closed-loop" economy is represented in **Figure 1.2(c)**. Besides, the "closed-loop" economy would reduce the excesses of food waste, which disposals have increased up to 1.3 billion per year, becoming a relevant problem (Dilucia et al., 2020). The main food wastes correspond to fruit and vegetable by-products in form of pomace, seed, pulp, peel remained from the production of wines, oils, and juices (Dilucia et al., 2020). These agro-food wastes are full of bioactive molecules and macromolecules, which may confer additional valuable properties to the material. For instance, mechanical when incorporated into different natural blends like chitosan or wheat gluten, and the barrier properties against oxygen and water vapor were enhanced with the incorporation of olive pomace (Boudria et al., 2018; de Moraes Crizel et al., 2018). Besides, the desired biomolecules can be isolated from the food discard in form of extracts (liquid) or powder (solid) (Esparza et al., 2020). Pectin is an example of a biomacromolecule located in the external cell-wall of several fruit and vegetables like orange, apple, kiwis, etc, (Güzel & Akpınar, 2019). This ubiquitous biomacromolecule can be easy isolated from the fruit peel by heating an acidic aqueous solution. (Güzel & Akpınar, 2019). Apple and orange pectins, extracted from apple pomace and citrus peel, are currently used in the food industry as stabilizing, thickening, texturing, etc (Celus et al., 2018; Güzel & Akpınar, 2019). The chemical extraction and functionalization of cellulose from lignocellulose biomass derived from wood have been widely studied. The wide versatility of this promising biopolymer allowed to obtain cellulose in different forms such as in monomers to polymerize, in form of natural fibers, nanocrystals, cellulose derivatives, according to the chemical treatment performed (Shaghaleh et al., 2018). Interestingly, the addition of vegetal waste has enhanced the biodegradation of some bioplastics derived from petroleum-resource. For example, rice-husk flour enhanced the biodegradation in soil of poly(butylene succinate) (PBS) and PCL when loaded in 40 and 50 wt.%, respectively (H. S. Kim et al., 2006; Zhao et al., 2008).

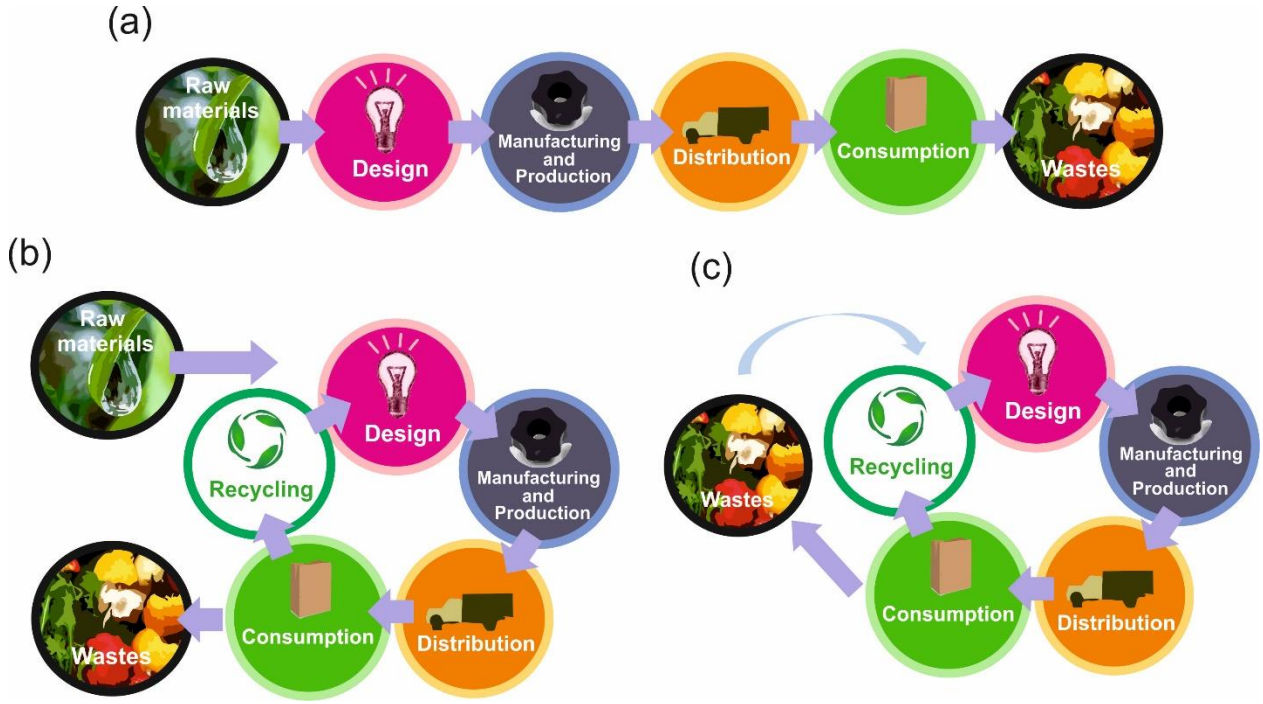

Figure 1.2 (a) Schematic representation of the linear economy. **(b)** Schematic representation of the circular economy with polymer recycling **(c)** Schematic representation of the "closed-loop" economy, wastes re-enter the economy as valuable products.

1.2 Bioplastic production and applications

The general tendency is to replace conventional petroleum-based materials with renewable biodegradable bioplastics. However, sustainable bioplastics are still far from occupying the whole market. A promising solution is modifying and improve their functionality when combined with other materials (other polymers, additives, fillers, among others) to offer a broader spectrum of application and to improve the characteristics of the final product. In addition, in combination with powerful compounds, they can acquire extraordinary properties (Siracusa et al., 2008).

1.2.1 Strategy for improving bioplastic production

Generally, petroleum-based materials with biodegradable backbones like PVA or PCL, present optimum processability that facilitates their production and scalability in the market. PVA is a semi-crystalline and transparent bioplastic, water-soluble, and with high-biocompatibility. These attributes have led to the application as a medical device, as tissue scaffolding or healing

wounds (Guzman-Puyol et al., 2015; Hassan & Peppas, 2000). However, the strong sensitivity of moisture and poor mechanical resistance can limit the application of PVA in certain areas (Guzman-Puyol et al., 2015; Yang et al., 2020). PCL is hydrophobic and easy processable-polymer via extrusion or injection molding at low temperatures, which may avoid the thermal degradation of additives. Moreover, PCL presents good mechanical properties and good biocompatibility leading to broad-spectrum applications like tissue engineering, agriculture, or food packaging. (Maraveas, 2020; Mi et al., 2014; Rešček et al., 2015; Salmoria et al., 2017). However, on several occasions, the biodegradability of fossil-derived polymers are limited to certain unrealistic environmental conditions. For example, Asma S. Al Hosni *et al.,* (2019) studied the biodegradability of different polymers PCL, polyhydroxybutyrate (PBS), polylactic acid (PLA), and poly(1,4 butylene) succinate (PBS) in soil and compost at controlled temperatures. Results indicated that polymers were totally (PCL and PLA) or partially (PHB and PBS) biodegradable only when treated at 50°C, while they barely biodegraded at 25°C and 37 °C (Al Hosni et al., 2019). The current challenges in the management of plastic wastes hamper the control of the disposal, occurring an uncontrolled-biodegradation that ends up increasing plastic pollution (RameshKumar et al., 2020).

Novel bio-based polymers, like cellulose derivatives, chitosan, thermoplastic starch (TPS) are completely biodegradable and independent of any petroleum resource. The main challenge in manufacturing biopolymers is related to the difficult processability and economic-feasibility of the production methods (B. Khan et al., 2017). Among biopolymers, PLA and TPS are becoming the growing alternative as green packaging materials due to their large availability, low cost, and easy processability (Ajay et al., 2019). PLA is a linear aliphatic thermoplastic polyester derived from lactic acid obtained from the fermentation of several plants, such as corn, rice, and sugar feedstock. This promising polymer is biocompatible, scalable via melt extrusion, and presents good barrier properties. However, the low flexibility, less than 10% of elongation, as well as the low crystallization of PLA, hinder the processability of the PLA with high crystallinity using injection molding (Jiang et al., 2007; Muller et al., 2017). Thermoplastic starch (TPS) comes from polysaccharide resources. It is a rubbery bioplastic, cheap, elastic, and with good oxygen barrier properties. However, the main drawbacks of TPS reside in poor mechanical properties and water sensitivity, limiting its manufacturing and application range (B. Khan et al., 2017; Muller et al., 2017).

A promising approach to resolve the limitations of bioplastics is polymer blending to form renewable materials with more competitive properties. The incorporation of chitosan and other minor additives into a PCL matrix enhanced the biodegradation rate to 6 months, against 24 months in neat PCL (Cesur et al., 2018). Cellulose fibers have been widely used to reinforce thermoplastic polymers when added as a filler, or in forms of cellulose nanocrystals (CNC) (Shaghaleh et al., 2018). For example, CNC reinforced the mechanical and thermal properties of neat PVA, and the wettability character of the neat polymer decreased with the cellulose content (Yang et al., 2020). Also, a cellulose matrix was performed via extrusion, by grafting the cellulose fibers with PHB obtaining a material with better performance than the single biopolymers (Formela et al., 2018). Besides, the poor moisture barrier properties of starch were improved by blending the biopolymer with the hydrophobic PLA polymer via injection molding (Ajay et al., 2019; Muller et al., 2017). In addition, the incorporation of additives like inorganic nanoclays can interact with the polymer matrix, modifying the entanglements and organization of the polymer chains. This can lead to modifications of the crystallinity, with important consequences of the mechanical and thermal properties (Jiang et al., 2007; Liang et al., 2013; Paula et al., 2019). These fillers can hamper the passage of surrounding vapors enhancing the barrier properties (Rešček et al., 2015). Moreover, inorganic salts can act as moisture dry desiccants by absorbing moisture, ensuring low-humidity environments (Gaikwad et al., 2019; Rešček et al., 2015). The incorporation of inorganic filler at high concentrations may reduce the percentage of a polymer-based material, saving cost and reducing the environmental impact of polymer manufacturing.

Interestingly, smart and novel materials can be developed by incorporating active molecules with innovative characteristics. For example, starch nanocomposite films showed strong UV-barrier properties caused by the addition of TiO_2, which absorbs UV-light (Oleyaei et al., 2016). UV-blocking properties also elongate the shelf-life of materials, preventing photodegradation, useful for long-term application materials, and to avoid the accumulation of micro-plastics in soils (Maraveas, 2020). Electric conductivity was implemented in materials based on crop plants with the incorporation of graphene nanoparticles (Cataldi et al., 2018). Antioxidant activity was developed in films of carboxymethyl cellulose with the incorporation of an antioxidant α-tocopherol (Martelli et al., 2017). Interestingly, the bioactive molecules can be immobilized in the polymer matrix to elongate the shelf life of the material, or to be released as interactive material. A promising alternative is extracted these valuable molecules from natural sources or even agro-

food. Vegetables are rich in polyphenols and other bioactive molecules with antioxidant and antimicrobial properties. The incorporation of plant derivatives in form of extract or powder directly to the polymer matrix can provide these extraordinary characteristics to the final material. For example, the extract of black chokeberry pomace was immobilized in chitosan to provide colorimetric pH-sensing properties (Halász & Csóka, 2018). While ethanolic extracts of cinnamon, guarana, rosemary, and boldo-do-chile plants were added into gelatin-chitosan edible films to confer antioxidant and antimicrobial properties against *S. aureus* and *E. coli*, the main microorganisms that cause foodborne-disease (Bonilla & Sobral, 2016). Additionally, agro-food wastes can be processed to fabricate bioplastics with competitive mechanical and thermal properties (Bayer et al., 2014; Perotto et al., 2018). For example, the mechanical strengths of films made up of cocoa pod husk were comparable to engineering polymers such as PET (Bayer et al., 2014).

1.2.2 Fields of application: Food packaging

The implement of the new properties on polymeric materials may improve significantly the functionality of the material in different fields, like biomedical, preservation of the cultural heritage, or materials for the packaging of cosmetics and foodstuffs. The incorporation of antibiotics into the polymer matrix may lead to the fabrication of antibiotic films for skin and wound healing application (Contardi et al., 2017). While antioxidant and anti-inflammatory cellulose-based materials were obtained adding different seaweeds (Guzman-Puyol et al., 2017). On the other side, coatings with UV-light protection and antimicrobial properties were very useful for the preservation of textiles (Zahid et al., 2019). However, the serious environmental consequences associated with plastics used for food packaging have led us to focus this thesis on the development of active materials with a promising application as food packaging.

Food-packaging material may provide the protection and isolation of foods from external agents, such as the variation of temperature, moisture, and harmful light-radiation, to elongate the shelf-life of foods (Kirwan et al., 2011). The oxidation reactions are the main reason for the loss of nutritional value and quality of foodstuffs (Johnson & Decker, 2015). The most representative active agents are oxygen and UV-light, which trigger the generation of radicals that start the oxidation reaction (Tian et al., 2013). The incorporation of natural antioxidants and UV-blocking

biomolecules can protect food from oxidation via scavenging reactions against oxygen, or from UV-light by absorbing light in that range of the spectrum (Peschel et al., 2006). Besides the protection against oxidation, food-packaging materials should provide good barrier properties that prevent oxygen and water permeation, mechanical strength, and transparency (Del Nobile & Conte, 2013; Gaikwad et al., 2019; Wyrwa & Barska, 2017). The moisture sensibility of foods is also critical, especially in foods rich in lipids and proteins, like meat and fish, in which the humidity enhanced the growth of mold and microorganisms (Gaikwad et al., 2019). The incorporation of fillers into the polymeric matrix hampers the passage of water vapors through the film, avoiding high humidity conditions inside the packaging atmosphere. For example, the water resistance and the mechanical strength of the natural cassava starch films were improved with the incorporation of cellulose nanocrystals (CNC) (Kargarzadeh et al., 2017). Hydrophobic molecules, such as essential oils or wax, have demonstrated that enhance the water barrier properties when loaded into the package. Tea tree oil essential oil reduced the water vapor permeability down to 40% of a composite made up of chitosan with respect to the neat chitosan film (Sánchez-González et al., 2010).

The development of novel sensing-indicator devices, able to monitor in real-time the food quality, has increased rapidly in recent years. The implementation of these devices in food packaging may reduce the chances of intoxication or foodborne by the consumption of spoilage food. Besides, more awareness of the food quality-conditions may result in a reduction of the food wastes, discarded when they are still suitable for consumption (Yousefi et al., 2019). Most of the methods used for monitoring are linked to a colorimetric change of the packaging-device. The release of basic molecules occurring in meats and seafood has been used to detect food spoilage with a low pH-sensitive indicator. For example, yellowish films of curcumin and k-carrageenan turned red when pork and shrimps showed signs of spoil (J. Liu et al., 2018).

A revolutionary new sector for the application of biopolymers in food packaging is edible packaging. The use of edible biopolymers as packaging has been presented as a potential alternative to protect and elongate the shelf life of minimally-processed foods. Usually, they are applied directly to the food surface to form a coating (via spray, dipping, or brushing), or covering the food as a film by casting (Otoni et al., 2017). The edible matrix must be composed of only food-grade components, including the additives (Otoni et al., 2017). Naturally occurring

polysaccharides and proteins comply with those demands and they are the best used because of their versatility and film-forming properties (Otoni et al., 2017). Some examples of biopolymers used for this kind of package are cellulose, chitosan, pectin, zein, and collagen. The main goal of edible films and coatings is to provide a semi-permeable barrier against gases and vapor (Embuscado & Huber, 2009). However, they can also act as drug-deliverer when active molecules, such as antioxidants or antimicrobials, are embedded. For example, loading pomegranate peel extracts into chitosan matrix retarded the growth of pathogens on meat and seafood when incorporated as a coating (Licciardello et al., 2018; Surendhiran et al., 2020). Coatings of chitosan containing orange essential oil also prevented the microbial growth on coated pink shrimps (Alparslan & Baygar, 2017).

The major limitation of these innovative materials is that most of the production processes reported in the literature are limited to small-scale techniques (De Azeredo et al., 2014). The typical production steps are represented in **Figure 1.3**. Basically, the mixture of components (solvent, biopolymer matrix, and additives) is mix and homogenized, wherein the inner network of the biopolymer is altered via chemical reactions (hydrolysis, cross-linking, and more), the conditions of temperature and the reaction time may be fixed previously, which are crucial for the developing of the desired properties. In many cases, the mixture is very dense, and applying the vacuum atmosphere is required to ensure the loss of the excess of gas inside the solution (De Azeredo et al., 2014). At this point, the dispersion can be poured into a mold to create an edible film, or applied directly onto the food surface as an edible coating through diverse methods: dipping, brushing or spraying. The drying time in castings depends on the solvent used, additives, and temperature (De Azeredo et al., 2014). Among the edible coatings, dipping is the easiest method, in which highly viscous solutions are required to ensure the homogeneous dispersion of the coating in the entire food (Valdés et al., 2015). Brushing is applied when the coating may act only in a specific part of the food product, while spraying is strongly recommended in low dense solutions (Valdés et al., 2015). Diversely to brushing and dipping, spraying-coatings does not form a layer on the food surface, but small drops, which limit significantly the barrier properties of the coating. However, the encapsulation of the bioactive molecules in drops also speeds up the release, becoming very useful when a rapid response is desired (Valdés et al., 2017).

Edible materials may accomplish some requisites in order to extend the food shelf life. These properties, however, are strongly linked to the physicochemical characteristics of the food itself. For example, the application of biocoatings/biofilms with low water permeation is not recommended for dry foods, while they are ideal for allowing the metabolic respiration of fruits and vegetables (De Azeredo et al., 2014). Finally, the edible materials may preserve the taste and organoleptic properties of the characteristic of the product, except if the modification of these properties may be desired or compatible with the food (De Azeredo et al., 2014).

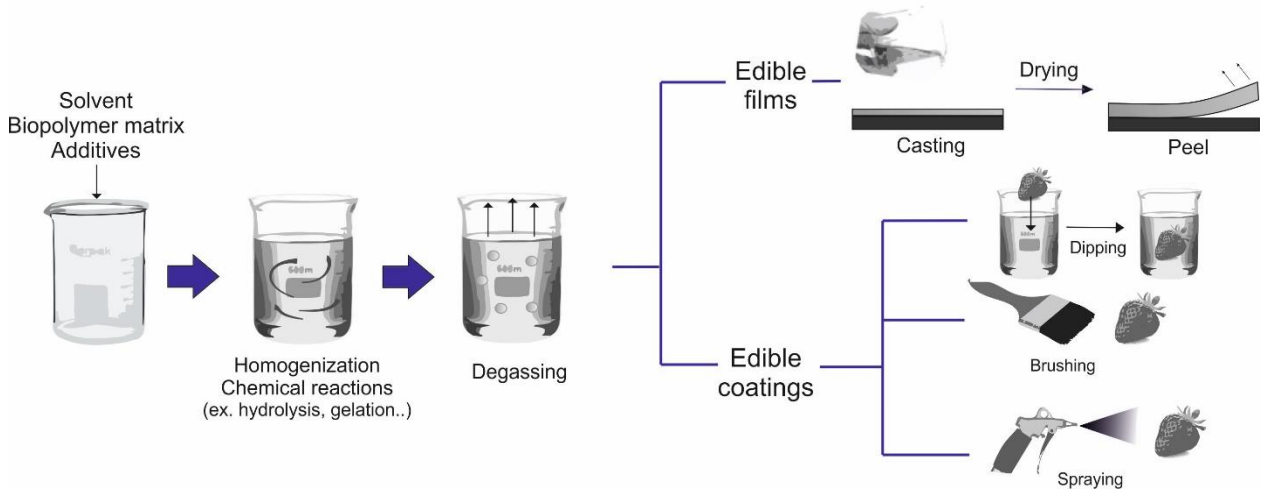

Figure 1.3 Schematic representation of the production of edible films and coatings.

Chapter 2: Improve the barrier properties of polymers using natural additives

2.1 UV-Blocking, Transparent, and Antioxidant Polycyanoacrylate Films

Poly(alkyl cyanoacrylate)s are transparent cyanoacrylic esters with biodegradable biocompatible properties (Irache et al., 2011; S. Kim et al., 2013; Tripodo et al., 2011). Cyanoacrylates monomers are characterized by undergoing a spontaneous polymerization in presence of moisture, which leads to the formation of a strong network in a short time, acting as an excellent adhesive (Mizrahi et al., 2011). The great selling capability has promoted the application of cyanoacrylates as alternative materials for surgical adhesives or wound closing glue (Mizrahi et al., 2011). Besides, biodegradable cyanoacrylates have been used for drug-delivering devices, improving the bio-ability and absorption of some bioactive molecules (Irache et al., 2011; S. Kim et al., 2013; Yao et al., 2020). For example, the oral absorption and control release of tea extract-chelated Zn nanoparticles were achieved through the encapsulation with poly(butyl-2-cyanoacrylate) in (Yao et al., 2020). The application of cyanoacrylates for the fabrication of bio-coatings for food packaging has been risen recently, due to the heat-salable, block-resistant, and good barrier properties (Samyn, 2013). Acrylic polymers are well-dispersed in water and they have been successfully used to created compostable materials, such as paper coatings (Samyn, 2013). However, the application of cyanoacrylate-films has been greatly limited by low flexibility and easy-breakability (Mizrahi et al., 2011; Tripodo et al., 2011). Incorporating plasticizers in form of small molecules such as phthalates, glycols, and phosphates may overcome the brittleness of cyanoacrylates (Tripodo et al., 2011; Vieira et al., 2011). However, these kind of plasticizers present a high risk of being leached or released into food or biomedical–cosmetic products (Paraskevopoulou et al., 2012). The incorporation of a transparent, elastic and biodegradable polymer like poly(propylene carbonate) (PPC) has been proposed to enhance the mechanical properties without compromising the performance of neat PECA films.

Poly(propylene carbonate) (PPC) is a bioplastic derived from the recycling of carbon dioxide and biodegraded to H_2O and CO_2 (Corre et al., 2013). The production of this polymer through the use of the CO_2 emitted by the industry reduces massively emission of greenhouse gases and global charming (H. Pan et al., 2017). This transparent polymer is generally used as a plasticizer in different polymers to enhance elastic properties due to its large elongation at break value (Corre et al., 2013). The incorporation of PECA up to 5.0 wt.% improved the elongation and showed high transparency. It has been demonstrated that low concentrations of PPC (i.e., 2.5 wt.%) were sufficient to increase the ductility of PECA up to 10 times. Besides, the transparency of films

was maintained even though the apparent low compatibility between the two polymers. Films were activated adding a natural antioxidant molecule, caffeic acid (CA). Caffeic acid is a phenolic acid that belongs to hydroxycinnamic acid family, which has exhibited a great capacity to prevent several diseases (cancer, coronary heart disease, diabetes, etc.) (Monteiro Espíndola et al., 2019). In fact, in the last years, novel antioxidant materials based on caffeic acid have been developed with the application food packaging field. For instance, films composed of caffeic acid and chitosan have exhibited a great capacity for preventing the lipid oxidation of fish oil emulsion and bacterial growth (Yu et al., 2013). Most of these natural bioactive molecules exhibit strong UV-blocking properties, which are very important to limit radical lipid oxidation, especially in fatty foods (Johnson & Decker, 2015; Tian et al., 2013). However, natural UV-blocking molecules present some challenges related to the strong coloration that limits their application as a food package, like lignin or curcumin (Ma et al., 2017; Tedeschi et al., 2020). Therefore, transparent and UV-blocking films based on the activity of a natural caffeic acid represented a great success.

2.2 Materials

Ethyl 2-cyanoacrylate monomer (ECA, Permabond 101), poly(propylene carbonate) resin (typical average Mw 89,000–98,000 g/mol, 98% hydrolyzed), caffeic acid, and cyclopentanone ReagentPlus® (≥99%), were purchased from Sigma Aldrich (St. Louis, MO, USA) and used as received. Deionized water was obtained from Milli-Q Advantage A10 Ultrapure Water Purification device (Merck, Darmstadt, Germany). DPPH (2,2-diphenyl-1-picrylhydrazyl) was purchased from Alfa Aesar (Kandel, Germany) and ethanol (≤100%) was purchased from Merck and both were used as received.

2.2.1 Preparation of the films

The elaboration of the PECA films was performed through the polymerization of ethyl cyanoacrylate monomers (ECA) in a solution of cyclopentanone with dispersed PPC and caffeic acid. The slow evaporation of the solvent leads ECA monomers to form transparent PECA films, see **Figure 2.1**. The PECA-PPC samples were labeled as PECA-2.5 and PECA-5 when PPC was added in 2.5 wt.% and 5 wt.% with respect to the PECA (on dry basis). Caffeic acid was added in 1.0 wt.% and 2.0 wt.% with respect to PECA on dry basis, to PECA-2.5 and PECA-5, respectively.

The final antioxidant films were labeled as PECA-2.5-1 and PECA-5-2. As an example, once the proper quantities of PPC and CA were added into the cyclopentanone solution, ECA monomer was added dropwise until reaching 13.0 wt.% of ECA with respect to the solution. The polymer solution was mixed with a vortex mixer, and then, sonicated in a water bath for 90 min at room temperature with a frequency of 59 kHz. Subsequently, solutions were poured into a glass petri dish mold (90 mm diameter). Films were placed under a chemical hood overnight at room temperature. After drying, the transparent films were easily peeled off the molds. The chemical composition of samples is summarized in **Table 2.1**.

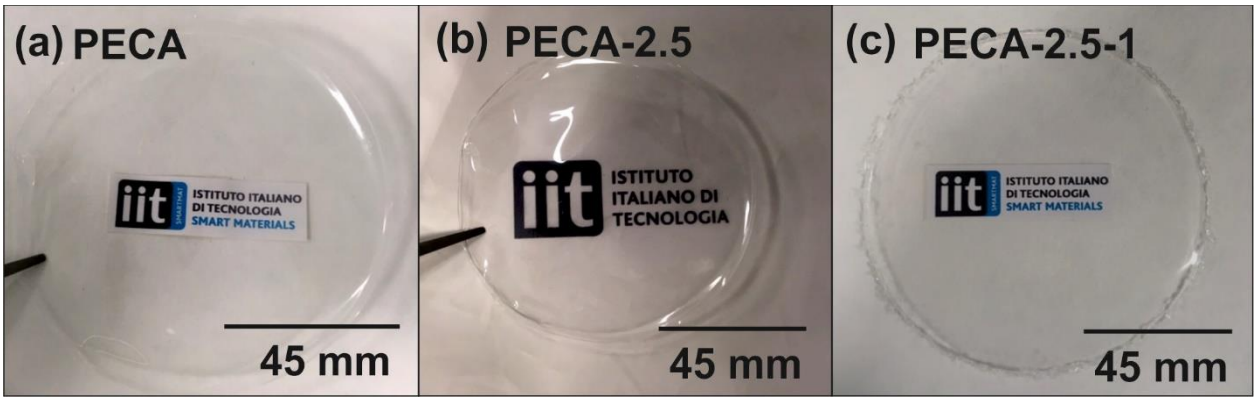

Figure 2.1 The transparent films corresponding to **(a)** PECA, **(b)** PECA-2.5 and **(c)** PECA-2.5-1.

Table 2.1. Composition of the dry PECA-PPC blends. Poly(ethyl-cyanoacrylate), Poly(propylene carbonate) polymers, and caffeic acid are labeled as PECA, PPC, and CA, respectively.

Labeled samples	Concentration of PPC (wt.%)	Concentration of CA (wt.%)
PECA	-	-
PECA-2.5	2.5	-
PECA-2.5-1	2.5	1.0
PECA-5	5.0	-
PECA-5-2	5.0	2.0

2.3 Analysis methods

2.3.1 Attenuated Total Reflection Fourier Transform Infrared (ATR-FTIR) Spectroscopy

Infrared spectra were obtained with a single-reflection attenuated total reflection (ATR) accessory (MIRacle ATR, PIKE Technologies, Madison, MI, USA) coupled to a Fourier Transform Infrared (FTIR) spectrometer (Vertex 70V, Bruker, Ettlingen, Germany). All spectra were recorded in the 3800 to 600 cm^{-1} wavenumber range with a resolution of 4 cm^{-1}, accumulating 128 scans to reduce the spectral noise.

2.3.2 Scanning Electron Microscopy (SEM), Atomic Force Microscopy (AFM)

Surface and cross-section morphologies of solvent cast films were characterized by scanning electron microscopy (SEM), using a JEOL JSM-6490LA microscope working in high vacuum mode, with an acceleration voltage of 10 kV. Before the analysis, samples were mounted on conductive stubs and coated with 10 nm of gold using Cressington sputter coater 208 HR. The surface topography of the films was studied using atomic force microscopy (AFM) system E-100 (Park systems, Suwon, South Korea), with high-resolution imaging; scan size 50 × 50 μm. The size distribution and the number of voids and PPC-domains of the films obtained from several different SEM images have been estimated by using ImageJ commercial software. In order to characterize the microscale PPC rubbery domains within the bulk of the PECA films, PPC was etched by immersing the films in acetone for two days. Acetone immersion tests with pure PECA showed no dissolution during the immersion tests in acetone.

2.3.3 Light Transmittance Analysis

The optical transmittance of films was determined using a Varian CARY 6000i Scan UV-Vis spectrophotometer (Walnut Creek, CA, USA) over the wavelength range from 200 to 800 nm. For the measurements, the freestanding films with a thickness of around ~80 μm were placed in a compartment with a light pathway of 2 cm × 2 cm. An empty test cell was used as a reference.

2.3.4 Mechanical characterization

Mechanical properties of the films were measured by uniaxial tensile tests on a dual column Instron 3365 universal testing machine (High Wycombe, England). Dog-bone shaped samples had a gauge length of 25 mm and a width of 4 mm. Strain displacement was applied with a rate of 10 mm/min. Stress-strain curves were recorded at 25 ◦C and 44 % relative humidity (RH). At least ten measurements were conducted for each sample and results were averaged to obtain a mean value. The stiffness of the material was defined with the Young's modulus value, calculated from the slope of the linear part of the stress-strain curve (before elastic limit).

2.3.5 Water uptake

For water uptake measurements, samples were first dried by conditioning them in a desiccator until no change in sample weight was measured. Dry samples were weighed on a sensitive electronic balance and then placed in a 100% relativity humidity (RH) chamber at 25 ℃. Once the equilibrium was reached, each sample was again weighed and the amount of adsorbed water was calculated as the difference between the final and the initial dry weight. Percent of water uptake was calculated as represented below in **Equation 1**:

$$\text{Water uptake (\%)} = \frac{m_f - m_0}{m_0} \text{ x } 100 \quad (\mathbf{1})$$

where m_f is the sample weight at 100% RH and m_0 is the sample weight at 0% RH. Three measurements were taken and the results were averaged to obtain a mean value.

2.3.6 Water contact static angle measurement

Static water contact angle measurements were performed by using the sessile drop method using a Dataphysics 0CAH 200 contract angle goniometer equipped with a charge-coupled device (CCD) camera and image processing software operating under laboratory conditions (temperature 22–25 ℃ and relative humidity 50–60%). For the characterization, droplets of 5 µL volume MilliQ water were used. Up to 10-contact angle measurements were carried out on every sample at random locations and their average values are reported.

2.3.7 Water Vapor and Oxygen Barrier Measurements

Water vapor permeability (WVP) of all samples was determined at 20℃ under 100% relative humidity (ΔH%). As a desiccant anhydrous calcium chloride ($CaCl_2$) was placed inside the test permeation cell (7 mm inside diameter, 10 mm inner depth), maintaining 0% RH inside the permeation cell. Films were cut into circles and mounted on top of the permeation cell. The permeation cells were placed in a 100% RH using deionized water container. The water vapor transferred through the film was determined from the weight change of the permeation cell every hour over a 7 h-period using an electronic analytical balance, Sartorius CPA225D (0.01 mg accuracy). The weight gain of the films was then plotted as a function of time. The slope of each line was calculated by linear regression and the water vapor transmission rate (WVTR) was determined as below in **Equation 2**:

$$\mathrm{WVTR}(\mathrm{g/m^2 d}) = \frac{\text{Slope}}{\text{Area of the sample}} \quad (\mathbf{2})$$

WVP measurements were conducted three times for each sample. The WVP of the sample was then calculated indicated in **Equation 3**, displayed below:

$$\mathrm{WVP}(\mathrm{g/m^2 d\ Pa}) = \frac{\mathrm{WVTR\ x\ L\ x\ 100}}{\mathrm{p_s\ x\ \Delta RH}} \quad (\mathbf{3})$$

where L (m) is the film thickness measured with a micrometer with 0.001 mm accuracy, ΔRH (%) is the percent relative humidity gradient, and p_s (Pa) is the saturation water vapor pressure at 25 ◦C (3168 Pa). Films were measure in triplicate for each sample.

The oxygen permeation tests of blend films were performed using an Oxysense 525oi device (Oxysense, USA) equipped with a film permeation chamber. This machine was operated according to ASTM Method F3136-15. The test was performed at standard laboratory conditions,

i.e., 23°C and 40% relative humidity. The permeation chamber consisted of a cylinder divided into two parts (sensing well and driving well). The sensing well was instrumented with a fluorescence sensor called oxydots, sensitive to the oxygen concentration. This chamber was purged with nitrogen while the other one (driving well) was kept open to ambient air. The films were cut into a rectangular piece (6 cm x 6 cm) and placed inside the chamber. An OxySense fiber optic pen measured the oxygen reading from the oxydots, at specific time intervals. Oxygen transmission rates (OTRs) of the blend films were measured by monitoring the oxygen uptake with time using Oxysense OTR software. At least ten measurements were taken for each sample with a minimum coefficient of determination (R^2) value of 0.95.

2.4.8 Migration of caffeic acid and antioxidant activity

The migration of caffeic acid from the polymer films was measured by studying the specific migration of the antioxidant into the fatty food simulant, according to established liquid immersion protocols (Benbettaieb et al., 2018; López-De-Dicastillo et al., 2010). The method described by Lopez-de-Dicastillo et al. was followed with some modifications (López-De-Dicastillo et al., 2010). Films were cut into pieces of 3 mg and immersed in 3 mL of pure ethanol. The concentration of caffeic acid released from the film into the solution was analyzed by measuring the characteristic absorption peak of CA (327 nm) with Varian CARY 6000i Scan UV-Vis spectrophotometer (Belay et al., 2016). Prior to measurements, a calibration curve was constructed correlating the absorbance intensity of caffeic acid at 327 nm in ethanol by using several caffeic acid–ethanol solutions, see **Figure 2.2**. Results were represented in terms of milligrams of caffeic acid released per gram of original dry film.

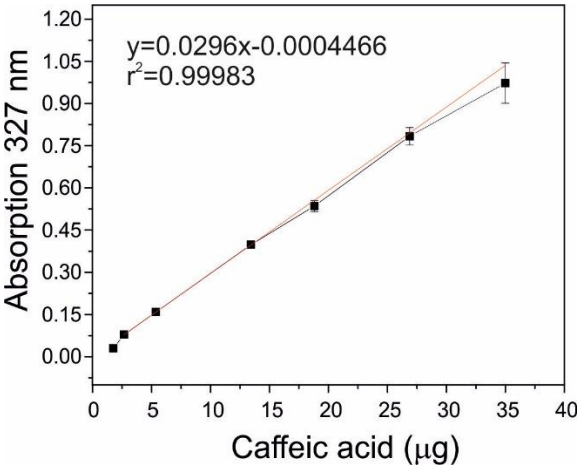

Figure 2.2 The calibration curve obtained representing the concentration of caffeic acid (µg) against the absorption value of the characteristic peak (327 nm).

2.4.9 Evaluation of the antioxidant activity

The antioxidant capacity of the films was represented in terms of the scavenging activity of the caffeic acid released from the films against a free stable radical, 2,2-diphenyl-1-picrylhydrazyl radical (DPPH·). The radical solution was prepared following the method reported by (Bayer et al., 2014). In there, 0.1 mM of DPPH was dissolved in ethanol, then the solution was diluted until the characteristic absorption peak (517 nm) reached ~0.8 a.u. The PECA blends were cut (3 mg) and introduced in 3 mL of the radical solution. The antioxidant effect of CA would induce a color change of the radical solution, from violet to yellow, diminishing the absorption of the characteristic at 517 nm as the release takes place. The antioxidant capacity was determined by collecting the UV-absorption spectra of the liquid at certain immersion time-intervals and the percent radical inhibition was calculated following **Equation 4**:

$$\text{Radical scavenging activity (\%)} = \frac{A_1 - A_2}{A_1} \text{ x } 100 \quad (\mathbf{4})$$

A1 is the absorbance of the sample solution with DPPH· 517 nm and A_2 is the absorbance of the DPPH· control solution. All measurements were performed at least five times to ensure reproducibility.

2.4 Results and discussion

2.4.1 Physicochemical characterization

The chemical characterization of the PECA-PPC blends was performed using infrared spectroscopy. The infrared spectra of the neat PECA, PPC, and PECA-2.5 are represented in **Figure 2.3(a)**. The spectra of PECA showed the characteristic peaks of cyanoacrylate polymers, nitrile stretching vibration ν(C≡N) at 2230 cm^{-1}, the conjugated C=O stretching bond at 1742 cm^{-1}, the double bond (C=C) at 1614 cm-1, and the vibration band of ν(C-O) at 1248 cm^{-1} (Mankidy et al., 2008; Masood et al., 2018). PPC polymer exhibited a sharp stretching band of C=O at 1739 cm^{-1} and ν(O-C-O) vibrations at 1314, 1263, and 1236 cm^{-1}. The infrared spectra of PECA-PPC blends coincided with the bands of PECA, while the low concentration of PPC polymer in the blends led to the poor visibility of the PPC bands in the spectra.

The range of the infrared spectra that correspond to the vibration band of the carbonyl group of ν(C=O) at round 1740 cm^{-1} of PECA, PPC, and PECA-PPC blends are magnified and represented in **Figure 2.3(b)**. The band of the carbonyl group of the blends with 2.5 wt.% and 5 wt.% content of PPC, namely PECA-2.5 and PECA-5, respectively, displayed a shift towards higher wavelengths, especially in blends with 2.5 wt.% of PPC (PECA-2.5). This displacement indicated that PPC weakened the intramolecular interactions between PECA chains (Fei et al., 2004). The lack of hydrogen donor groups in both PECA and PPC polymers limited the PECA-PPC interaction to dipole-dipole forces (Ajitha et al., 2020).

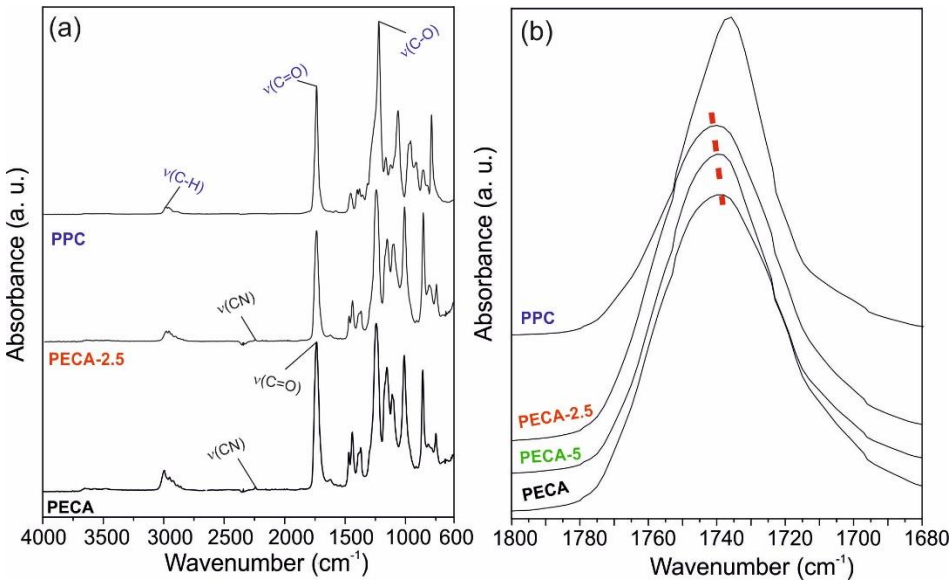

Figure 2.3 (a) The infrared spectra of the pristine PECA, blend PECA-2.5, and neat PPC, ranged from 4000 cm^{-1} to 600 cm^{-1}. The characteristic peaks of PECA, PPC are shown in black and blue, respectively. **(b)** Stretching vibration band of the carbonyl group ν(C=O) of pristine PECA, PPC, and PECA-PPC blends in 2.5 and 5 wt% of CA, labeled PECA-2.5 and PECA-5, respectively.

Figure 2.4(a) shows structural characteristics of caffeic acid, PPC, and PECA, while the infrared spectra of caffeic acid, PECA, PPC, and PECA-5-2 are represented in **Figure 2.4(b)**. The infrared spectra of caffeic acid exhibited the vibration bands associated with common hydroxycinnamic acids (Ge et al., 2006). The stretching vibration ν(O-H) was attributed to the carboxylic acid and hydroxyls groups of the benzene moiety, located in the range of 4000-2600 cm^{-1}, while the ν(C=O) vibration band of α,β-unsaturated carboxylic acid was located at 1645 cm^{-1}. The stretching vibrations of the alkene group ν(C=C) associated with the benzene group and acyclic double bond, conjugated in parallel with carboxylic acid produced vibration bands within 1640-1445 cm^{-1} (Ge et al., 2006; Yu et al., 2013). The spectra of PECA-5 filled with 2 wt.% of caffeic acid, exhibited the corresponding bands of PECA and some stretching bands attributed to the polyphenol. Peaks associated to the aromatic ring in the region 1680–1491 cm^{-1}, and the bands at 1645 cm^{-1} and the broadband ranging 4000-2600 cm^{-1}, corresponding to the ν(C=O) and ν(O-H) of the carboxylic group, respectively. Caffeic acid did not show noticeable changes or shifts in the main vibration bands of PECA in blends containing CA.

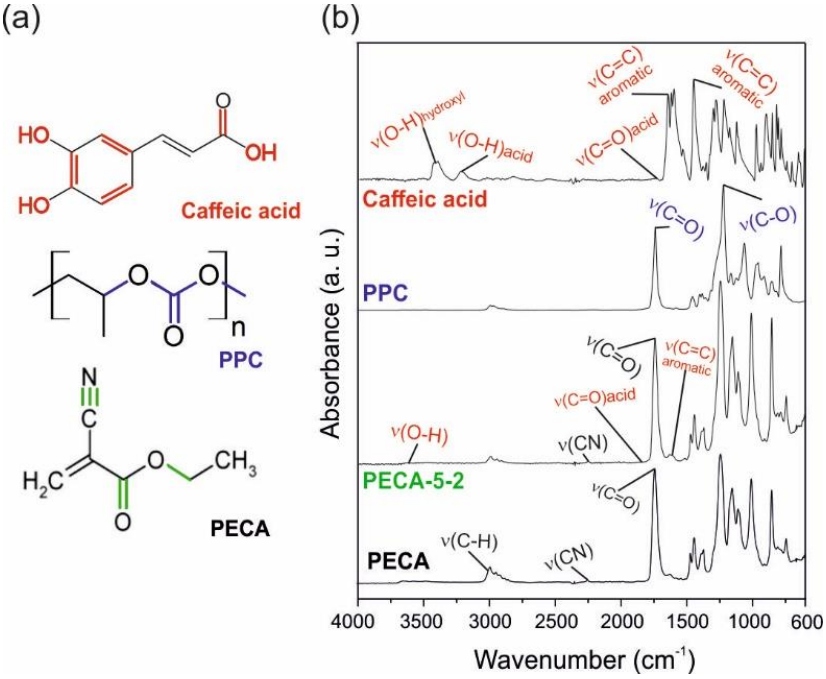

Figure 2.4 (a) The corresponding chemical structures caffeic acid, PPC, and PECA. The chemical bonds observed in the infrared spectra are marked in red, blue, and green for CA, PPC, and PECA, respectively. **(b)** The infrared spectra of the pristine PECA, PECA-5-2, caffeic acid, and PPC, ranged from 4000 cm^{-1} to 600 cm^{-1}. The characteristic peaks of PECA, PPC, and caffeic acid, are shown in black, blue, and red, respectively.

2.4.2 Morphological analysis

The morphology study was studied using electronic microscopy (SEM). **Figure 2.5(a-f)** shows the micrograph of the surface of the samples. The surface of neat PECA and PPC films were smooth and homogeneous, **Figure 2.5(a-b)**. The incorporation of PPC in 2.5 wt.% and 5 wt.%, modified the morphology of the surface in PECA blends, resulting in the formation of voids. These morphological defects are easily observed in immiscible polymer blends due to the phase-separation during the solvent evaporation. For example, Poly(3-hydroxybutyrate-co-3-hydroxyvalerate) and PPC blending films exhibited the same void patterns due to the low miscibility between the components (H. Pan et al., 2017; S. Zhang et al., 2015). The evaluation of the diameter of the voids of different samples was performed, and the histograms of the diameter of the voids are located inset each **Figure 2.5(c-f)**. PECA-2.5 showed very uniform-size voids varying from 1 µm to 2.5 µm (average diameter of 1.77 ± 0.29 µm), while the diameter of the voids

ranged from 2 µm to 4.5 µm in PECA-5 (average diameter 2.89 ± 0.25 µm). Interestingly, the caffeic acid modified the surface morphology of PECA-2.5 and PECA-5. In **Figure 2.5(e)**, PECA-2.5-1 showed a surface with a wider range of voids' diameter, varying from 0.5 µm to 6 µm, and a greater average of the diameter of voids with respect to PECA-2.5, showing 2.35 ± 1.27 µm and 1.77 ± 0.29 µm, respectively. In PECA-5-2 the diameter of voids ranged from 0 µm to 7 µm, and an average diameter was 2.09 ± 1.64 µm. This means that the size of voids was reduced to ~1 µm with the loading of 2 wt.% of caffeic acid in PECA-5 blends, while the overall dimension was more irregular. Nonetheless, these morphological defects did not affect the high transparency of the films.

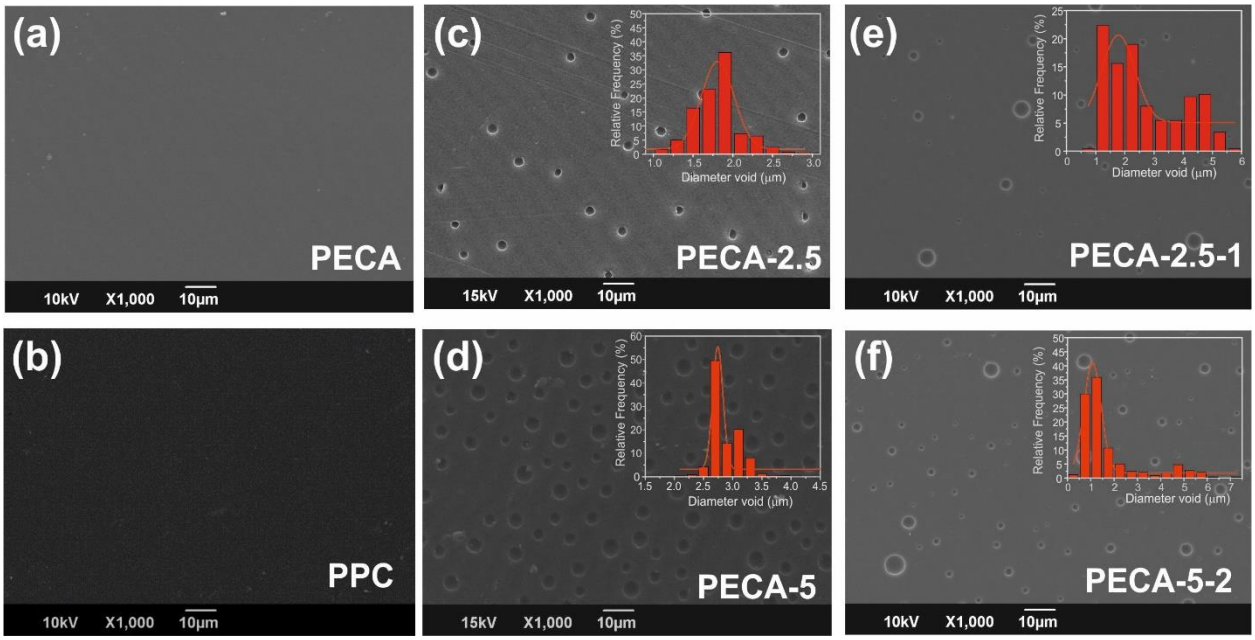

Figure 2.5 The surface images of **(a)** PECA and **(b)** PPC. The surface images and void diameter histograms inset of **(c)** PECA-2.5, **(d)** PECA-5, **(e)** PECA-2.5, and **(f)** PECA-5.2.

A further study of the surface-morphology was performed with a contact atomic force microscope (AFM). The topographic images of the samples are displayed in **Figure 2.6(a-d)**. These images were collected as a result of the signal sent by a cantilever that interacts with the surface detecting the defects and irregularities, like voids in this case. In **Figure 2.6(a-b)**, the surface of PECA-2.5 and PECA-5 blends present a higher density of voids (number of

voids/surface), with a constant size. Blends loaded with caffeic acid exhibited lower voids density and higher variability of the void's size. These results are in agreement with the size distribution analysis of SEM images, **Figure 2.5(c-f)**. Besides, the surface morphology is strongly linked to the interaction and dispersion in the inner matrix. It has been demonstrated that poly-disperse matrix present surfaces with random roughness, while voids-like surfaces are generally observed in the mono-dispersed matrix, **Figure 2.6(e-f)**.

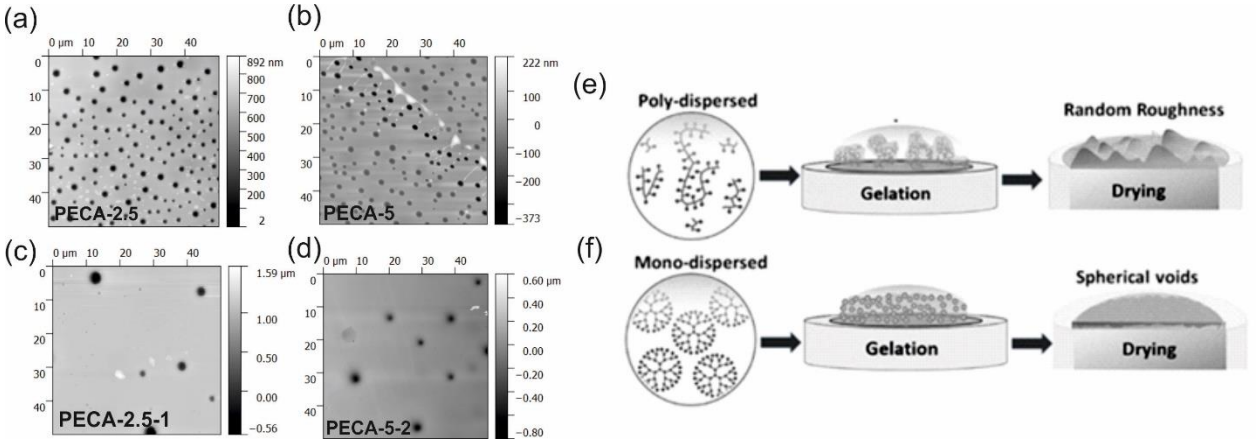

Figure 2.6 The topography AFM images of **(a)** PECA-2.5, **(b)** PECA-5, **(c)** PECA-2.5-1, and **(d)** PECA-5-2. **(e)** Poly-dispersed matrix results in films with random roughness. **(f)** Mono-dispersed matrix shows voids in the surfaces after the drying process.

The distribution of the PPC component was studied by analyzing the SEM images of the cross-section of the sample before and after etching-out the PPC with acetone. **Figure 2.7(a-h)** shows the SEM cross-section images of PECA blends. In **Figure 2.7(a-d)**, the cross-section images before etching out were highly homogeneous, while voids were distinguished only on the surface. However, after the immersion in acetone, numerous voids are displayed in the cross-section of films, **Figure 2.7(e-f)**. Results showed that PPC is distributed uniformly within the PECA matrix in form of micro-domains with the typical sea-island structure (Erba et al., 2019; S. Zhang et al., 2015).

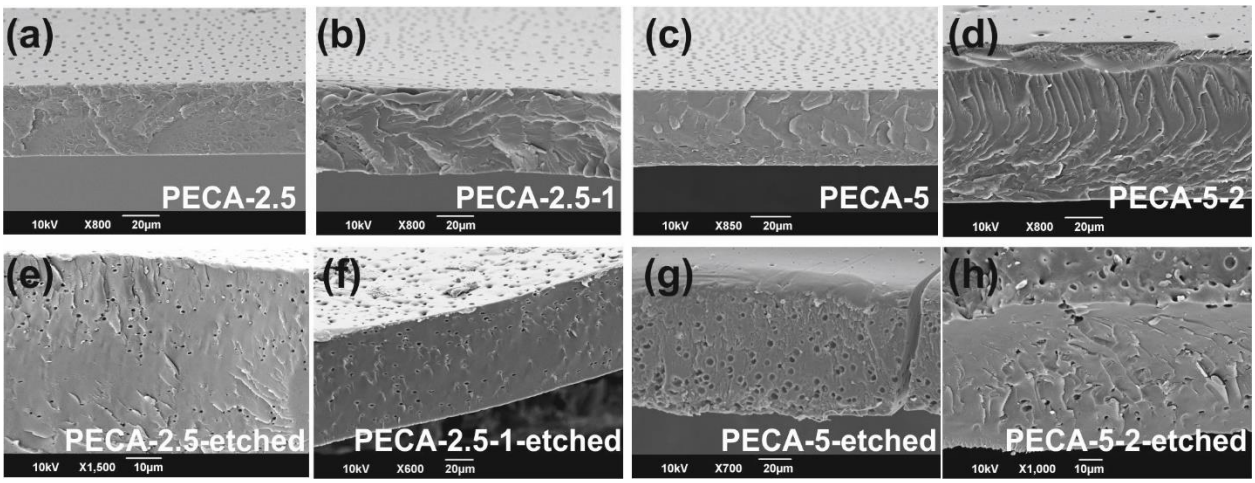

Figure 2.7 The SEM micrographs of smoothed and etched surfaces of **(a-e)** PECA-2.5, **(b-f)** PECA-2.5-1, **(c-g)** PECA-5, and **(d-h)** PECA-5-2.

2.4.3 Transparency and UV-blocking properties

The optical properties were measured in terms of transmittance, which is the percentage of light that passes through a material (percent transmission). The transmittance spectra in the range from 800 nm to 200 nm of all blends are represented in **Figure 2.8**. Transparency is desired for the application in the food packaging industry, providing a realistic perception of food conditions. Besides, UV-light blocking properties are strongly important for elongate food preservation during storage. This radiation promotes the generation of reactive oxygen species that contribute to the oxidation of lipids, which generates a loss of quality and the release of off-odor molecules from foods rich in fat, like meat and seafood (Tian et al., 2013).

The transparency is determined within the range from 800 to 400 nm. **Figure 2.8(a)** showed that the transparency decreased with the loading of PPC in 2.5 wt.%, to 80% with respect to ~100% displayed in neat PECA. When the content of PPC was doubled in PECA-5, the transparency dropped down to 60%, as exhibited in **Figure 2.8(b)**. Interestingly, results displayed in **Figures 2.8(a-b)** indicated that the transparency slightly increased with the incorporation of caffeic acid, independently of the concentration. The correlation between the transparency and the dispersion degree of the blend components is well-known (Oleyaei et al., 2016). As expected, caffeic acid also provided UV-blocking properties to PECA blends, avoiding the passing light in the entire range of the hazarding UV-light radiation (UVA, UVB, and UVC) (de Moraes Crizel et al., 2016).

Commonly, natural molecules absorb the radiation in the range of the UV. However, the strong color affects negatively the transparency, obtaining materials with high opacity (Eça et al., 2015; Xu et al., 2018). Concentrations of caffeic acid in 1 and 2 wt.% were enough to block the UV-light, avoiding the loss of transparency.

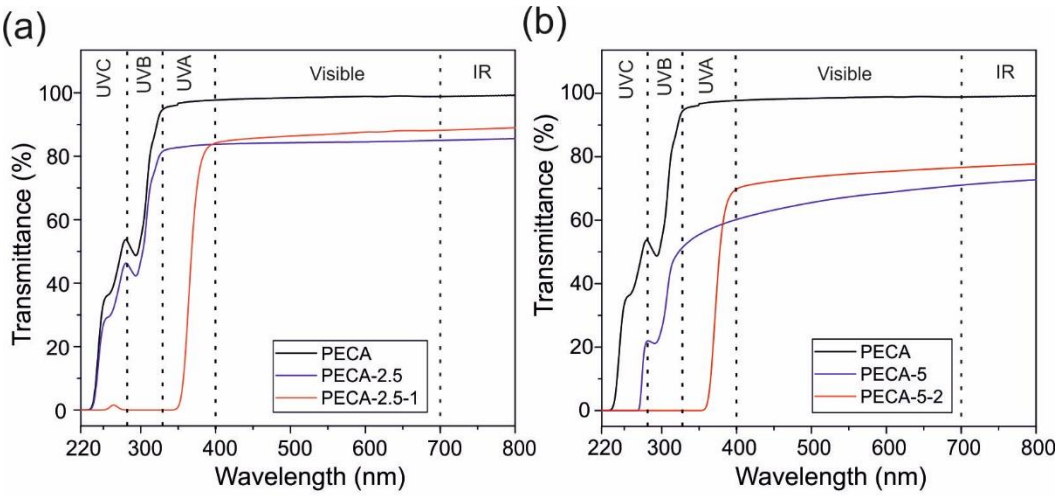

Figure 2.8 The transmittance spectra in a range from 800 to 220 nm of pristine PECA, PECA-2.5, and PECA-2.5-1, marked in black, blue, and red, respectively. **(b)** PECA, PECA-5, and PECA-5-2, colored in black, blue, and red, respectively. The UV-radiations are indicated. The thickness of all samples was around ~80 nm.

2.4.4 Mechanical behavior

Figure 2.9(a) exhibits the stress-strain curve of pristine PECA and PECA-PPC blends. The values of Young's Modulus (YM) and elongation at break (%) are represented in the table of **Figure 2.9(b)**. Pristine PECA exhibited a brittle behavior with ~1.4 GPa of YM and 1.7% of elongation, typical of cyanoacrylates, while pristine PPC showed elongation values of three measure-unites above the elongation of the acrylic polymer, ~1440% (Mizrahi et al., 2011). The incorporation of PPC maintained the values of YM of the neat PECA but improved greatly the elasticity, in ten and two times respect to the neat PECA film, for PECA-2.5 and PECA-5. The plasticizing character of PPC, loaded in 2.5 wt.%, was already observed in the infrared spectra, whose displacement of the band corresponding to the carbonyl group indicated the weakening of the intermolecular bonding of PECA, see **Figure 2.3(b)** The incorporation of caffeic acid reduced

slightly the YM of the films in comparison to the respective PECA-PPC blends. Besides, the elongation of PECA-2.5-1 decreased to half of the value obtained in PECA-2.5. The elongation of PECA-5 blends was slightly improved with the incorporation of 2 wt.% of caffeic acid, from ~3.3% to ~5.2%.

(a) (b)

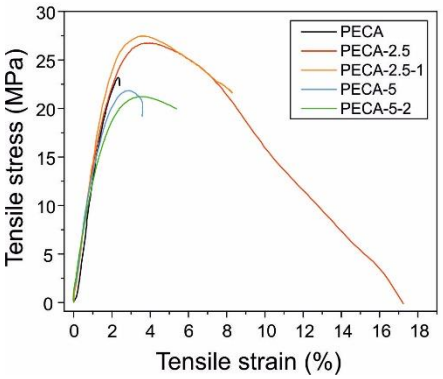

Sample labeled	Elastic modulus (MPa)	Elongation (%)
PECA	1344 ± 268	1.67 ± 0.6
PPC	22.05 ± 4.1	1438.4 ± 62.6
PECA-2.5	1254 ± 11	17.4 ± 0.2
PECA-2.5-1	1185 ± 349	8.9 ± 0.9
PECA-5	1323 ± 137	3.34 ± 0.8
PECA-5-1	1328 ± 322	3.4 ± 1.2

Figure 2.9 (a) The tensile stress-strain curve of PECA (black), PECA-2.5, and PECA-5, represented in red and blue, respectively. PECA-2.5-1 and PECA-5-2 are plotted in orange and green, respectively. **(b)** Table with Young's modulus (MPa) and percent elongation values calculated for all blends.

2.4.5 Hydrophobicity and Water vapor uptake measurements

Pristine PECA and PECA-PPC films exhibited a high hydrophobic character with an average static contact angle of about 100%, similar to polyethylene and low polyethylene-based materials (Panrong et al., 2019; Zia et al., 2019). The incorporation of caffeic acid did not modify the hydrophobicity and the values of the static contact angle were similar. The water uptake results are represented in **Figure 2.10**. PECA-PPC films showed water uptake values below 5%, which indicated a strong hydrophobic character. The incorporation of caffeic acid led to higher values of water uptake, 7% and 10% in PECA-2.5-1 and PECA-5-2, respectively, due to the hygroscopic nature of the polyphenol (S. S. Khan et al., 2016). Generally, low water sensitivity is desired for developing food-packaging materials (Gaikwad et al., 2019). Containing-CA blends exhibited lower water uptake values, equal to other polymers designed for packaging applications, such as PCL-starch blends (Alix et al., 2013).

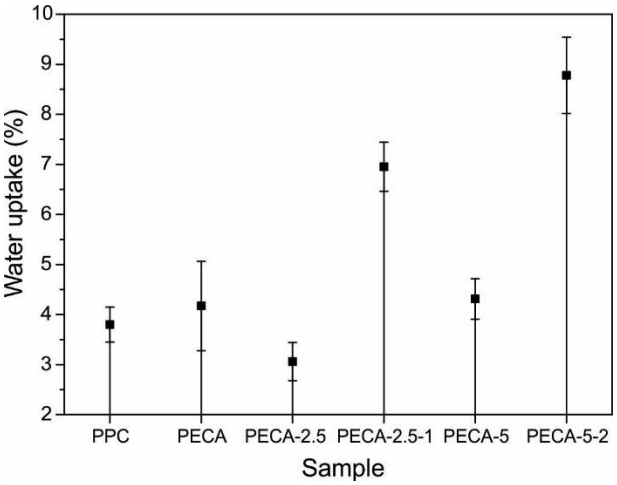

Figure 2.10 Values of the water uptake of all film blends when exposed to an environment of 100% humidity.

2.4.6 Water vapor barrier properties

The values of water vapor permeability of PECA blends are represented in **Figure 2.11(a)**. Blending PECA with PPC improved further the water vapor barrier properties, in around one unit independently to the amount of PPC added. The WVP responses of films containing caffeic acid were linked to the polyphenol-concentration. In PECA-2.5-1, the incorporation of 1 wt.% of caffeic acid slightly reduced the water permeability of PECA-2.5, while 2 wt.% of CA led to higher water vapor permeability, see PECA-5-2. As explained below, the hygroscopic character of caffeic acid likely promoted the water permeation at a high relative humidity (100%). **Figure 2.11(b)** compares the WVP obtained in PECA-PPC films with commercial polymers for packaging. Noticeably, the water vapor permeability of PECA blends was comparable to HPDE and PCL, which demonstrated the great water vapor barrier performance of current PECA blends (Bastarrachea et al., 2011; Figueroa-Lopez et al., 2018; Sharmin et al., 2012).

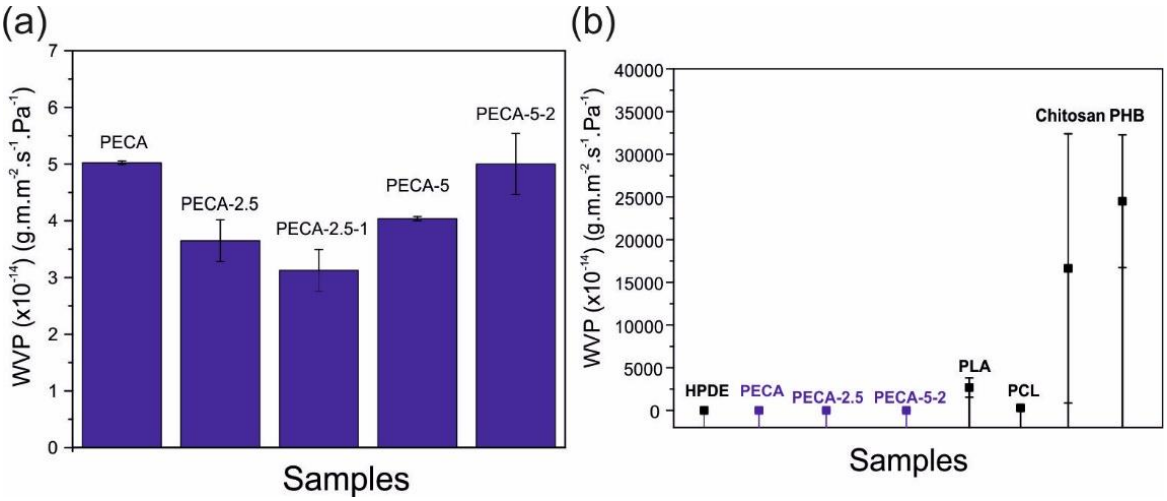

Figure 2.11 (a) Water vapor permeability values of all PECA blends. **(b)** Comparison of water vapor permeability (WVP) with commercial polymers such as high-density polyethyelene (HDPE) (Bastarrachea et al., 2011), poly(lactic acid) (PLA) (Armentano et al., 2015; Patwa et al., 2018), polycaprolactone (PCL) (Figueroa-Lopez et al., 2018; Sharmin et al., 2012), chitosan (Lozano-Navarro et al., 2017; Sharmin et al., 2012), polyhydroxybutyrate (PHB) (Armentano et al., 2015), low-density polyethylene (LDPE), LDPE with 1% wt. of linanool (LDPE*) (Bastarrachea et al., 2011).

2.4.7 Oxygen barrier properties

Figure 2.12(a) displays the barrier properties against oxygen of PECA blends. Contrary to the water vapor permeability, PPC blending facilitates the oxygen transmission, especially in PECA-2.5 while PECA-5 did not cause any significant change with respect to neat PECA. This behavior could be related to the chemical modification resulted when PPC in 2.5 wt.% was incorporated into the structure, more noticeable than in PECA-5 blends. The scavenging activity of caffeic acid reduced greatly the passing of oxygen through the PECA-2.5 blend, while the value of oxygen permeability of PECA-5-2 remained similar to the film without caffeic acid (PECA-5). The fact that PECA-2.5-1 and PECA-5-2 did not deteriorate OP performance of pure PECA is encouraging considering other benefits such as UV-blocking properties and the ductility of the blend. Nevertheless, in **Figure 2.12(b)**, films exhibited excellent oxygen permeability properties in comparison with conventional polymers used in packaging, only overcame by PLA, PCL, and chitosan (Armentano et al., 2015; Figueroa-Lopez et al., 2018; Patwa et al., 2018; Sharmin et al.,

2012).

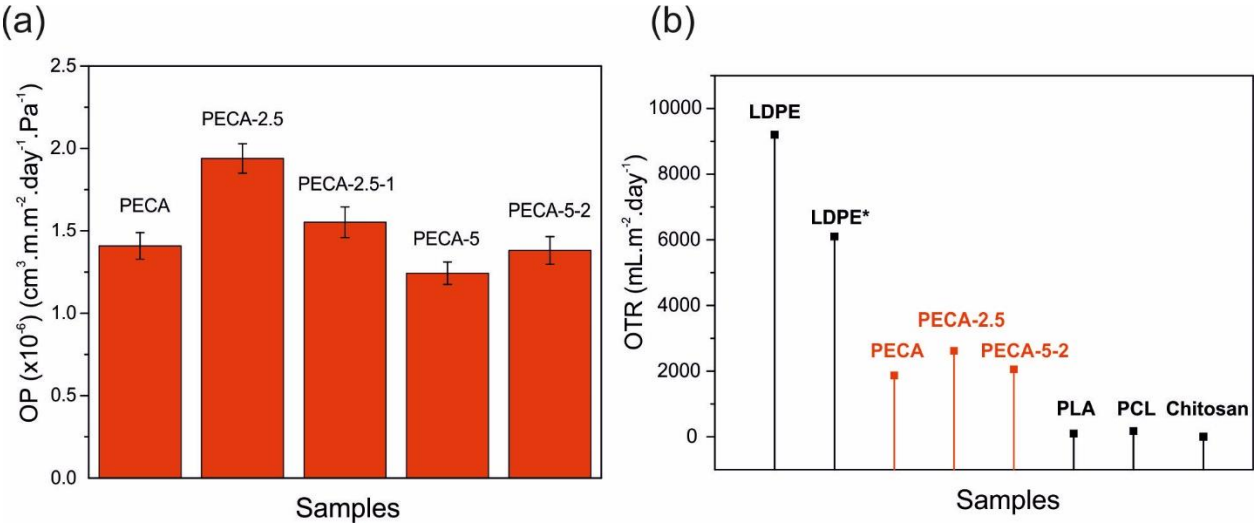

Figure 2.12 (a) Oxygen permeability (OP) values of all PECA-blends. **(b)** Comparison of oxygen transmission rate (OTR) with commercial polymers such as high-density polyethyelene (HDPE) (Bastarrachea et al., 2011), poly(lactic acid) (PLA) (Armentano et al., 2015; Patwa et al., 2018), polycaprolactone (PCL) (Figueroa-Lopez et al., 2018; Sharmin et al., 2012), chitosan (Lozano-Navarro et al., 2017; Sharmin et al., 2012), polyhydroxybutyrate (PHB) (Armentano et al., 2015), low-density polyethylene (LDPE), LDPE with 1% wt. of linanool (LDPE*) (Bastarrachea et al., 2011).

2.4.8 Migration study

The release of the antioxidant was measured by monitoring the immersed samples at different collection times. The calibration curve of the concentration of caffeic acid against the absorption value of the characteristic peak of CA (327 nm), displayed in **Figure 2.2** (section 3.4.8), permitted obtaining the concentration of CA released when the peak at 327 was measured at different time-points, **Figure 2.13(a)**. Ethanol is considered the main solvent used for preparing fatty food simulant solution, thus, this solvent was used to simulate the migration of caffeic acid from the film into foods with a food system rich in lipids (Benbettaieb et al., 2018; Zia et al., 2019). The high solubility of caffeic acid in ethanol, against water, enhanced the release out of the sample with time. **Figure 2.13(b)** represents the migration values in terms of mg caffeic acid/g film of PECA-2.5-1 and PECA-5-2 against the release time. After 24 hours of release, PECA-2.5-1

released about 11 mg/g film of antioxidant, and PECA-5-2 released 25 mg/g film. Generally, high values of migration are linked to strong antioxidant activity. Besides, samples displayed a controlled-migration with no burst, which highlighted the suitability in drug delivery (J. H. Lee & Yeo, 2015).

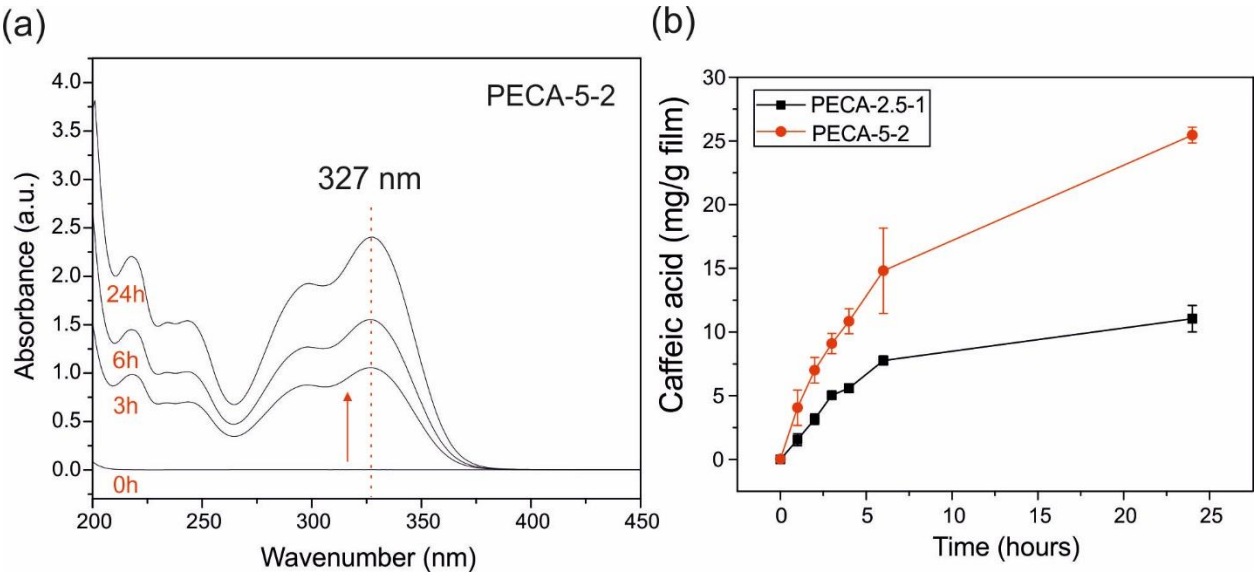

Figure 2.13 (a) The UV-vis spectrum of the monitoring of the caffeic acid release from PECA-5-2 film at 0h, 3h, 6h, and 24h, an ethanolic solution. The characteristic peak of caffeic acid (327 nm) is remarked. **(b)** The kinetic release of caffeic acid, in terms of mg/g film, in fatty food simulant measured for 24 hours.

2.4.8 Antioxidant activity

Oxidation is the main problem for the preservation of foods leading to loss of quality and nutrients reducing the shelf-life. Radicals participate actively in food oxidation, the release of antioxidants annul the radicals via scavenging limiting these damaging reactions (Tian et al., 2013). Sample (3 mg) was immersed in 3 mL of $DPPH^{\cdot}$ radical solution and the radical scavenging activity (RSA) was evaluated via UV-spectroscopy. Figure **2.14(a)** shows the UV-vis spectra of the characteristic band of the radical (517 nm) and the real pictures of the radical solution at the beginning of the experiment and after 4 hours. At time-point zero, the peak at 517 nm was very intense, but then, when films were immersed, the characteristic peak decreased over time. The antioxidant activity of PECA-PPC films was monitored at different times against the radical

DPPH·, represented in **Figure 2.14(b)**. Furthermore, 100% of radical inhibition was attained after 2 hours for both films corresponding to 3 and 7 mg/g film of caffeic acid for PECA-2.5-1 and PECA-5-2, respectively. This reveals the great antioxidant capacity of caffeic acid when is released in a fatty environment and underlines the potential of these blend films to preserve foods rich in lipids, such as meats and oils, to avoid undesired lipid oxidation. Such an effect was also observed by immobilization of caffeic acid on commercial polypropylene films against the oxidation of linoleic acid and β-carotene, found in high concentrations in oils (Arrua et al., 2010).

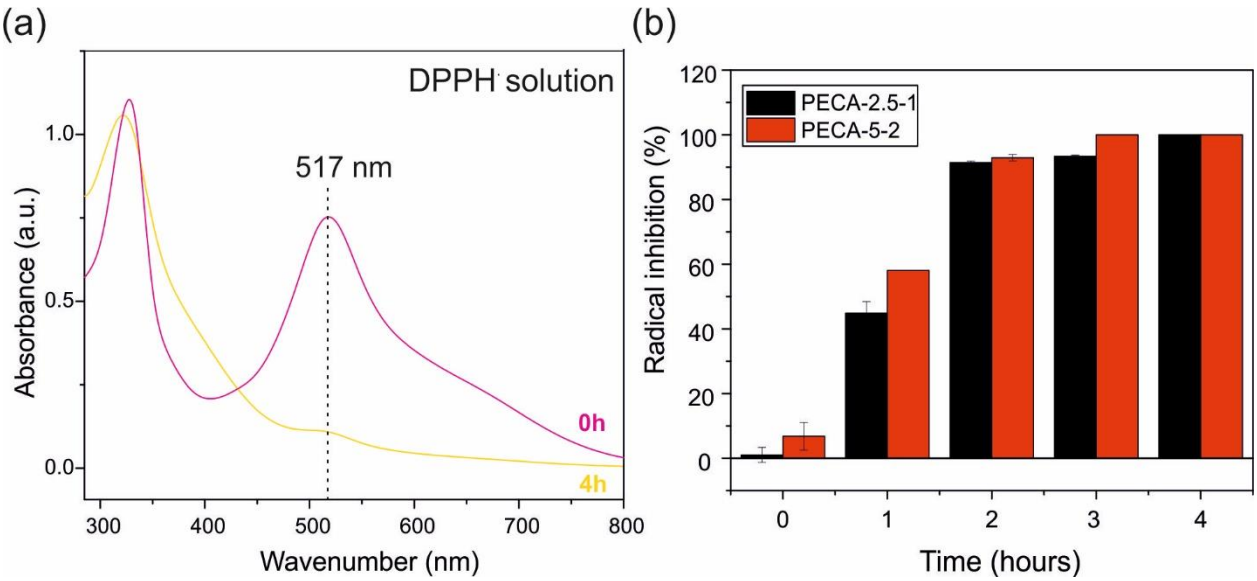

Figure 2.14 (a) The characteristic absorption peaks of DPPH· the radical solution at the beginning of the experiment, in violet, and after four hours in contact with the antioxidant (yellow lines). **(b)** The radical inhibition values (%) of PECA-2.5-1 and PECA-5-2, represented in black and red, respectively, for each hour during four hours of the experiment.

2.5 Conclusion

Transparent, UV-blocking, and antioxidant PECA–PPC polymer blend films containing caffeic acid were fabricated from biodegradable polymers. The films demonstrated multifunctional properties such as good UV-blocking capability, antioxidant effect, maintaining the good water vapor and oxygen barrier properties of typical acrylics. Films were colorless and highly transparent, contrary to the characteristic colorful materials obtained from natural antioxidants.

Besides, films exhibited a controlled-release of the antioxidant into food simulant. Therefore, these new transparent and active bioplastics present suitable properties for replacing inert and environmental-damaging plastics used daily in the food-packaging industry.

Chapter 3: Using food-wastes to create active and antioxidant bioplastics

3.1 Comparison of physicochemical, mechanical, and antioxidant properties of polyvinyl alcohol films containing green tealeaves waste extracts and discarded balsamic vinegar

The food waste discards reached 1.3 billion annually around the world (Dilucia et al., 2020). These residues ended up accumulating in landfills or incinerating with important environmental consequences (ex. emission of greenhouse gases or methane) (Dilucia et al., 2020). Among food wastes, the excesses of vegetable and fruit by-products represent 40-50% of the total discards. However, fruit and vegetable by-products are a source of macromolecules and antioxidant and antimicrobial compounds that can be used as a substrate to produce new materials or to activate daily-life polymers used in packaging application (Munteanu & Vasile, 2020). These materials will provide many advantages such as economic feasibility and low-environmental impact.

The oxidation in foods leads to several physicochemical changes that result in the loss of the nutrients and quality of the food products (Munteanu & Vasile, 2020). Synthetic antioxidants, such as butylhydroxyanisole (BHA) and butylhydroxytoluene (BHT), have been added to the packaging with the aim to reduce the oxidation reaction effects. However, these additives exhibited carcinogenic effects and toxicity, as well as ecological impact, which promoted the searching for new natural antioxidants derived from natural resources (R. Liu & Mabury, 2020). Food discards have been demonstrated to be an excellent alternative to replace these damaging antioxidants. Food wastes can be processed to obtain an extract, isolating the molecules of interest, or added directly to the polymeric matrix.

The well-known antioxidant capacity of green tea leaves derives from a type of polyphenols called catechins. The main catechins present in green tea: (-)-epigallocatechin gallate (EGCG), (-)-epigallocatechin (EGC), (-)-epicatechin gallate (ECG), (-)-epicatechin (EC), gallocatechin gallate (GCG), (+)-gallocatechin (GC), catechin gallate (CG), and (+)-catechin (C). Moreover, these bioactive molecules have shown antimutagenic, anticarcinogenic, and UV-protector properties (Gramza et al., 2005). The efficacy of tea catechins has been already demonstrated in the food industry, when the incorporation of green tea into thermoplastic starch-based films reduced the lipid oxidation of soybean oil by up to 38%, as well as extending the shelf-life of bacon slides (Panrong et al., 2019). Balsamic vinegar is a natural product prepared with cooked and concentrated locally grape must, rich in polyphenols, especially colored and uncolored melanoidins (Arvanitoyannis et al., 2011). Arvanitoyannis *et al.,* has demonstrated the

antimicrobial capacity of balsamic vinegar inhibiting the growth of psychrotrophic bacteria on lettuce (Arvanitoyannis et al., 2011). Besides, the chemical composition of the vinegar has provided health benefits, such as exceptional antimicrobial, antidiabetic, and antihypertensive properties (Ho et al., 2017).

Polyvinyl alcohol (PVA) is a common biodegradable, biocompatible, and transparent polymer with good oxygen barrier properties. The great solubility of PVA in aqueous solution has promoted its application in many fields including controlled drug delivery systems, film formation, and packaging (Hassan & Peppas, 2000). Novelty properties have been developed in PVA films by incorporating natural derivatives like seaweed extracts and pomegranate peel (Guzman-Puyol et al., 2017; He et al., 2019). However, direct incorporation of processed plant food waste or its extracts into PVA polymer is rather scarce. For instance, the development of polyvinyl alcohol and apple pomace (apple juice waste) bio-composite films with antioxidant properties for active food packaging applications was reported using direct mixing in hot water (Gaikwad et al., 2016).

The current project presents one-pot fabrication approach to fabricate antioxidant PVA films containing significant amounts of antioxidants from processed green tealeaves waste and commercially discarded balsamic vinegar. No prolonged and multistep procedures are needed to produce such antioxidant polymer films. Dried used green tealeaves were dispersed in formic acid and after filtering out; the solution was combined with a PVA-formic acid solution. In the case of discarded vinegar, the vinegar was directly added to aqueous PVA solutions, and films were cast and dried in both cases. Up to 50 wt.% of used green tealeaves waste extracts and discarded balsamic vinegar could be incorporated in PVA using this simple one-pot approach. Very high yields (>95%) of gallated catechins were extracted using formic acid such as a potent antioxidant known as epigallocatechin gallate (EGCG). Both formic acid (residual) and balsamic vinegar effectively plasticized PVA with elongation at break values of 150% and 30%, respectively. Discarded balsamic vinegar was also effective as an antioxidant, also improving oxygen barrier properties of PVA.

3.2 Materials

Formic acid (≥98%), polyvinyl alcohol (PVA) (typical average Mw 89000-98000 g/mol, 98% hydrolyzed), ABTS (2,2-azino-bis-(3-ethylbenz-thiazoline-6-sulfonic acid), Trolox ((±)-6-

hydroxy-2,5,7,8-tetra-methylchromane-2-carboxylic acid) and gallic acid were purchased from Sigma-Aldrich Chemie (Steinheim, Germany). India origin green tea bags (Everton Tea India Pvt., Ltd.) were purchased from a local supermarket. Discarded balsamic vinegar (Aceto Balsamico Di Modena Igp) was donated by Villa Matilde SpA, Italy. Deionized water obtained from a Milli-Q Advantage A10 Ultrapure Water Purification device. DPPH (2,2-diphenyl-1-picrylhydrazyl) was purchased from Alfa Aesar (Germany).

3.2.1 Chemical characterization of tea waste extract

The chemical composition of the tealeaves and tealeaves waste extracts with water and formic acid was evaluated with high-resolution ultra-performance liquid chromatography (UPLC) with mass spectroscopy (UPLC-MS/MS) using a Waters (Milford, MA, USA) QToF Synapt G2 HDMS mass spectrometer coupled to an Acquity UPLC system. Extracts were prepared by adding 3 g of dry material in 60 mL of solvent (water and formic acid) stirring for 120 minutes at room temperature and filtered through Whatman N°1 filter paper. The corresponding solution was diluted 50 times in 3% acetonitrile for UPLC-MS/MS analysis. The separation of metabolites was performed using a reversed-phase C18 column (BEH 2.1 X 50 mm, 1.7 micron particle size) by using a linear gradient of acetonitrile in water (5 to 100% in 5 minutes). Flow rate was set to 0.5 mL/min. Both eluents (water and acetonitrile) were added with 0.1% formic acid. Five microliters of samples were injected into the system. Mass spectra were acquired in negative electrospray mode (ESI-) in the 50-1200 m/z mass range. Tandem mass spectra were continuously acquired in MSe mode over the same mass range. Leucine encephalin 2 µg/mL was continuously infused in the Lockspray source for on-line spectral recalibration. Tea metabolites were identified based on their accurate mass (within 3 ppm mass accuracy), the corresponding calculated brute formula and isotopic profile, and, whenever possible, their MS/MS spectrum. METLIN and HMDB publicly available databases were consulted for the identification of catechins. A scheme image of the UPLC-MS/MS technique was displayed in **Figure 3.1.**

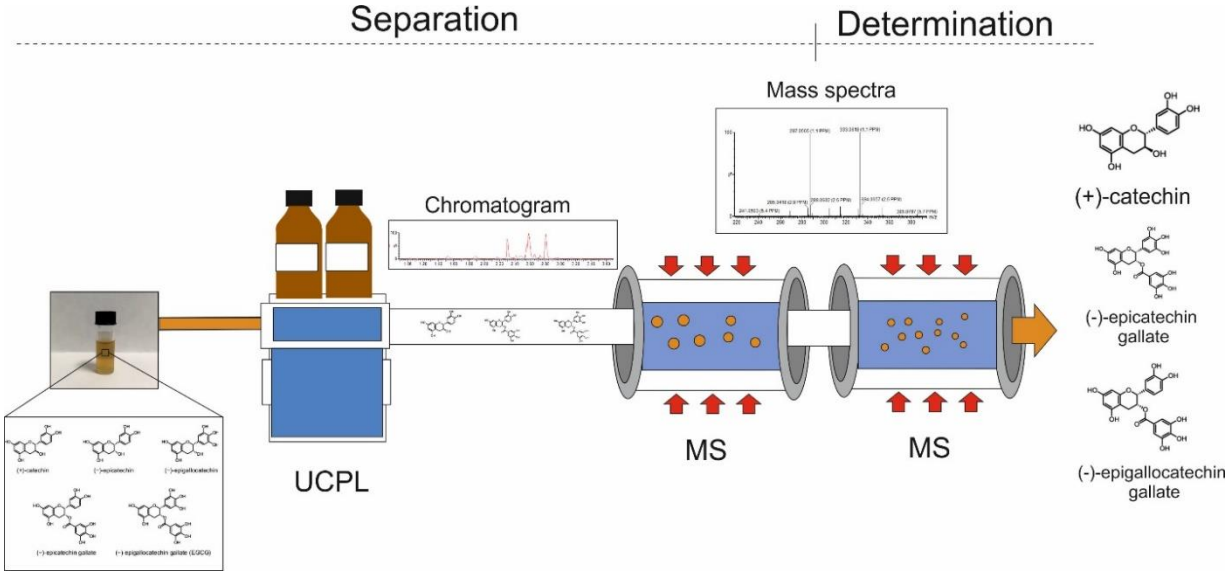

Figure 3.1 Operating schema of UCPL-MS/MS to isolate and identify the molecules contained in the tea biomass.

3.2.2 Preparation of the films

The fabrication procedures for the antioxidant discarded vinegar films are schematically shown in **Figure 3.2**. Tea waste was obtained by immersion of 20 paper bags (one bag contains 2 g processed tealeaves) of commercial green tea bags into pre-boiled 5 L of tap water at 100 °C while stirring. After 30 minutes, tea bags were collected and introduced in the convection oven at 70 °C until complete drying. Then, the recovered tealeaves (waste tealeaves) were extracted adding 3 g of waste tealeaves in 60 mL of formic acid and stirring for 120 minutes at room temperature. The extract solution was filtered through Whatman N°1 filter paper. Then, different volumes of waste tea extract (14.48 mg/mL ± 1.64) were added directly to a formic acid solution of PVA (15 mg/mL) while stirring to ensure a homogeneous blend. A control PVA film in formic acid was also casted with the same concentration of 15 mg/mL. Then, PVA with formic acid and tea films were made by casting equal volumes of each solution in polystyrene Petri dish molds (90 mm in diameter). The solutions were allowed to dry under a chemical hood for 6 days. Resultant films were colored but transparent containing various concentrations (i.e., 5, 10, 20, and 50 wt.%) of used green tea extracts. These films were labeled as Tw5, Tw10, Tw20, and Tw50.

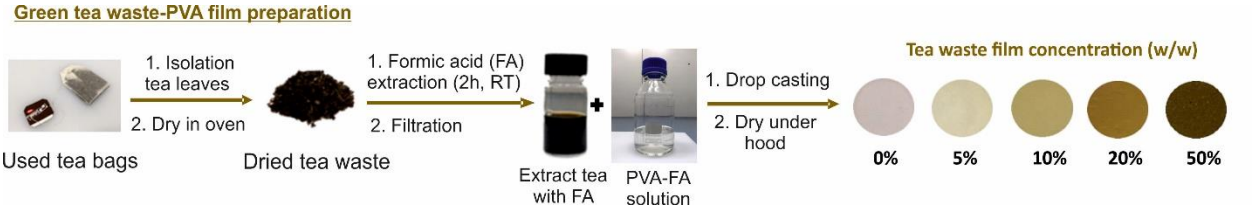

Figure 3.2 Fabrication scheme of the PVA films filled with the tea-waste extract.

Figure 3.3 shows the fabrication method of PVA films based on balsamic vinegar, balsamic vinegar-PVA films were fabricated by dissolving PVA (15 mg/mL) in boiling water and stirring until complete dissolution. Then, different volumes of balsamic vinegar waste (182 mg/ml: concentration calculated based on drying vinegar) were added to the PVA aqueous solution. A control PVA film in water was also casted with the same concentration of 15 mg/mL. Solutions were poured into polystyrene Petri dish molds (90 mm in diameter) and dried in an oven at 70 °C overnight. Films containing 5, 10, 20, and 50 % (w/w) of balsamic vinegar waste were fabricated. These films were labeled as DV5, DV10, DV20, and DV50. Pure PVA films cast from water and formic acid were labeled as PVAw and PVAf, respectively. Films were briefly conditioned at 70^{o}C to remove any adsorbed water and measurements were immediately conducted.

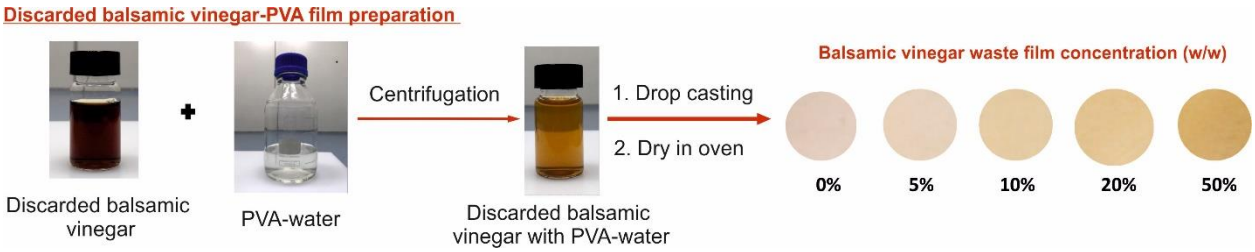

Figure 3.3 Fabrication scheme of the PVA films filled with balsamic vinegar discarded.

3.3 Analysis methods

3.3.1 Attenuated Total Reflection Fourier Transform Infrared (ATR-FTIR)

Infrared spectra were obtained with a single-reflection attenuated total reflection (ATR) accessory (MIRacle ATR, PIKE Technologies) coupled to a Fourier Transform Infrared (FTIR)

spectrometer (Equinox 70 FT-IR, Bruker). All spectra were recorded in the 3800 to 600 cm^{-1} range with a resolution of 4 cm^{-1}, accumulating 64 scans to reduce the spectral noise.

3.3.2 X-ray diffraction

XRD measurements were performed by using a PANalytical Empyrean X-ray diffractometer equipped with a1.8 kW Cu Kα ceramic X-ray tube, PIXcel3D 2X2 area detector, and operating at 45 kV and 40 mA. The diffraction patterns were collected in Parallel-Beam (PB) geometry and symmetric reflection mode using a zero-diffraction silicon substrate over an angular range: 2θ = 5-70°, with a step size of 0.026°. XRD data analysis was carried out using HighScore 4.5 software from PANalytical.

3.3.3 Fluorescence spectroscopy

The fluorescence spectroscopy of catechins in waste tealeaves extracts was made by inserting dry films in a Horiba Jobin Yvon Fluoromax-4 spectrofluorometer. Emission spectra of PVA-tea waste films with different concentrations at 60° were recorded in the range of λ=300-500 nm at an excitation wavelength λ_{ex}=280nm. Results were normalized to the thickness of the film. Fluorescence photomicrographs were obtained with a fluorescence confocal microscope Nikon A1 using 405 laser for excitation and 450-50 bandpass filter for the emission modes. A magnification of 20× was used for imaging.

3.3.4 Scanning Electron Microscopy (SEM)

Surface and cross-section morphologies of samples were characterized by scanning electron microscopy (SEM), using a JEOL JSM-6490LA microscope working in high vacuum mode, with an acceleration voltage of 10 kV of accelerating voltage. For the cross-section analysis, samples were immersed for a few seconds in liquid nitrogen to enhance the break and then, scratched with the aid of tweezers. Before the analysis, samples were mounted on stubs and coated with 10nm of gold.

3.3.5 Stress-Strain measurements

Mechanical properties of the films were measured by uniaxial tensile tests on a dual column Instron 3365 universal testing machine. Dog-bone shaped samples had a gauge length of 25 mm and a width of 4 mm. Strain displacement was applied at the rate of 20 mm/min. Stress-strain curves were recorded at 25°C and 44% RH. At least ten measurements were conducted for each sample and results were averaged to obtain a mean value. The Young modulus and elongation at break values were calculated from the stress-strain curves using the built-in software of the tensile tester.

3.3.6 Antioxidant activity against different radicals, and TEAC evaluation

The antioxidant capacity of the PVA-blends was determined by measuring the free radical scavenging activity of antioxidants molecules released from the sample by standard (2,2-azino-bis-(3-ethylbenz-thiazoline-6-sulfonic acid) ($ABTS^{+\cdot}$) and 2,2-diphenyl-1-picrylhydrazyl radical ($DPPH^{\cdot}$) methods. Briefly, when the antioxidant film, 78.54 mm^2 (10 mm of diameter), is immersed in 3 mL of the radical solution, the antioxidant migrated from the film react against the radical leading to a UV-Vis detectable color change. The $ABTS^{+\cdot}$ cation radical solution is prepared by the reaction of 7 mM ABTS stock solution with 2.45 Mm potassium persulfate in the dark at room temperature within 12 to 16 h. For preparing $DPPH^{\cdot}$ radical solution, 0.1 mM of DPPH was dissolved in ethanol. Tests were done by diluting the radical solution with water until its abortion reached 0.8 a.u. at the characteristic absorption band, 734 nm and 517 for $ABTS^{+\cdot}$ and $DPPH^{\cdot}$ radicals, respectively. Extracts from the solutions were collected at certain immersion time-intervals from 0 to 24 hours for waste tealeaves samples and up to 72 hours for vinegar waste samples. The absorption values were collected by a Cary JEOL UV-spectrophotometer. The antioxidant activity (radical scavenging activity, RSA) was estimated using **Equation 1** below.

$$\text{Radical scavenging activity (\%)} = 1 - \frac{A_1 - A_2}{A_3} \text{ x } 100 \quad (\mathbf{1})$$

In the equation above, A_1 is the absorbance of the sample solution with $ABTS^{+\cdot}$ at 734 nm, A_2 is the absorbance of the sample solution at the same wavelength (734 nm), and A_3 is the absorbance

of the $ABTS^{+\cdot}$ control solution. All measurements were performed at least five times to ensure reproducibility.

The antioxidant capacity of the composite films was also evaluated using a standard protocol known as Trolox equivalent antioxidant capacity (TEAC) per weight of the dried film, expressed as μmoles of trolox/g dried film. For this, only selected polymer film samples were utilized. This analysis allows us to compare the antioxidant effect with other published systems containing natural antioxidants. For this, only selected polymer film samples containing 10 wt.% and 50 wt.% of waste were utilized. The calibration curve that represents the concentration of Trolox (μg/mL) against RSA of the $ABTS^{\cdot+}$ and $DPPH^{\cdot}$ were displayed in **Figure 3.4(a-b)**, respectively. The values of RSA obtained against each radical following the methods described in (Pellegrini et al., 2003) when films were immersed for one hour in the radical solution was plotted and the Trolox equivalent (μmoles of trolox/g dried film).

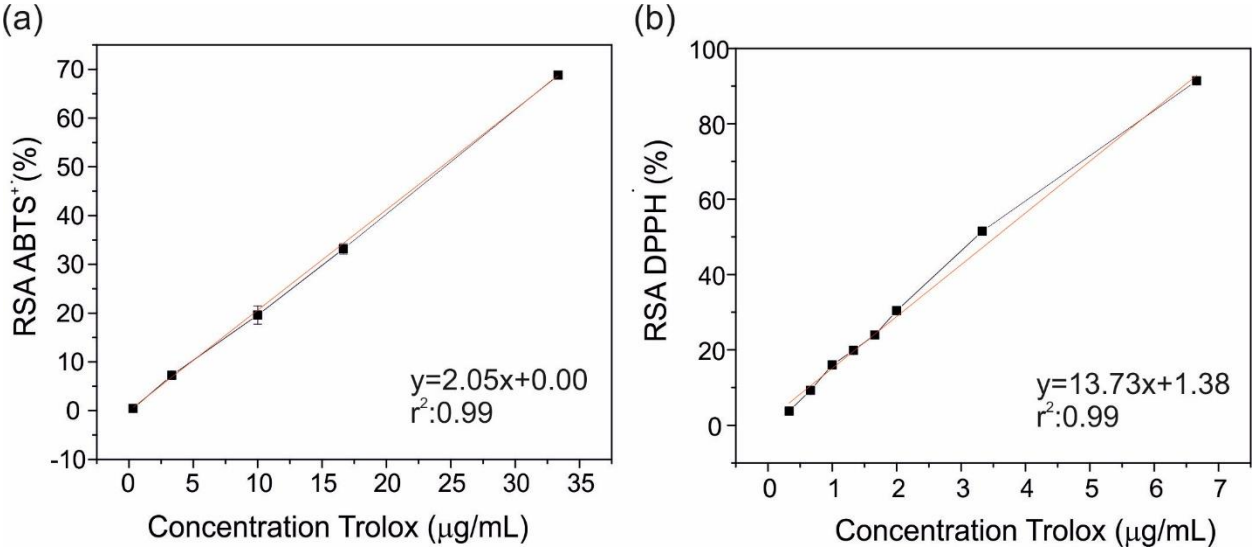

Figure 3.4 The curve obtained from representing the concentration of Trolox (Mm) against the radical scavenging activity (%) of **(a)** the radical $ABTS^{+\cdot}$ and **(b)** $DPPH^{\cdot}$.

3.3.7 Calculation of IC50 value

The half-maximal inhibitory concentration (IC50) indicates the concentration of antioxidant that inhibits 50% of the radical (Pasrija et al., 2015). This value indicates the

antioxidant capacity of the solutions and was calculated for discarded balsamic vinegar, the solutions of unused tea extracted with water and formic acid, and the solutions of tea waste extracted with water and formic acid. To obtain the IC50 values, the radical scavenging activity (RSA) of the set of the antioxidant solutions at different concentrations was calculated following the procedure explained in section 4.36. The radical scavenging activity (RSA) against the cation radical $ABTS^{\cdot+}$ was plotted against the concentration of the antioxidant in the solution, varying the volume of the extract from 100 µl to 1000 µl. Then, these vials were filled until 1 ml with water. The antioxidant assay was performed adding 2 ml of the cation radical solution to all vials reaching a final volume of 3 ml. Measurements were conducted after 60 minutes for the ABTS assay (L. S. Lee et al., 2014). The calibration curve represented the concentration of the antioxidant solutions versus the radical scavenging activity (RSA). All measurements were performed five times to guarantee reproducibility results.

- IC50 tea in water

The stock solution of tea water extract had a concentration of 14.5 mg/ml. Two different solutions were prepared by diluting the stock solution in water. Solution A (SA) had a dilution ratio of 1:40 mother solution while the solution B (SB) solution had a dilution ratio of 1:800. **Table 3.1** shows the volume extracted (µl), concentration (µg/ml), and the radical scavenging activity (%) values obtained in ABTS assay. The concentration of solution against the radical scavenging activity (RSA) was represented in **Figure 3.5(a)**. The calibration curve obtained was $y = 5.98199x + 1.28138$ with a r^2 of 0.987 and IC50 value was 8.57 µg/ml.

Table 3.1 Further details of the calibration curve plotted in **Figure 3.5(a).**

Solution	Volume (µl)	Concentration (µg/ml)	RSA value (%)
SA-1	100	0.6	1.847
SA-2	200	1.2	6.848
SA-3	400	2.41	13.425
SA-4	800	4.83	28.189
SB-1	100	12.08	65.707

- IC50 tea in formic acid

The stock solution of tea formic acid extract had a concentration of 23.16 mg/ml. The calibration curve was performed using different volumes of solution A (SA) with a dilution ratio of 1:40. **Table 3.2** below shows the volume extracted (µl), concentration (µg/ml), and the radical scavenging activity (%) values obtained in the ABTS assay. The concentration of solution against the radical scavenging activity (RSA) was represented in **Figure 3.5(b)**. The calibration curve obtained was $y = 5.49632x + 5.3629$ with r^2 of 0.997 and the IC50 value was 8.12 $\mu g/ml$.

Table 3.2. Further details of the calibration curve are plotted in **Figure 3.5(b).**

Sample	Volume (µl)	Concentration (µg/ml)	RSA value (%)
SA-1	100	0.965	9.745
SA-2	200	1.93	16.681
SA-3	700	6.755	45.09
SA-4	1000	9.65	57.819

- IC50 tea waste in water

The stock solution of tea water extract had a concentration of 2.58 mg/ml. The calibration curve was performed by diluting the stock with water. Solution A (SA) with a ratio dilution of 1:5 while solution B (SB) 1:10. **Table 3.3** below shows the volume extracted (µl), concentration (µg/ml), and the radical scavenging activity (%) values obtained in the ABTS assay. The concentration of solution against the radical scavenging activity (RSA) was represented in **Figure 3.5(c)**. The calibration curve obtained was $y = 0.63747x + 3.20431$ with a r^2 of 0.998 and the IC50 value was 73.408 µg/ml.

Table 3.3. Further details of the calibration curve are plotted in **Figure 3.5(c).**

Sample	Volume (µl)	Concentration (µg/ml)	RSA value (%)
SB-1	100	17.2	13.48
SA-1	300	25.8	20.15
SB-2	300	34.4	25.127
SA-2	500	43	30.95
SA-3	700	60.2	41.624

SA-4	1000	86	57.87

- IC50 tea waste in formic acid

The stock solution of tea water extract had a concentration of 16.18 mg/ml. The stock solution was diluted at 1:10 and 1:20, named Solution A (SA) and solution B (SB), to prepare the solutions for the calibration curve. **Table 3.4** below shows the volume extracted (µl), concentration (µg/ml), and the radical scavenging activity (%) values obtained in the ABTS assay. The concentration of solution against the radical scavenging activity (RSA) was represented in **Figure 3.5(d)**. The calibration curve obtained was $y = 0.39884x + 20.8508$ with a r^2 of 0.992. and the IC50 value was 73.084 µg/ml.

Table 3.4. Further details of the calibration curve plotted in **Figure 3.5(d)**

Sample	Volume (µl)	Concentration (µg/ml)	RSA value (%)
SA-1	100	0.054	40.57
SA-2	150	0.0809	54.397
SA-3	200	0.10786	66.68
SA-4	300	0.1618	84.648

- IC50 vinegar

Vinegar solution (182 mg/ml) was diluted with water to create a solution 1:10 used to prepare the calibration curve. Then, the stock solution was centrifuged and the supernatant was recovered and used for the analysis. **Table 3.5** below shows the volume extracted (µl), concentration (µg/ml), and the radical scavenging activity (%) values obtained in the ABTS assay. The concentration of solution against the radical scavenging activity (RSA) was represented in **Figure 3.5(e)**. The calibration curve obtained was $y = 0.02279x + 7.91441$ with a r^2 of 0.9943 and the IC50 value was 1846.669 µg/ml.

Table 3.5. Further details of the calibration curve are plotted in **Figure 3.5(e).**

Sample	Volume (µl)	Concentration (µg/ml)	RSA value (%)

Stock-1	100	606.66	21.057
Stock-2	150	910	30.019
Stock-3	200	1213.33	39.759
Stock-4	300	1820	50.656
Stock-5	400	2426.66	62.603

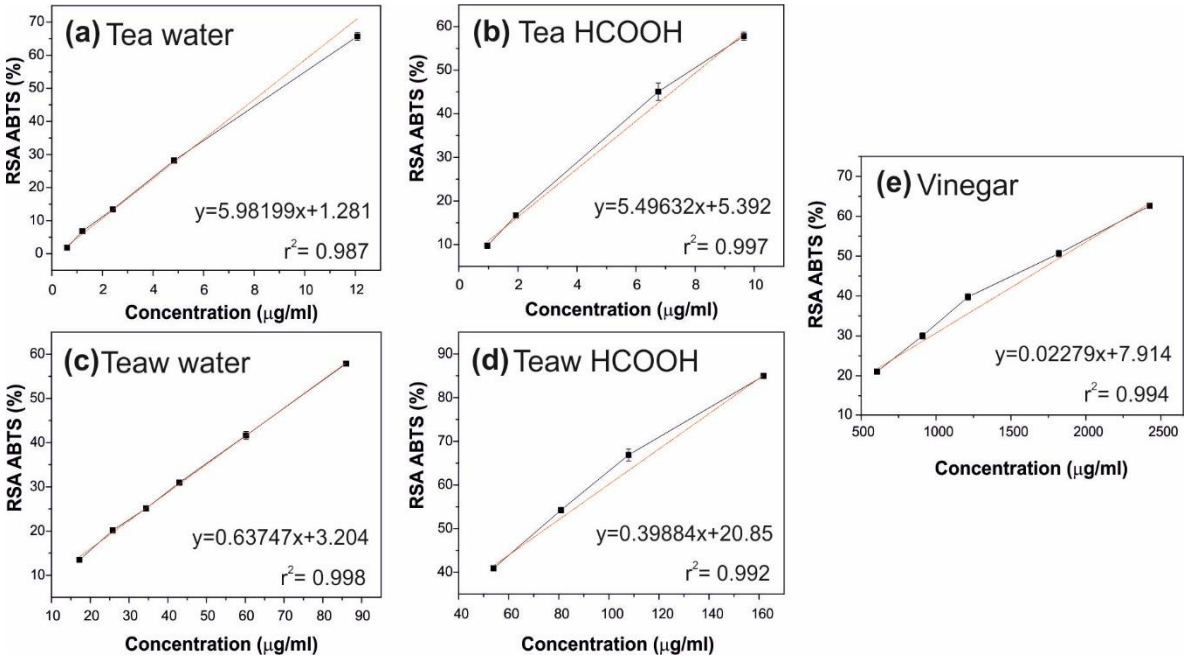

Figure 3.5 The IC50 graph obtained from representing the concentration against the radical scavenging activity (%) in ABTS assay of **(a)** tea extracted with water, **(b)** tea extracted with formic acid (HCOOH), **(c)** tea waste extracted with water **(d)** tea waste extracted with formic acid (HCOOH) and **(e)** vinegar.

The IC50 values for the radical DPPH$^{\cdot}$ were calculated to understand whether the antioxidant agents present in vinegar and tea waste with formic acid solutions react against this radical. The sample preparation followed the same steps as performed with ABTS$^{+\cdot}$, but with slight modifications related to the radical method (more details in section 4.3.6), ethanol was used to fill the vials, and the reaction time was 30 minutes (L. S. Lee et al., 2014). Noted that vinegar solutions

were diluted in water because a lot of precipitates were formed in ethanol. All measurements were performed five times to guarantee reproducibility.

- IC50 tea waste

In the case of tea samples, just tea waste extracted with formic acid was studied. The concentration of tea waste was 8.54 μg/ml. Two solutions with a dilution ratio of 1:5 and 1:20 called SA and SB respectively were prepared to measure the calibration curve. **Table 3.6** below shows the volume extracted (μl), concentration (μg/ml), and the radical scavenging activity (%) values obtained in the DPPH assay. The concentration of solution against the radical scavenging activity (RSA) was represented in **Figure 3.6(a)**. The calibration curve obtained was $y = 0.4255x + 7.06275$ with a r^2 of 0.971 and the IC50 value was 100.89 μg/ml.

Table 3.6. Further details of the calibration curve are plotted in **Figure 3.6(a).**

Sample	Volume (μl)	Concentration (μg/ml)	RSA value (%)
SB-1	100	2.84	7.954
SB-2	200	5.693	8.94
SB-3	400	11.38	17.21
SB-4	700	19.926	23.32
SA-1	200	113.866	52.265
SA-2	250	142.233	67.735
SA-3	300	170.8	77.05

- IC50 vinegar

Vinegar diluted in water in a dilution ratio of 1:10 was used to prepare the solution for the calibration curve. Then, the stock solution was centrifuged and the supernatant was recovered and used for the analysis. **Table 3.7** below shows the volume extracted (μl), concentration ($\mu g/ml$), and the radical scavenging activity (%) values obtained in the DPPH assay. The concentration of solution against the radical scavenging activity (RSA) was represented in **Figure 3.6(b)**. The

calibration curve obtained was $y = 0.026x + 4.72491$ with a r^2 of 0.99606 and the IC50 value was 1746.051 $\mu g/ml$.

Table 3.7. Further details of the calibration curve are plotted in **Figure 3.6(b).**

Sample	Volume (µl)	Concentration (µg/ml)	RSA value (%)
Stock-1	100	606.66	21.644
Stock-3	200	1213.33	36.089
Stock-4	300	1820	52.153
Stock-5	400	2426.66	60.379

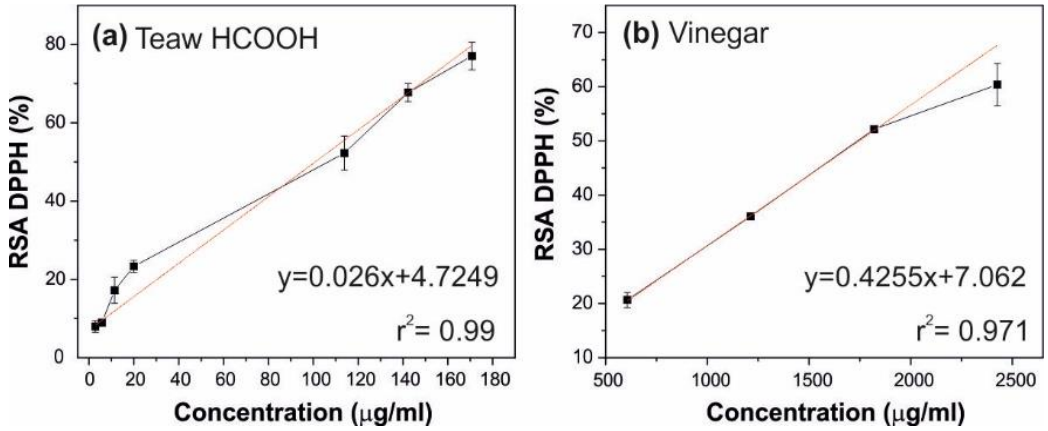

Figure 3.6 The IC50 graph obtained plotting the concentration against the radical scavenging activity (%) in DPPH assay of tea waste extracted with **(a)** formic acid and **(b)** vinegar**.** Noted that the calibration curve and the error (r^2) obtained were represented.

3.3.8 Contact angle analysis

Static water contact angle measurements were performed by using the sessile drop method using a Dataphysics 0CAH 200 contract angle goniometer equipped with a CCD camera and image processing software operating under laboratory conditions (temperature 22-25 °C and relative humidity 50-60%). For the characterization, droplets of 5 µl of MilliQ water were used. Up to 10 contact angle measurements were carried out on every simple at random locations and their average values are reported.

3.3.9 Water uptake

For water uptake measurements, samples were first dried by conditioning in a desiccator until no change in sample weight was measured. Dry samples were weighed (-weight) on a sensitive electronic balance and, then, placed in a 100% relativity humidity (RH) chamber at 25 degrees. Once the equilibrium was reached, each sample was again weighed and the amount of adsorbed water was calculated as the difference with the initial dry weight. Three measurements were taken and the results were averaged to obtain a mean value. Water uptake, in percentage, was calculated as **Equation 2** describes:

$$\text{Water uptake } (\%) = \frac{m_f - m_0}{m_0} \text{ x } 100 \quad (\mathbf{2})$$

where m_f is the sample weight at 100% RH and m_0 is the sample weight at 0% RH.

3.3.10 Oxygen permeability measurements

The oxygen permeation tests of blend films were performed using an Oxysense 525oi device (Oxysense, USA) equipped with a film permeation chamber. This machine was operated according to ASTM Method F3136-15. The test was performed at standard laboratory conditions, *i.e.,* 23°C and 40% relative humidity. The permeation chamber consisted of a cylinder divided into two parts (sensing well and driving well). The sensing well was instrumented with a fluorescence sensor called oxydots, sensitive to the oxygen concentration. This chamber was purged with nitrogen while the other one (driving well) was kept open to ambient air. The films were cut into a rectangular piece (6 cm x 6 cm) and placed inside the chamber. An OxySense fiber optic pen measured the oxygen reading from the oxydots, at specific time intervals. Oxygen transmission rates (OTRs) of the blend films were measured by monitoring the oxygen uptake with time using Oxysense OTR software. At least ten measurements were taken for each sample with a minimum coefficient of determination (R^2) value of 0.95.

3.4 Results and discussion

3.4.1 Extraction analysis by UPLS-MS/MS

Vegetal biomass is composed of a wide variety of biochemical, from macromolecules to small phenolic acids, providing great heterogeneity (Esparza et al., 2020). The final properties of the material depend on the chemical composition of the vegetal extract, and the selection of the proper solvent is crucial. The solvent plays an important role in the extraction of specific molecules, favoring the extraction of the molecules with higher affinity and solubility, and thus, tuning the characteristics of the extract solution (Ziarno, 2007). The analysis of the chemical composition of tea and tea waste extracted with water and formic acid was performed using high-performance liquid chromatography (HPLC). The extracts obtained from raw tea leaves in water and formic acid are labeled as “Tea water” and “Tea FA”, respectively. While the extracts obtained from the tea leave waste using water and formic acid are labeled “Teaw water” and “Teaw FA”, respectively. The photography of extracts solutions and chromatograms obtained are represented in **Figure 3.7** The chromatograms represent the percentage of each molecule at different retention times. The peaks of the major species eluted at a given retention time were identified and labeled from 1 to 12.

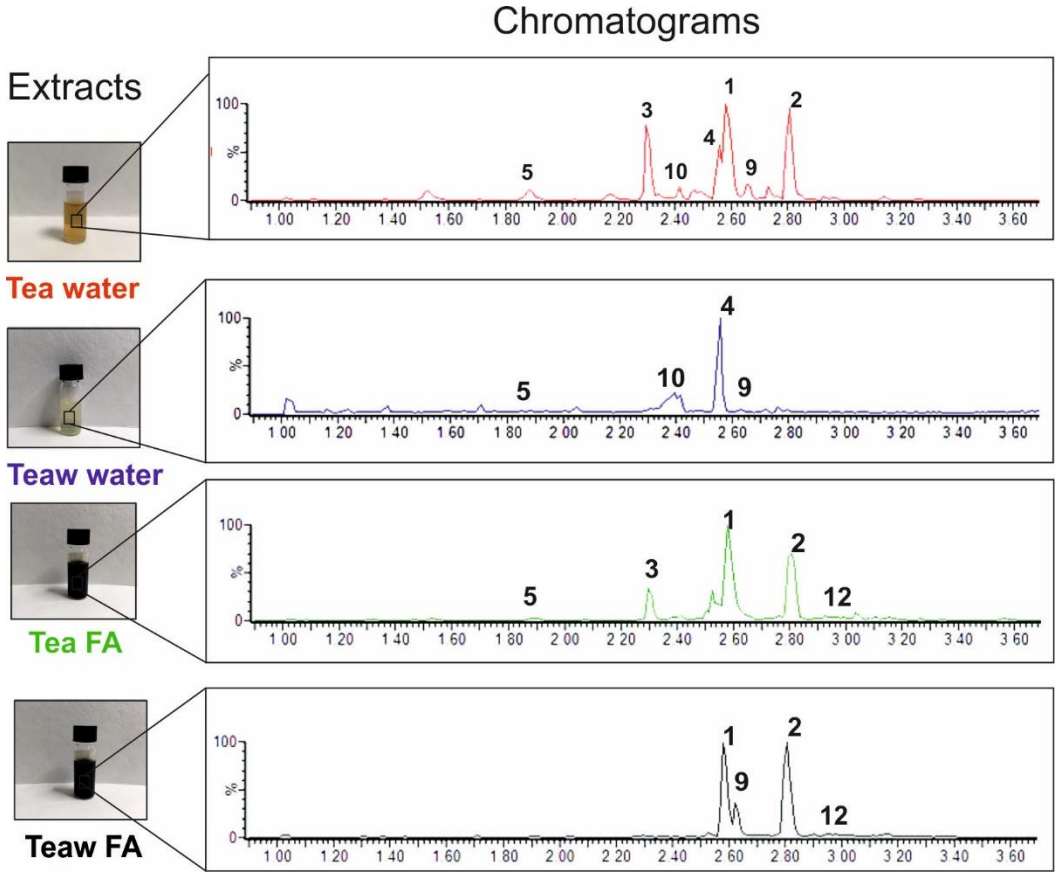

Figure 3.7 Chromatograms of the tea (Tea) and tea waste (Teaw) solutions extracted with water and formic acid.

Mass spectrometry was used to identify all metabolites and their percentage, reported in **Table 3.8**. As expected, more metabolites were obtained in unused tea extracts, in more than two measurement units in the case of water extracts. Then, the metabolites were classified and as gallated and no-gallated catechins, and the percentage was displayed in the last two rows. As (Yashin et al., 2015) reported, gallated catechins present a very strong antioxidant and scavenging activity, overcoming non-gallated catechins. Belong the used solvents, formic acid showed higher affinity to extract of gallated catechins, especially in waste tea leaves (96% of gallated catechins against 4% non-gallated catechins). This result points to formic acid as the best solvent to extract the antioxidants.

Table 3.8. Details of the metabolites present in the tea and tea waste solutions extracted with water and formic acid.

ID	Metabolite	Aqueous extracts		Formic acid extracts	
		Tea	**Tea waste**	**Tea**	**Tea waste**
1	Epigallocatechingallate (EGCG)	6839 (29%)	53 (8%)	8603 (40%)	3458 (45%)
2	Epicatechingallate (ECG)	5293 (23%)	30 (4%)	7803 (36%)	3975 (51%)
3	Epigallocatechin (EGC)	4075 (17%)	9 (1%)	2482 (11%)	75 (1%)
4	Epicatechin (EC)	2341 (10%)	425 (62%)	880 (4%)	56 (1%)
5	Gallocatechin (GC)	908 (4%)	21 (3%)	423 (2%)	28 (0%)
6	Catechin (C)	591 (3%)	89 (13%)	358 (2%)	34 (0%)
7	Epicathechinglucuronide	272 (1%)	5 (1%)	79 (0%)	nd
8	Quercetin glucosylrhamnoside	661 (3%)	15 (2%)	186 (1%)	14 (0%)
9	Feruloylglucose	1018 (4%)	21 (3%)	423 (2%)	28 (0%)
10	Epicathechinepicathechin	752 (3%)	30 (4%)	92 (0%)	nd
11	Theasinensin C	489 (2%)	5 (1%)	54 (0%)	nd
12	Epiafzelechin 3-gallate	103 (0%)	nd	312 (1%)	84 (1%)
	Total area	**23332**	**682**	**21725**	**7735**
	Gallated catechins	12132 (52%)	83 (12%)	16406 (75%)	7433 (96%)
	Non-gallated catechins	11200 (48%)	599 (88%)	5319 (25%)	302 (4%)

Interestingly, in chromatographs reported in **Figure 3.8**, formic acid extracts exhibited a single peak at 2.5 min. This peak presents a mass-charge ratio (m/z) of 331.1 g/mol, which corresponds to Barceloneic acid B. This bioactive polyphenol is an anticancer molecule commonly found in the fungus, Penicillium Albocoreium (Overy et al., 2005). The presence of such an unexpected compound may be a result of reactions between formic acid and certain compounds present in tea leaves, creating useful and naturally found polyphenols.

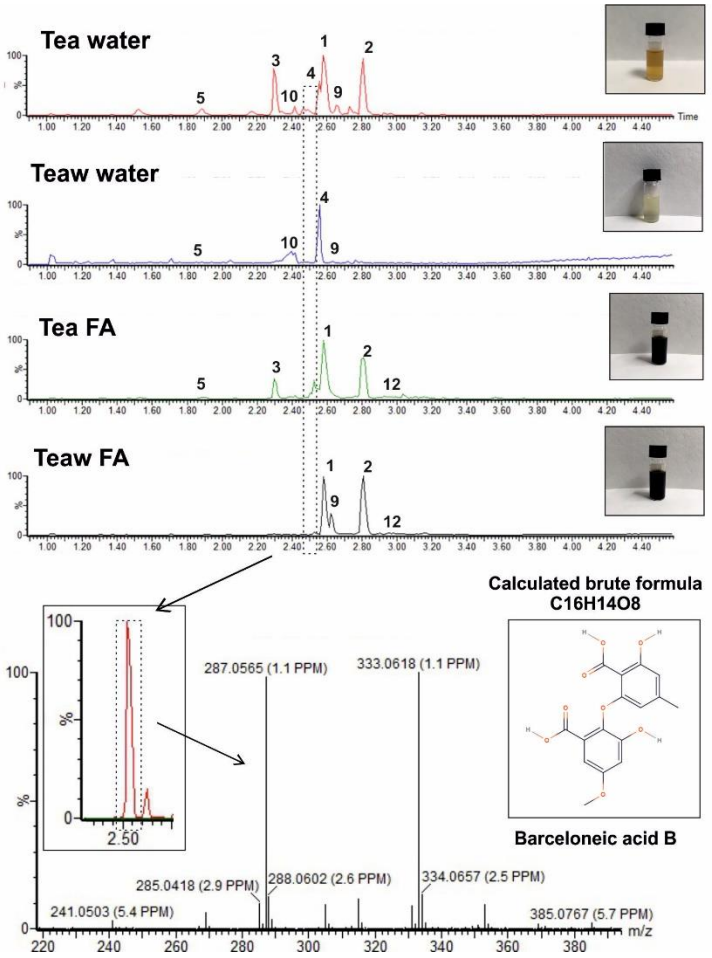

Figure 3.8 The characteristic peak of Barceloneic acid B was detected in the chromatograms and mass spectra.

The chemical characterization of balsamic vinegar was not performed using UPLC-MS/MS analysis as no extraction or chemical processing of the as-received balsamic vinegar was conducted. Besides, in bibliography there were very accurate publications on the comprehensive metabolite composition of balsamic vinegars (Arvanitoyannis et al., 2011; Ho et al., 2017). Summarily, balsamic vinegars contain a significant amount of polyphenols, and among them, tannins contributed to about 50% of the antioxidant activity of the total polyphenolic fraction. The residual antioxidant activity is assigned to melanoids (Tagliazucchi et al., 2008; H. Zhang et al., 2018).

3.4.2 Chemical characterization by ATR-FTIR

Figure 3.9(a) shows the infrared spectra of PVA cast from water (PVAw), PVA cast from formic acid (PVAf), and formic acid (FA). The infrared spectrum of PVAw displayed typical absorption bands of PVA, such as OH stretching mode at 3277 cm^{-1}, asymmetric and symmetric CH_2 stretching modes at 2935 and 2852 cm^{-1}, respectively. A low-intensity peak attributed to the C=O stretching vibration of residual acetate groups is located at 1682 cm^{-1}, CH_2 bending mode at 1420 cm^{-1}, and C-O stretch, assigned to secondary hydroxyl groups at 1086 cm^{-1}, are observed (He et al., 2019). In the case of PVAf, in addition to PVA vibrations, two new absorptions peaks appeared at 1701 and 1171 cm^{-1} corresponding to C=O and C-O stretching modes, associated with formic acid appeared (Bellamy, 2013).

The ATR-FTIR spectra of tea waste (tea after boiling, labeled Teaw) polymeric films corresponding to PVAf and the PVAw containing 10 wt.% used or tea extracts (Tw10), are represented in **Figure 3.9(b)**. The bands assigned to the Teaw were OH stretching mode at 3283 cm^{-1}, asymmetric and symmetric CH_2 stretching modes at 2917 and 2981 cm^{-1}, respectively. At lower wavenumbers, the stretching vibrations of the carbonyl group of ester C=O at 1730 cm^{-1}, C=C stretching mode of aromatics at 1615 cm^{-1}, and the C-O stretching at 1015 cm^{-1} appeared. (Y. Liu et al., 2019). All these bands can be associated mostly with the catechins molecules found in the tea extract by UPLC analysis (section 4.4.1). The infrared spectra of Tw10 featured characteristic bands of both PVA and tea waste extract, such as the C=C stretching band corresponded to aromatic molecules of tea waste, and the C-O stretch of secondary hydroxyl groups.

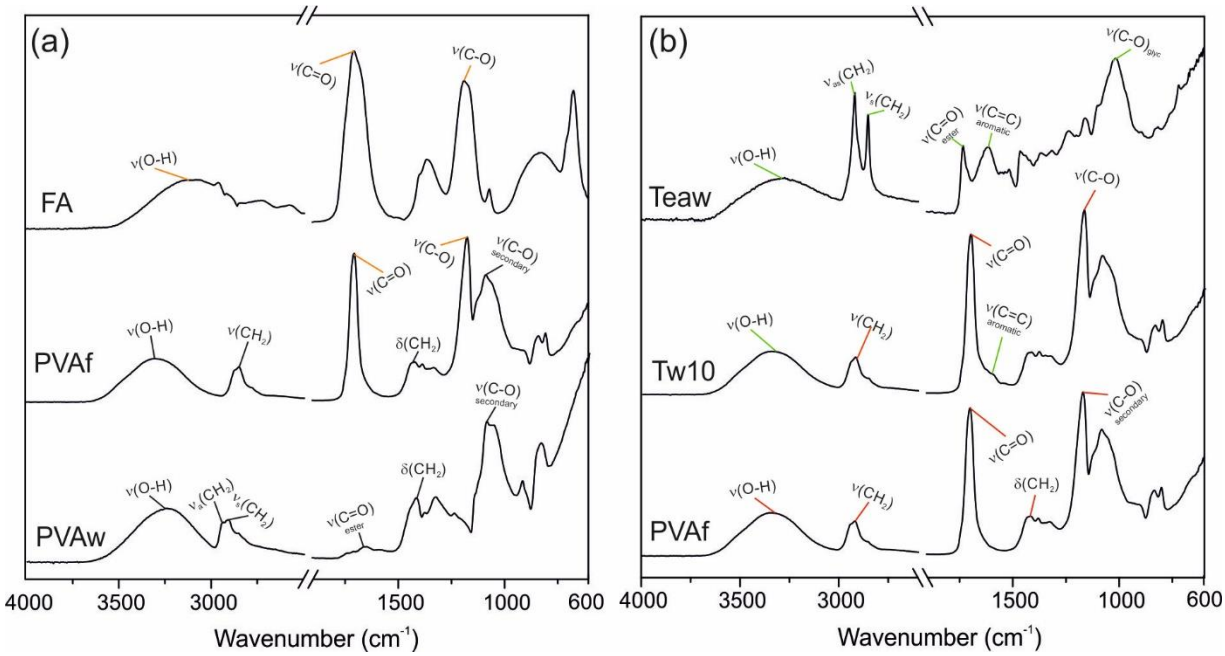

Figure 3.9 The infrared spectra ranged from 4000 cm^{-1} to 600 cm^{-1} of **(a)** formic acid (FA) PVAf, and PVAw, and **(b)** boiled tea (Teaw), Tw10, and PVAf.

A deeper analysis of the FTIR spectra of PVA-tea blends in **Figure 3.10(a)** indicated a shift in the wavenumber of the OH stretching mode, depending on the relative concentrations. The position of this absorption significantly decreased from 3460 cm^{-1} for Tw5 to 3280 cm^{-1} for Tw50 (a reduction of 180 cm^{-1}). The OH stretching wavenumber for Tw50 was found to be close to that of tea waste (3275 cm^{-1}). From this, the energy of the H-bonds (E_H) was calculated as following **Equation 3** (Ciolacu et al., 2012):

$$E_H = \frac{1}{k} \cdot \frac{(\nu_0 - \nu)}{\nu_0} \quad (3)$$

where *k* is a constant with a value of 1.68×10^{-2} $kcal^{-1}$, ν_0 is the standard wavenumber of the OH stretching mode ascribed to hydroxyl groups that do not interact by H-bonds (3600 cm^{-1}), and ν is the experimentally observed wavenumber of the samples.

As reported in **Figure 3.10(b)**, the E_H parameter was increased with the tea extract content in PVA. Interestingly, the energy of H-bonds for T20 and T50 films was higher than the value for

PVAf (calculated as 4.53 kcal corresponding to 3339 cm^{-1}), indicating that the polyphenols at high concentrations might reinforce the H-bonding network of PVA matrixes.

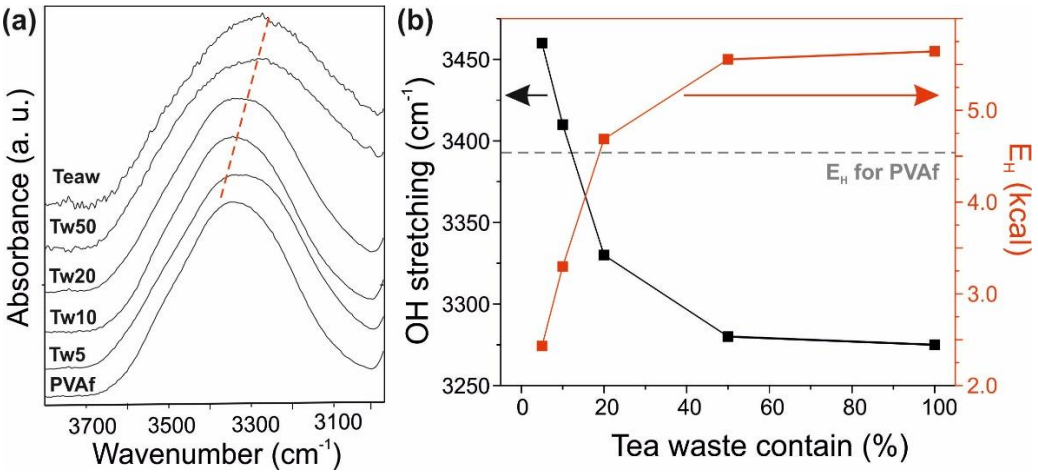

Figure 3.10 (a) The infrared spectra of the tea waste and tea waste-PVA blends maximized in the range of the hydroxyl stretching vibration. The red dashed line is a visual guide to highlight the shift of the band **(b)** The shift of the OH stretching mode (black) and variation of the energy of the H-bonds (E_H) with the tea content, in red. The gray dashed line indicates the value of E_H for the PVAf sample.

Similarly, the ATR-FTIR spectra of discarded balsamic vinegar, PVA cast from water (PVAw) and PVA film containing discarded balsamic vinegar 10 wt.% (DV10) are represented in **Figure 3.11(a).** The characteristic bands of PVAw are already described above. The infrared spectra of the discarded vinegar exhibited a strong band corresponding to the stretching vibration of the hydroxylic groups ν(O-H) at 3500 cm^{-1}, also a peak at 1800 cm^{-1} attributed to the vibration of the carbonyl group of the organic acids present in vinegar. The vibrations of C=C of aromatic rings attributed to the polyphenolic groups are located at 1600-1580 cm^{-1}, and a strong peak at 1100 cm^{-1} belongs to the stretching vibration of C-O, corresponding to sugars. A more careful analysis of the FTIR spectra of discarded vinegar-PVA blends in **Figure 3.11(b)** showed that the hydroxyl bands shifted towards higher wavenumbers in the OH stretching region, depending on the relative concentrations of agro-food waste. This means that the presence of discarded vinegar in the PVA matrix decreases H-bonding energy and this might be partially reflected as a plasticization effect as opposed to tealeaves waste extract containing films (Fei et al., 2004).

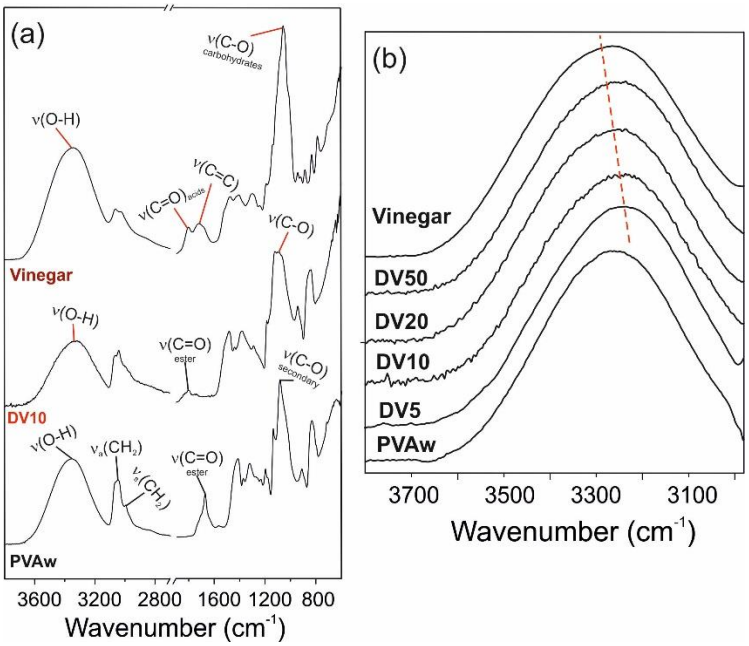

Figure 3.11 (a) The infrared spectra, ranged from 4000 cm^{-1} to 600 cm^{-1}, of **(a)** discarded vinegar, DV50, and PVAw. **(b)** The infrared spectra of PVAw, DV5, DV10, DV20, DV50, and discarded vinegar maximized in the range of the hydroxyl stretching vibration. The red dashed line is a visual guide to highlight the shift of the band.

3.4.3 Microstructural analysis

All films had a uniform and homogeneous surface. **Figure 3.12(a)** shows the cross-section micrograph of PVAf, PVAw, and PVA samples with the 50 wt.% of agro-food waste, DV50, and Tw50. PVAw, PVAf, and DV50 films showed a smooth and homogeneous cross-section morphology, while the presence of lignocellulosic residues of tea leaves provided some roughness to the Tw50 sample. **Figure 3.12(b)** corresponds to the XRD patterns of the semicrystalline PVAw and PVAf. PVAw showed a sharp peak at 20° and a small peak at 40° associated with the semi-crystalline structure of PVA (Y. N. Chen et al., 2018). These peaks were noticeably broader in PVA films treated with formic acid, PVAf, revealing that formic acid influenced negatively on the polymer crystallinity.

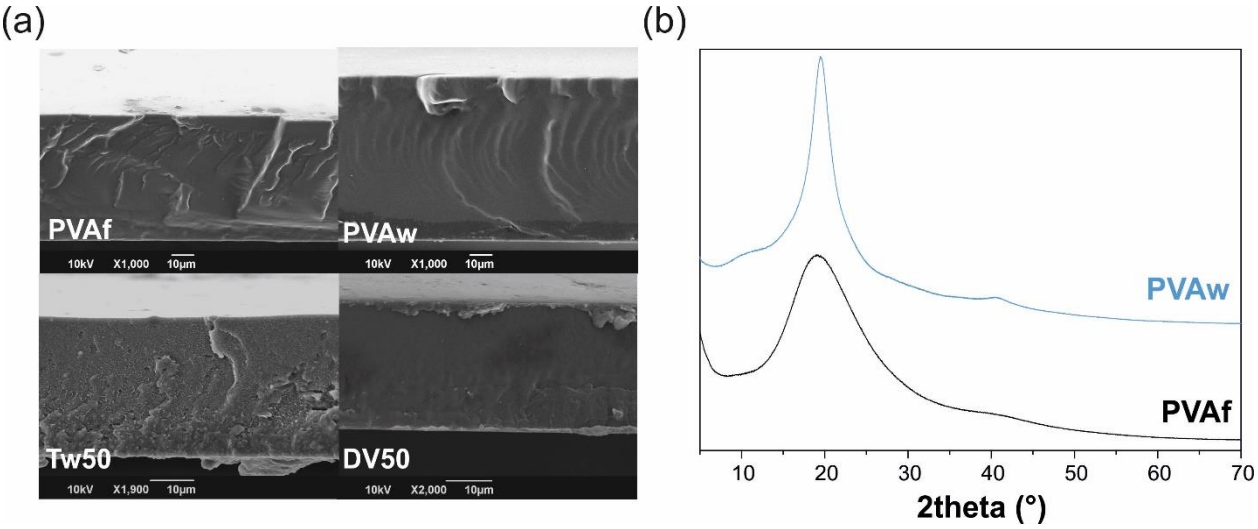

Figure 3.12 (a) SEM micrographs of the cross-section of PVAf, PVAw, Tw50, and DV50 films. **(b)** XRD patterns of PVAw and PVAf samples.

3.4.4 Fluorescence analysis

The analysis of the dispersion of the green tea additives was performed using the fluorescence emission of catechins (Papadopoulou et al., 2005; Snitsarev et al., 2013). In **Figure 3.13(a-b)**, the emission spectra of PVA-tea waste films (thickness normalized), and tea waste solution at different concentrations (1.43 and 8.6 mg/mL) with excitation at 280 nm, were displayed. In **Figure 3.13(a)**, Tw5 showed a weak and broad emission band located at around 360 nm associated with polyphenols in low concentrations (Snitsarev et al., 2013). Up to 20 wt.% of tea waste concentrations in films, the band intensity was increase with concentration, and a shoulder at 430 nm appeared. This shoulder is related to the interactions of the aromatic structure of the polyphenols, observed in other natural polyphenols like hydroxycinnamic acids (Belay et al., 2016). The intensity of the band dropped in films with 50 wt.% of tea waste (Tw50), and the main band shifts towards 375 nm, attributed to the quenching effect of catechin-catechin interactions, as observed in other natural compounds embedded within the polymer matrix, as tocopherols (Martelli et al., 2017). At high concentrations, catechins tend to aggregate in both solution and polymeric matrices, leading to lower intensities of fluorescence peaks (Trnková et al., 2011). This effect was confirmed in **Figure 3.13(b)**, where the more-diluted solution exhibited peaks with higher intensity peaks.

Then, the fluorescence activity of catechins was used to analyze the distribution of the tea waste in the film, **Figure 3.13(c)**. The fluorescence image collected from a randomly chosen T20 sample cross-section indicated homogeneously dispersed tea waste biomass within the composite films, see **Figure 3.13(d).**

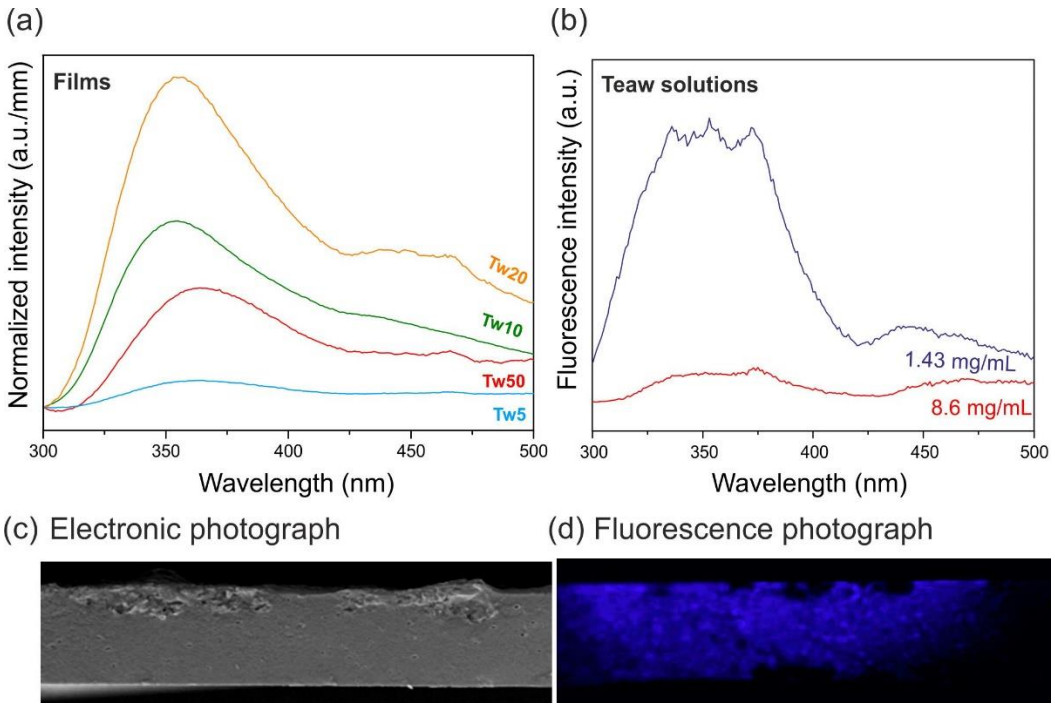

Figure 3.13 (a) The emission spectra of fluorescence, represented in a range from 300 nm to 500 nm, of Tea-waste films at different concentrations (Tw5, Tw10, Tw20, and Tw50) normalized by the thickness. **(b)** The emission spectra of fluorescence, represented in a range from 300 nm to 500 nm, of tea-waste solutions of 1.43 mg/mL and 8.6 mg/mL.

3.4.5 Mechanical properties

The strain-stress curves of PVAf film and tea waste films were displayed in Figure **3.14(a)**, while the values of Young's modulus and elongation are represented in **Figure 3.14(b)**. The mechanical behavior of films with a concentration of tea waste below <10 wt.%, did not generate significant modifications on the mechanical properties of PVAf. Above 10 wt.% of tea waste extract, the elongation dropped down to 10 times-folds with respect to PVAf, while the Young's modulus raised 1600 MPa. The stiffness behavior of Tw20 and Tw50 films may be attributed to

the movement restrictions between the polymer chains attributed to the agglomeration of lignocellulose biomass (Munteanu & Vasile, 2020).

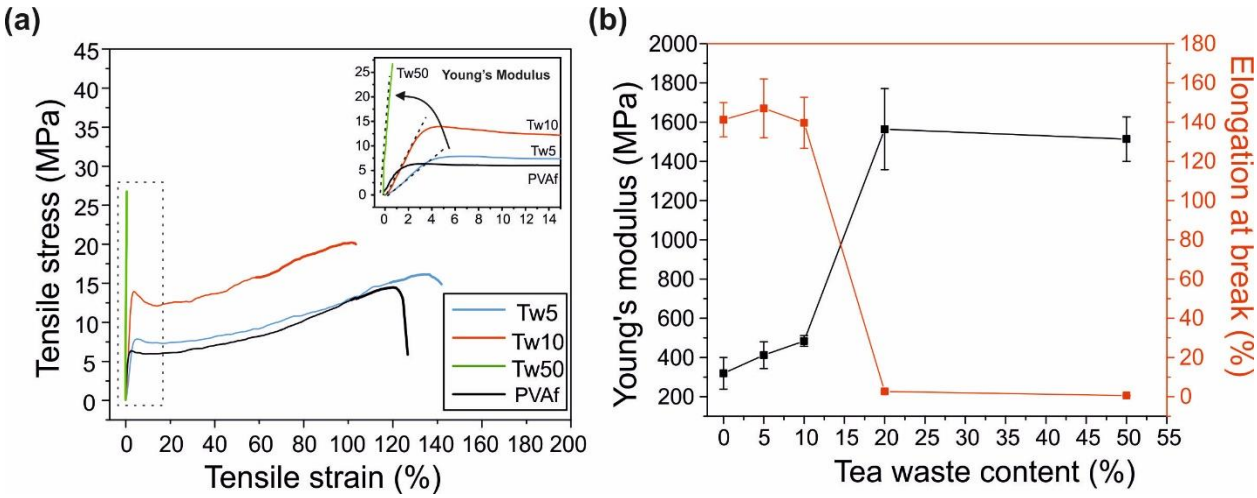

Figure 3.14 (a) The stress-strain curve and **(b)** the values of elongation at break and Young's modulus of PVAf and tea waste-PVA blends.

Figure 3.15(a) shows the stress-strain curve of the PVAw and PVA films filled with discarded vinegar. The elongation was increased with the content of discarded vinegar with respect to the PVAw film, while the Young's modulus almost 3 times in PVA films with 50 wt.% of discarded vinegar. This plasticizing behavior was justified with the chemical composition of vinegars, mainly composed of small molecules of acetic acid, glycerol and sugars, which weaken the inner structure of the polymer matrix (Nogueira et al., 2019; Tagliazucchi et al., 2008).

Interestingly, formic acid also acted as a plasticizer, the elongation of PVAf films was 10 times greater with respect to the PVAw films, see **Figure 3.15**.

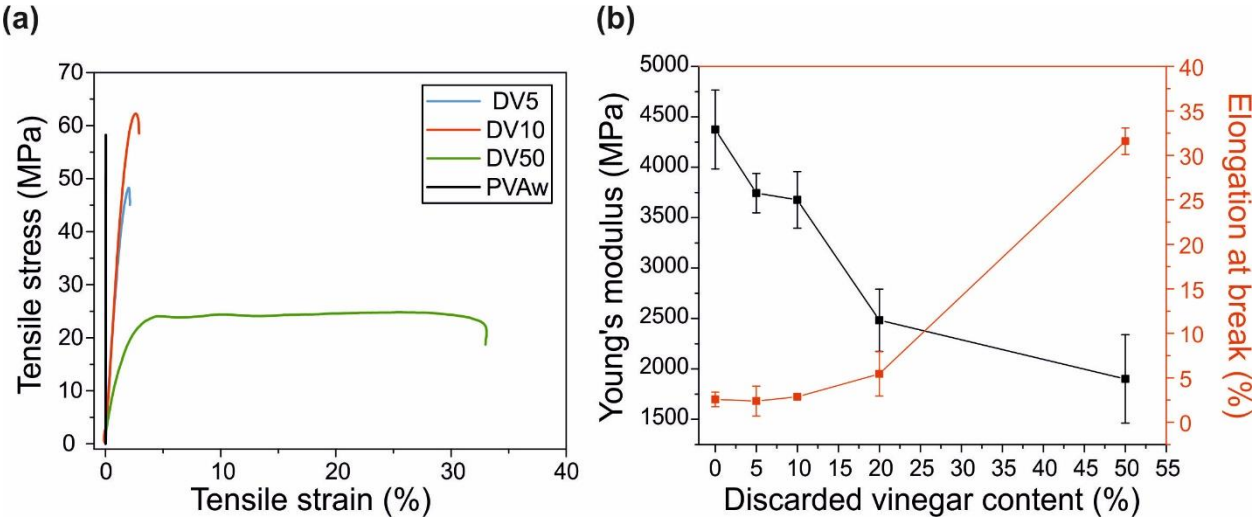

Figure 3.15 (a) The stress-strain curve and **(b)** the values of elongation at break and Young's modulus of PVAw and PVA blends loaded with discarded balsamic vinegar.

3.4.6 Antioxidant activity

The antioxidant capacity of tea extracts and discarded vinegar were evaluated with the half-maximal inhibitory concentration (IC50), see **Figure 3.16**. IC50 indicates the concentration of the antioxidant that inhibits the 50% of a radical in solution, low values of IC50 are associated with high antioxidant effectivity. This analysis was performed using $ABTS^{+\cdot}$ as a standard radical. Tea and tea waste extracted with water (Tea water and Teaw water) showed IC50 values of ~8.6 and ~73.4 µg/mL, respectively. IC50 of formic acid extracts were ~8.1 and ~73.1 µg/mL for tea leaves and tea waste (Tea FA and Teaw FA), respectively. These results indicate that extracts of unused tea leaves were around 10 times more antioxidant than extracts of tea waste, independently of the solvent. Tea solutions extracted with formic acid were slightly more antioxidant than the water-based solution. This is in agreement with the chemical analysis in Section 4.4.1, wherein extracts of unused tea in FA showed a greater concentration of catechins, especially gallated catechins, with higher antioxidant capability. The IC50 of discarded vinegar was found to be ~1846.7 µg/mL with $ABTS^{+\cdot}$, and 1746 µg/mL against $DPPH^{\cdot}$ radical, two orders of magnitude above any of the tea extracts discussed before. However, discarded balsamic vinegar was a powerful antioxidant in comparison with other agro-food wastes, such as citrus fruit peels, with IC50 equal to ~3600 µg/mL (Ghasemi et al., 2009).

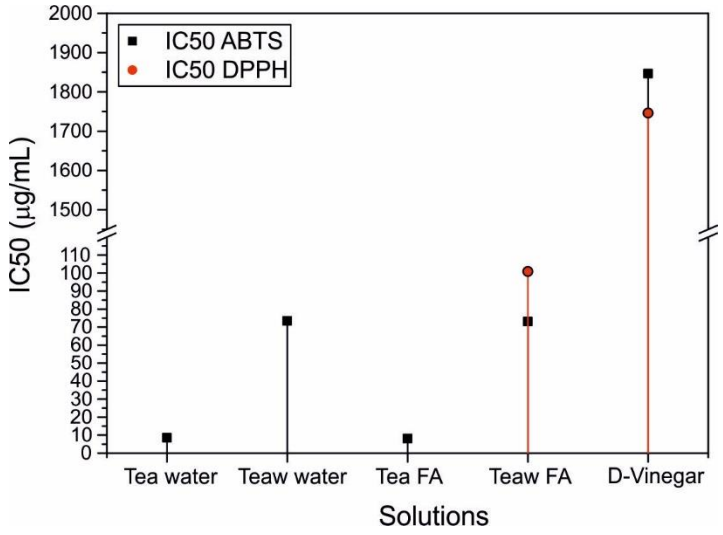

Figure 3.16 IC50 values of the extract solutions of unused tea (Tea) and tea waste (Teaw) using water and formic acid (FA) as solvents. $ABTS^{+\cdot}$ was selected to perform the experiments (in black). The IC50 values of discarded vinegar (D-Vinegar) and Teaw FA (samples selected to fabricate the films), were calculated with $ABTS^{+\cdot}$ (black) and $DPPH^{\cdot}$ (in red).

The antioxidant activity of the antioxidant migrated into $ABTS^{+\cdot}$ medium, from PVA-tea waste and PVA-discarded balsamic vinegar, are represented in **Figure 3.17(a-b)**, respectively. Tea waste films showed a controlled and concentration-dependent antioxidant response, see **Figure 3.17(a)**. Films exhibited an excellent antioxidant activity, excluding the sample with 5 wt.% of tea waste (Tw5), all films achieved 100% of the radical inhibition after 24 hours. **Figure 3.17(b)** shows the antioxidant capability of discarded balsamic vinegar films.

The concentration of discarded vinegar in films determined the antioxidant properties of films. Concerning tea-waste films, discarded-vinegar films responded slower against the radical, only films DV20 and DV50 could reach approximately 90% inhibition levels within 3 days. Films DV5 and DV10 reached inhibition levels of 70% and 40%, respectively at the end of 3 days. The lower antioxidant activity of the discarded vinegar (IC50: ~1846.7 µg/mL), against the tea waste extracted in formic acid used for the elaboration of films (IC50: ~73.1 µg/mL), may justify the different antioxidant migration results.

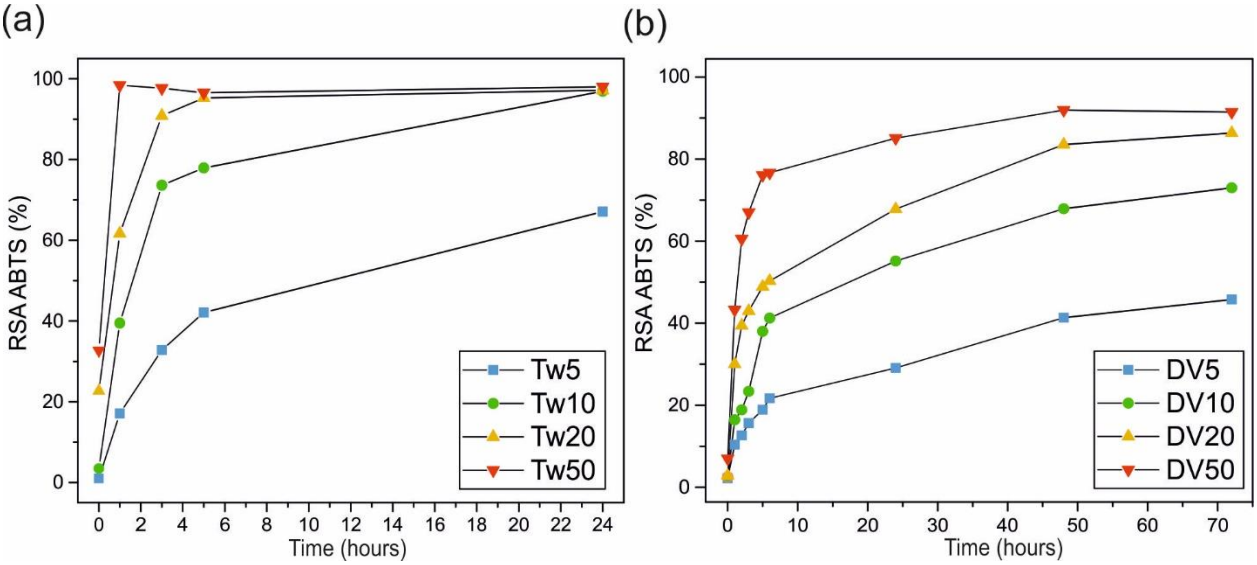

Figure 3.17 Kinetic profiles of the antioxidant response against $ABTS^{+\cdot}$ of **(a)** tea-waste films in 24 hours, and **(b)** discarded-vinegar films for 3 days.

In **Figure 3.18**, the antioxidant activity of the antioxidant migrated into $DPPH^{\cdot}$ media, from PVA-tea waste and PVA-discarded balsamic vinegar, are represented. **Figure 3.18(a)** shows all films of tea-waste extract achieved the 100% of RSA within 24 hours. The great affinity of ethanol, the solvent used in this experiment, with tea polyphenols may justify the exceptional results (Gramza et al., 2005). However, tea-waste films released slower respect to the ABTS assay, due to the slower diffusion of the ethanol through the PVA matrix, against water, the solvent used in the ABTS experiment, represented above **Figure 3.18**. **Figure 3.18(b)** shows that only VD50 responded against the radical after several days, discarded vinegar films loaded in 5, 10, and 20 wt.%, had an absent antioxidant activity in $DPPH^{\cdot}$ media, diversely to ABTS assay wherein all films responded. Since the content of the antioxidant compounds in discarded vinegar had shown to respond against the $DPPH^{\cdot}$ radical, see **Figure 3.16**, with an IC50 value of 1746 µg/mL. The low diffusion of ethanol into the PVA matrix and the low antioxidant activity of discarded vinegar may lead to a lack of antioxidant response (Lopes & Simoneau, 2017).

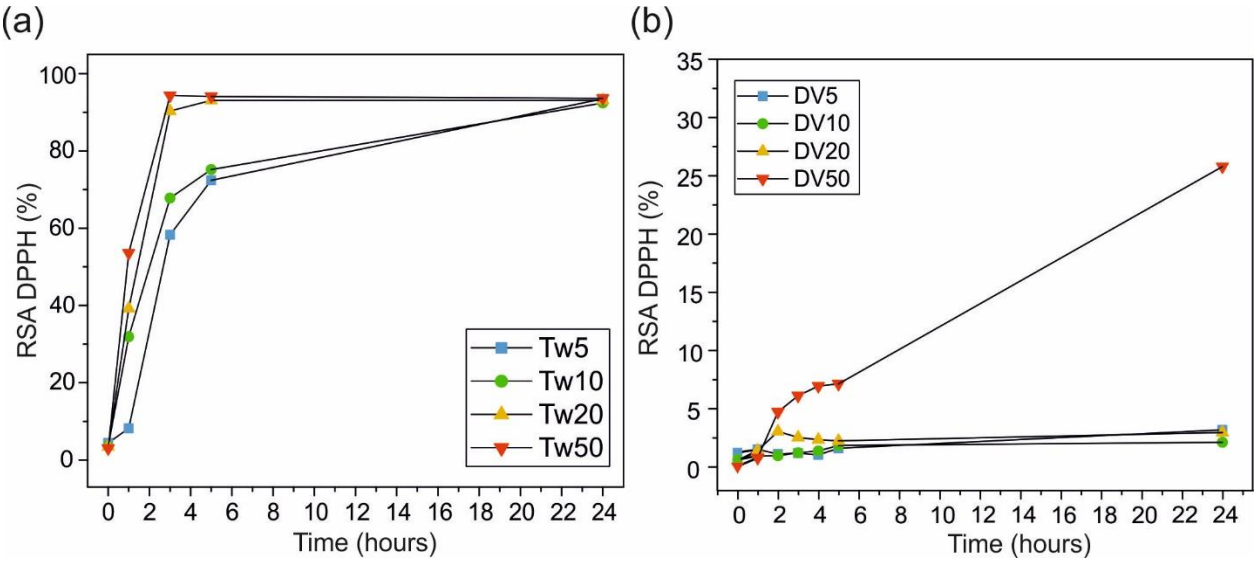

Figure 3.18 Kinetic profiles of the antioxidant response against DPPH· of **(a)** tea-waste films in 24 hours, and **(b)** discarded-vinegar films for 3 days.

Finally, the antioxidant activity of representative antioxidant films (T10, T50, V10, and V50) was compared with other published bio-based films are represented in **Figure 3.19**. The antioxidant activity was represented in terms of the Trolox equivalent antioxidant capacity (TEAC) in μmoles of trolox/g dried film, after one hour of immersion in the radical solutions. Summarizing, tea waste-PVA films displayed better results in ABTS assay, ~4.0 to ~13.1 μmoles of trolox/g dried film for Tw10 and Tw50, respectively; whereas discarded balsamic vinegar films showed ~2.7 and ~5.1 μmoles of Trolox for DV10 and DV50, respectively. For the DPPH assay, ~4.5 and ~8.5 μmoles of trolox/g dried film were measured for Tw10 and Tw50 films, respectively. These results were only overcome by (FLE), a film of fish-skin gelatin with lemon extract (Tongnuanchan et al., 2012).

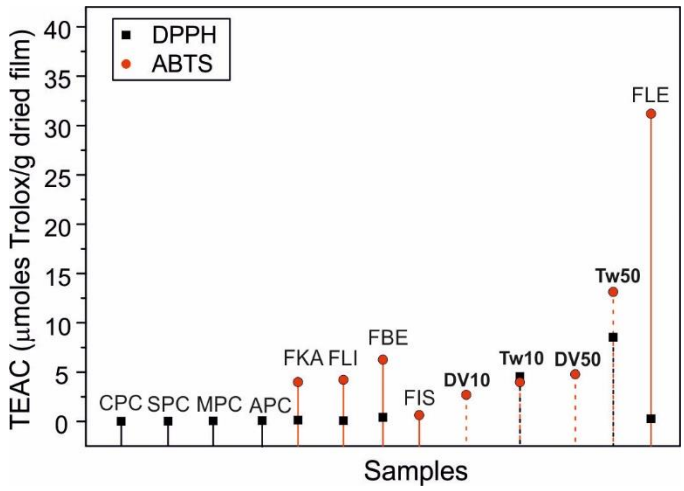

Figure 3.19 Comparison of the antioxidant capability, express in TEAC as µmol TEAC/g dried film, of DV10, DV50, Tw10, and Tw50 after 1 hour of release, and films reported in bibliography. CPC: Cashew Apple-Pectin, SPC: Strawberry-Pectin, MPC: Fruit Mixture-Pectin and APC: Acerola-Pectin (Eça et al., 2015); FKA: Fish Skin Gelatin-Kaffir-Lime, FLI: Fish Skin Gelatin-Lime, FBE: Fish Skin Gelatin-Bergamot, FIS: Fish Skin Gelatin, and FLE: Fish Skin Gelatin-Lemon (Tongnuanchan et al., 2012).

3.4.7 Water sensibility

Generally, vegetal wastes biomass is mainly composed of hydrophilic compounds, like saccharides, phenolic acids, cellulose (Munteanu & Vasile, 2020). The hydrophobicity of the films was analyzed measuring the water static contact angle (WCA) represented in Figure **3.20**. Higher values of WCA are associated with a more remarkable hydrophobic character. PVA, with WCA ≥ 90°, can be considered hydrophobic. For both food by-products, the incorporation of hydrophilic

molecules reduced the WCA from 100° (PVA films) to ~40°, see **Figure 3.20(a-b)**.

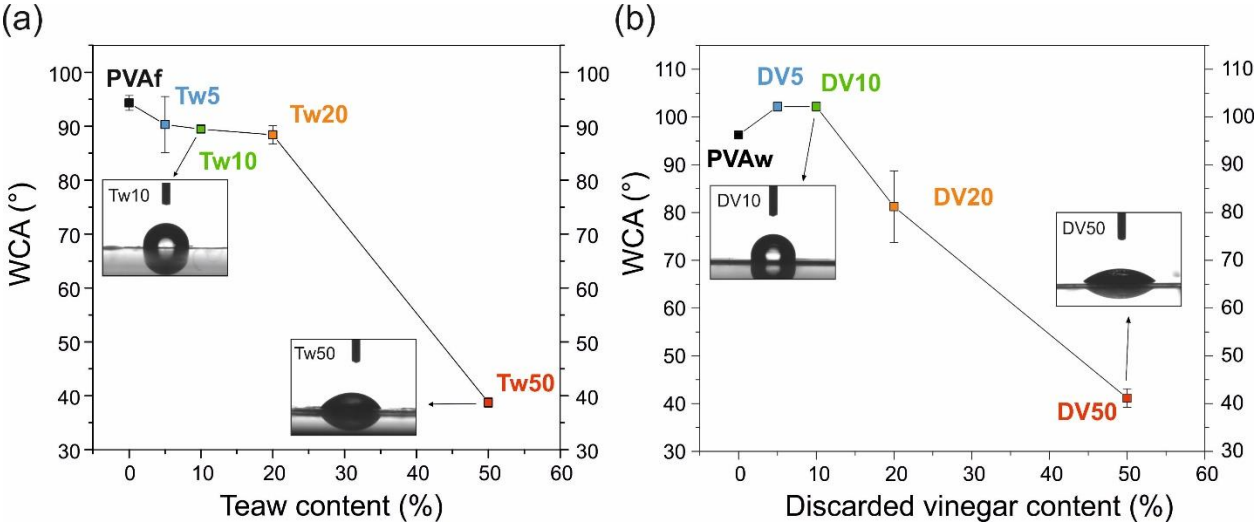

Figure 3.20 The water static contact angle (WCA) of **(a)** PVAf and films loaded with tea-waste extract, and **(b)** PVAw and discarded vinegar-PVA blends.

Figure 3.21 exhibits the water uptake results of PVAw, PVAf, and waste-containing films measured at different moisture conditions. **Figure 3.21(a)** shows that tea wastes enhanced the water uptake with loading. However, low concentrations of tea waste (5, 10 wt.%) reduced the moisture absorption of the neat PVA film (PVAf). This indicated that tea waste polyphenols interact with PVA via hydrogen bond reducing the availability of the hydroxylic groups of the polymer to interact with the water molecules, showing lower values of water uptake (Y. Liu et al., 2019). Above these concentrations, the excess of lignocellulosic biomass may retain the moisture molecules (Munteanu & Vasile, 2020). In **Figure 3.21(b)**, the water uptake of the samples increased with the concentration of discarded balsamic vinegar up to reaching almost 70% at 100% relative humidity. The high moisture sensibility may be attributed to the high content of sugars and glycerol, whose hydrophilic characters have resulted in an increment of moisture content and sensibility of many polymer matrices (Ilyas et al., 2018; Kurek et al., 2019).

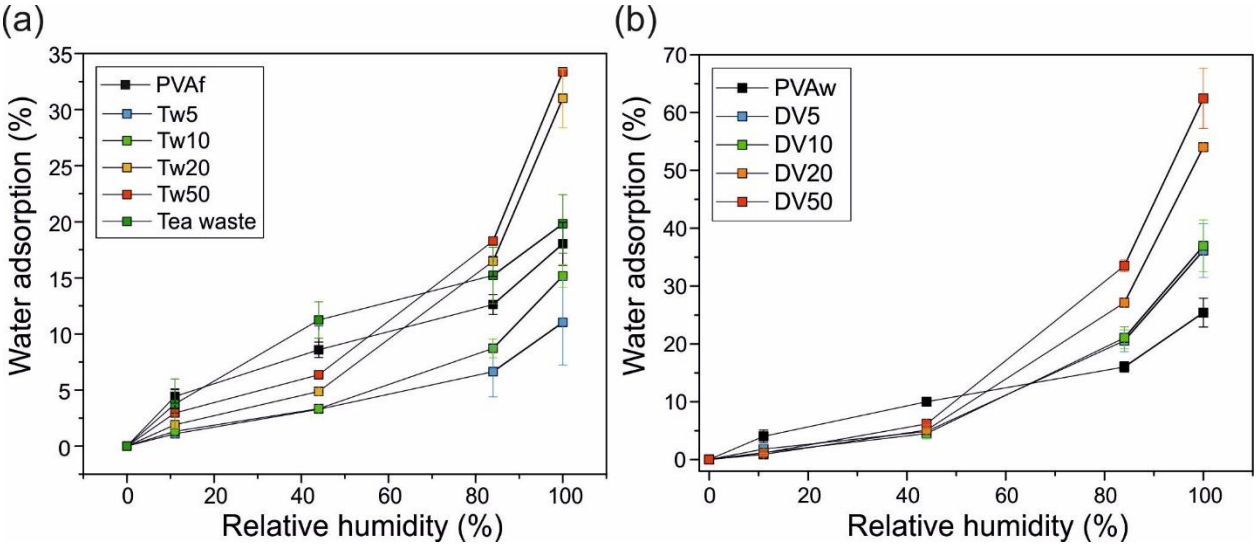

Figure 3.21 The water adsorption values collected at different humidity conditions (11%, 44 %, 84%, and 100%) **(a)** of tea waste-based, and **(b)** discarded vinegar-based PVA blends.

3.4.8 Oxygen gas permeability

The oxygen permeability (OP) of PVAw, PVAf, and Tw20 and DV20 are displayed in **Figure 3.22**. PVAf displayed the poorest oxygen barrier properties, five times over the PVAw. Balsamic vinegar induced structural modifications in the PVA matrix, which led to a decrease of crystallinity (**Fig. 3.12**), enhancing the oxygen molecules passing (Armentano et al., 2015). In turn, the agro-food wastes improved significantly the oxygen barrier properties with respect to neat PVA. Food waste is a source of antioxidants that react with oxygen molecules limiting the permeability of this gas (Collazo-Bigliardi et al., 2019).

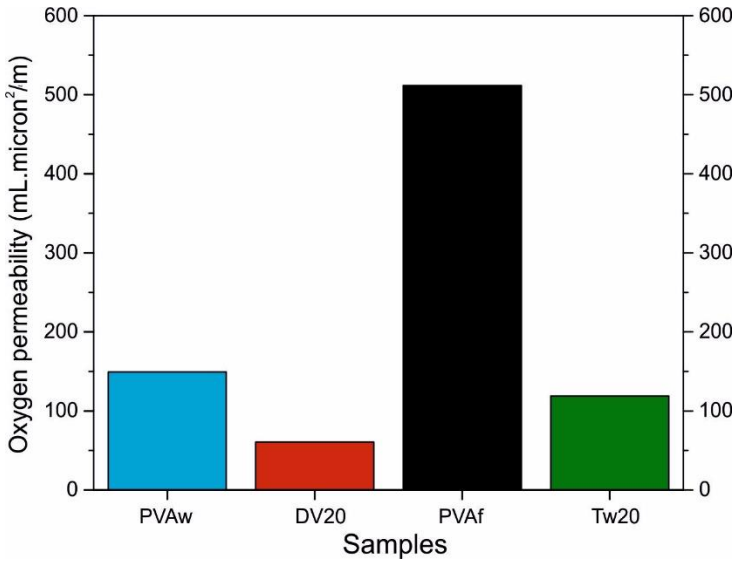

Figure 3.22 The oxygen permeability values of PVAw, PVAf, and PVA films loaded with discarded balsamic vinegar (DV20) and waste of tealeaves extract (Tw20).

3.5 Conclusion

Two major plant food industry wastes have been effectively valorized by following a simple one-pot plastic fabrication process. Efficient antioxidant bioplastics were made based on used green tea and quality control failed discarded balsamic vinegar. Formic acid was used to extract useful organics from dried tea waste while simultaneously dissolving PVA. Discarded vinegar was blended with a water solution of PVA and in both cases, antioxidant films were produced by solution casting and drying. The polymer could be loaded up to 50 wt.% by both waste components allowing maximum utilization of useful organics from both discarded foodstuffs. Formic acid enabled the extraction of gallated catechins with very high yields (>95%) from tea waste including a powerful biomedical compounded known as epigallocatechin gallate (EGCG). Both formic acid (residual) and balsamic vinegar effectively plasticized PVA with elongation at break values of 150% and 30%, respectively. Tea waste extracts exhibited better inhibitory concentration levels (IC50) of ~73.1 µg/ml and discarded vinegar ~1846.7 µg/ml, respectively. Antioxidant films also had better oxygen barrier properties than pure PVA, regardless of the solvent used.

Chapter 4: Functionalize paper biocomposites with natural biomolecules

4.1 Freshness sensitive and antioxidant paper-PCL biocomposites loaded with pomegranate peel and curcumin

Paper is a network of cellulosic fibers found in woods, easily-recyclable, biodegradable, with low-weight and economic price. These advantages have facilitated the scaling-up of paper offering a large range of applications, from building to the packaging industry (Vuoti et al., 2013). The major limitation of the neat paper is related to the high porosity of the fiber network, and the hygroscopic character of cellulose, which result in poor gas barrier properties and high wettability (Gällstedt et al., 2005; Khwaldia, 2013; W. Zhang et al., 2014). The food-packaging material may prevent the passing of oxygen molecules, which leads to the oxidation reaction of foods resulting in loss of quality and nutrients, and high humidity conditions promote the growth of microorganisms and mold (W. Zhang et al., 2014).

To resolve these limitations, the paper has been combined with diverse polymers, some highly hazardous to the environment like fluorinated, to reduce the high wettability and permeability (Mazzon et al., 2017; Zahid et al., 2019). For example, (Mazzon et al., 2019) used an emulsion of a derivative of polydimethylsiloxane (PDMS) with polyurethane to obtain superhydrophobic cotton fibers for application in the preservation of historical textiles. In addition to coatings based on hydrophobic biopolymers (like corn zein and soy proteins) have enhanced the water-resistance of paper (Parris et al., 2000; J. W. Rhim et al., 2006). Nevertheless, besides the application of coatings, paper can be treated by hot-pressing, which is an eco-friendly, free-solvent alternative method used in food packaging to form multilayer systems, preferred to reduce costs and processing times (Asgari et al., 2020; Martin et al., 2001). Hot-pressing paper with a hydrophobic polymer, such as polycaprolactone (PCL), might enhance the water-resistance and mechanical strength of paper. PCL is a petroleum-based, hydrophobic, biodegradable, and biocompatible polymer, which has shown to have excellent thermo-mechanical properties (Sharmin et al., 2012). The hydrophobic properties of PCL have been used previously to enhance the water-resistance of active gelatin-based fibers and wheat starch (Figueroa-Lopez et al., 2018; Martin et al., 2001). PCL powder can be processed by extrusion to obtain a scaling-up material. Similar to other industrial processes, PCL can be combined with an inorganic filler at high concentrations to reduce the costs and the percentage-average of petroleum-based material of the final product. In the current study, the inorganic salt magnesium carbonate ($MgCO_3$) was loaded in 10 wt.% and 25 wt.% through extrusion obtaining a more economical and sustainable material.

Additionally, paper sheets have also presented great versatility and easily-functionalized properties, which in combination with active molecules, can acquire innovative and intelligent properties. For instance, the incorporation of the active molecules of citric acid into a gelatin-coated paper incorporated antioxidant and antimicrobial properties, while adding a natural pigment, such as alizarin, provided the pH-sensitivity to a starch-cellulose paper developing a freshness-monitor system (Battisti et al., 2017; Ezati et al., 2019). In this project, the versatility of the paper-PCL biocomposite was proved by developing two different active systems, an agri-food byproduct like pomegranate peel, and curcumin. The functionalization of the paper has been performed by dipping in the solutions of pomegranate peel extract and curcumin, separately. Then, the active paper sheets were combined with PCL-$MgCO_3$ blend by hot-pressing obtaining a final active material containing ~30 wt.% of cellulose.

Pomegranate peel is an agro-food waste rich in hydrophilic antioxidants and antibacterial polyphenols, such as ellagic derivatives and gallic acid (Negi et al., 2003). The high contain of active-polar compounds allows water-extracts with high antioxidant capacity, avoiding toxic solvents commonly used in these extractions (He et al., 2019; Zhuang et al., 2019). Films and coatings made of pomegranate peel extract have been demonstrated to improve the preservation and food-quality of different foodstuffs, like curd (Sandhya et al., 2018), white shrimps (Licciardello et al., 2018), and bighead carp fillets (Zhuang et al., 2019).

Curcumin is a linear polyphenol with two o-methoxy phenolic groups linked by a seven carbon chain containing an α,β-unsaturated β-diketo moiety group, with excellent antioxidant and antibacterial properties (Bagchi et al., 2015; N. Pan et al., 2019). Nevertheless, the most interesting application of curcumin for the food industry is the colorimetric change with the pH, which has provided the monitoring of the freshness of foods that change the pH when spoiled (J. Liu et al., 2018; N. Pan et al., 2019). Moreover, the high solubility of curcumin in ethanol provided high antioxidant activity in fatty food simulants (ethanol-water, 50% v/v) (Ma et al., 2017; Zia et al., 2019). However, the hydrophobic character of curcumin results in low water solubility, which leads to low bioavailability, limiting the use of this promising natural compound for pharmacological applications (Bagchi et al., 2015). Encapsulation of curcumin and complexation with metals are some examples of the possible solutions to increase the solubility in water and promoting its bioactivity (Bagchi et al., 2015). In this work, the presence of magnesium in the form

of $MgCO_3$ in PCL-paper blends promoted the release of curcumin in aqueous food simulant media (ethanol-water, 5% v/v) due to the formation of Mg-Curcumin complex, exhibiting higher antioxidant activity with respect to the blend without the filler. The applicability of curcumin biocomposite as a freshness-food indicator has been tested when the sample was stored with fresh shrimps.

In this project, a novel paper-PCL biocomposite composed of ~30% cellulose was developed using free-solvent processing-methods, like extrusion and hot-pressing. Moreover, the versatility and wide range of application of the biocomposite were demonstrated by functionalizing the paper with food byproduct and curcumin, incorporating excellent antioxidant protection and the pH-sensitive colorimetric properties successfully tested with different foods.

4.2. Materials and Methods

4.2.1 Materials

Poly(ε-caprolactone) (PCL) powder with a molecular weight of 50.000, was purchased from Polysciences, Inc. Magnesium carbonate ($MgCO_3$), potassium persulfate ($K_2S_2O_8$), Curcumin from Curcuma longa (Turmeric powder), were purchased from Sigma Aldrich. Kimberly-Clark 05511 Kimtech® Science Precision Tissue Wipers were used as pure cellulose mats. ABTS (2,2-azino-bis-(3-ethylbenz-thiazoline-6-sulfonic acid) was purchased from Sigma-Aldrich Chemie (Steinheim, Germany). Potassium dihydrogen phosphate (KH_2PO_4) and dipotassium phosphate (K_2HPO_4). Shrimps and pomegranate were purchased from a local supermarket. Deionized water was obtained from a Milli-Q Advantage A10 Ultrapure Water Purification device, and ethanol (<=100%) was purchased from Merck.

4.2.2 Preparation of PCL-Mg samples

The processing methods performed for the elaboration of the PCL-$MgCO_3$ blends starting from the powders of PCL and $MgCO_3$ is schematically represented in **Figure 4.1.** Before extrusion, PCL flakes and $MgCO_3$ powders were kept in a lab oven overnight at 40°C to ensure the removal of any trace amounts of moisture. Afterward, the flakes and the powder were mechanically mixed such that two $MgCO_3$ in PCL concentrations were set namely, 10 wt.% and 25 wt. % (w/w). The

mix was then fed to a single screw extruder having six heating zones (Rheoscam extruder, Scamex-France) with a screw of 20 mm in diameter having a length to diameter ratio (L/D) of 20. The screw fed the extrudes to a circular die of 2 mm in diameter at the extrusion point, and its rotation speed was maintained at 50 rpm throughout the extrusion process. The temperature conditions across the six extrusion heating zones were 75°C/ 80°C/ 85°C/ 90°C/ 95°C/ 100°C. Continuous filaments (2 mm in diameter) were extruded and cooled to room temperature before cutting into pellets. Pellets were hot-pressed under 2 tons for 2 minutes at 85 °C, followed by a cooling step to room temperature under the same pressure, to obtain the films using a hydraulic press (Carver Inc. Model 3853, USA). Note that the pellets were covered with Teflon sheets to prevent adhesion to the heated platens.

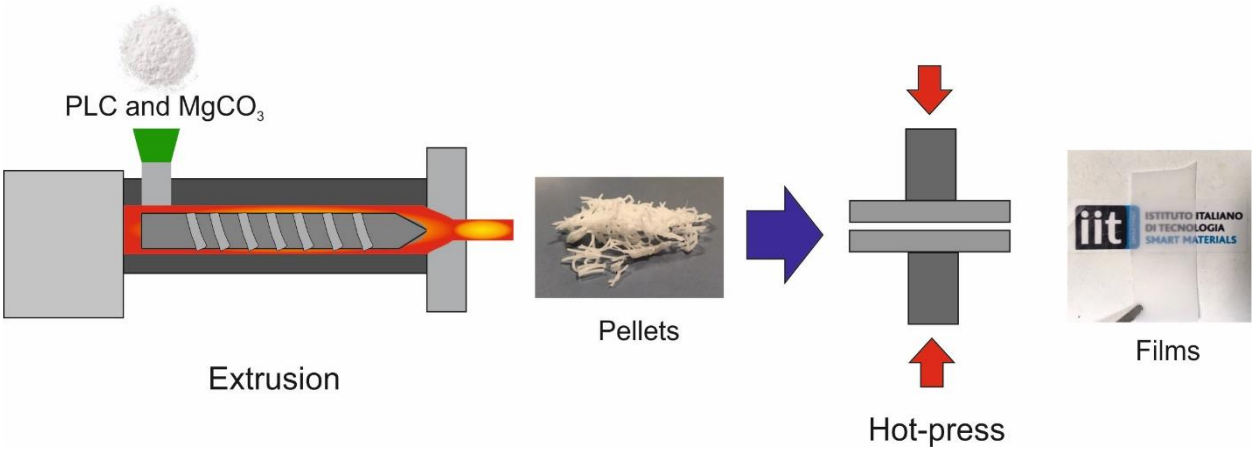

Figure 4.1 Fabrication scheme of blends composed by PCL and $MgCO_3$.

4.2.3 Fabrication of cellulose-PCL composite

Four paper sheets (11 cm x 21 cm) located at both sites of the PCL-$MgCO_3$ composites film were hot-pressed at 85 °C and under 2.1 tons for 20 seconds, obtaining the paper-PCL biocomposite with ~30 wt.% content of cellulose and different concentrations of $MgCO_3$ (10 and 25 wt.%). See **Figure 4.2.**

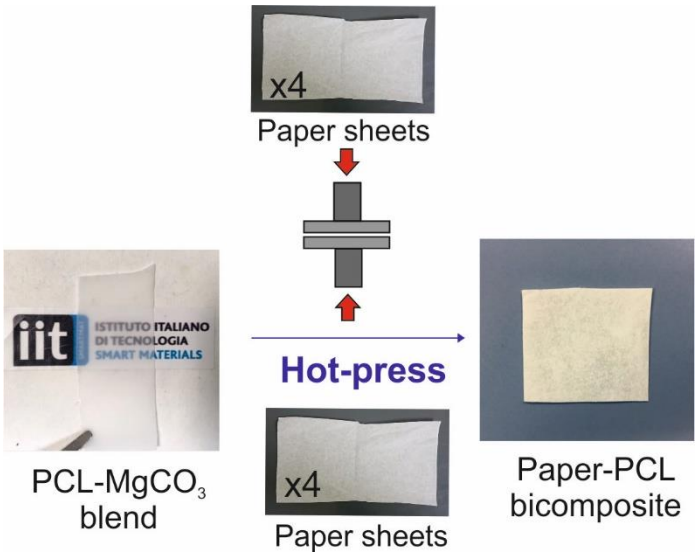

Figure 4.2 Fabrication scheme of the biocomposites paper-PCL.

4.2.3 Cellulose mat functionalization and preparation of bio-composites

The pomegranate peel extract was obtained following the procedure described in (Nadagouda et al., 2014). Briefly, the pomegranate peel was dried overnight in an oven at 40 °C, mashed, and sieve to obtain a powder with an average size of 300 µm powder. Ten grams of the powdered pomegranate peel were stirred for 2 minutes in 150 mL of distilled water. Then, the solution was kept in the dark at -4 °C for 4 hours and filtered with Whatman paper. The final solution was diluted to a final volume of 100 mL such that the extract concentration was 31.68 ± 0.00 mg/mL. This concentration was determined by weighting the dry matter of a known volume of the extract solution. The cellulose mats (11 cm x 21 cm) were dip-coated in the pomegranate peel extract for 30 seconds. Then, the stained tissue papers were vertically hanged under the chemical hood until it stops dripping. Then, paper sheets were left to dry in the oven at 40 °C for 30 min. The functionalization with curcumin was performed following a similar procedure, with small modifications. The cellulose tissues were dipped in an ethanol solution of curcumin (1 mg/ml) for 30 s and hanged under the chemical-hood. Hanging for 15 min was enough to dry the cellulose sheets, due to the high volatility of ethanol with respect to water. **Figure 4.3(a)** describes schematically the process of functionalization of the paper sheets.

Similar to paper-PCL composites, the active cellulose mats were placed on both sides of the PCL-$MgCO_3$ composite films and pressed at 85 °C and under 2.1 tons for 20 seconds, obtaining the final active materials. **Figure 4.3(b)** shows the processing to obtain the pomegranate peel extract and curcumin biocomposites.

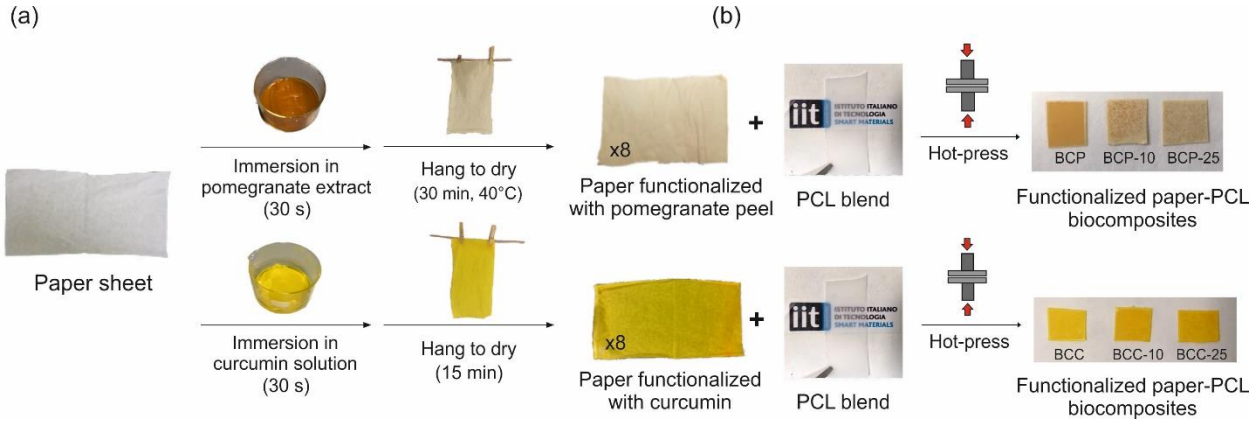

Figure 4.3 (a) Fabrication scheme of the functionalized paper with pomegranate peel extract (top) and curcumin (bottom). **(b)** Fabrication scheme of the functionalized paper-PCL biocomposites with pomegranate peel extract (top) and curcumin (bottom), labeled BCP, BCP-10, and BCP-25 and BCC, BCC-10, BCC-25, respectively, regarding the $MgCO_3$ content.

Samples were labeled as indicated in **Table 4.1** displayed below:

Table 4.1 Composition of the paper biocomposites of the current work.

SAMPLES	REMARKS
PCL/PCL-10/PCL-25	PCL samples with 0/10/25 wt.% of $MgCO_3$
BC/10/25	Samples with ~30% of cellulose and 0/10/25 wt.% of $MgCO_3$ with respect to the PCL content
BCP/10/25	Samples with ~30% of cellulose coated with pomegranate peel extract and 0/10/25 wt.% of $MgCO_3$ with respect to the PCL content
BCC/10/25	Samples with ~30% of cellulose coated with curcumin and 0/10/25 wt.% of $MgCO_3$ with respect to the PCL content

4.2.4 Scanning Electron Microscopy (SEM) with Energy-dispersive X-ray spectroscopy (EDS) and confocal.

Surface and cross-section morphologies of samples were characterized by scanning electron microscopy (SEM) using a JEOL JSM-6490LA microscope (JEOL Ltd., Japan), operating at 10 and 15 kV of accelerating voltage and equipped with energy dispersive spectroscopy (EDS) for the chemical identification of $MgCO_3$ particles in the polymer matrix. Before the analysis, the samples were previously coated with a 10-nm-thick gold layer with a Cressington 208HR sputter coater (Cressington Scientific Instrument Ltd, U.K.).

4.2.5 Thermal analysis: Differential scanning calorimetry (DSC)

The thermal stability of the neat PCL and PCL blends containing $MgCO_3$ in 10 wt.% and 25 wt.% was investigated with thermos-gravimetric analysis (TGA) using TGA Q500 system. The measurements were carried out on samples weighted in aluminum pans and heated from 30°C to 800°C with a heating rate of 10°C/min under an air of a constant flow rate of 50 mL/min.

The thermal behavior of PCL and PCL-$MgCO_3$ blends were analyzed by differential scanning calorimetry (DSC) using DSC Q20 (TA Instrument, Guyancourt, France) from -70 to 180 °C under dry N_2 flow (50 mL/min) at 10°C/min, using non-hermetic aluminum pans. The degree of crystallinity for the blends was calculated following **Equation 1** below as reported in:

$$X_C\ (\%) = \frac{\Delta H_m}{\Delta H_f} \text{x } 100 \quad (\mathbf{1})$$

H_m corresponds to the heat of fusion (endothermic), while H_c is the heat of cold-crystallization (exothermic). H_f corresponds to the heat of fusion for 100% of the crystalline PCL, 139.5 J/g (Zhu et al., 2005).

For the determination of crystallinity of composites, **Equation 1** above, becomes **Equation 2**, where W_f is the weight fraction of the additive content in a composite.

$$X_C\,(\%) = \frac{\Delta H_m}{\Delta H_f(1 - W_f)} \text{x } 100 \quad (\mathbf{2})$$

4.2.6 X-ray diffraction (XRD)

XRD patterns were recorded using a Rigaku SmartLab X-ray diffractometer, equipped with a 9 kW CuKα rotating anode, operating at 40 kV and 150 mA. A Göbel mirror was used to obtain a parallel beam and to suppress the Cu Kβ radiation (1.392 Å). The diffraction patterns were collected at room temperature over an angular range 8°−50°, with a step size of 0.05°. High Score 4.1 software from PANalytical was used for phase identification.

The degree of crystallinity (X_c) for the samples has been determined by deconvoluting peaks of amorphous and crystalline phases according to the following **Equation 3**:

$$X_C\,(\%) = \frac{I_c}{(I_c - I_a)} \text{x } 100 \quad (\mathbf{3})$$

where I_c is the total crystalline area under the crystalline PCL peaks and I_a the amorphous PCL area under the halo at 21°.

The XRD spectra of the neat PCL, PCL-10, and PCL-25, represented in **Figure 4.4(a-c)**. The spectra show the deconvolution of the crystalline and amorphous peaks to determine the crystallinity degree as shown in **Equation 3**.

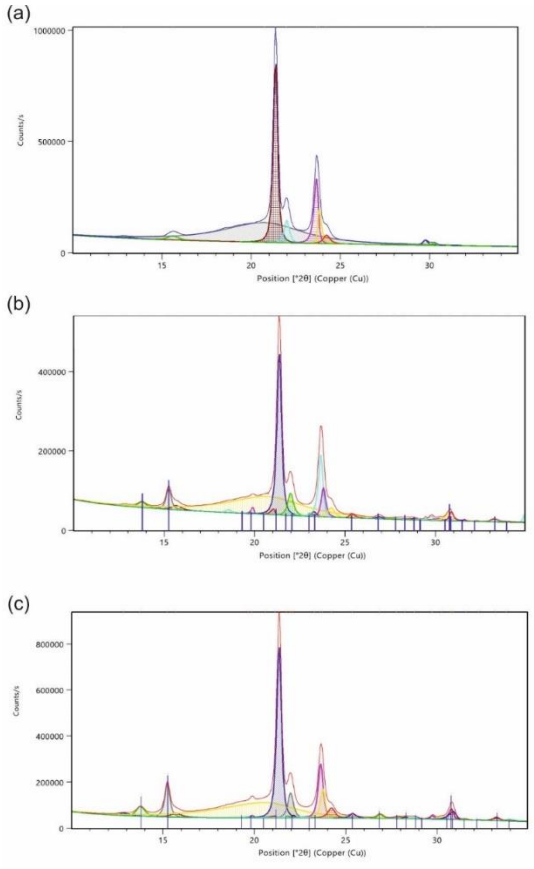

Figure 4.4 The XRD patterns with the deconvolution of the peaks belonged to **(a)** pure PCL, **(b)** PCL-10, and **(c)** PCL-25 samples. The vertical blue lines in **(b)** and **(c)** are referred to as the peak position reference for $Mg_5(OH)_2(CO_3)_4$ (magnesium carbonate hydroxide hydrate, ICSD 98-000-2341).

4.2.7 Mechanical characterization

Mechanical properties of the films were measured by uniaxial tensile tests on a dual column Instron 3365 universal testing machine. Dog-bone shaped samples had a gauge length of 25 mm and a width of 4 mm. Strain displacement was applied at a rate of 10 mm/min. Stress-strain curves were recorded at 25 °C and 44 % relative humidity (RH). At least three measurements were conducted for each sample and results were averaged to obtain a mean value. The stiffness of the material was defined with the Young's modulus value, calculated from the slope of the linear part of the stress-strain curve (before elastic limit). Both Young's modulus and elongation at break values were estimated using the built-in software of the tensile tester. The tensile strength of eight

paper sheets and cellulose-PCL blends were measured in the warp and the weft direction. For this purpose, test pieces were cut from the specimen parallel to the other perpendicular to the same edge of the specimen (Das, 2017).

4.2.8 Water uptake

For water uptake measurements, samples were first dried by conditioning in a desiccator until no change in sample weight was obtained. Then, dry samples were weighed on a sensitive electronic balance and placed in a sealed chamber under different humidity conditions (RH) at 25 ºC. The following humidity conditions were set to 0%, 15%, 45%, 85% and 100%. Samples were measured after two days to be sure that the equilibrium was reached, each sample was again weighed and the amount of adsorbed water was calculated as the difference with the initial dry weight. Three measurements were taken and the results were averaged to obtain a mean value. Water adsorption, in percentage, was calculated as indicated in **Equation 4**:

$$\text{Water uptake (\%)} = \frac{m_f - m_0}{m_0} \text{x } 100 \quad (\mathbf{4})$$

where m_f is the sample weight at different RH conditions and m_0 is the sample weight at 0% RH.

4.2.9 Water absorption

The water absorptiveness was calculated using the method described by (Sharmin et al., 2012). Eight neat cellulose sheets and cellulose-PCL blends (1 x 1 cm) were dried overnight at 40 °C in a vacuum oven. Then, the sheets were immersed in 10 mL of water for 48 hours. After this time, the water was discarded, and the excess surface water on the sample was removed by wiping it with tissue paper. The water absorption was calculated following **Equation 5** displayed below:

$$\text{Water absorption (\%)} = \frac{m_f - m_0}{m_0} \text{ x } 100 \quad (\mathbf{5})$$

where W_0 and W_f are the weight before and after the immersion, respectively.

4.2.10 Gas permeability of cellulose-PCL composites

Water vapor permeability (WVP) of samples was determined at 25 °C and under 100% relative humidity gradient (ΔRH %) according to the ASTM E96 standard method. In this test, the permeation chamber with a 7 mm inside diameter and a 10 mm inner depth were used filled with 400 µm of deionized water (which generates 100 % RH inside the permeation cell). The samples were cut into circles and mounted on the top of the permeation chambers. The permeation chambers were placed in a 0% RH desiccator with anhydrous silica gel, which was used as a desiccant agent to maintain 0% RH in the desiccator. The water transferred through the film was determined from the weight change of the permeation chamber every hour during a period of 8 h using an electronic balance (0.0001 g accuracy) to record mass loss over time. The mass loss of the permeation chambers was plotted as a function of time. The slope of each line was calculated by linear regression. Then, the water vapor transmission rate (WVTR) was determined as below in **Equation 6**:

$$\mathrm{WVTR}(\mathrm{g/m^2 d}) = \frac{\text{Slope}}{\text{Area of the sample}} \quad (\mathbf{6})$$

WVTR measurements were replicated three times for each film. The WVP of the sample was then calculated as **Equation 7** indicates below:

$$\mathrm{WVP}(\mathrm{g/m^2 d\ Pa}) = \frac{\mathrm{WVTR\ x\ L\ x\ 100}}{\mathrm{p_s\ x\ \Delta RH}} \quad (\mathbf{7})$$

where L (m) is the thickness of the sample, measured with a micrometer with 0.001 mm accuracy, ΔRH % is the percentage of relative humidity gradient, and ρ_S (Pa) is the saturation water vapor pressure at 25 °C.

The oxygen permeation tests of samples were performed using an Oxysense 525oi device (Oxysense, USA) equipped with a film permeation chamber. This machine was operated according to ASTM Method F3136-15. The test was performed at standard laboratory conditions, *i.e.*, 23°C and 40% relative humidity. The permeation chamber consisted of a cylinder divided into two parts (sensing well and driving well). The sensing well was instrumented with a fluorescence sensor

called oxydots, sensitive to the oxygen concentration. This chamber was purged with nitrogen while the other one (driving well) was kept open to ambient air. The films were cut into a rectangular piece (6 cm x 6 cm) and placed inside the chamber. An OxySense fiber optic pen measured the oxygen reading from the oxydots, at specific time intervals. Oxygen transmission rates (OTRs) of the blend films were measured by monitoring the oxygen uptake with time using Oxysense OTR software. At least ten measurements were taken for each sample with a minimum coefficient of determination (R^2) value of 0.95.

4.2.11 Migration study

The characterization of the migration of the antioxidants from the samples to two different food simulants aqueous food simulant and fatty food simulant was performed. Pomegranate peel and curcumin paper sheets and biocomposites were cut in pieces (1 cm x 1 cm) and immersed in 3 mL aqueous and fatty food simulants composed of 95% v/v water-ethanol, and 50% v/v water-ethanol, respectively. The release of the active molecules was monitored measuring the absorbance of the characteristic absorption bands at different time-intervals with Varian CARY 600i Scan UV-vis spectrophotometer. The absorption value of the characteristic peaks of curcumin and pomegranate peel extract, located at 429 nm and 370 nm, respectively (Biao et al., 2018; Mondal et al., 2016). The concentrations of active compounds migrated in samples are calculated by plotting the absorption against different volumes of a known concentration of curcumin (16.66 µg/mL) and pomegranate peel extract (2.6 mg/mL). The equation obtained from the calibration curve obtained for curcumin was: y=0.103x+000364 and y=0.00129x-0.000209 for pomegranate peel extract. Results were represented in terms of percentage of release with respect to the maximum obtained in the same weight of coated paper (40 mg). The experiment was performed in triplicate to ensure the veracity of the results.

4.2.12 Antioxidant activity

The antioxidant activity was measured by analyzing the radical scavenging activity (RSA) of the antioxidants against the cation radical 2,2-azino-bis-(3-ethylbenz-thiazoline-6-sulfonic acid) (ABTS). Briefly, the $ABTS^{\cdot+}$ a radical solution was produced by the reaction between 7 mM ABTS solution with 2.45 mM potassium persulfate solution in the dark at room temperature for 12-16

hours (Guzman-Puyol et al., 2017). The solution of the radical cation ($ABTS^{\cdot+}$) was diluted in water to obtain an optical absorbance around ~0.8 at 734 nm, 2 mL $ABTS^{\cdot+}$ and 1 mL of water. Then, different volumes of the extract solution, 1 mL of curcumin extract in aqueous food simulant, 0.1 mL of curcumin extract in fatty food simulant, and 0.05 mL of pomegranate peel extract in both aqueous and fatty food simulants, were diluted with water up to reach 1 mL and immersed in 2 mL of $ABTS^{\cdot+}$ radical solution. The reaction between the antioxidants with the cation radical leads to a colorimetric change, from dark blue to yellow, and a reduction of the characteristic absorption band of the cation radical ($ABTS^{\cdot+}$). The measurements were taken after 6 minutes and at least in triplicate to ensure reproducibility (Pérez-Jiménez & Saura-Calixto, 2006). RSA was calculated following the next **Equation 8**:

$$\text{Radical scavenging activity (\%)} = \frac{A_1 - A_2}{A_1} \text{ x } 100 \quad (\mathbf{8})$$

Where A_1 is the absorbance of the sample solution with $ABTS^{+\cdot}$ at 734 nm and A_2 is the absorbance of the $ABTS^{\cdot+}$ control solution. All measurements were performed at least five times to ensure reproducibility.

Then, the antioxidant activity of the samples was represented in terms of Trolox Equivalent Antioxidant Capacity (TEAC). To perform the curve, different concentrations of Trolox (6-hydroxy-2,5,7,8-tetramethylchroman-2-carboxylic acid) solutions (0.001-0.03 µg/mL) were represented against the RSA values, obtained using the $ABTS^{+\cdot}$ assay. The calibration curve obtained was defined with the following equation: y=3263.95x-0.927. The values RSA obtained with the extract solutions can be substituted in the equation above to obtain the equivalents of Trolox.

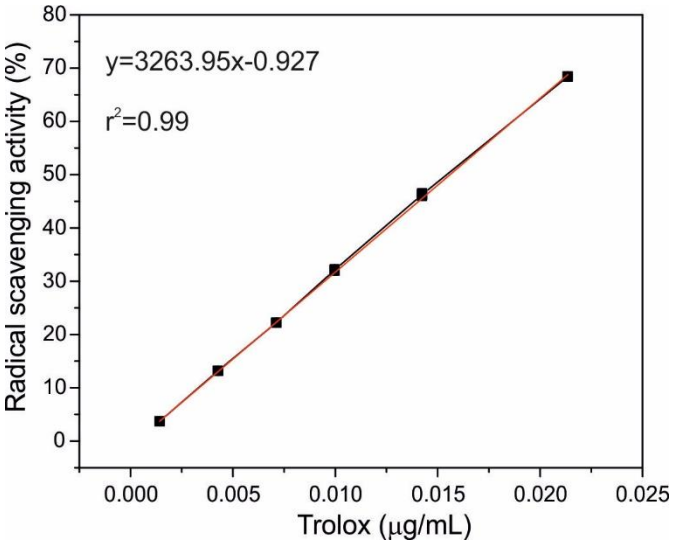

Figure 4.5 The curve obtained from representing the concentration of Trolox (µg/mL) against the radical scavenging activity (%).

The half-inhibitory concentration (IC50) values of a curcumin pomegranate extract were calculated. IC50 indicates the concentration of the antioxidant solution (µg/mL) required to inhibit the radical $ABTS^{+\cdot}$ to 50% of RSA. This parameter is important to understand the antioxidant character of the natural coatings. Different concentrations of the antioxidant solutions were prepared and immersed in the $ABTS^{+\cdot}$ solution to create a calibration curve. The radical scavenging activity (RSA) of each concentration was calculated using **Equation 8**. Then the RSA was represented against the concentration of the antioxidant solution, obtaining a linear tendency. The IC50 was calculated for curcumin and pomegranate peel extract solutions, see **Figure 4.6(a-b)**.

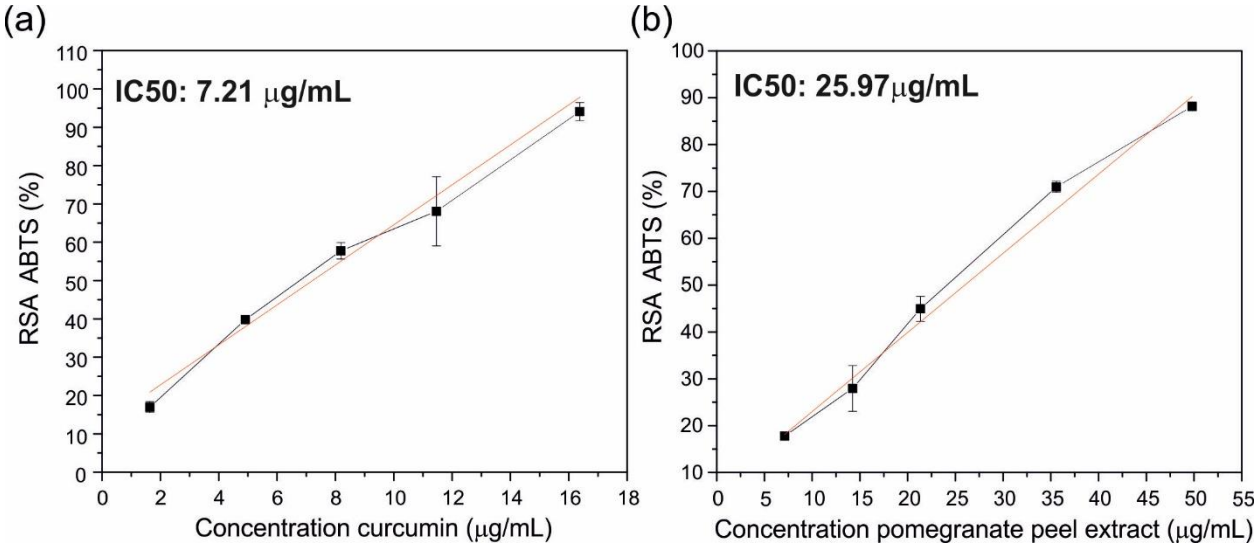

Figure 4.6 The IC50 graph obtained plotting the concentration of the active compound versus the RSA in $ABTS^{+\cdot}$, to obtain the half-inhibitory concentration, IC50 (μg/mL) of **(a)** curcumin and **(b)** pomegranate peel extract.

4.2.13 pH-colorimetric change

The sensitivity to pH of the curcumin biocomposites was analyzed when immersed in a buffer solution of potassium dihydrogen phosphate (KH_2PO_4) and dipotassium phosphate (K_2HPO_4) in the range from 6.5 to 9 pH. The colorimetric parameters, L (lightness), a (redness-greenness), and b (yellowness-blueness), were collected under the same light and distance from the sample and using a free mobile app called "ColorDetector". These values were used to obtain the total color difference with respect to the blank sample, defined as ΔE following **Equation 9** below, as reported in (Halász & Csóka, 2018):

$$\Delta E = [(L - L^*)^2 + (a - a^*)^2 + (b - b^*)^2]^{0.5} \quad (\mathbf{9})$$

where L*, a*, and b* are the parameters of the blank dry sample before the immersion.

4.2.14 Sensitivity to basic vapors

The color changes of the curcumin samples when exposed to ammonia vapor was evaluated. The biocomposites were placed at the top of a flask at a 10 cm distance from 50 µL of NH_4OH solution. All photos were collected with the free mobile app called "ColorDetector under the same light conditions. The sensitivity is represented with the color parameters in RGB code, where R, G, and B, represent red, green, and blue, respectively. These values were collected at different times and evaluated following **Equation 10** below (H. zhi Chen et al., 2020):

$$S_{RGB} = \frac{|R - R^*| + |G - G^*| + |B - B^*|}{R^* + G^* + B^*} \text{ x } 100 \quad (\mathbf{10})$$

Where R^*, G^* and B^* were the values recorded at zero time point, while R, G, and B are the values recorded after 30 s and 10 min.

The color reversibility of samples was measured by evaluating the total color difference (ΔE) between the sample after exposure to the basic vapors for 30 s, and the sample placed at room conditions overnight after the exposure. Results were represented following **Equation 9** displayed in section 5.2.13.

4.2.15 Food experiment

Shrimps were thawed at refrigerator temperature (4 °C) before the experiment. After immersing the food samples under tap-water to get the room temperature. Then, the shrimps were placed in sterilized plastic Petri-dishes (ø=90 mm). The curcumin indicators (1 cm x 1 cm) were stuck inside the cap of the petri-dish without coming into contact with the food. The sensitivity of the volatile amines was monitored at different times during the experiment 4h, 24h, 48h, and 72h, following **Equation 10** reported in section 5.2.14.

4.3. Results and discussion

4.3.1 PCL-$MgCO_3$ blends

The morphology, structural and thermal properties of polymeric blends made for PCL and $MgCO_3$ in 10 wt.% (PCL-10) and 25 wt.% (PCL-25) were characterized in this section.

4.3.1.1 Morphological study: SEM/EDS

The surface and cross-section morphology of PCL-$MgCO_3$ pellets are represented in **Figure 4.7**. The top-view microphotographs of samples showed that neat PCL and PCL contained 10 wt.% of $MgCO_3$ (PCL-10) pellets exhibited equally smooth surfaces, while the incorporation of filler at higher concentrations (25 wt.%) resulted in a rough morphology (PCL-25), see **Figure 4.7(a-c)**. The study of the cross-section of the pellets was performed by combining SEM and EDS analysis, **Figure 4.7(d-f)**. Similar to surface images, PCL and PCL-10 showed a homogeneous dense bulk-structure, whereas PCL-25 displayed a cross-section full of voids. The distribution of the inorganic filler in the matrix was identified using the EDS elemental mapping of Mg, exposed in the bottom right side of **Figure 4.7(d-f)**. Mg particles, colored in red, were distinguished in the EDS mapping images of PCL-10 and PCL-25 blends, **Figures 4.7 (e-f)**, respectively. The EDS images indicated that the $MgCO_3$ formed agglomerates when the concentration of the inorganic salt increased.

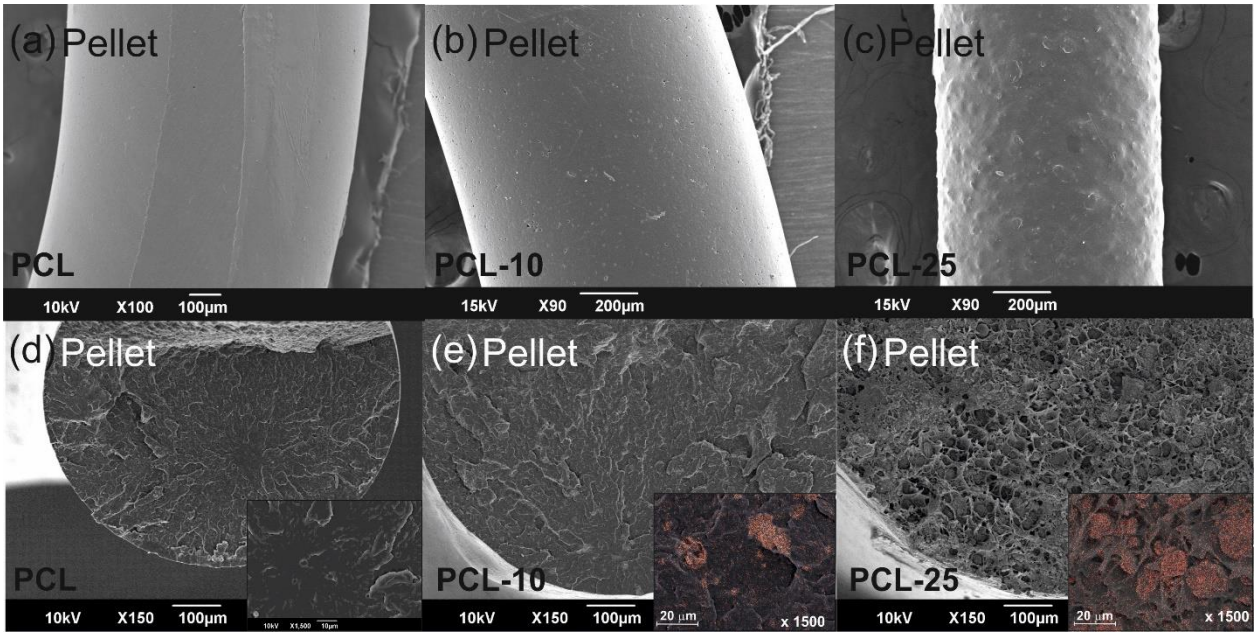

Figure 4.7 Surface images of the pellets **(a)** PCL, **(b)** PCL with 10 wt.% of $MgCO_3$, and **(c)** PCL with 25 wt.% of $MgCO_3$. The cross-section images of the pellets **(d)** PCL, **(e)** PCL with 10 wt.% of $MgCO_3$, and **(f)** PCL with 25 wt.% of $MgCO_3$. The quantitative EDS maps for Mg, with magnification x1500, are placed as an inset of the cross-section images **(d, e, f).**

The elemental analysis of the pellets was studied with energy-dispersive X-ray spectroscopy. The EDS spectrum of PCL-10 and PCL-25 are represented in **Figure 4.8(a-b)**, respectively. As expected, the peak corresponding to Mg (K_α=1.253keV), pointed with an arrow, was more intense in pellets with a higher content of $MgCO_3$. The SEM and EDS images of the sections of the samples analyzed are located in the top right section of the image, with the Mg colored in red.

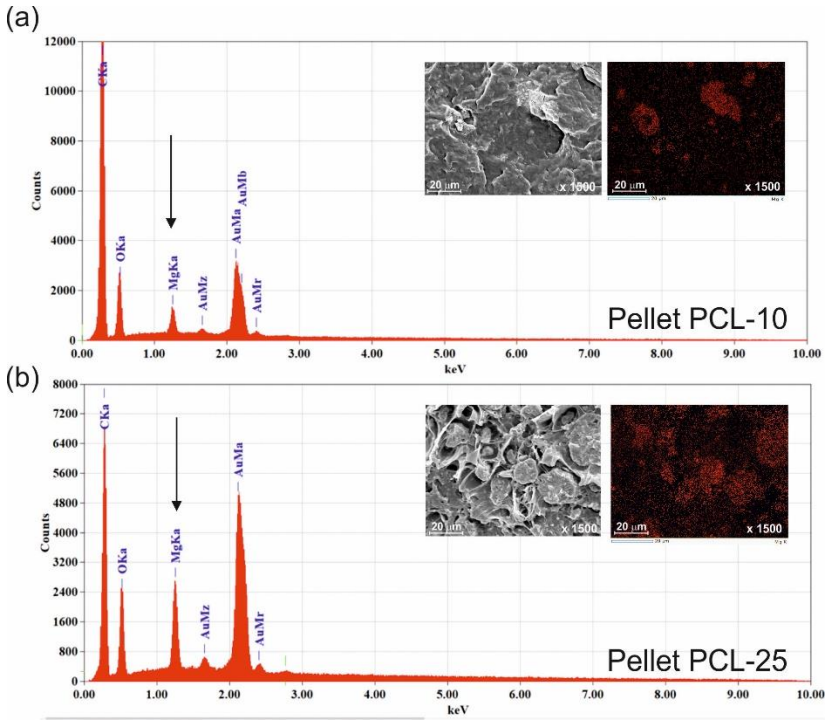

Figure 4.8 (a) The EDS spectrum shows the X-ray lines of the elemental composition of the pellets PCL-10, with the SEM and the corresponding EDS map for Mg (K_α=1.253keV) in red. **(b)** The EDS spectrum shows the X-ray lines of the elemental composition of the pellets PCL-25, with the SEM and the corresponding EDS map for Mg (K_α=1.253keV) in red. Note that the peak corresponding to Mg is remarked with a black arrow.

After hot-pressing the pellets, the morphology study of PCL and PCL-$MgCO_3$ films was performed with SEM and EDS and reported in **Figure 4.9**. The images of the surfaces of samples displayed in **Figure 4.9(a-c)** indicated that all samples had a regular and homogeneous surface, independently of the $MgCO_3$ content. In **Figure 4.9 (d-f)**, films also present a dense cross-section morphology, free from physical defects, indicating a strong interface interaction (Mi et al., 2014). An inset of the EDS images of the cross-section indicated that Mg particles were well dispersed throughout the matrix, contrary to the agglomerates observed in pellets, see **Figure 4.7(e-f)**.

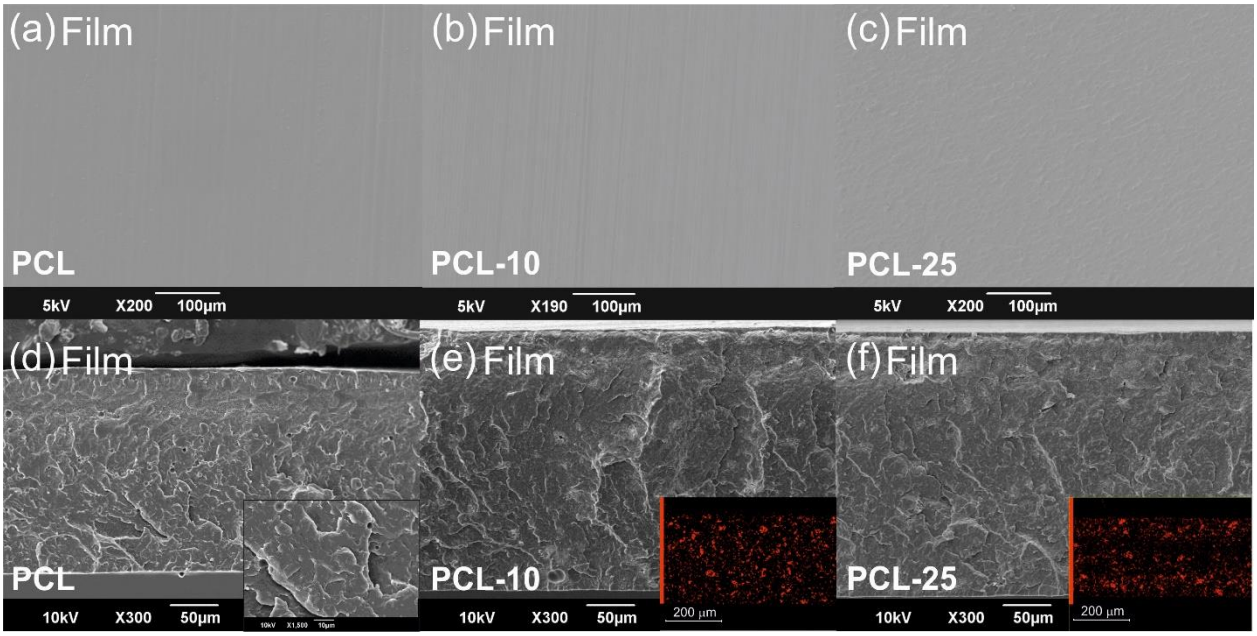

Figure 4.9 Surface images of the films **(a)** PCL, **(b)** PCL with 10 wt.% of $MgCO_3$, and **(c)** PCL with 25 wt.% of $MgCO_3$. The cross-section images of the films **(d)** PCL, **(e)** PCL with 10 wt.% of $MgCO_3$, and **(f)** PCL with 25 wt.% of $MgCO_3$. The EDS maps for Mg are placed as an inset of the cross-section images **(d, e, f).**

4.3.1.2 Crystallization behavior and thermal stability.

PCL is a semi-crystalline polymer with a melting point of ~60°C and glass transition located around -60°C (Khalid et al., 2018). The crystallinity of PCL and PCL-$MgCO_3$ blends can be calculated using the enthalpy of the melting point peaks obtained with the differential scanning calorimetry (DSC). In **Figure 4.10(a)**, the DSC thermograms showed the endothermic peak of the melting point of PCL, PCL-10, and PCL-25. PCL presents a melting process below 60 °C, with a T_m=54.3 °C, related to the crystalline phase. The changes in the melting temperatures were insignificant with the incorporation of 10 wt.% and 25 wt.% of $MgCO_3$, 54.2 °C and 54.4°C for PCL-10 and PCL-25, respectively. The crystallinity of neat PCL was calculated with **Equation 1**, while the crystallinity of PCL blends was calculated using **Equation 2**. PCL film showed a crystallinity degree (X_C) of 49%, while the X_c of blends increased the incorporation of the filler, to 53% and 54% for PCL-10 and PCL-25, respectively. The enhancement of crystallinity with the $MgCO_3$ content can be attributed to the formation of nucleation sites that promote the

crystallization of the polymer (Liang et al., 2013). The same tendency has been reported with other PCL blends, containing cellulose nanocrystals (Mi et al., 2014), and calcium carbonate (Liang et al., 2013).

The crystallinity degree of PCL-Mg blends was also calculated using the X-ray diffraction technique (XRD). The XRD pattern of pure PCL showed three strong diffraction peaks at 2θ = 21.4°, 22° and 23.7° which correspond to the orthorhombic planes (110), (111), (200) and a halo centered at 21°, assigned with the PCL reference (CCDC WMXAR01 P212121), represented in orange in **Figure 4.10(b)** (Jing et al., 2017; Salmoria et al., 2017). The peaks of the $MgCO_3$ salt, colored in light green, did not coincide with the $MgCO_3$ with reference number (JCPDS 01-071-1534) colored in dark green, but with a hydrated-form, called magnesium carbonate hydroxide hydrate ($Mg_5(OH)_2(CO_3)_4$), with reference number (ICSD 98-000-2341), represented in pink (Choi et al., 2013)(Yin et al., 2014). The utilization of the hydrate-form of the magnesium carbonate, or the majority, is not an inconvenience because the role of the filler is only to reduce the content of petroleum-based material. Actually, magnesium hydrates are widely used as inorganic fillers to provide fire retardant properties (Hornsby, 1994, 1996). Peaks belonged to PCL and ($Mg_5(OH)_2(CO_3)_4$) were assigned to the XRD patterns of PCL-10 and PCL-25, indicated with orange square and pink stars, respectively. Furthermore, the peaks related to the hydrated magnesium carbonate were more intense in films with higher content of filler, PCL-25 (Mi et al., 2014). The degree of crystallinity (X_c) of all samples was obtained using the **Equation 3** and the deconvolution XRD-pattern reported in **Figure 4.4** (section 4.2.6).

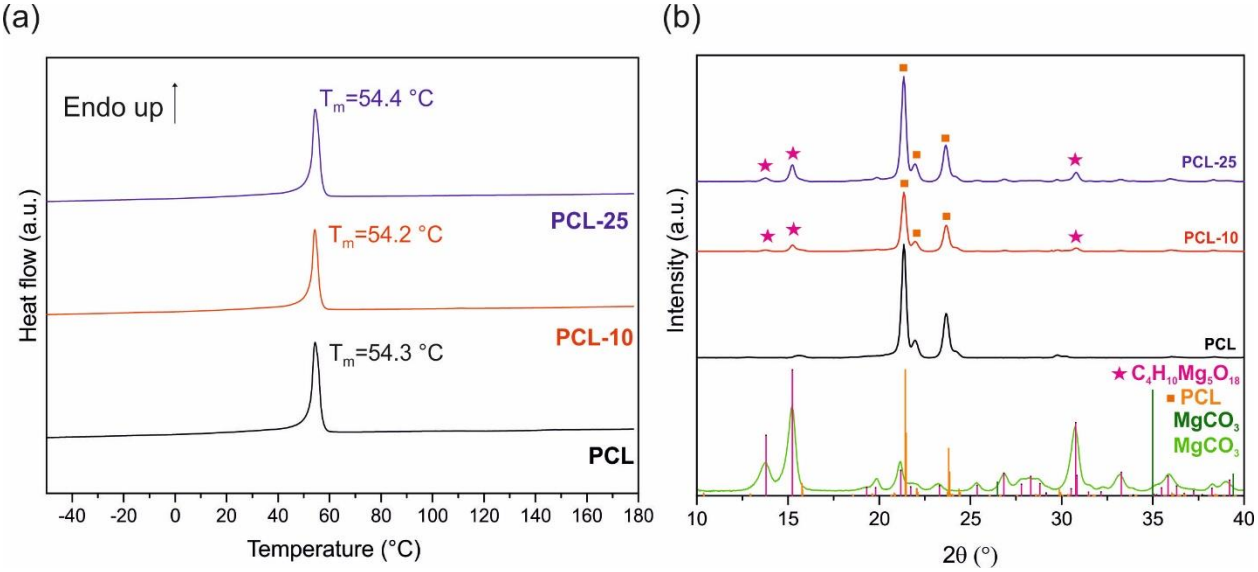

Figure 4.10 (a) The melting point temperature (T_m) peak and the melting enthalpy (ΔH_m) for PCL, PCL-10, and PCL-25 films, obtained from the DSC analysis. **(b)** XRD patterns of PCL (black), PCL-10 (red) and PCL-25 (blue), $MgCO_3$ salt (light green) with the expected peak position references for PCL (CCDC WIMXAR01 P212121, orange), $MgCO_3$ (ICSD 98-009-4579 $MgCO_3$, dark green), and ($Mg_5(OH)_2(CO_3)_4$) (magnesium carbonate hydroxide hydrate, ICSD 98-000-2341, pink).

In agreement with DSC results, the crystallinity degree was found to increase from 48% in neat PCL to 51% and 56% for PCL-10 and PCL-25, respectively. The crystallinity (X_c) and thermal parameters of PCL and PCL-$MgCO_3$ blends obtained with DSC and XRD analysis were represented in **Table 4.2.**

Table 4.2. Melting temperature (T_m), melting enthalpy (ΔH_m), and crystallization degree (X_c) obtained with DSC and XRD, for PCL, PCL-10, and PCL-25 samples.

Sample	T_m (°C)	ΔH_m (J/g)	X_c (%) DSC	X_c (%) XRD
PCL	54.3	69.35	49	49
PCL-10	54.2	67.34	53	51
PCL-25	54.4	56.53	54	56

The thermal degradation behaviors of PCL-$MgCO_3$ blends were analyzed using thermal gravimetric analysis (TGA). As observed in **Figure 4.11**, the neat PCL sample exhibited a single degradation curve at about 400°C (Hollingbery & Hull, 2012). The thermal stability of PCL decreased with the filler content, down to 315 °C and 220 °C for PCL-10 and PCL-25, respectively. Generally, fillers generate thermal degradation-sites in the polymer matrix, which promote degradation at lower temperatures (Kumar & Nayak, 2020). PCL-10 displayed a single degradation step at 325 °C associated with the degradation of the polymer. The great similarity between PCL-10 and neat PCL highlighted the well-distribution of the hydrated magnesium carbonate inside the polymeric matrix (X. Liu et al., 2014). However, different degradation steps resulted in the TGA thermogram of PCL-25, which indicated that the sample was made up of different phases. The first mass-loss step was assigned to the degradation of the polymer, while the second degradation step

was related to the loss of crystallization-water molecules belonged to the hydrated $MgCO_3$ nanoparticles, also observed in XRD spectra (**Figure 4.10**) (Yin et al., 2014). The formation of high char yield in PCL-25 (~8%), with respect to PCL-10 (~2%) is attributed to the higher concentrations of the inorganic filler in the polymer matrix.

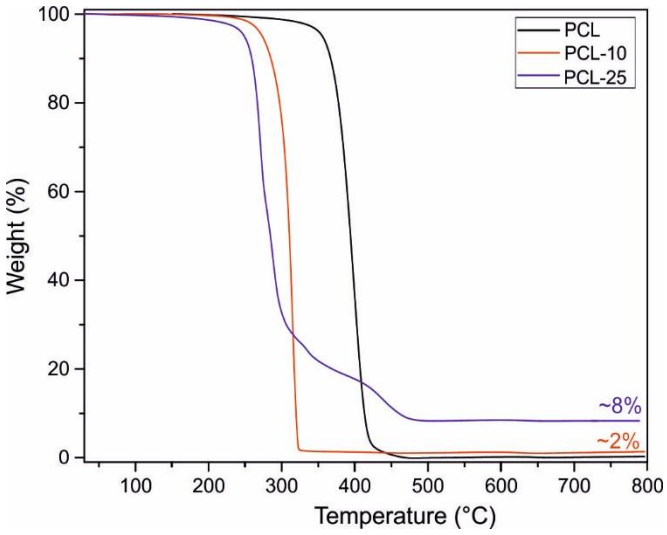

Figure 4.11 The thermogravimetric analysis of neat PCL (marked in black) and PCL blends with 10 wt.% and 25 wt.% of $MgCO_3$, in red and blue respectively.

4.3.1.3 Mechanical characterization

Figure 4.12 shows the tensile strength and elongation of the inorganic filler effect on the PCL matrix. In **Figure 4.12(a),** the stress-strain curve of neat PCL and PCL-$MgCO_3$ blends showed that the elongation was slightly reduced with the content of filler, from 800% to ~700% in both PCL-$MgCO_3$ films. The magnification of the slope of the stress-strain curve is located in an inset of **Figure 4.12(a).** The increase in slope with the filler concentration indicated that its loading reinforced the material strength. The values of the mechanical parameters with the content of filler were represented in **Figure 4.12(b)**. According to the stress-strain curve results, the elongation was decreased with the filler content, while the Young's modulus was increased by 50% in films with 25 wt.% content of $MgCO_3$. This tendency is commonly observed in other nanocomposites, associated with the dispersion and physical defects at a high concentration of the fillers (Dutta & Maji, 2020; Jiang et al., 2007).

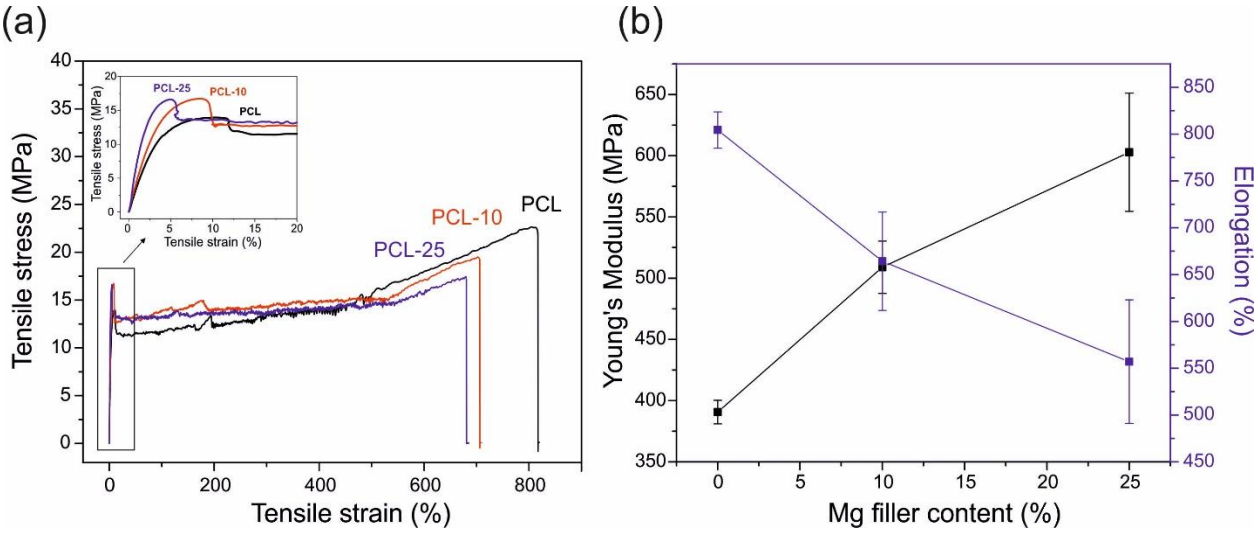

Figure 4.12 (a) The stress-strain curve of the PCL blends with different contents of hydrated $MgCO_3$. **(b)** The values of Young's Modulus (MPa) and elongation of the PCL blends.

4.3.1.4 Moisture adsorption and wetting properties

The water resistance properties are very important for different applications like building construction or clothing. In packaging, materials with high water-resistant are more effective to preserve food quality and nutrients. Generally, low values of water uptake and WVP are desired to avoid the high humidity ambient that promotes the growth of microorganisms, as well as the loss of the characteristic crispy texture of dry foods (Gaikwad et al., 2019). The water uptake values of the PCL and PCL-$MgCO_3$ blends measured at a different relative humidity (from 11 to 100 %) are represented in **Figure 4.13(a)**. The sample showed negligible weight variations when exposed to diverse humidity conditions. These results were attributed to the high hydrophobic character of PCL. The maximum value of water uptake was obtained at 100%, where PCL showed less <1 % of water uptake, and PCL-10 and PCL-25 showed 1.13 ± 0.31 % and 1.95 ± 0.27 %, respectively. Noticeably, the good water resistance properties were maintained even with the high concentration of the hygroscopic inorganic salt.

Figure 4.13(b) shows the water vapor permeability values obtained for PCL samples. The high hydrophobicity nature of PCL decreased the passage of water molecules through the film, obtaining great water vapor barrier features (Sharmin et al., 2012). The incorporation of $MgCO_3$ in 10 wt.% (PCL-10) reduced in almost four times the good water vapor permeability of the neat

PCL film, while the water vapor permeability of PCL-25 was slightly lower than PCL. These results were attributed to the homogeneous dispersion of filler within the polymer matrix, which reduced the permeation of water molecules (Siracusa, 2012). Neat PCL has shown to have excellent water vapor barriers in comparison with other commercial bioplastics. For instance respect to PLA, the WVP of PLA is $2 \cdot 10^{-6}$ Kg.mm/m^2.s.Pa, while PCL has exhibited values $\sim 2 \cdot 10^{-10}$ Kg.mm/m^2.s.Pa (Patwa et al., 2018).

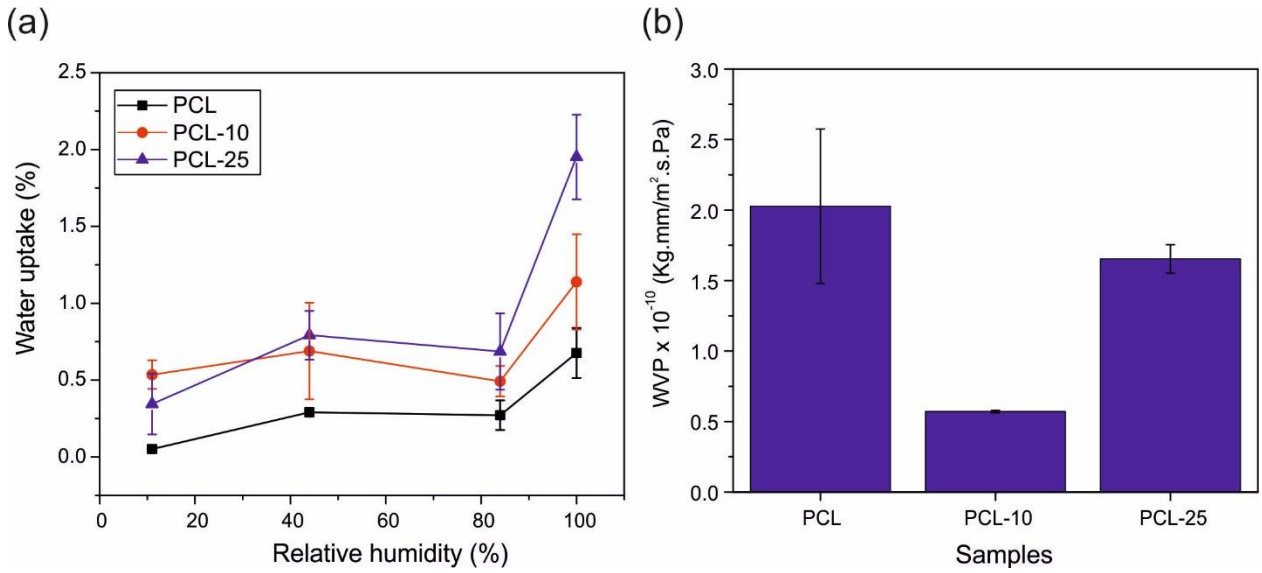

Figure 4.13 (a) The water uptake values of PCL-$MgCO_3$ blends measured at 11%, 44 %, 84%, and 100% of relative humidity. **(b)** The water vapor permeability properties (Kg.mm/m^2.s.Pa) of PCL, PCL-10 and PCL-25.

4.3.2 Paper-PCL biocomposites

The structural, mechanical, and water resistance properties of PCL-biocomposites constituted by 30 wt.% of neat cellulose matter have been evaluated in this section.

4.3.2.1 Structural analysis

The SEM images of the top-view and cross-section of the neat paper sheets and multilayer composites are displayed in **Figure 4.14**. The photograph of the neat paper is displayed in **Figure 4.14(a).** The SEM image of the paper surface showed an irregular and porous structure attributed

to cellulose fibers, **Figure 4.14(b)**. The flaws associated with the fibrous structure of paper were easily noticed in the cross-section image, **Figure 4.14(c)**. The photograph of the paper-PCL biocomposite (BC) is displayed in **Figure 4.14(d)**. The SEM images of the top-view and cross-section of the BC sample are displayed in **Figure 4.14(e-f)**. Contrarily to neat cellulose sheets, BC exhibited a smooth surface, indicating the penetration of the cellulose fibers into the polymer matrix, filling the inter-fibrillar space between the cellulose fibers, **Figure 4.14(e)**. The cross-section image confirmed the embedding of the cellulosic layer, showing a more-packed structure free from physical defects, **Figure 4.14(f)**.

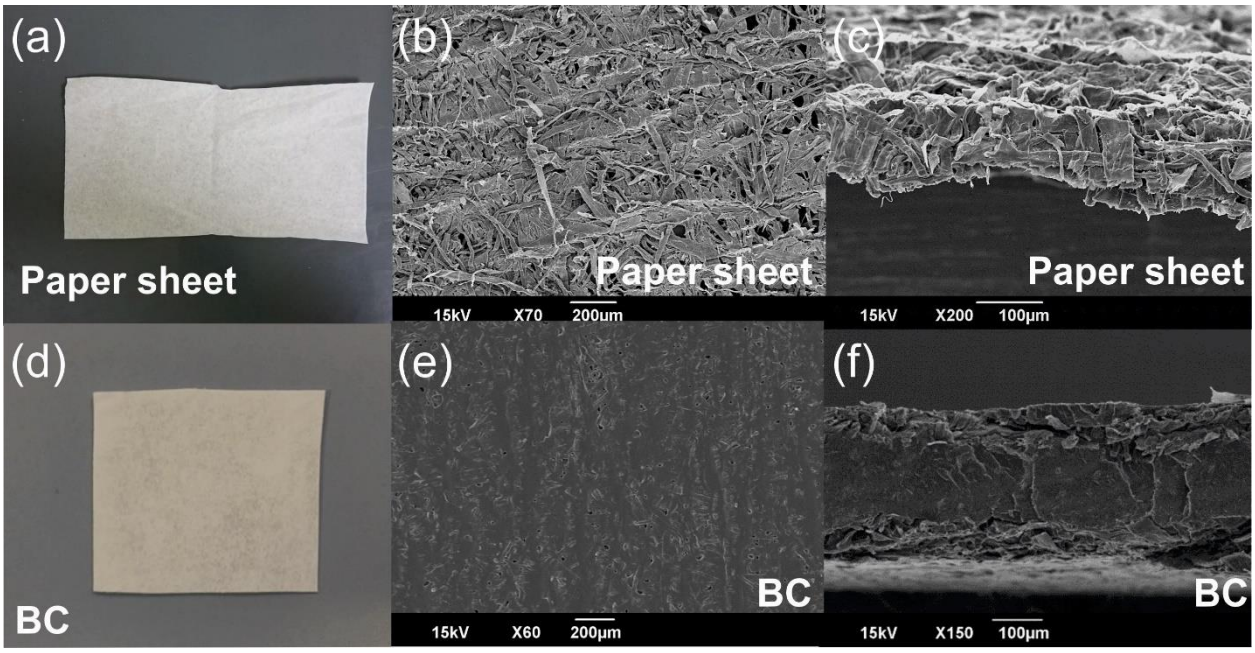

Figure 4.14 (a) Photo of the neat cellulose sheet used to prepare the composites. SEM micrograph of **(b)** the surface (magnification x70) and **(c)** the cross-section of the cellulose sheet (magnification x200). **(d)** Photo of the antioxidant paper-PCL biocomposite (BC), and SEM micrograph of **(e)** the surface (magnification x60) and **(f)** the cross-section of BC (magnification x150).

4.3.2.2 Mechanical behavior

As widely known, the mechanical properties of cellulose sheets depend on different factors such as the nature of the fibers, length, and bonding strength between the fibers (Battisti et al., 2017). The microstructure images of the cellulose fiber network in the longitudinal (warp) and transverse (weft) directions, **Figures 4.15(a-b)**, respectively. Stretching in the longitudinal or

transverse direction results in diverse mechanical behaviors. The arrangement of the cellulose fibers is associated with the industrial fabrication process, which orients the fibers in the machine direction (Das, 2017).

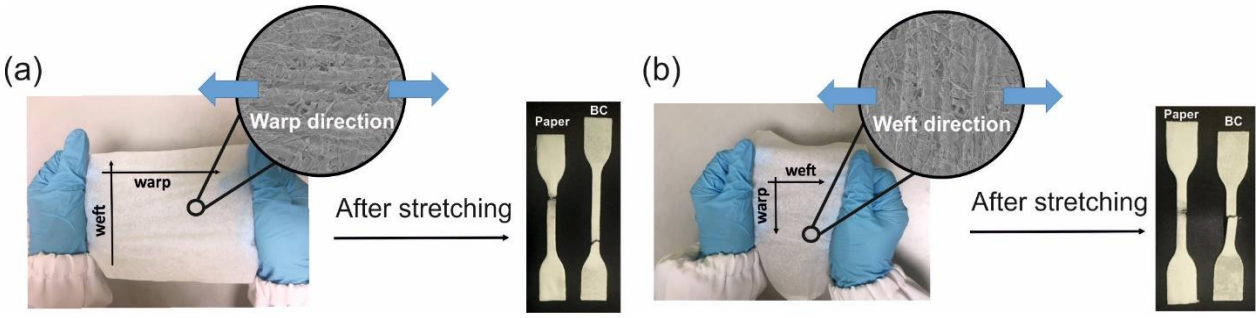

Figure 4.15 Schematic image of the anisotropic-structure of the paper sheets and mechanical results when stretching in **(a)** warp and **(b)** weft directions.

The mechanical properties, represented in terms of the elastic modulus and elongation at break of paper sheets and paper composites are displayed in the warp and weft direction in the table of **Figure 4.16**. The mechanical behaviors varied significantly between stretching in warp and weft directions. In the neat paper, the elastic modulus of sample stretched in weft direction was ten-fold the value obtained in the warp direction, while the elongation was higher in the warp direction, 38.86% versus 7.4 % obtained in the warp direction. PCL composites reinforced the cellulose-structure in both stretching directions. In warp direction, the elastic modulus was in 40 times with respect to the value obtained in the neat paper, while in weft direction paper strength was improved in a factor of ten. The blending did not affect significantly the elongation of paper. Even though the mechanical properties were improved with all PCL samples, BC-25 showed the poorest results. The poor dispersion and agglomerates attributed to the high concentration of filler may result in breaking points, weakening the mechanical performance (Dutta & Maji, 2020; Rešček et al., 2015).

(a) Warp direction

Sample	Elastic Modulus (Mpa)	Elongation (%)
Paper sheets	21.33 ± 1.75	38.86 ± 1.95
BC	821.96 ± 152.08	43.1 ± 1.5
BC-10	984.95 ± 78.19	43.53 ± 1.05
BC-25	811.04 ± 106.01	39.26 ± 1.35

(b) Weft direction

Sample	Elastic Modulus (Mpa)	Elongation (%)
Paper sheets	122.05 ± 13.57	7.4 ± 0.1
BC	2062.09 ± 252.76	7.1 ± 0.85
BC-10	1751.08 ± 238.2	6.26 ± 0.28
BC-25	1059.91 ± 100.29	6.16 ± 0.32

Figure 4.16 The Elastic modulus (MPa) and elongation (%) values are obtained when the force is applied in **(a)** the warp direction and in **(b)** the weft direction.

4.3.2.3 Moisture and liquid water sensitivity

The remarkable water sensitivity of paper leads to poor water resistance and wettability properties, limiting the application. The enhancement of water resistance of paper is essential for the manufacturing of paper-based materials (Rastogi & Samyn, 2015; Samyn, 2013). The weight gain when paper sheets and cellulose composites were exposed to different relative humidity has been represented in terms of water uptake in **Figure 4.17(a)**. Results showed that paper was greatly dependent on the humidity degree, weighing up to 16% more at 100% of relative humidity conditions. Blending cellulose with a hydrophobic PCL-$MgCO_3$ blend halved the water uptake obtained in cellulose sheets at 100% humidity, 8% against 16% in neat paper sheets. The content of $MgCO_3$ did not affect significantly the moisture sensitivity of paper composites.

The absorption of liquid water when samples were immersed in water was represented in **Figure 4.17(b)**. After 48h of water immersion, paper sheets gained around 560% of their initial weight. Blending paper with PCL blends reduced the water absorption values down to ~40% of water absorption, around 14 times less than the absorption of neat cellulose sample. Similar results were reported in B. J. Rhim et. al., when the water absorbance of the paperboard coated with poly-lactic acid polymer was reduced by 12-18 times respect with neat paperboard (B. J. Rhim et al., 2007).

The water vapor permeability of paper composites is represented in **Figure 4.17(c)**. The fibrous structure of paper results in many pores and so, high values of water permeation (close to 7×10^{-9} $Kg/m^2.s.Pa$). The incorporation of PCL and PCL-$MgCO_3$ blends by hot-pressing clogged the pores present in the cellulose fibers web, reducing the permeability of the material, see surface images in **Figure 4.14**. In **Figure 4.17(c)**, the water vapor permeability was reduced in more than seven-folds with the PCL blending. Similar to PCL blends containing $MgCO_3$, the dispersion of nanoparticles of the inorganic salt through the matrix limited the transmission of water molecules, while in BC-25 the high concentration of filler may lead to physical defects promoting the gas permeation (Siracusa, 2012).

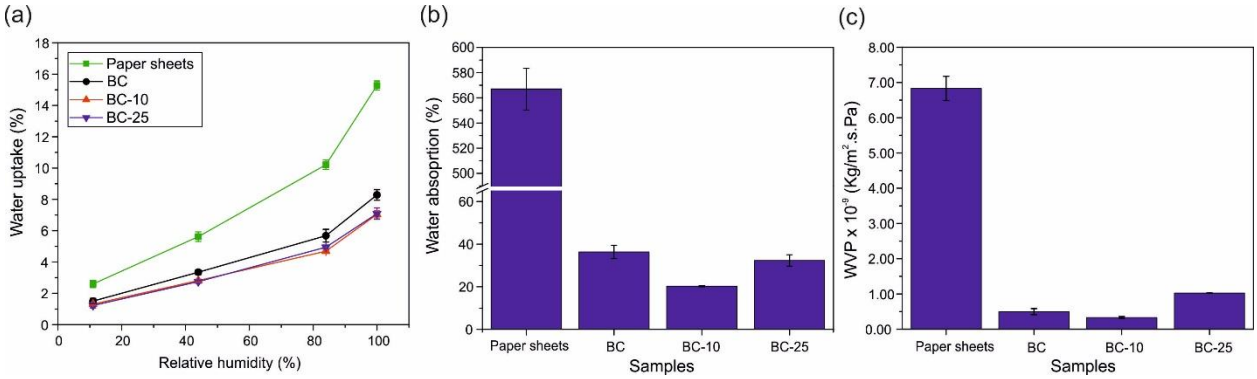

Figure 4.17 (a) Water uptake (vapor), **(b)** Water absorption (liquid), and **(c)** Water vapor permeability of paper sheets and paper-PCL biocomposites, labeled BC, BC-10, BC-25.

4.3.2.4 Oxygen gas permeability

Table 4.3 shows the oxygen permeability of neat paper-PCL blends (BC) and with 10 wt.% of $MgCO_3$ content (BC-10). The incorporation of $MgCO_3$ resulted in a decrease of the oxygen permeation due to the percolation network of nanoparticles (Siracusa, 2012).

Table 4.3. The oxygen permeability values of BC and BC-10 samples.

Sample	Oxygen permeability (mL. µm/m2.day)
BC	34.34
BC-10	29.01

4.3.3 Functionalized-biocomposite with pomegranate peel extract and curcumin

In this section evaluation of the migration properties, antioxidant, and pH-colorimetric sensing in different media of the biocomposites functionalized with pomegranate peel-extract and curcumin was performed.

4.3.3.1 Migration study

The characterization of the kinetic release from the samples into two different food simulants by UV-vis spectroscopy is performed in this section. Samples were cut into squares (1 x 1 cm) and immersed in 3 mL of food simulant solutions recommended by the US Food and Drug

Administration: aqueous food simulant (water/ethanol 95%, v/v) and fatty food simulant (water/ethanol 50%, v/v). The concentration of antioxidant released was periodically measured using UV-spectroscopy for 24 hours, up to reach an equilibrium state (plate line) for most of the samples. Controlled-release is desirable to ensure the bioactivity effectiveness, limiting toxicity and providing a long shelf-life of the device (J. H. Lee & Yeo, 2015). The controlled-release systems are characterized by a high initial release towards a constant drug release rate. Blending paper with PCL may slow down the migration of bioactive molecules into the food simulants, providing a controlled-release via diffusion (J. H. Lee & Yeo, 2015). The migration of molecules were represented in terms of percentage release with respect to the maximum released from the blank sample (8 sheets of functionalized-paper). The 100% of curcumin released was 111.7 ± 3.71 $\mu g/cm^2$, and 4286 ± 50.71 $\mu g/cm^2$ of pomegranate peel extract. The percentage release of biomolecules from pomegranate peel and curcumin into the solution of fatty food simulant (water/ethanol 50%, v/v) are displayed in **Figure 4.18 (a-b)**, respectively. In **Figure 4.18(a)**, the release of pomegranate peel extract films showed that paper sheets reached the maximum drug released in 1 hour (100%). Paper-PCL composites achieved a maximum of ~60% at the end of the experiment attributed to the low permeation of the solvent through the polymeric matrix. The migration rate was slightly enhanced with the presence of inorganic filler. The incorporation of fillers such as cellulose nanocrystals has demonstrated to promote the release of the embedded bioactive molecules, such as citric acid or silver nanoparticles (Fortunati et al., 2013; Yang et al., 2020).

In **Figure 4.18(b)**, the kinetic curves of curcumin samples were comparable to the curves observed in pomegranate-peel samples. The high solubility of curcumin in ethanol promoted the rapid release in paper sheets, reaching 100% after 1 hour. However, the release was strongly reduced in PCL and PCL-Mg samples, independently to the amount of Mg nanoparticles, and with a maximum drug-released of ~40% after 4 hours of the immersion, which was maintained until the end of the experiment (24 hours). Results showed that the kinetic was also enhanced with the incorporation of filler, especially in BCC-25 films. These samples showed a great migration activity in comparison to other composites found in bibliography, such as for low-density polyethylene extruded with 5 wt.% curcumin, which exhibited 10 times less migration activity in ethanol than the current samples (Zia et al., 2019).

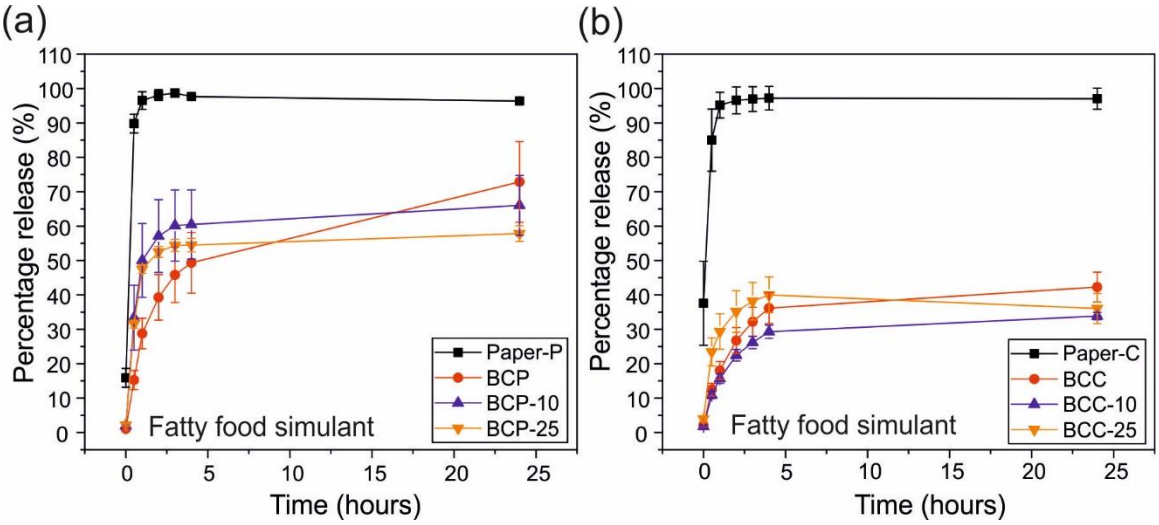

Figure 4.18 The release-monitoring of bioactive molecules in fatty food simulant from **(a)** pomegranate peel-extract biocomposites and **(b)** curcumin biocomposites.

The percentage release of biomolecules from pomegranate peel and curcumin into the solution of aqueous food simulant (water/ethanol 95%, v/v) are displayed in **Figure 4.19(a-b)**, respectively. In **Figure 4.19(a)**, the drug released was not complete in sheets of pomegranate peel-paper did not release, reaching up to 70%. Among biocomposites, the sample filled with 25 wt.% of Mg nanoparticles (BCP-25), exhibited the maximum and faster released (70%), followed by the BCP-10 and BCP (45%), the latter with slower migration rate. These results indicated that the nanoparticles of Mg enhanced the release in an aqueous solution (95 % v/v).

The release of curcumin in aqueous food simulant is displayed in **Figure 4.19(b)**. Paper sheets released around 4% of curcumin after 1 hour, which was halved in the following hours. The chemical structure of curcumin confers a strong lipophilic character, which leads to extremely low water solubility, and undergoes rapid hydrolytic degradation under neutral or alkaline conditions (Tønnesen et al., 2002; Zebib et al., 2010). The low stability has strongly limited the applicability and processability of this promising molecule. BCC sample did not show any migration response in the entire experiment as a result of the low solubility of the curcumin. However, curcumin migrated in samples containing $MgCO_3$, greater with the magnesium salt content. BCC-25 showed the maximum release of ~6%, followed by the BCC-10 with ~3 % of percentage release after 24

hours. These values overcame the concentration of curcumin released from paper sheets after 24 hours from the immersion.

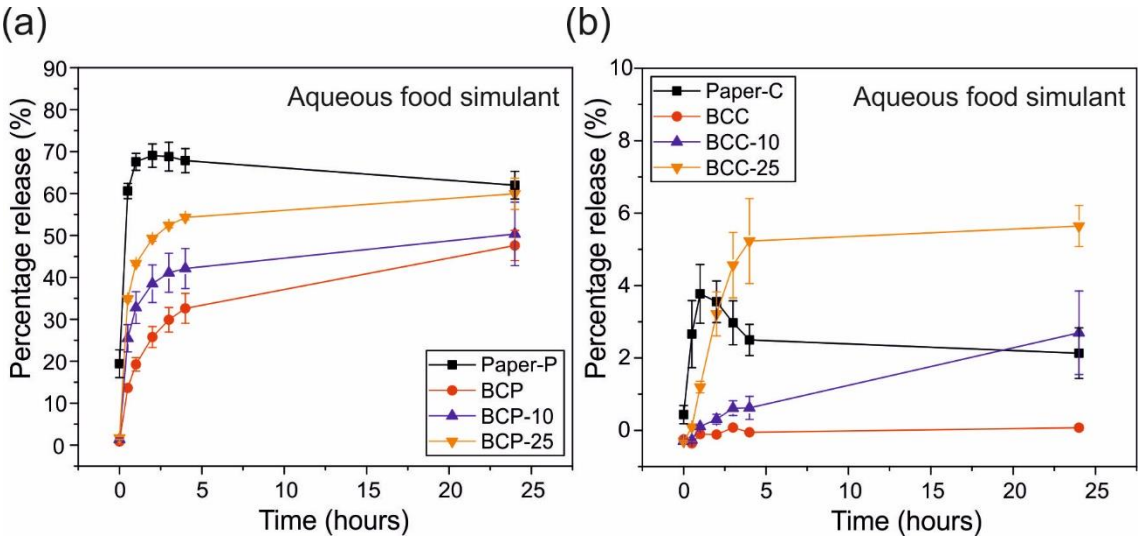

Figure 4.19 The release-monitoring of bioactive molecules in aqueous food simulant from **(a)** pomegranate peel-extract biocomposites and **(b)** curcumin biocomposites.

The increase in the water solubility of curcumin in the biocomposites with Mg was led by the stabilization of curcumin through the interaction by complexation (Zebib et al., 2010). Zebib *et al*., has demonstrated that the metallo-curcumin complexes were highly stable in purified water during 30 hours, while curcumin alone degraded in more than 90% after one hour at neutral pH (Zebib et al., 2010). The complex Cur-Mg with a stoichiometry 1:1 is represented in **Figure 4.20(a)** (Zebib et al., 2010). The complexation causes considerable changes in the electronic structure of curcumin that can be easily observed in the UV-vis absorption bands. In **Figure 4.20(b)** the UV-vis spectra of the curcumin-extract solutions of paper sheets and BCC-25 after 24 hours from the immersion are represented. The paper sheets displayed the typical spectra of the curcumin in water, with an absorption peak at 427 nm and a shoulder at 350 nm (Bagchi et al., 2015). The maximum absorption peak (427 nm) is related to the π-π orbital conjugation of the phenolic groups presented in the curcumin structure, the delocalization of the π-electrons provides the strong yellow coloration (Bagchi et al., 2015). The complexation of curcumin reduced the two peaks into a wide single-peak located at slightly higher wavelengths (432 nm), acquiring a reddish coloration.

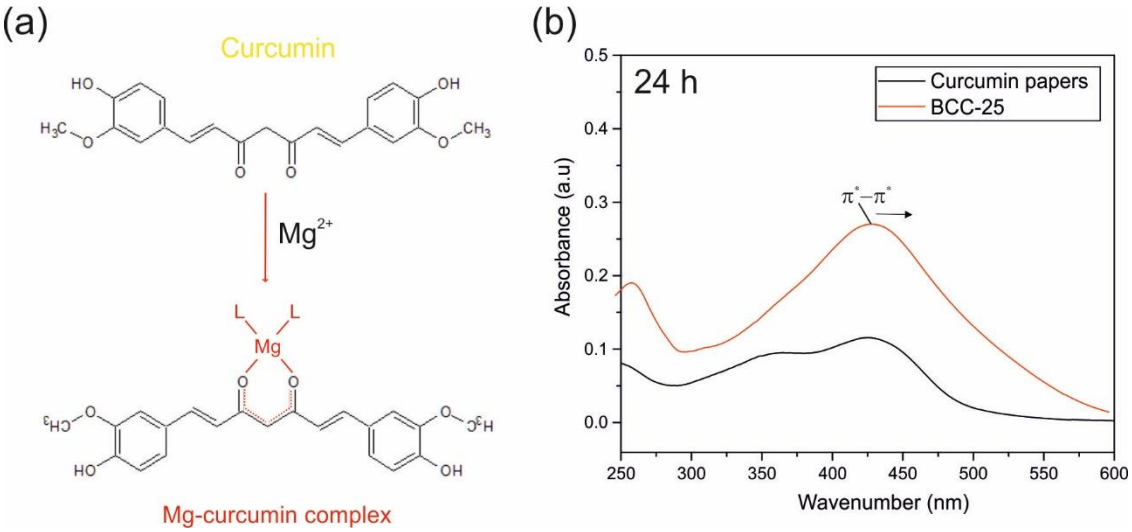

Figure 4.20 (a) The interaction of curcumin molecule with the divalent metal ions of magnesium that promote the reddish-shift. **(b)** The UV-vis spectra of the 24h-extract solution of paper sheets and BCC-25 (PCL with 25 wt.% of $MgCO_3$). The characteristic bands of curcumin changed with the interaction with the Mg divalent cations, leading to a slight shift towards higher wavenumbers and the shoulder was disappeared.

The spectroscopic changes observed in the UV-vis absorption bands due to the formation of the Cur-Mg complex were also visible in the extract solutions, during the release experiment, displayed in **Figure 4.21(a-b)**. In fatty food simulant solutions, **Figure 4.21(a)**, all samples showed a strong yellow coloration due to the release of curcumin after 15 min from the immersion. After 24 hours, the extract solutions of paper and BCC were bright yellow due to the migration of curcumin, while the extraction solution of samples with Mg nanoparticles, BCC-10 and BCC-25, became slightly reddish, as well as the films. This coloration corresponded to the formation of complex Cur-Mg. **Figure 4.21(b)** displays the release of curcumin-samples in aqueous food simulant. After 15 min of immersion, BCC-25 became red, but all samples exhibited colorless solutions. After 24 hours, BCC-10 turned reddish while the extract solution of the BCC-25 sample acquired was lightly red. The rest maintained the uncolored aspect for 24 hours.

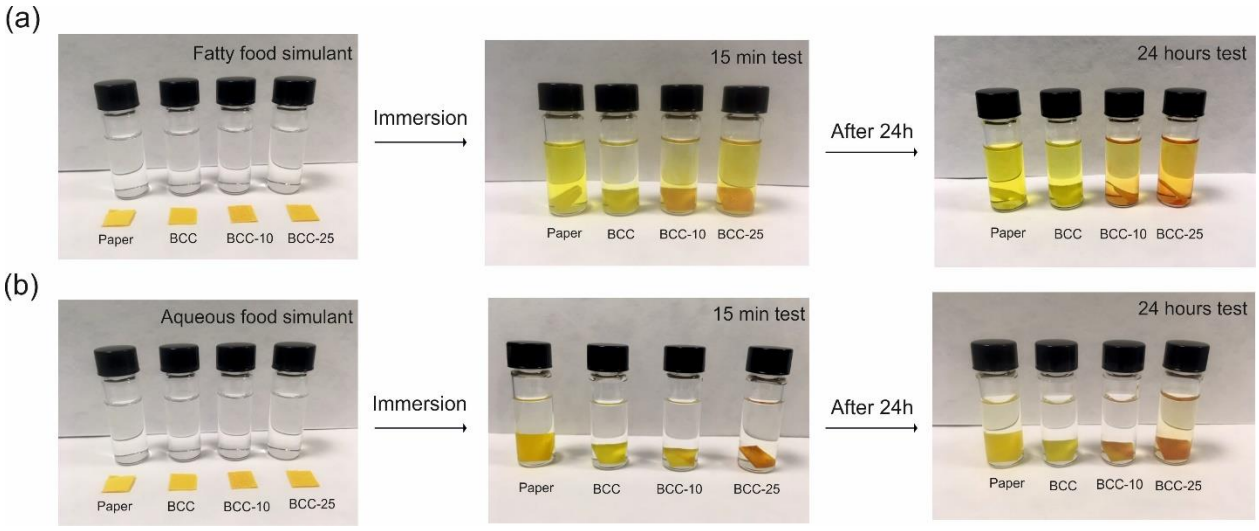

Figure 4.21 Photographs of the migration process of curcumin samples in **(a)** fatty food simulant media and **(b)** aqueous food simulant media.

4.3.3.2 Antioxidant activity

The antioxidant capacity of curcumin and pomegranate immersion solutions are represented in terms of the half-inhibitory concentration, IC50 (µg/mL). IC50 indicates the concentration of the solution that inhibits 50% of the radical (Pasrija et al., 2015). This parameter is important to understand the antioxidant character of the compounds that functionalized the paper sheets. Using the calibration curve of **Figure 4.6,** curcumin showed an IC50 value of 7.21 µg/mL, while the pomegranate peel-extract solution showed an IC50 of 25.97 µg/mL. This means that curcumin had a stronger antioxidant activity, since less concentration of curcumin, with respect to pomegranate peel, was needed to reduce the radical activity to 50%. The antioxidant activity was measured against $ABTS^{+\cdot}$ radical cation. The neutralization of the cation radical results in a colorimetric change where $ABTS^{+\cdot}$ radical solution (strong blue) becomes yellow/transparent, as **Figure 4.22(a)** displays. The antioxidant activity was measured by UV-vis spectrophotometry, the reaction between the antioxidants with the cation radical ($ABTS^{\cdot+}$) leads to a reduction of the characteristic absorption band of the cation radical at 734 nm, remarked in **Figure 4.22(b)**. Despite the greater antioxidant capacity of curcumin, the higher concentration of pomegranate in paper sheets might correspond to stronger bioactivity of pomegranate peel biocomposite, 535.7 ± 6.33 µg/cm^2 of pomegranate peel extract-paper against 13.95 ± 3.71 µg/cm^2 in curcumin-paper.

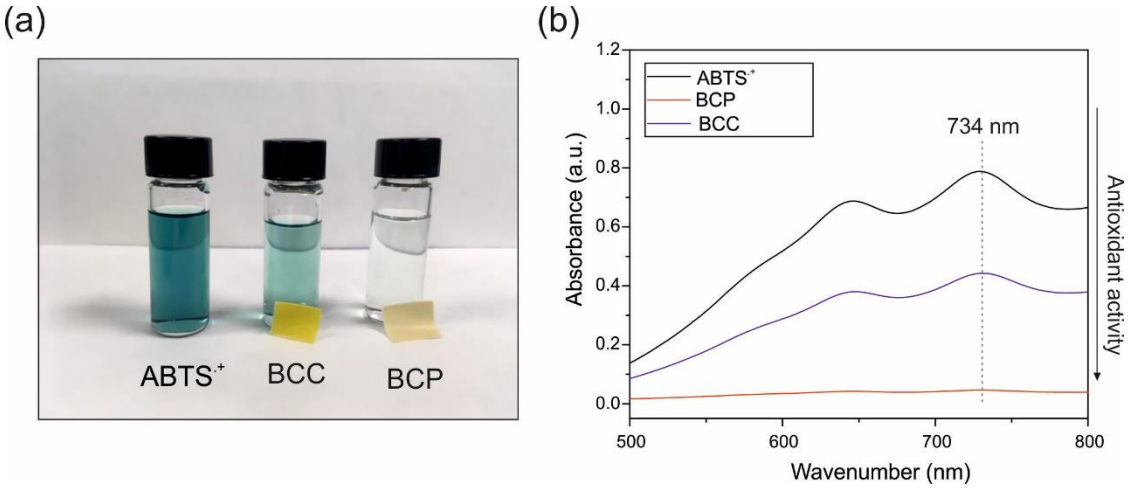

Figure 4.22 (a) Photograph of the solutions of $ABTS^{\cdot+}$, $ABTS^{\cdot+}$after adding the 24h-extract solution of BCC film and BCP. The interaction between the cation radical and the antioxidant promoted the color change from strong blue towards a transparent solution with the increase of antioxidant activity. **(b)** The UV-vis spectra of the $ABTS^{\cdot+}$ solution when the antioxidant extract solution was added. The reduction of the intensity of the characteristic peak of the radical $ABTS^{\cdot+}$ (734 nm) was related to the antioxidant activity.

The antioxidant results were represented in terms of TEAC (mM Trolox/g film) in **Figure 4.23.** In **Figure 4.23(a)**, the pomegranate films exhibited greater antioxidant capacity in both solutions, with better results in fatty food simulants. Curcumin biocomposites showed antioxidant behavior in fatty food simulant, while in aqueous food simulant the antioxidant was almost absent due to the low solubility of curcumin in aqueous solution, in **Figure 4.23(b)**. The great migration activity of pomegranate in different food simulants indicated the promising application as food packaging material. The antioxidant activity of curcumin samples was limited to fatty foods; however, curcumin presents other characteristics that promote its application as a food packaging

device.

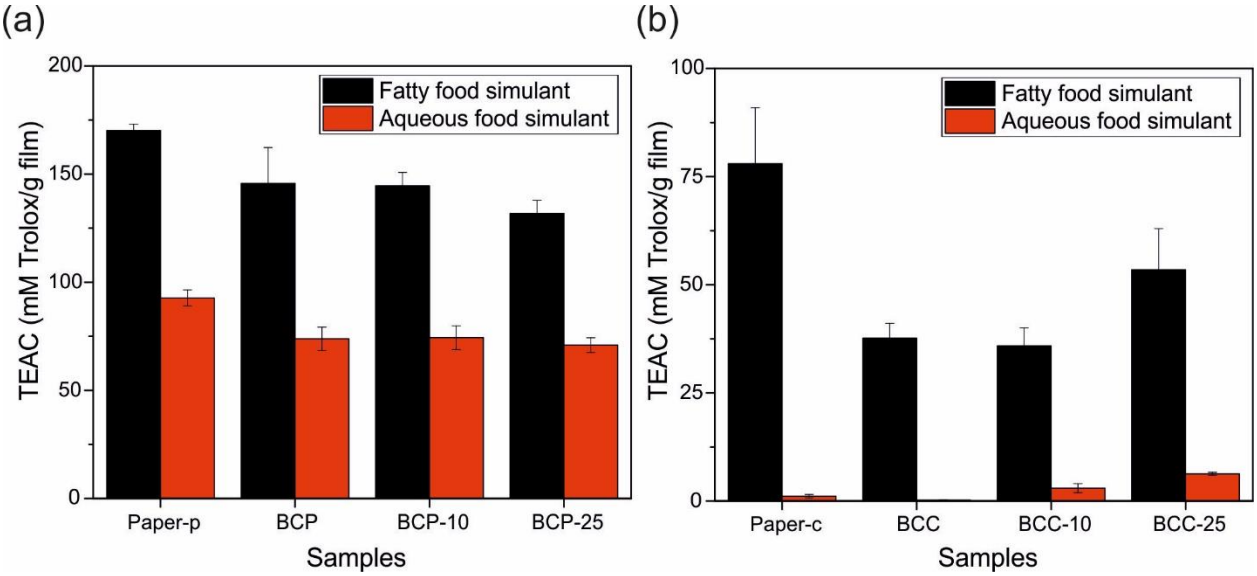

Figure 4.23 The antioxidant activity represented in terms of TEAC (mM Trolox/ g film) for fatty food simulant solution (black columns) and aqueous food simulant solution (red columns) for **(a)** pomegranate peel-extract biocomposites and **(b)** curcumin biocomposites.

4.3.3.3 Colorimetric change when exposed to different pH buffer solutions

The great sensitivity of curcumin to the pH has enhanced its use as a natural colorimetric-pH indicator in the food industry (H. zhi Chen et al., 2020; J. Liu et al., 2019). **Figure 4.24(a)** shows the colorimetric changes of curcumin paper when immersed at different pH in the range 6.5 to 9.5. The sensitivity to pH is related to the chemical structure of curcumin, which presents three labile protons that can be lost at different pH acquiring negative charge: H_2Cur^-, $HCur^{2-}$ and Cur^{-3}, showed in **Figure 4.24(b)** (W.-H. Lee et al., 2013; Priyadarsini, 2014).

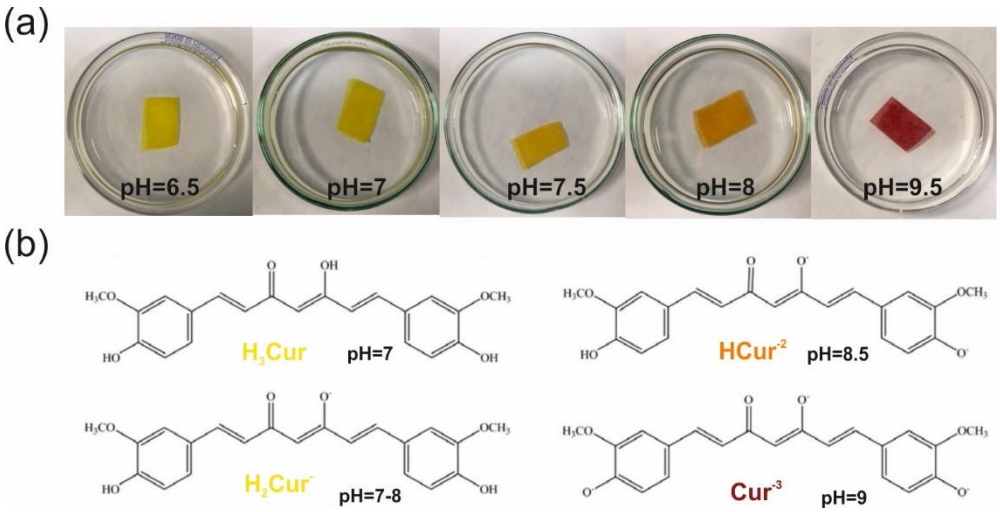

Figure 4.24 (a) Color response of curcumin-site composite when immersed in different pH buffer solutions. **(b)** The neutral and acidic forms of curcumin: H_3Cur (yellow), H_2Cur^- (yellow), $HCur^{2-}$ (orange), and Cur^{3-} (red).

The total color change of curcumin samples when they are exposed to different pH buffer solutions with respect to the dry sample is represented in **Figure 4.25**. Results showed that the color change was easily-perceived in all samples, from bright yellow at neutral pH towards the violet color at basic environments.

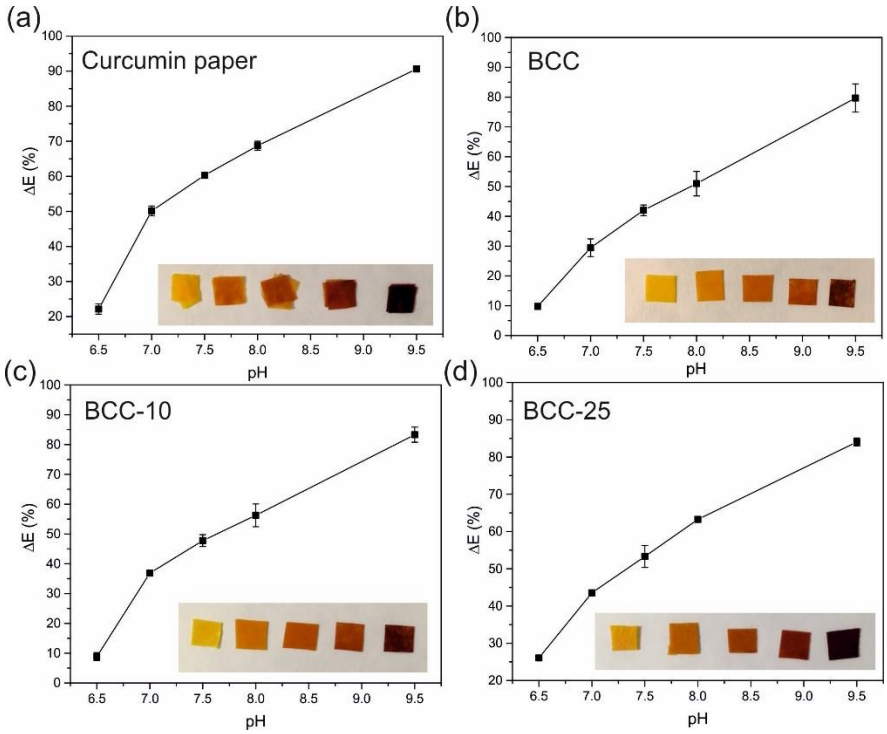

Figure 4.25 The total colorimetric changes and the photographs when immersed at different pH buffer **(a)** paper sheets, **(b)** BCC, **(c)** BCC-10, and **(d)** BCC-25.

The color-reversibility of samples have been tested with the view of being reused and giving a more eco-sustainable approach. **Figure 4.26(a)** shows the real photograph of the curcumin sample after the basic-bath (9.5 pH). In **Figures 4.26(b-c)**, curcumin biocomposites recovered the yellowish color after one minute of immersion in acidic buffer solution (pH 6.5), evidencing that samples showed a great color-reversibility.

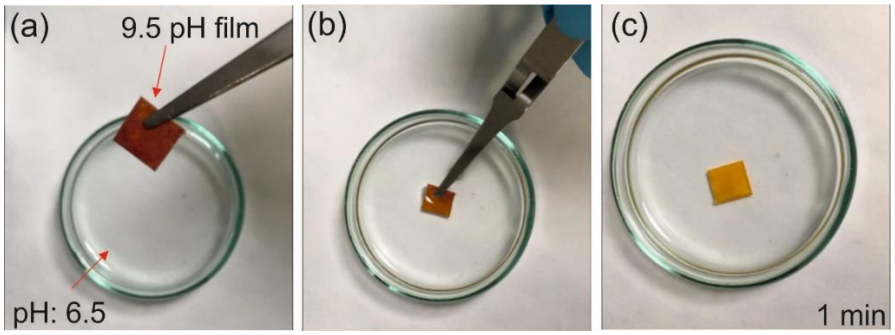

Figure 4.26 (a) The BCC sample after immersion in pH 9.5 buffer solution. **(b)** Immersion of red sample in neutral aqueous buffer solution at pH 6.5. **(c)** The sample turned yellow after the immersion of 1 min in the solution 6.5 pH.

4.3.3.4 Colorimetric change when exposed to basic vapors

After the great colorimetric-change responses of curcumin samples against the different pH buffer solutions. The sensitivity of the curcumin biocomposites to basic vapors of ammonia was evaluated. For this experiment, the sample was cut into circles (ø=14 mm) and placed on the top of a vial (13 mL of capacity) covered with a short screw-threat cap (ø=15 mm) with the sample exposed for both sides. Then, 50 µL of a basic solution NH_4OH (33% ammonia) was lodged at the bottom of the vial, see **Figure 4.27(a)**. The volatile basic ammonia molecules led to the color variation in 30 seconds from strong yellow to dark red, see **Figure 4.27(a-b)**, respectively. The sensitivity to ammonia gases after 30 seconds and 600 seconds is represented in **Figure 4.27(c)**. Paper sheets revealed a more obvious color change than the biocomposites with PCL, 70% in the paper against 45% in PCL samples. The maximum sensitivity of the indicator was reached after 30 seconds and remained stable with time, after 600 seconds. This remarked the rapid response and stability of samples when exposed to small quantities of basic vapors (50 µL). Besides, the fast color reaction suggested a promising application as a pH indicator for the development of intelligent sensing devices useful for the food packaging industry.

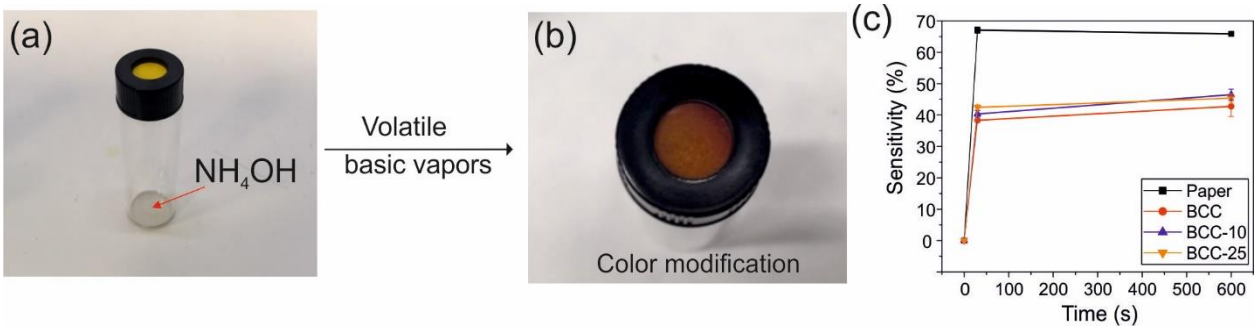

Figure 4.27 (a) Scheme of the vapor exposure conditions and **(b)** the colorimetric changes of samples. **(c)** The sensitivity of samples to volatile ammonia vapors and the color stability with time.

Contrary to the color-reversibility of alkaline samples when immersed in a neutral pH buffer solution, reddish samples did not shift into yellow when they were exposed to acid vapors (HCl), even at high volumes. However, as displayed in **Figure 4.28**, the yellowish coloration was recovered when samples were placed at room conditions overnight, which suggested the possibility of recycling and re-use these materials without using extra-solvents, providing cost-savings and promoting sustainability.

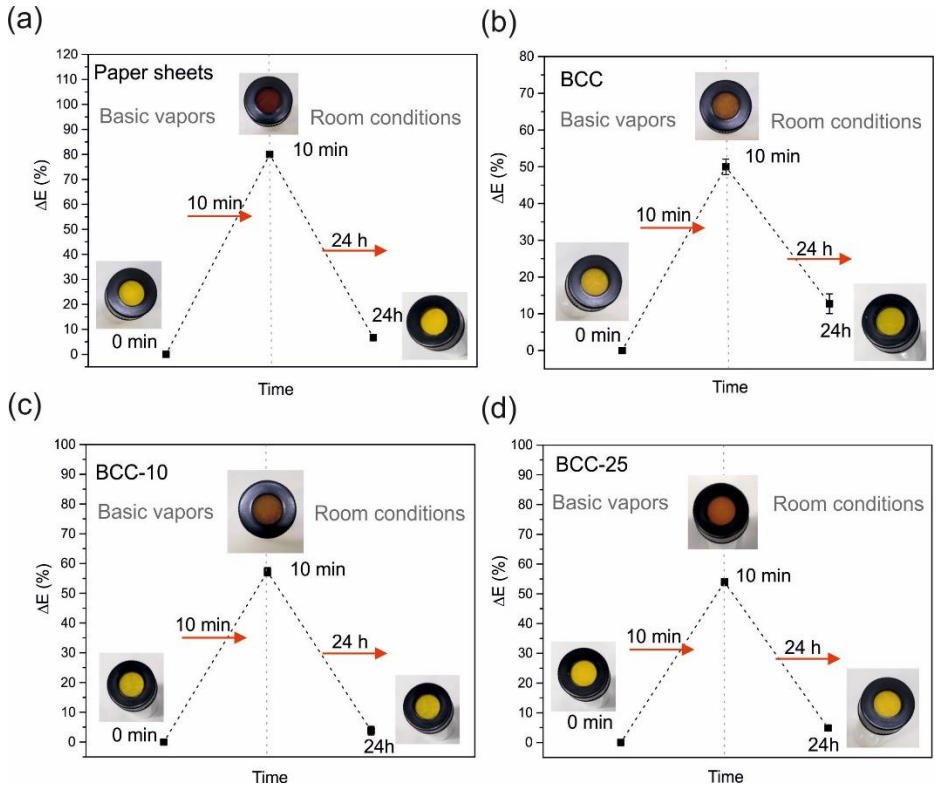

Figure 4.28 The total color change of curcumin after exposure for 10 min to ammonia basic vapors (shifting to red), and the yellow-shift after exposure at room conditions overnight of **(a)** paper sheets, **(b)** BCC, **(c)** BCC-10, and **(d)** BCC-25.

4.3.3.5 Evaluation of the potential application for food-freshness monitoring

Most of the animal-based foods present the degradation of proteins during the storage, which generates high levels of basic volatile substances called TVBN that also provides the characteristic putrefactive odor. The release of the basic molecules has been used to evaluate the freshness of the foodstuff (Alparslan & Baygar, 2017; Ezati et al., 2019). The noticeably

colorimetric-changes of the curcumin biocomposites, when exposed to a small amount of basic substances, revealed the promising application as a spoilage indicator in seafood. Therefore, samples were attached to the tap of the sterilized Petri dishes where the shrimp was placed. The petri dish was hermetically closed and the colorimetric changes of samples were measured at different times during 3 days. After this time, shrimps acquired a yellowish coloration due to the degradation reactions and emitted a nasty smell, which indicates the release of TVBN and the loss of freshness of food. In **Figure 4.29(a)**, the photo of the Petri dishes with the shrimp and curcumin biocomposites are represented. In **Figure 4.29(a)**, the curcumin paper sheets changed slightly the color after one day, while the samples experimented with a strong redness-shift after the 2 days. The color variation in BCC samples was less evidence up to the second day, see **Figure 4.29(b)**. However, the colorimetric-change of BCC-25 samples was strongly noticed after the first day and turned into a strong red after 2 days, as **Figure 4.29(c)** shows.

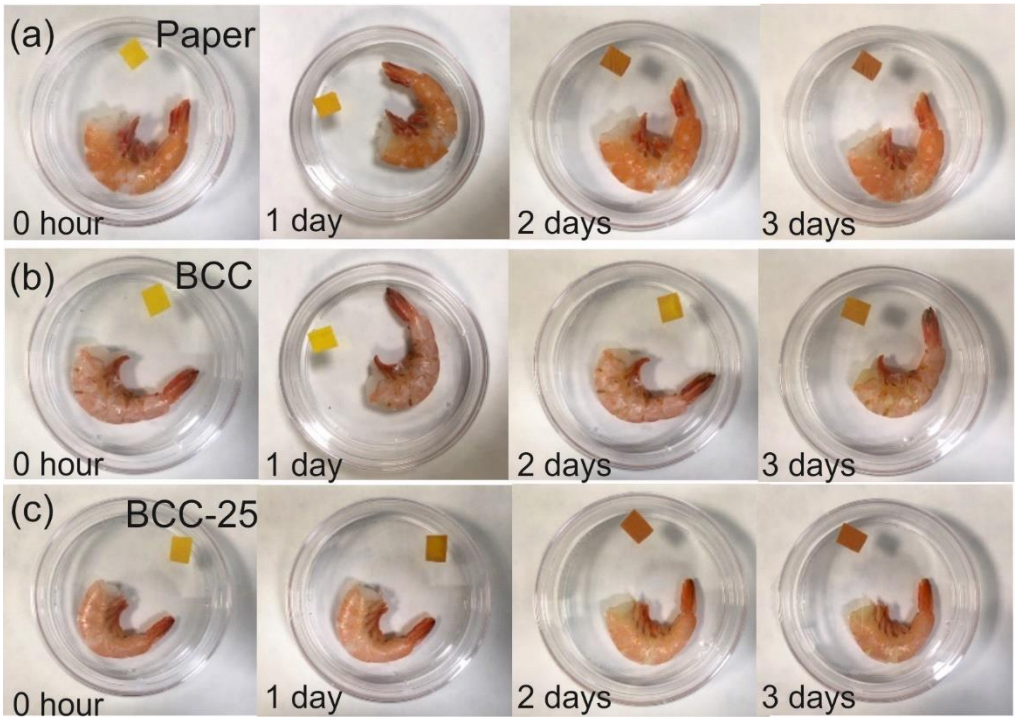

Figure 4.29 The packaged shrimps with **(a)** paper sheets, **(b)** BCC, and **(c)** BCC-25, after 1, 2, and 3 days. The color change of all samples was observed with respect to the control sample.

Certainly, to evaluate the freshness-indicator properties, the spoilage degree of shrimps may be monitored during the storage time, such as the total volatile basic nitrogen test (TVBN). Kuswandi B. *et al.* showed that shrimps storage at ambient conditions got spoil (levels of TVBN>20 mg N/100 g) after 10 hours (Kuswandi et al., 2012). The sensitivity of curcumin samples during the food monitoring experiment is represented in **Figure 4.30(a-c)**. Results showed that the color increased with time. In **Figure 4.30(c),** BCC-25 showed the faster response, achieving a maximum of ~40% sensitivity after 24 hours, according to the values obtained in the ammonia experiment, see **Figure 4.27(c)**. While BCC reached the ~25% at the end of the experiment with slow color changes, **Figure 4.30(b)**. Interestingly, paper and BCC-25 showed significant color changes after 4 hours, around 20% of sensitivity, highlighting the high-sensitivity of these biocomposites to detect the modification and loss of the food-freshness.

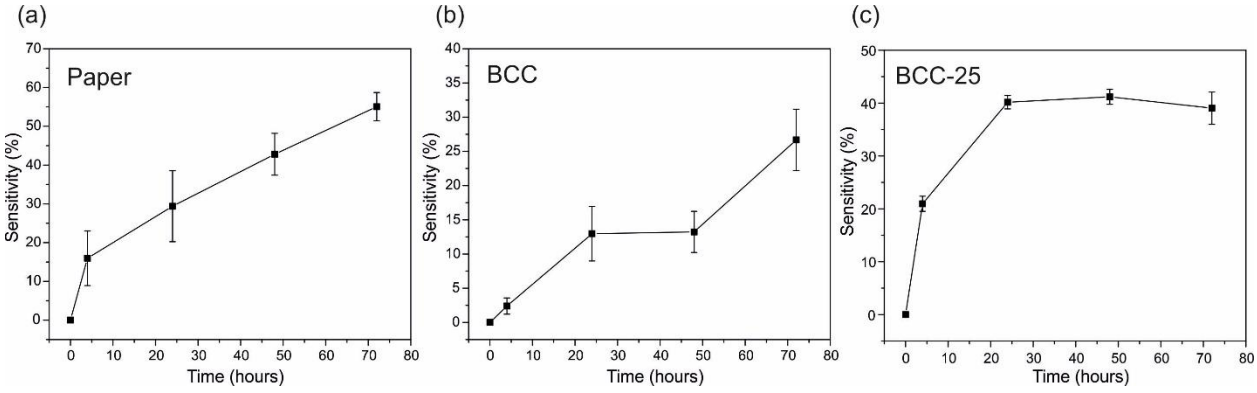

Figure 4.30 The sensitivity of on-package colorimetric films for shrimp spoilage. **(a)** Paper sheets, **(b)** BCC, and **(c)** BCC-25, measured at 4, 24, 48, and 72 hours.

4.4 Conclusion

In this work, the moisture sensitivity and barrier properties of paper were significantly improved by embedding the cellulose matrix in a blend of PCL. Free-solvent processing-methods, like extrusion and hot-press, were used to fabricate a final biocomposite with 30% cellulose content. Then, biocomposites were easily functionalized with a natural derivate, curcumin, and a food by-product, extract of pomegranate peel. Samples acquired different properties linked to the chemical characteristic of the natural additive. Strong antioxidant and migration capability were developed by adding pomegranate peel extract into the paper biocomposites. Whereas curcumin

provided colorimetric pH sensitivity against different unspoiled environments (buffer solutions and basic vapors), but also against food-spoilage, as proved during the exposure to stored commercial shrimps.

Chapter 5: Edible materials using food waste as packaging matrix

5.1 Edible and antioxidant orange peel films/coatings

The potential properties of fruit pectins have promoted their application in the food industry as a thickening, gelling, and emulsifying agents to prepare bakery products, candies, and jellies (Güzel & Akpınar, 2019; Lara-Espinoza et al., 2018; Müller-Maatsch et al., 2016). Pectin is an ubiquitous biomacromolecule present in non-woody parts of terrestrial plants. Among most fruits and vegetables, orange peel stands out for its high content of pectin (Müller-Maatsch et al., 2016). However, a great part of fruit and vegetable by-products, rich in pectin and other valuable biomolecules, ends up accumulated in landfills or incinerated with adverse ecological consequences (Esparza et al., 2020). A promising solution is providing a second life to food discards to develop edible-materials for packaging. This leads to the "truly" circular economy, with zero-waste, diminishing the environmental impact and obtaining new valuable products (Otoni et al., 2017; Valdés et al., 2015). The aim of edible materials is not to substitute ordinary packaging, but to elongate the shelf-life of highly perishable foods, acting as an extra-packaging (De Azeredo et al., 2014). They are eatable, fully-biodegradable, and can be applied in form of films or coatings. Edible films are related to stand-alone structure performed separately from the food that can be applied on the food surface or sealed into edible pouches, while edible coatings are formed directly onto the surface of the food products forming a part of the product (De Azeredo et al., 2014; Embuscado & Huber, 2009).

Pectin is a natural heteropolysaccharide polymer, formed mainly by homogalacturonan (HG), rhamnogalacturonan-I (RGI), and rhamnogalacturonan-II (RGII), with α-1,4-D-galacturonic acid residue (Gawkowska et al., 2018). It is the main compound located in the external cell-wall of fruit and vegetables, providing strength and firmness to the structure (Gawkowska et al., 2018; Pettolino et al., 2012). Pectin can form gels under acidic conditions through hydrogen bonding and hydrophobic interactions (Gamonpilas et al., 2015). The physicochemical characteristics of the gel are closely related to the methylation degree (DE) of the pectin in solution, which indicates the percentage of carboxylic group methylated in the pectin chains (Celus et al., 2018). Pectins with a methylation degree (DE) <50 % are denominated low-methoxyl pectin (LMP), while high-methoxyl pectin (HMP) present DE>50% (Gamonpilas et al., 2015). Besides, the free carboxylic groups can form gels creating cross-linking interactions with divalent cations like (Mg^{+2}, Ca^{+2}, Cu^{+2}, Pb^{+2}, etc…) building a tridimensional structure called egg-box (Gawkowska et al., 2018; Moreira et al., 2014). **Figure 5.1** shows a schema of the egg-box, wherein the pectin structure and

the interaction between the carboxylic group (COOH) and the calcium ions are exposed. In the current study, two different sources of divalent calcium ions have been used to cross-link the orange peel matrix. Calcium chloride ($CaCl_2$), has been widely used as a food preservative and filming agent with pectin extracted from vegetables and fruits, whereas calcium carbonate ($CaCO_3$) is added into foods to enhance the nutritional value (Martín-Diana et al., 2007). Interestingly, the different physicochemical properties of the inorganic salts will lead to different gelation environments. Calcium chloride is highly water-soluble and pH-inert, whereas $CaCO_3$ presents low solubility in water and basic nature. The variation of pH caused by the $CaCO_3$ may modify chemically the structure of the pectin in solution, and thus, the final functional properties (Martín-Diana et al., 2007; Sriamornsak et al., 2007).

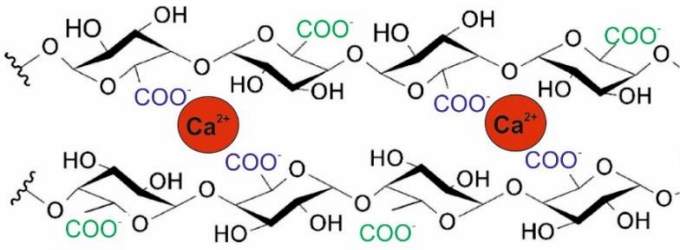

Figure 5.1 The conjunction zones of the pectin gelation with the divalent cations of calcium. Egg-box model.

Besides, the functional characteristics of the orange peel (OP) films can be enhanced with the incorporation of additives, such as essential oils or plasticizers. Orange essential oils (OEOs) can provide powerful antimicrobial and antioxidant properties to orange peel materials, but also improve the water barrier properties due to their hydrophobic character (Du et al., 2009). Glycerol is a well-known plasticizer incorporated to improve the mechanical functionalities, and the molecules dispersion in the OP matrix (Embuscado & Huber, 2009). In this project, materials with the promising application as edible films/coatings for food preservation have been fabricated based only on 100% of an agro-food waste (orange peel) and water as the only solvent. The great sustainable approach based on the circular economy and the low cost of the reagents and processing highlighted the promising future of these kinds of materials.

5.2. Materials and Methods

5.2.1 Materials

Oranges were provided by local vegetable processors as unusable waste from their production line, citric acid, calcium carbonate, glycerol, ethanol Tenax®, 2,2-diphenyl-1-picrylhydrazyl (DPPH) were purchased from Sigma-Aldrich, calcium chloride salt purchased from Merk. The orange essential oil "Arancio rosso" was purchased from Maitreya Nature, Italy. Deionized water was obtained from a Mili-Q system (Q-POD Element, Merck Millipore). Cellulose nanocrystals (CNC) was purchased from CelluForce. The orange peel powder was obtained by peeling-off the oranges and placed to dry in the oven at 40 °C for 2 days. Then, the peel was cut and mashed to obtain a powder, ground with a maximum dimension of 300 µm diameter.

5.2.2 Preparation of orange peel and standing-films samples

The scheme of the orange peel processing to obtain the standing-film samples is displayed in **Figure 5.2**. The orange peel solution (5 wt.%) was prepared in 20 mL of 1 mM of citric acid to stir for 24 hours (pH=2.15). Three different sets of samples will be prepared, neat orange peel (OP), orange peel with $CaCl_2$ (OP-Cl), and orange peel with $CaCO_3$ (OP-CO3). Then, for each sample, the additives orange essential oil (OEO), or OEO and glycerol (Gly), were added to the solution. The acronyms (–OEO) and (-OEO-Gly) will be used for labeling the samples.

After the acidic hydrolysis, calcium salts were added to prepare solutions 10 mM $CaCl_2$ (pH:2.15) and 12.5 mM $CaCO_3$, (pH: 4.5), for OP-Cl and OP-CO3 films, respectively. The solution was stirred and cross-linking for 90 min. For the set of samples with orange essential oils, OP-OEO, OP-Cl-OEO and OP-CO3-OEO, and glycerol, OP-OEO-Gly, OP-Cl-OEO-Gly and OP-CO3-OEO-Gly, orange essential oil at 1.5 % (v/v) and 25% glycerol (w/w of pectin), were added. The film mixture was homogenized with a probe sonicator tip (750 W, 20 kHz, 40% amplitude) performed using a Sonics & Materials, Inc. (Model Num. VCX750) for one minute in pulse mode, with ON and OFF cycles of 15 s to avoid the overheating. Then, solutions were cast onto sterile plastic petri-dish (ø=90 mm) and conditioned at 30°C for 2 days to dry.

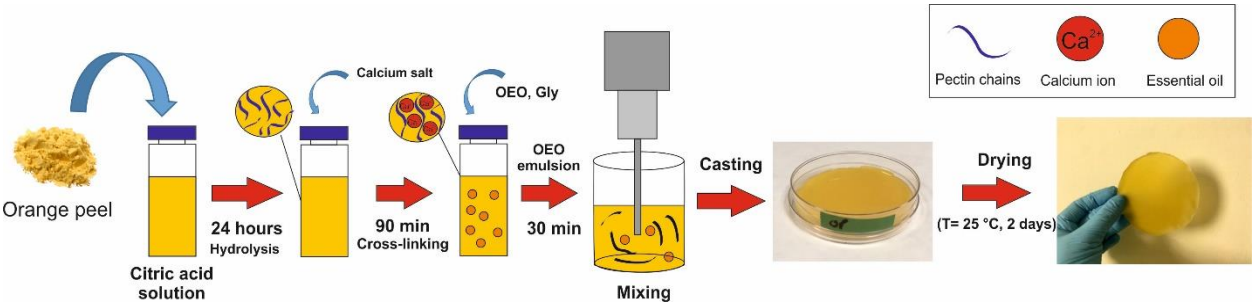

Figure 5.2 Fabrication scheme of orange peel films.

5.2.3 Attenuated Total Reflection Fourier Transform Infrared (ATR-FTIR)

Infrared spectra were obtained with a single-reflection attenuated total reflection (ATR) accessory (MIRacle ATR, PIKE Technologies) coupled to a Fourier Transform Infrared (FTIR) spectrometer (Equinox 70 FT-IR, Bruker). All spectra were recorded in the 3800 to 600 cm^{-1} range with a resolution of 4 cm^{-1}, accumulating 64 scans to reduce the spectral noise.

The esterification degree (DE) was calculated by determining the peak area values of the free carboxyl groups, located at 1630 cm^{-1}, with respect to the esterified groups, located at 1740 cm^{-1}, following the **Equation 1** below (Güzel & Akpınar, 2019):

$$R = \frac{A_{1740}}{A_{1740} + A_{1630}} \quad (\mathbf{1})$$

Where A_{1740} and A_{1630} are the areas of the infrared peaks related to the esterified and non-esterified, respectively.

5.2.4 Scanning Electron Microscopy (SEM)

Surface and cross-section morphologies of samples were characterized by scanning electron microscopy (SEM) using a JEOL JSM-6490LA microscope (JEOL Ltd., Japan), operating at 10 and 15 kV of accelerating voltage. Before the analysis, the samples were previously coated with a 10-nm-thick gold layer with a Cressington 208HR sputter coater (Cressington Scientific Instrument Ltd, U.K.).

5.2.5 X-ray diffraction analysis (XRD)

XRD measurements were performed by using a PANalytical Empyrean X-ray diffractometer equipped with a1.8 kW Cu Kα ceramic X-ray tube, PIXcel3D 2X2 area detector, and operating at 45 kV and 40 mA. The diffraction patterns were collected in Parallel-Beam (PB) geometry and symmetric reflection mode using a zero-diffraction silicon substrate over an angular range: 2θ = 5-70°, with a step size of 0.026°. XRD data analysis was carried out using HighScore 4.5 software from PANalytical.

5.2.6 Optical characterization

The optical transmittance of films was determined using a Varian CARY 6000i Scan UV-Vis spectrophotometer over the wavelength range from 200 to 800 nm. For the measurements, the freestanding films were placed in a compartment with a light pathway of 2 cm × 2 cm. An empty test cell was used as a reference. The opacity values of the samples were calculated following the next **Equation 2**:

$$\text{Opacity} = \frac{A_{600}}{d} \quad (\mathbf{2})$$

Where A_{600} is the absorbance at 600 nm and d is the thickness of the material in mm.

5.2.7 Mechanical characterization

Mechanical properties of the films were measured by uniaxial tensile tests on a dual column Instron 3365 universal testing machine. Dog-bone shaped samples had a gauge length of 25 mm and a width of 4 mm. Strain displacement was applied at a rate of 10 mm/min. Stress-strain curves were recorded at 25 °C and 44 % relative humidity (RH). At least ten measurements were conducted for each sample and results were averaged to obtain a mean value. The stiffness of the material was defined with the Young's modulus value, calculated from the slope of the linear part

of the stress-strain curve (before elastic limit). Both Young's modulus and elongation at break values were estimated using the built-in software of the tensile tester

5.2.8 Solubility

The solubility was determined in terms of the percentage of the film dry matter that solubilizes in water. Films were cut (1 cm x 4 cm) and kept in a vacuum oven overnight at 40°C to remove all moisture content from the samples. The films were weighed (W_0). Films were dipped in 50 mL of deionized water in a glass beaker and kept for 48 hours. Thereafter, the films were removed from the beakers and dried at 40°C overnight in the vacuum oven. The samples were weighed after dried (W_f). The solubility is calculated following **Equation 3** below:

$$\text{Solubility (\%)} = \frac{W_0 - W_f}{W_f} \text{ x } 100 \quad (\mathbf{3})$$

5.2.9 Water vapor permeability

Water vapor permeability (WVP) of samples was determined at 25 °C and under 100% relative humidity gradient (ΔRH %) according to the ASTM E96 standard method. In this test, the permeation chamber with a 7 mm inside diameter and a 10 mm inner depth were used filled with 400 µm of deionized water (which generates 100 % RH inside the permeation cell). The samples were cut into circles and mounted on the top of the permeation chambers. The permeation chambers were placed in a 0% RH desiccator with anhydrous silica gel, which was used as a desiccant agent to maintain 0% RH in the desiccator. The water transferred through the film was determined from the weight change of the permeation chamber every hour during a period of 8 h using an electronic balance (0.0001 g accuracy) to record mass loss over time. The mass loss of the permeation chambers was plotted as a function of time. The slope of each line was calculated by linear regression. Then, the water vapor transmission rate (WVTR) was determined as **Equation 4** indicates below:

$$\text{WVTR}(g/m^2 d) = \frac{\text{Slope}}{\text{Area of the sample}} \quad (\mathbf{4})$$

WVTR measurements were replicated three times for each film. The WVP of the sample was then calculated as **Equation 5** below:

$$\mathrm{WVP(g/m^2 d\ Pa)} = \frac{\mathrm{WVTR\ x\ L\ x\ 100}}{\mathrm{p_s\ x\ \Delta RH}} \quad (\mathbf{5})$$

where L (m) is the thickness of the sample, measured with a micrometer with 0.001 mm accuracy, ΔRH % is the percentage of relative humidity gradient, and ρ_S (Pa) is the saturation water vapor pressure at 25 °C.

5.2.10 Antioxidant activity

The antioxidant capacity of the orange peel films was calculated by measuring the free radical scavenging activity of antioxidants molecules released from the sample by standard 2,2-diphenyl-1-picrylhydrazyl radical (DPPH$^{\cdot}$) methods. Briefly, when the antioxidant film, (ø= 12 mm), was immersed in 3 mL of a radical solution, the antioxidant migrated from the film react against the radical leading to a UV-Vis detectable color change. For preparing the radical solution of DPPH$^{\cdot}$, 0.1 mM of DPPH was dissolved in ethanol. Tests were done by diluting the radical solution with water until its abortion reached ~1 a.u. at the characteristic absorption band at 517 nm. Extracts from the solutions were collected at certain immersion time-intervals from 0 to 24 hours. The absorption values were collected by a Cary JEOL UV-spectrophotometer. The antioxidant activity (radical scavenging activity, RSA) was estimated using **Equation 6** below.

$$\text{Radical Scavenging Activity (\%)} = \frac{\mathrm{A_1 - A_2}}{\mathrm{A_1}}\ \mathrm{x}\ 100 \quad (\mathbf{6})$$

Where A_1 is the absorbance of the DPPH$^{\cdot}$ radical, while A_2 is the absorbance of the sample at 517 nm.

5.2.11 Food contact Migration

The migration of components from the different bioplastics in the food was tested using Tenax® as a simulant for dry food. The methodology for the analysis was similar to (Perotto et al.,

2018). All samples were cut in circles (ø=25 mm) and placed in a clean glass vial with 80 mg of Tenax®. Then, vials were stored in the oven for 2 hours at 70°C. The overall migration was obtained by calculating the mass difference of Tenax® before and after the treatment.

5.3 Results and discussion

5.3.1 Film-forming capability of samples

In **Figure 5.3(a)** the real photographs and the values of the thickness (mm) of the set of the films without additives: without a cross-linking agent (OP), OP cross-linked with $CaCl_2$ (OP-Cl), and OP cross-linked with $CaCO_3$ (OP-CO3). In **Figure 5.3(b)** the corresponding films loaded with OEO (OP-OEO, OP-Cl-OEO, OP-CO3-OEO) are displayed, while films contained OEO and Gly (OP-OEO-Gly, OP-Cl-OEO-Gly, OP-CO3-OEO-Gly) are exposed in **Figure 5.3(c)**. Each set of samples exhibited some physical particularities; films without a cross-linking agent and OP film cross-linked with $CaCl_2$ were uniform, bright orange, and showed great film-forming properties. On the other hand, OP films cross-linked with $CaCO_3$ (OP-CO3 and OP-CO3-OEO) were whiter and very rigid, while the OP-CO3-OEO-Gly was orangish and easy to handle. The incorporation of inorganic salts increased the thickness of films with respect to the neat OP, while OEO led to a more compact structure in OP films. As expected, glycerol acted as a thickening agent for OP and OP-Cl films, increasing the thickness.

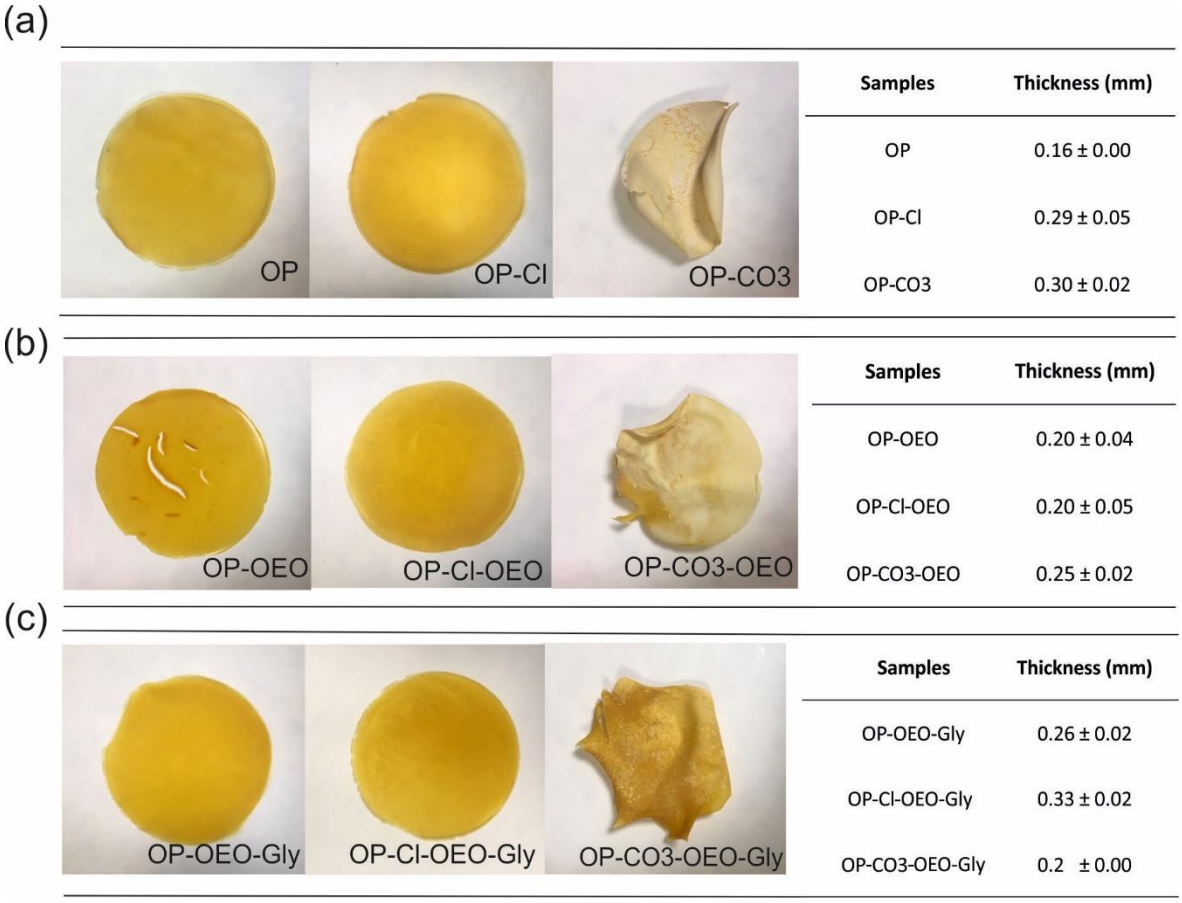

Figure 5.3 The real photographs and thickness of **(a)** OP, OP-Cl, and OP-CO3, **(b)** OP-OEO, OP-Cl-OEO, and OP-CO3-OEO, and **(c)** OP-OEO-Gly, OP-Cl-OEO-Gly, and OP-CO3-OEO-Gly.

5.3.2 Study of the orange pectin esterification degree

The esterification of the carboxylic group located in galacturonic acid is crucial for the inner interaction and organization of the pectin chains. The degree of methyl-esterification (DME) is the relationship between the free carboxylic groups and the methylated carboxylic groups presented in the pectin chain, marked in red and orange respectively, in **Figure 5.4**. This parameter is strongly related to the sensitivity of the pectin to the variation of the pH. Generally, a higher esterification degree (more occupied carboxylic groups), is related to less sensitive-pH pectin and thus, higher pH will be required for the gelation process.

The esterification degree obtained using **Equation 1** was 26%, which indicates that 74% of the carboxylic groups were free, while 26% were esterified. This result suggested that the starting material would be easily tuned when exposed to different pH environments, providing a

wide spectrum of samples with different physicochemical characteristics and with a large field of application. In concordance with literature, orange peel pectin belonged to low methoxyl pectin (LMP), when the degree of the esterification is less than 50 % (Müller-Maatsch et al., 2016).

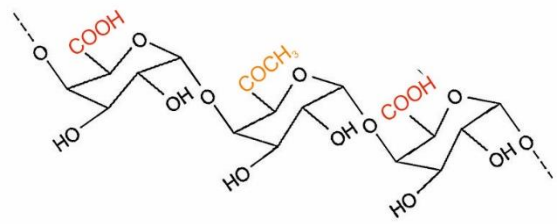

Figure 5.4 Structure of pectin. In red the free carboxylic groups, while in orange the methyl-esterified carboxylic groups are represented.

5.3.3 Study of pectin bonding-interaction: infrared spectroscopy

The free carboxylic groups contained in pectin are capable to acquire a negative charge at pHs above the isoelectric point (IP) of pectin (3.5 pH), promoting important structural modifications of the pectin chains (Han et al., 2017). **Figure 5.5(a-b)** shows the main chemical interactions between the pectin chains linked to the pH environment. At pH below the IP, the free carboxylic groups are protonated and hydrogen forces predominate between the pectin chains, as **Figure 5.5(a)** shows. At pHs above the PI, the free carboxylic groups deprotonate acquiring a negative charge (Gawkowska et al., 2018). This leads to electrostatic repulsion between the charged carboxylic groups and generating a more open-like structure, as shown in **Figure 5.5(b)**. Interestingly, unlike the protonated-pectin chains showed in **Figure 5.5(c)**, the negative charge of the free carboxylic groups allows the interaction with calcium ions via cross-linking, creating a tridimensional structure called egg-box, see **Figure 5.5(d)**.

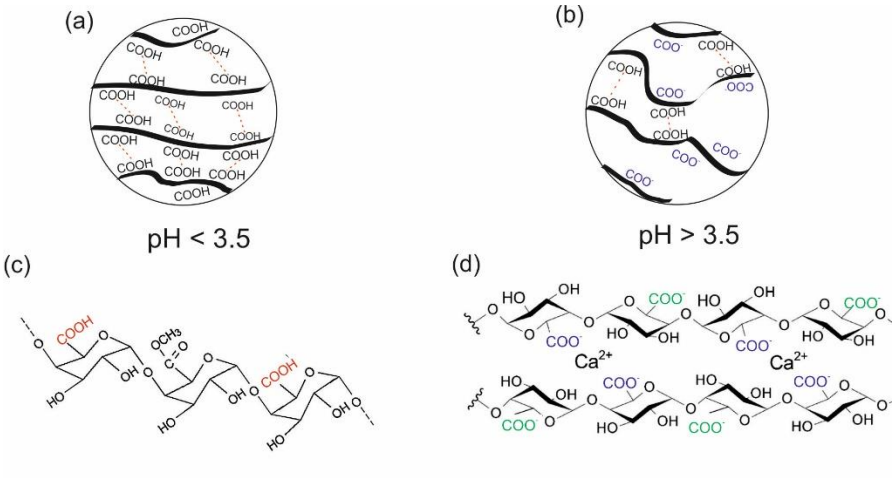

Figure 5.5 The main chemical interactions between the pectin chains at **(a)** pH below IP, **(b)** pH above IP. **(c)** Pectin structure at acidic conditions, **(d)** egg-box structure.

The physicochemical modification of pectin structure when the orange peel powder was immersed in the acidic hydrolysis of citric acid (pH 2.1) was studied with infrared spectroscopy. **Figure 5.6(a)** shows the comparison between the spectra of the powder orange peel and the film OP (without calcium salts). Orange peel powder presents a pH of about 4.3 and its infrared spectra are mainly constituted by the characteristic peaks of pectin. The broad and intense band related to the stretching vibration of the hydroxyl groups ν(O-H) and bound water is located at 3600-3200 cm^{-1}, while the asymmetric and symmetric stretching bands of C-H of the CH_2 groups appeared at 2975 cm^{-1} and 2950 cm^{-1}. The stretching vibration of the carbonyl groups belonged to the methyl-esterified carboxylic group, and the carboxylate group was at 1740 cm^{-1} and 1610 cm^{-1}, while the band related to the O=C-O structure was at 1420 cm^{-1}. Finally, the characteristic bands of the carbohydrates are shown at 1100 cm^{-1} (Manrique & Lajolo, 2002; Synytsya et al., 2003). The new peaks that appeared in OP film indicated the structural changes of the pectin after the acidic treatment. A small shoulder located at 2600 cm^{-1} belonged to the ν(O-H) in free carboxylic groups bonded by hydrogen bonds into dimers, which evidenced the protonation after the acidic treatment (Synytsya et al., 2003). A second intense band at 1647 cm^{-1} attributed to the bending vibration of the water δ(H_2O), belonged to the water molecules entrapped in the structure (Synytsya et al., 2003). Peaks that revealed the presence of protonated carboxylic groups were remarked in red, while the asymmetric vibration band of the carboxylate group placed at 1610 cm^{-1} was remarked

in blue. Nevertheless, the main modifications of the IR-spectra were observed in the range of the carbonyl group (2000 cm^{-1} to 1250 cm^{-1}), maximized in **Figure 5.6(b)**. The carbonyl group of the orange peel powder was quite less intense than the same peak correspondent to OP film. Moreover, the peak was shifted in 20 cm^{-1} towards higher wavenumbers, which indicated the increase of the interaction by hydrogen bonds between the carboxylic groups, as a result of the protonation via the acidic treatment. This response has been also observed in other natural organic molecules influenced by the variation of the pH (Francis et al., 2017).

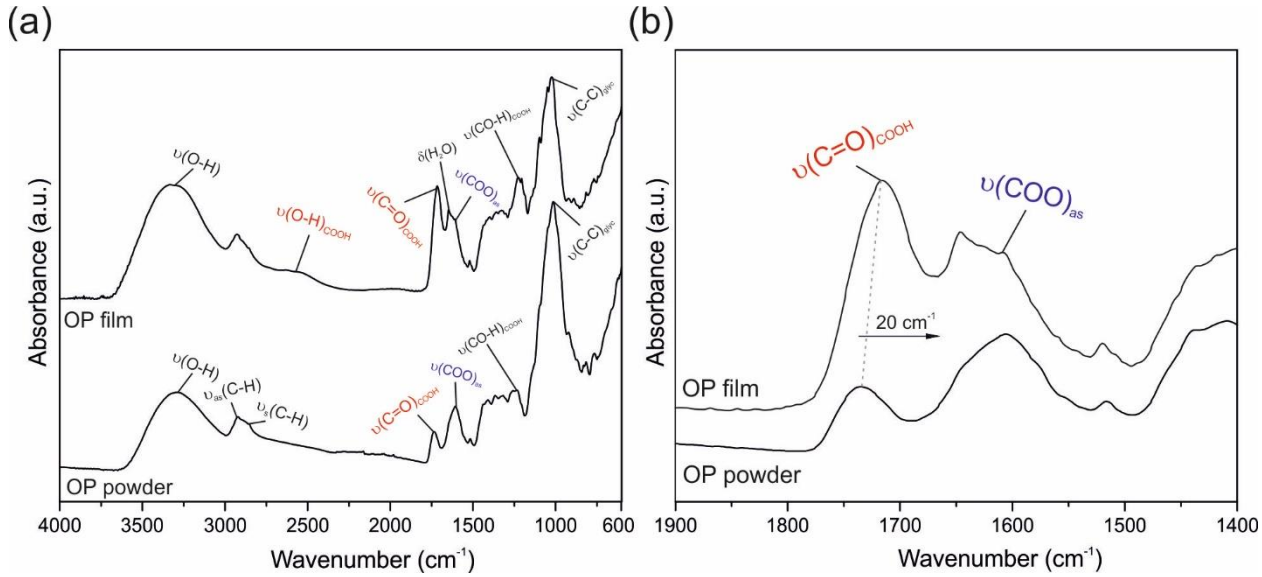

Figure 5.6 (a) The infrared spectra of the OP-powder (before the acidic treatment) and OP-film (after the acidic treatment). In red the peaks related to the carboxylic groups, while the peaks related to the carboxylate group are marked in blue. **(b)** The magnification of the infrared spectra ranging from 1900 cm^{-1} to 1400 cm^{-1}.

The chemical characterization of orange peel films with the loading of calcium salts, $CaCl_2$ and $CaCO_3$, was analyzed with infrared-spectroscopy. The infrared spectra of orange peel (OP), OP cross-linked with calcium chloride (OP-Cl) and OP bonded to calcium carbonate (OP-CO3), are represented in **Figure 5.7(a)**. The main differences observed in OP-Cl and OP-CO3 with respect to the OP sample were located in the range from 2000 cm^{-1} to 1250 cm^{-1}, **Figure 5.7(b)**. In the infrared spectra of OP-Cl films, the band correspondent to free carboxylic groups (1720 cm^{-1}) was slightly reduced, while the band related to the carboxylate groups ($\nu_{as}(COO^-)$) increased

consequently. OP-CO3 samples showed more relevant modifications, the peak of the free carboxylic group ($\nu(C=O)_{COOH}$) was barely noticed, while new peaks at 1610 cm^{-1}, 1550 cm^{-1}, 1410 cm^{-1}, and 1300 cm^{-1}, appeared with significant intensity. These bands corresponded to the asymmetric and symmetric stretching vibrations of the carboxylate group, $\nu_{as}(COO^-)$ and $\nu_s(COO^-)$, respectively, (Manrique & Lajolo, 2002). The higher conditions of pH led by the basic nature of $CaCO_3$ salt promoted the formation of the carboxylate groups ($-COO^-$). The similar pH conditions in OP-Cl and OP films resulted in scarce variations of the infrared spectra when $CaCl_2$ was incorporated. As explained in **Figure 5.5**, carboxylate groups participate with the calcium ions by cross-linking to form the tridimensional structure. The infrared study suggested that OP-CO3 films, which present more carboxylate groups, may present a higher cross-linking degree with respect to OP-Cl, which protonated structure hindered the interaction with calcium ions (Gawkowska et al., 2018). No significant variations of infrared spectra were observed with the loading of glycerol and orange essential oil to the samples.

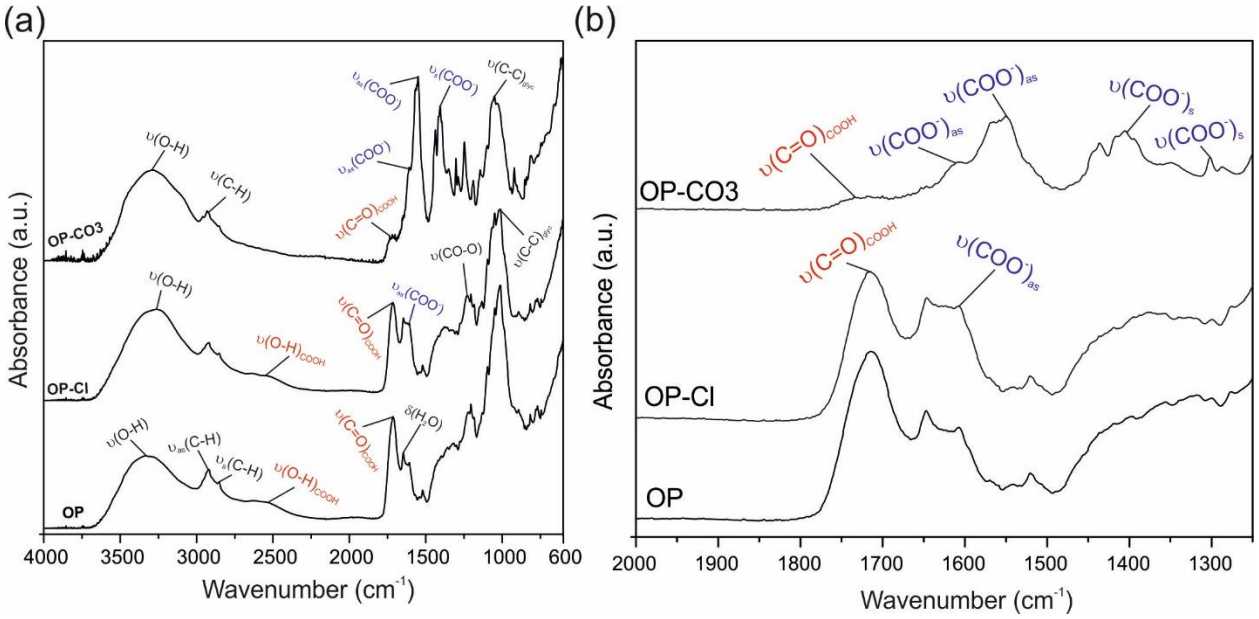

Figure 5.7 (a) The infrared spectra of the OP, OP-Cl, and OP-CO3. In red the peaks related to the carboxylic groups, while the peaks related to the carboxylate group are marked in blue. **(b)** The magnification of the infrared spectra in the range from 2000 cm^{-1} to 1250 cm^{-1}.

5.3.4 Microstructural analysis: SEM and XRD studies

Figure 5.8 shows the top-view and cross-section of images of OP, OP-Cl, and OP-CO3 samples collected with an electronic SEM microscope. In **Figure 5.8(a-b)**, OP and OP-Cl showed a uniform and smooth surface, while the surface of OP-CO3 was heterogeneous and rough, see **Figure 5.8(c)**. The magnified image (x1000) of the OP-CO3 surface inset in **Figure 5.8(c)** revealed that this sample hosted dispersed crystalline grains. The cross-section images of the OP and OP-Cl were homogeneous and free from defects, **Figure 5.8(d)** and **Figure 5.8(e)**, respectively. The cross-section of OP-CO3 showed the formation of two different phases, the darker phase may correspond to the pectin, while the brighter part was likely related to the crystalline precipitates observed in the surface, **Figure 5.8(f)**. Crystalline precipitates were found in other films based on a vegetal matrix (Assifaoui et al., 2010; Bayer et al., 2014; Perotto et al., 2018).

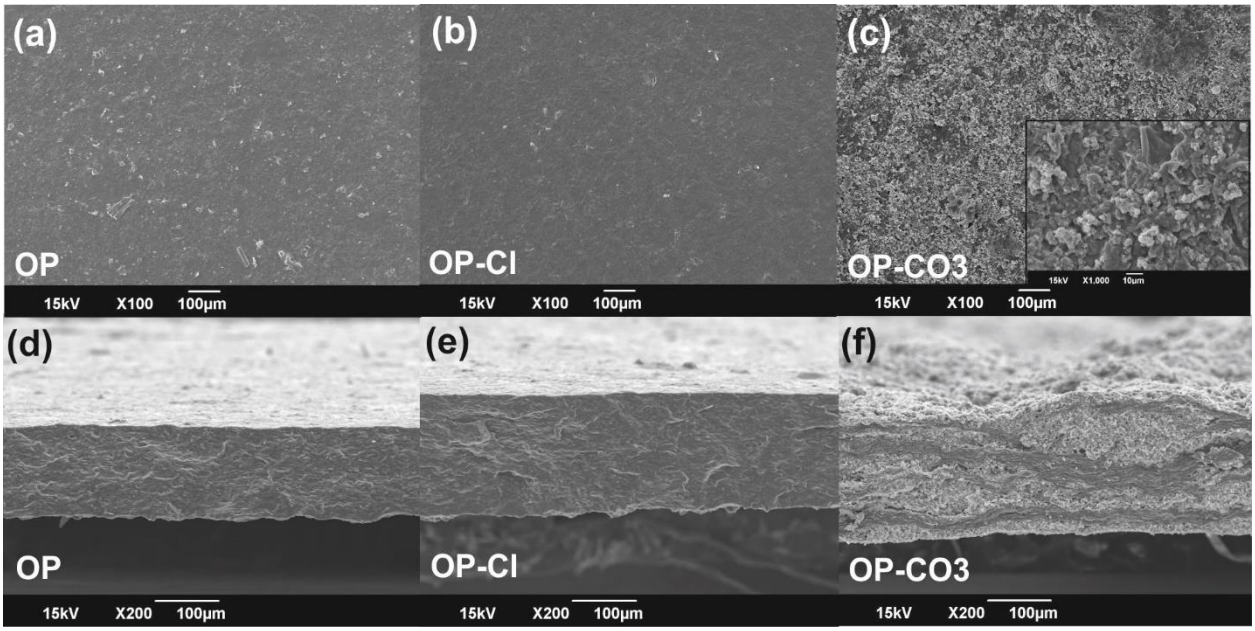

Figure 5.8 The top view of **(a)** orange peel film (OP), **(b)** orange peel with $CaCl_2$ (OP-Cl), and **(c)** orange peel with $CaCO_3$, with a magnification x200. The magnification x1000 of the precipitates formed in the surface of OP-CO3 films is placed as an inset of the image. The cross-section images of **(d)** OP, **(e)** OP-Cl, and **(f)** OP-CO3 films, with a magnification of x200.

The crystalline structure of neat orange peel powder and OP films (OP, OP-Cl) were evaluated with XRD analysis reported in **Figure 5.9.** The XRD patterns of orange peel powder showed two mains peaks located at 15.6 ° and 21.3 °, an intense sharp peak at 24°, and some peaks

ranged from 30-40 °. Any of these peaks correspond to pectin, which presents XRD patterns with sharp peaks at 9°, 12.7°, 18.4°, 28.2°, and 40.1° (Mishra et al., 2008; Ullah et al., 2019). However, the peak at 15.6 °, the small shoulder at 22.4°, and a small band at 34° correspond to the planes (110), (220), and (004) respectively, of the cellulose-I-structure (Thakur et al., 2020). The same patterns had been reported in other fruit-based materials (Bayer et al., 2014; Dai et al., 2018). The possible explanation may be associated with the re-precipitation of cellulose after the acidic hydrolysis treatment (Bayer et al., 2014; Ishak et al., 2018). The sharp peaks at 15°, 24.5°, and 30.5 ° coincided with the biogenic calcium oxalate (CaC_2O_4) present in significant amounts in vegetables (Bayer et al., 2014; da Costa et al., 2009; Perez-Pimienta et al., 2015). **Figure 5.9(a)** indicates that the XRD peaks of OP film coincided with the peaks observed in neat orange powder, which means that the acidic treatment did not affect the crystallinity. The XRD patterns of OP-Cl, OP-film, citric acid (powder), and the $CaCl_2$ are exposed in **Figure 5.9(b)**, to assign the peaks belonged to the OP-Cl sample. Results showed that all peaks of OP-Cl coincided with the XRD spectra of OP, corresponding to crystalline cellulose and calcium oxalate, which suggested that neither citric acid nor calcium chloride precipitated in form of crystals in OP-Cl film.

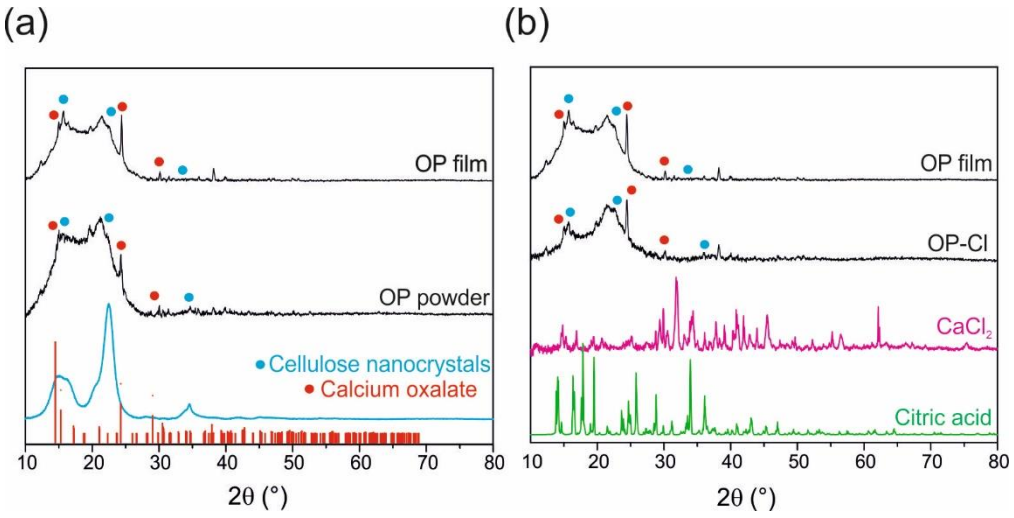

Figure 5.9 (a) XRD spectra of neat orange peel powder (OP powder), orange peel film after the acidic hydrolysis (OP film), calcium oxalate (ICSD 98-024-6004), and cellulose nanocrystals with correspondent peaks marked with a red and blue circle, respectively **(b)** The XRD spectra of citric acid, calcium chloride ($CaCl_2$), OP-Cl and OP film in order to analyze the presence of citric acid and $CaCl_2$ crystals in the OP-Cl sample.

The assignment of the XRD patterns of the OP-CO3 was evaluated in **Figure 5.10(a)**, which exhibited the XRD spectra of the OP-film, OP-CO3, citric acid (powder), the inorganic salts of $CaCO_3$ and Ca-citrate. The numerous sharp peaks in the entire range of the XRD-pectin patterns may be resulted due to the precipitation of crystalline compounds. The increase of the pH in the solution with the incorporation of $CaCO_3$ (4.5 pH respect to 2.1 in the OP and OP-Cl samples) may promote the precipitation of biomolecules with low solubility at those conditions, such as $CaCO_3$ and citric acid, which can react forming calcium citrate precipitates (Garcia et al., 2018; Sriamornsak et al., 2007). However, the high heterogeneity of the natural matrix may result in the formation of other precipitates that were not assigned in the XRD spectra. These precipitates may justify the different phases in the SEM image (**Fig. 5.8(f)**), in addition to the stiffness and whiteness color of OP-CO3 films, displayed in **Figure 5.10(b)**.

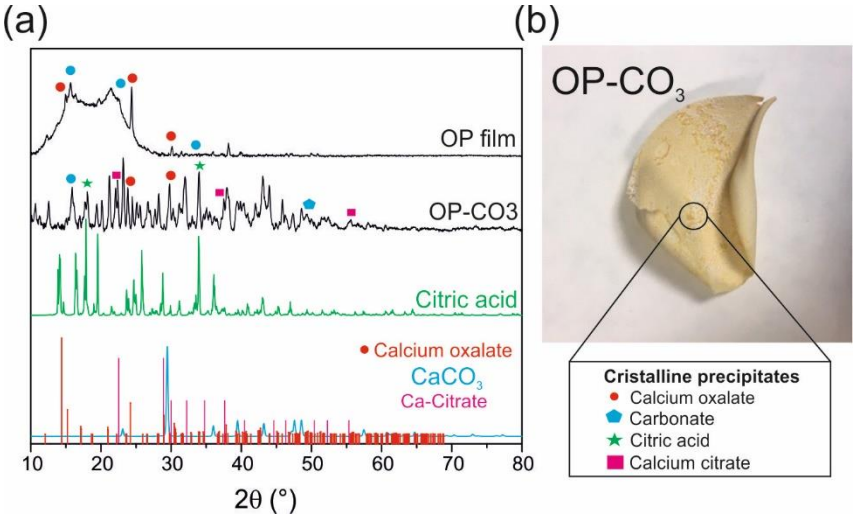

Figure 5.10 (a) The XRD patterns of OP-film, citric acid, calcium carbonate ($CaCO_3$) and calcium citrate (Ca-Citrate JCPDF:01-0008), calcium oxalate (ICSD 98-024-6004) with theirs peaks assigned in the XRD-spectra of OP-CO3 in orange, a green star, a blue pentagon, a pink square, and a red circle, respectively. **(b)** A real photograph of OP-CO3 film. The presence of crystalline precipitates justified the appeal of this sample.

Pectin presents a high hydrophilic character, thus, the loading of lipophilic molecules, such as essential oils, may promote the formation of phase separations, as observed in other citrus pectin-based samples (Nisar et al., 2018). The SEM cross-section images of films loaded with

orange essential oils (OEO) and glycerol (Gly) are represented in **Figure 5.11**. In **Figure 5.11(a-b)**, the micrographs of OP-OEO and OP-Cl-OEO films showed a rougher surface with respect to the neat films (**Figure 5.8 (a-b)**). The migration of the volatile compounds of essential oils upwards the film and the further evaporation may result in some surface irregularities (Almasi et al., 2020; Priyadarshi, Sauraj, Kumar, & Negi, 2018; Priyadarshi, Sauraj, Kumar, Deeba, et al., 2018; Sánchez-González et al., 2010). However, both films showed a homogeneous and dense structure, lack of phase separation, which indicated the great compatibility between the different components. Interestingly, the addition of essential oils reduced the agglomeration of precipitates within the OP-CO3 films, as **Figure 5.11(c)** shows. The cross-section images of films containing glycerol in addition to the OEO are represented in **Figure 5.11 (d-f)**. The addition of glycerol led to a smoother surface and more-compacted structure in all films (Daudt et al., 2016). The formation of precipitates and irregularities were also strongly reduced with the glycerol-loading, see OP-CO3-OEO-Gly film micrograph.

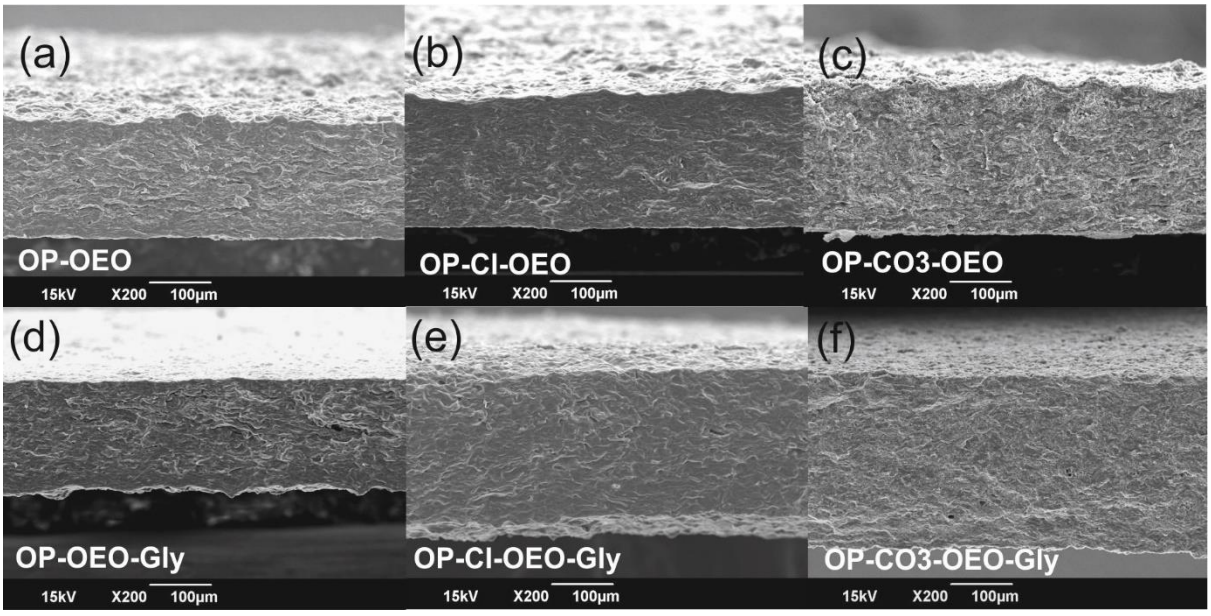

Figure 5.11 The cross-section of all orange peel-based films with OEO **(a-c)** and OEO and glycerol **(d-f)** with a magnification of x200.

The incorporation of OEO did not affect the crystallinity of the pectin-based material, while glycerol, a well-known plasticizer, altered the crystalline structure of OP films. The XRD spectra

of the orange peel films containing glycerol (OP-OEO-Gly, OP-Cl-OEO-Gly, and OP-CO3-OEO-Gly) were displayed in **Figure 5.12(a-c).** OP-OEO-Gly and OP-Cl-OEO-Gly did not show significant differences with the XRD patterns of the neat films in **Figure 5.12(a-b)**. Interestingly, the glycerol showed to have a strong influence on the crystallinity of OP-CO3 samples, as shown in **Figure 5.12(c)**. The XRD spectra of the OP-CO3-OEO-Gly displayed a broad peak that ranged from 14° to 27°, similar to the XRD patterns observed in orange peel. Such a result indicates that glycerol reduces the formation of crystalline precipitates enhancing the handling and application of the sample.

Nevertheless, the presence of an excess of calcium ions in the solution/film is interesting because these ions can interact with the pectin present in the fruit peel of the food products, reinforcing the structure and decreasing the permeability (Embuscado & Huber, 2009; Martín-Diana et al., 2007).

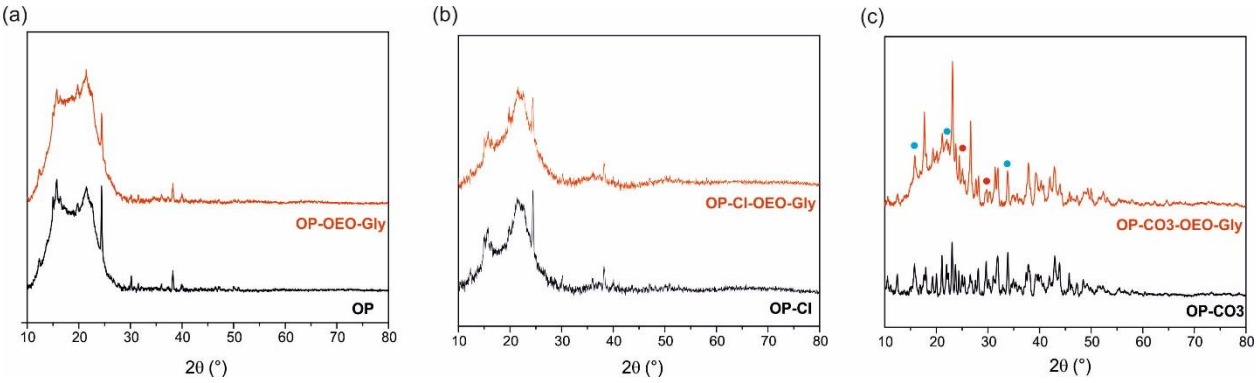

Figure 5.12 XRD-patters of **(a)** OP, OP-OEO-Gly, **(b)** OP-Cl and OP-Cl-OEO-Gly, and **(c)** OP-CO3 and OP-CO3-OEO-Gly. Near films were presented in black, while films with OEO and glycerol were red.

5.3.5 Evaluation of the optical properties: transparency and UV-blocking

Transparency is an important property to evaluate the suitability of the material for food packaging applications. Generally, transparency is desirable to facilitate the real perception of the food freshness to consumers (Priyadarshi, Sauraj, Kumar, & Negi, 2018). The parameter used to determine the transparency of materials is transmittance, which is defined as the percentage of radiation that passes through the film. For this measurement, the light passage in the UV-vis range of the electromagnetic spectrum is analyzed, from 800-200 nm. The visible light ranges from 800

nm to 400 nm, and the invisible UV radiation that corresponds to the range from 400 nm to 200 nm, as shown in **Figures 5.13 (a-b)**.

The percentage of transmittance of OP and OP-Cl samples in the range of 200-800 nm is represented in **Figure 5.13**. High values of transmittance are associated with transparent materials. The transmittance of OP-CO3 samples was not represented because they were opaque. **Figure 5.13(a)** showed that neat OP films exhibited the highest transmittance value (~10%), which decreased with the incorporation of additives, glycerol, and OEO. The same tendency was observed in OP-Cl films in **Figure 5.13(b)**. Moreover, the strong orange-colored samples led to light absorption in the range 500-400 nm, revealing lower transmittance in that range. Generally, samples derived from the vegetable matrix are highly colored and opaque. Loading vegetal extracts into a transparent matrix has been demonstrated to reduce transparency and enhance color saturation (Collazo-Bigliardi et al., 2019; Nogueira et al., 2019).

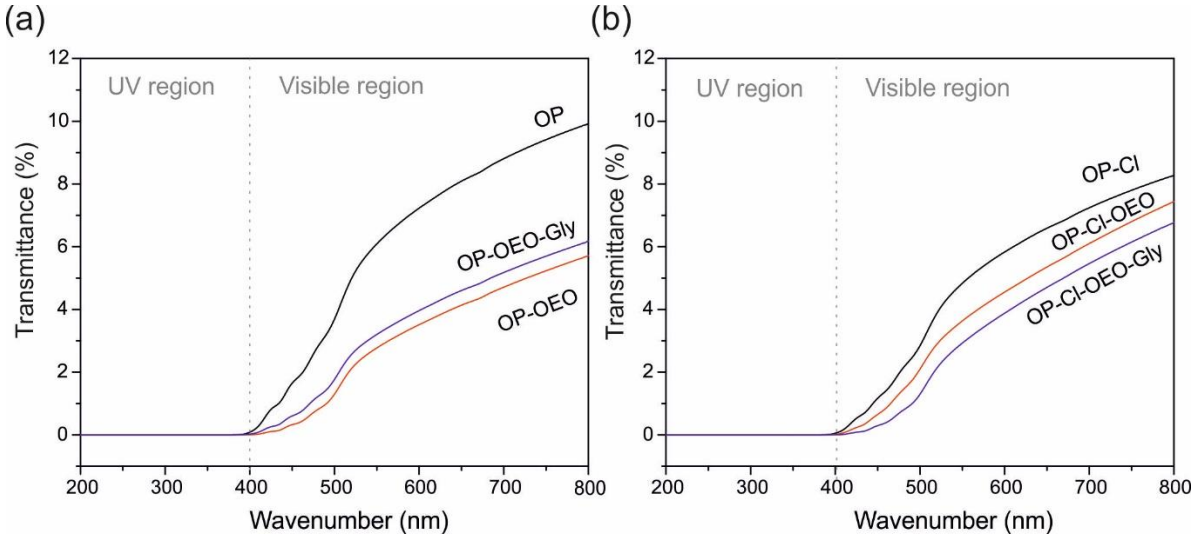

Figure 5.13 The transmittance spectra of **(a)** OP, OP-OEO, and OP-OEO-Gly films, and **(b)** OP-Cl, OP-Cl-OEO, and OP-Cl-OEO-Gly.

The dispersion of the matrix and the thickness are two important factors that strongly affect the transparency (Ilyas et al., 2018). The effect of the film thickness on the optical properties is considered in terms of opacity (%/mm). The values of the opacity of OP films are represented in **Figure 5.14(a)**. Results showed that glycerol enhanced the transparency in both OP films,

probably because the plasticizer improved the dispersion in the inner matrix (Villalobos et al., 2005). The high opacity of OP-Cl-OEO was likely resulted from the light-scattering and coalescence effect due to the distribution of the lipid particles within the film (Kaya et al., 2018; Nisar et al., 2018; Sánchez-González et al., 2010). The optical properties of OP film were compared with other biobased materials in **Figure 5.14(b)**. Overall, the opacity values of OP films were placed slightly above the rest of the samples. However, this result is a great success because means that the transparency of the current films, which present a matrix formed by 100% vegetal waste, was comparable to other samples based on commercial biopolymers.

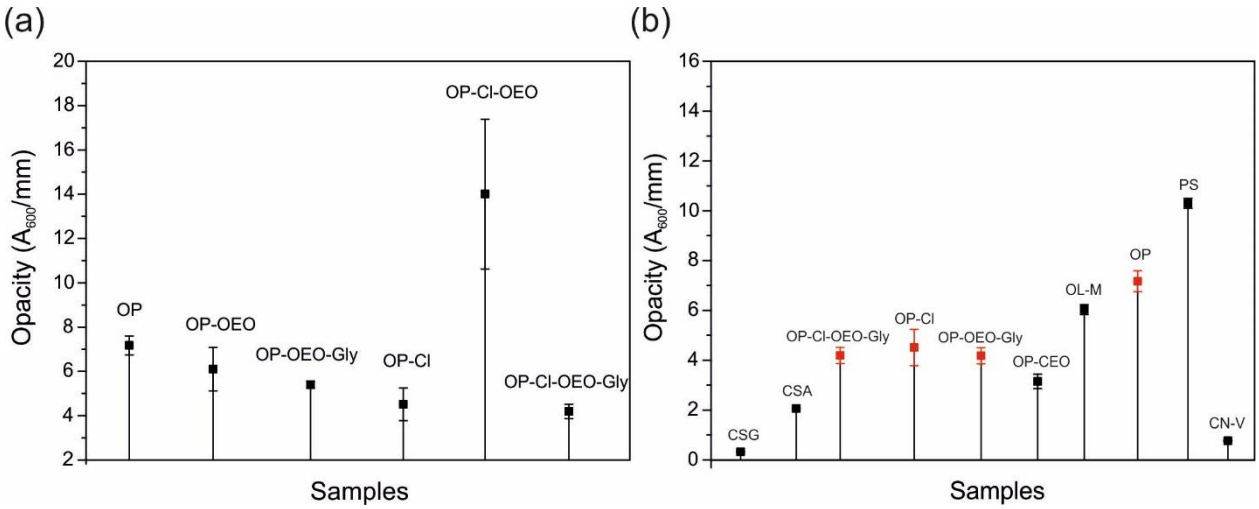

Figure 5.14 (a) Opacity values of the OP films. **(b)** Comparison of the opacity values of published materials. The acronyms and source are the following: **CSG**: Chitosan film with citric acid and glycerol (Priyadarshi, Sauraj, Kumar, & Negi, 2018), **CSA:** chitosan and apricot kernel essential oil (Priyadarshi, Sauraj, Kumar, Deeba, et al., 2018), **OP-CEO**: citrus pectin films with clove essential oil (Nisar et al., 2018). **OL-M**: chitosan with olive-pomace microparticles (de Moraes Crizel et al., 2018). **PS**: pinhão starch and flour (Daudt et al., 2016). **CN-V**: Chitosan with cellulose nanocrystals and grape pomace extracts (Xu et al., 2018).

A deeper analysis of **Figure 5.13**, showed that the transmittance spectra of all samples blocked 100% of the light in the range from 400 nm to 200 nm, correspondent to UV radiation. The UV-light is considered the main initiator of damaging oxidation reactions, like lipid degradation, which limited enormously the shelf-life of foodstuffs (Johnson & Decker, 2015). The high content of bioactive compounds in vegetal by-products results in a considerable number of films found in

bibliography with UV-blocking properties (de Moraes Crizel et al., 2016; Dou et al., 2018; Lozano-Navarro et al., 2017). However, not all these films blocked the entire UV range exhibiting values of transmittance, for example, chitosan-starch films filled with resveratrol showed a transmittance of ∼10% at 280 nm, besides tea polyphenols-containing films, which allowed the passage of ∼17% of light at the same range of wavenumbers (de Moraes Crizel et al., 2016; Dou et al., 2018).

5.3.6 Mechanical properties

Food packaging materials may offer great resistance to ensure the preservation of food during transportation and storage. Biopolymers present weak mechanical properties, placing biopolymers far away in the substitution of synthetic polymers as the main food package (Caz, 2017; Embuscado & Huber, 2009). However, these biomacromolecules can be applied as a secondary protection barrier in contact with food to elongate the shelf-life. The mechanical properties are very important for the functionality of edible films (Otoni et al., 2017). The elongation and Young's Modulus values obtained in OP and OP-Cl films are represented in **Figure 5.15(a-b)**, respectively. OP-CO3 samples were not considered in this section due to poor mechanical performance. Neat OP and OP-Cl samples showed similar values of Young's Modulus (~500 MPa) and elongation (<10%). For OP samples, the incorporation of OEO weakened the mechanical properties, while the OEO duplicated the flexibility in OP-Cl-OEO. The incorporation of glycerol doubled the elongation of OP films, from 8% to 25%, while the elongation of OP-Cl-OEO-Gly was 5 times over the elongation of neat OP-Cl samples, from 8% to 50%. Glycerol, as a plasticizer, weakened the intermolecular forces between the polymer chains, increasing the flexibility and mechanical resistance against the general brittle character of biopolymers (Caz, 2017).

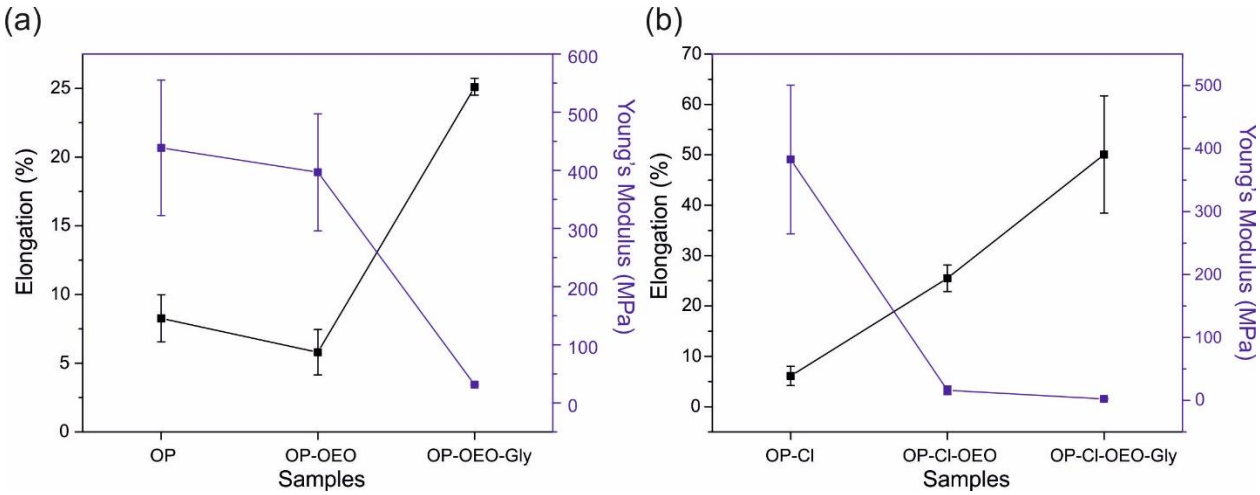

Figure 5.15 The Elastic modulus (MPa) and elongation (%) values of **(a)** OP set of samples and **(b)** OP-Cl set of samples.

The potential application of the OP films associated with the mechanical properties can be deduced through the comparison with other bio-based films with similar properties, displayed in **Figure 5.16(a,b)**. Overall, OP-OEO-Gly and Cl-OEO-Gly exhibited great flexibility with respect to the rest of the films, while the mechanical strength was lower. For example, PP films were enough flexible to seal a glass container, while CS films were used to create bioactive pouches to pack bread slices (Priyadarshi, Sauraj, Kumar, Deeba, et al., 2018; Wu et al., 2019). These results suggested that current OP films are suitable to be utilized as an edible active film in food packaging.

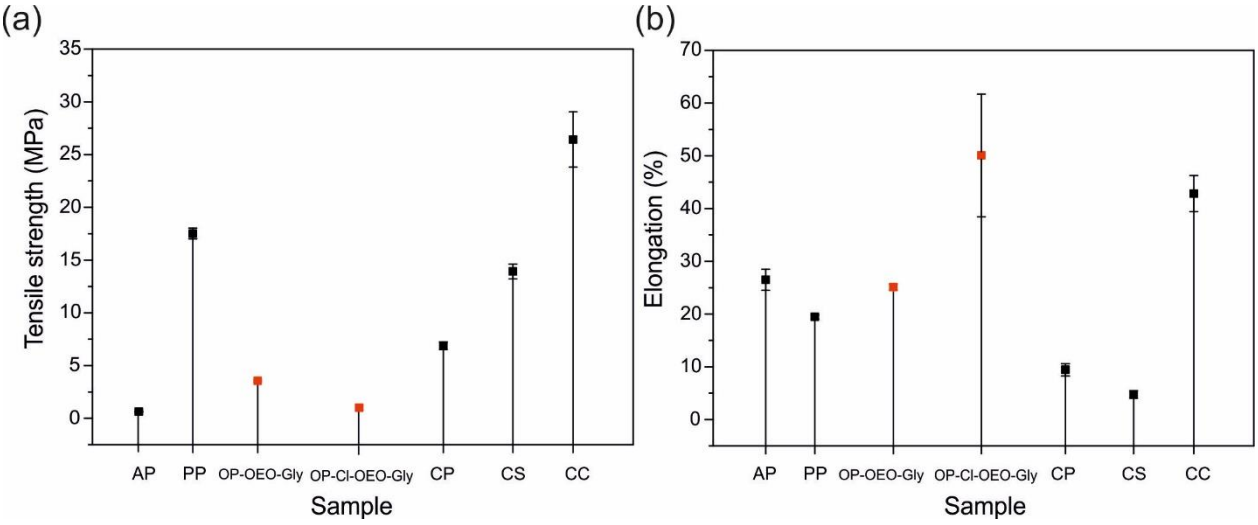

Figure 5.16 (a) The tensile strength and **(b)** elongation values were compared with other films based on vegetable byproducts. The acronyms and source are the following: AP: apple puree films with oregano essential oil (Rojas-Graü et al., 2006). PP: Pomelo peel-containing tea polyphenols (Wu et al., 2019). CP: Carrot puree film with starch (Wang et al., 2011). CS: chitosan with apricot oil (Priyadarshi, Sauraj, Kumar, Deeba, et al., 2018). CC: Chitosan with citric acid (Priyadarshi, Sauraj, Kumar, & Negi, 2018).

5.3.7 Water resistance properties

The strong hydrophilic nature of the macromolecules present in fruits and vegetables leads to a high moisture sensibility and water absorption (Ulusoy & Hecer, 2018). High relative humidity conditions in food-packaging atmospheres enhanced microorganism growth, especially in foods with high water activity, like meats and fish (Gaikwad et al., 2019). However, the application of a thick film/coating of hydrophilic polysaccharides onto food surfaces avoided the loss of moisture from fruits and vegetables. The hydrophilic layer can absorb the water released during the fruit transpiration, preventing dehydration of the food (Embuscado & Huber, 2009). Besides, hydrophilic coatings can prevent the migration of oil-based molecules like lipids migration from meats or volatile lipid essential oils (Caz, 2017; Embuscado & Huber, 2009).

The solubility degree is crucial for determining the application of the material, especially for edible coatings. High-soluble materials are preferred for ready-to-eat products, the coating/film may dissolve in boiling water during the cooking, or in the mouth when is consumed (Jirukkakul,

2016; Otoni et al., 2017). However, the use of materials with high solubility is not recommended for long storage times, low water sensitivity is required to ensure the integrity of the package for the entire food production chain (Borah et al., 2017). The solubility values of the samples are represented in **Figure 5.17(a)**. Results showed that all films had a high solubility degree, which varied with the content and nature of the calcium salt. OP films exhibited a percentage of solubility around 70%, with a slight increase when glycerol was loaded. The solubility raised in OP-Cl samples which results ranged 80-85 %, wherein OP-Cl-OEO-Gly showed the highest value. Contrary, OP-CO3, and OP-CO3-OEO exhibited a solubility of ~50% resulted from the strong bindings formed in gelation, which created a dense structure that reduced the passage of water (Kurek et al., 2019; Tulamandi et al., 2016). Glycerol strongly enhanced the film solubility as a result of its high hygroscopic nature and the plasticizer functionality, which interacted with the biopolymer weakening the inter-chain entanglement (Panrong et al., 2019; Peng et al., 2020). These results indicate that OP films are ideal for ready-to-eat products or food, as edible or easily removed when washing with water.

The water vapor permeability (WVP) is displayed in **Figure 5.17(b)**. OP film showed permeation values around $3.5 \cdot 10^{-9}$ g.m/m_2.s.Pa, and above $5 \cdot 10^{-9}$ g.m/m_2.s.Pa for OP-Cl and OP-CO3 films. These values are far superior with respect to commercial bioplastics, like poly(hydroxybutyrate) (PHA) with WVP ranged 7.9-9.5 x 10^{-12} g.m/m_2.s.Pa, or poly(lactic acid) (PLA) with 1.3-1.8 x 10^{-11} g.m/m_2.s.Pa (Arrieta et al., 2017). The high hydrophilicity of pectin facilitates the passage of water vapor molecules weakening the water barrier properties (Caz, 2017). The incorporation of nanocrystals to hinder the passing molecules, or the incorporation of lipid molecules (ex. essential oils), are widely used to improve the gas permeability (Embuscado & Huber, 2009). Orange essential oils reduced into half the values of water vapor permeability of OP-OEO and OP-CO3-OEO films, with respect to the neat samples, while the barrier properties of OP-Cl-OEO were reduced by half of OP-Cl. The reverse result was observed with the incorporation of the plasticizer glycerol, increasing the WVP by around 50% and 30% with respect to the films loaded only with essential oils. OP-CO3-OEO-Gly, in turn, preserved the good WVP of the analog OP-CO3-OEO. In this case, glycerol improved the dispersion and agglomerations in OP-CO3 samples, reducing the physical defects and thus, reinforcing the barrier properties.

All samples obtained WVP values were below 6, which is a great value with respect to other vegetable-based films like apple puree 17.1 ± 1.5 (Rojas-Graü et al., 2006) or papaya puree with 15.4 ± 1.35 (Tulamandi et al., 2016).

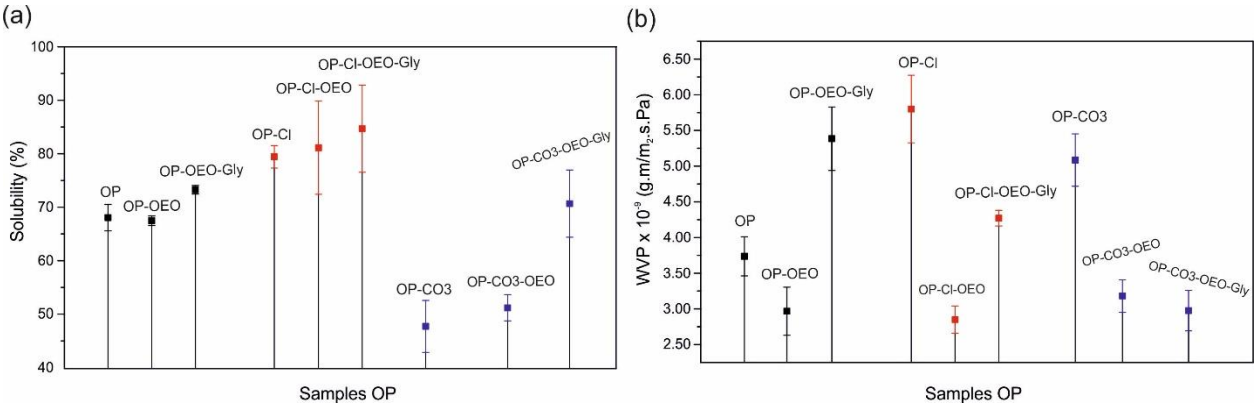

Figure 5.17 (a) The water solubility of the orange peel samples. **(b)** The water vapor permeability (WVP) of the OP films.

5.3.8 Antioxidant properties

Citrus peel is a source of strong antioxidants such as ascorbic acid, phenolic acids, and diverse types of flavonoids (Bocco et al., 1998). The main antioxidant response is fundamental in food packaging materials in order to prevent oxidation reactions that reduce the shelf-life and quality of foods (Burri et al., 2020; Marshall et al., 2000). The antioxidants can react via scavenging limiting the formation of radicals that trigger the oxidation reactions (Tian et al., 2013). To evaluate this, samples were cut in circles (ø= 12 mm) and immersed in 3 mL of DPPH˙ radical solution. **Figure 5.18(a)** shows the UV-vis spectra of the characteristic band of the radical (517 nm) and the real pictures of the radical solution at time-point zero, and when the test finished. At the beginning of the experiment, the DPPH˙ solution was violet and the peak at 517 nm was very intense, when films were immersed, the characteristic peak decreased over time, and the color of the solution turned yellow. The radical scavenging activity (RSA) at different time points for 24 hours was calculated following **Equation 6** (Materials and section methods 5.2.10), and represented in **Figures 5.18 (b-d),** for the set of samples OP, OP-Cl, and OP-CO3, respectively. After the first hour, most of the samples had inhibited all free radicals (~100% of RSA), demonstrating a strong antioxidant capability. The antioxidant migration rate was highly dependent on the cross-linking degree of the orange peel pectin, prolonging the drug release (Sriamornsak et al., 2007). Samples

with low cross-linking (set of OP and OP-Cl) showed faster release profiles with respect to OP-CO3 samples, which strong cross-linked structure led to a slower drug release. OP-Cl and OP-CO3 samples filled with OEO showed a slightly slower release. The well-interaction between the orange peel matrix and OEO compounds may delay the release, reducing the antioxidant activity in the first hours. The excellent properties of OP films were demonstrated when compared with other films based on orange peel pectin and essential oils that showed a maximum of inhibition of 64.73 % after 3 hours of immersion (Nisar et al., 2018).

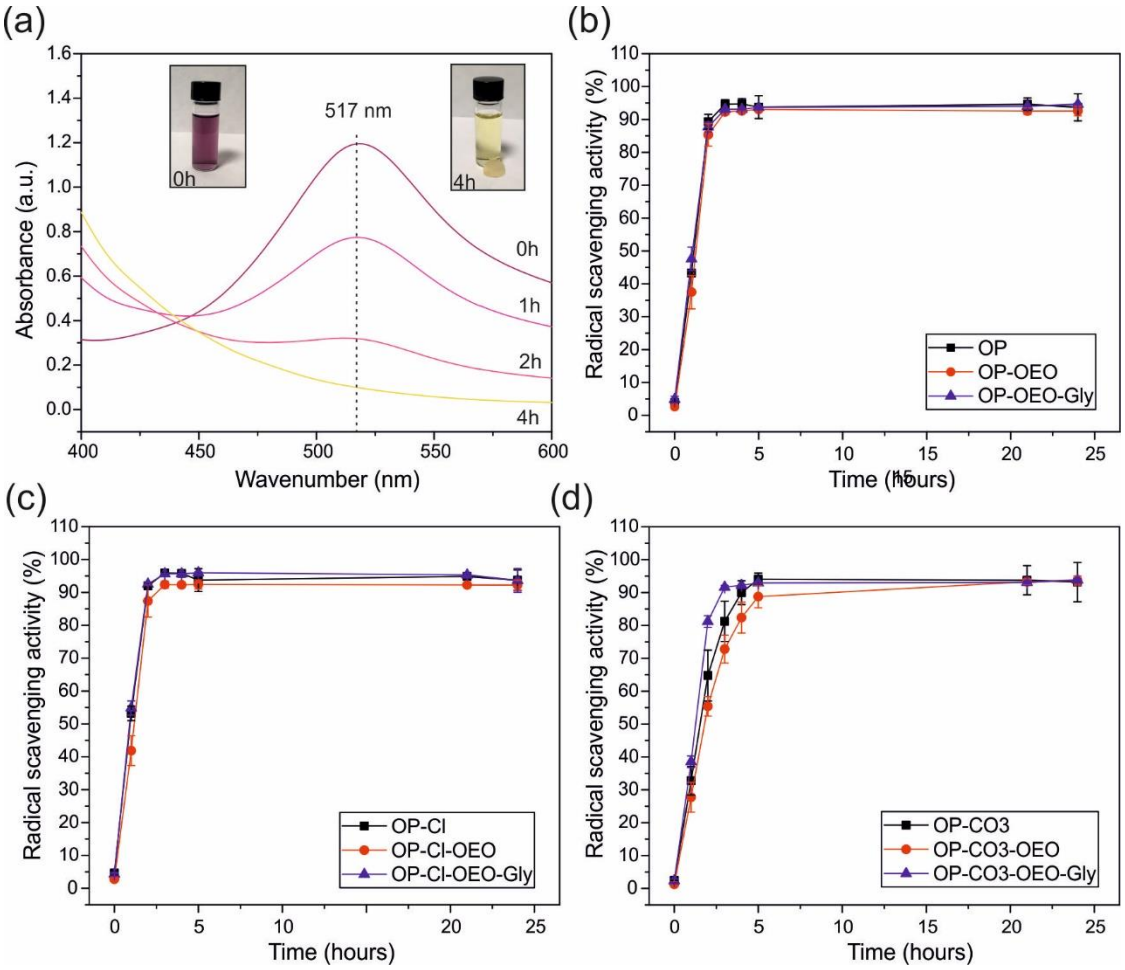

Figure 5.18 (a) UV-vis spectra of the radical reaction of DPPH˙, at point-time zero the radical solution is violet, but the inhibition of the radical shifted the coloration to yellow and the intensity of the peak was reduced over time. The radical scavenging activity profiles of **(b)** OP, OP-OEO-Gly, **(b)** OP-Cl, OP-Cl-OEO and OP-Cl-OEO-Gly and **(c)** OP-CO3, OP-CO3-OEO and OP-CO3-OEO-Gly samples, measured at every hour for 5 hours, 21 hours, and after 24 hours.

5.3.9 Preliminary coating experiments

Among the diverse coating methods, dipping is the simplest way to apply a coating on foods. Once the food product is dipped, the coating solution forms a protective layer onto the food surface Coatings may have good adhesion and dispersion to obtain a uniform layer, even on rough surfaces. The capability of the OP solutions to create uniform coatings have been evaluated by immersing glass pieces (~ 1 cm x 1 cm) at different dipping times (5s, 15s, 30s, 1 min) with no significant differences. **Figure 5.19 (a-c)** reported the real photo of a representative piece of glass for each solution: OP-OEO, OP-Cl-OEO, and OP-CO3-OEO-Gly. These samples were selected according to the barrier properties and the highest solubility to guarantee the removal. **Figure 5.19(a)** shows the lack of uniformity of the glass dipped in OP-OEO, more concentrated at the bottom part of the glass. Meanwhile, the solutions of OP-Cl-OEO and OP-CO3-OEO-Gly showed good adhesion to the glass, resulting in a homogeneous-distributed layer suitable for food coating.

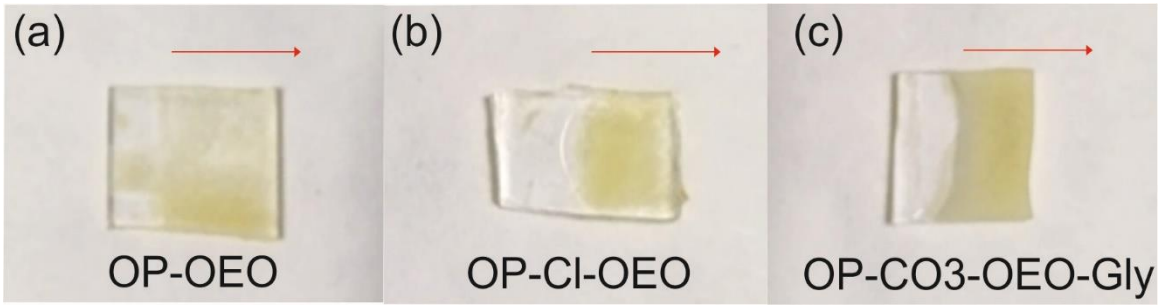

Figure 5.19 Pieces of glass (1x1 cm) dipped in **(a)** OP-OEO **(b)** OP-Cl-OEO and **(c)** OP-CO3-OEO-Gly solutions. OP-Cl-OEO and OP-CO3-OEO-Gly showed homogeneous and well-defined coatings.

Then, a dried piece of clementine-peel was dipped for 30 s in the OP solutions and left to dry. In **Figure 5.20(a-c)**, the SEM micrographs of the coated clementine peel slices are exposed. These micrographs showed that all coatings were well-dispersed onto the rough clementine-peel surface. Coatings covered all irregularities of the fruit surface, which may be a sign of promising barrier properties. The real photographs of the coated clementine after 1 hour from the immersion were inset on the top of the SEM images. The physical aspect of the clementine slices coated with OP-OEO and OP-Cl-OEO remained intact, without varying the physicochemical characteristics of the food. However, the layer of OP-CO3-OEO-Gly was easily perceived on the food surface.

Nevertheless, the photograph of the clementine peel slice after 10 days, **Figure 5.20(d-f)**, showed that part of clementine coated with OP-OEO and OP-Cl-OEO were visibly damaged. A minimum period of at least 2 weeks is required for practical purposes, allowing for packaging, transportation, etc, (Embuscado & Huber, 2009). The immersion in an acidic solution, 2.1 pH of the OP-OEO and OP-Cl-OEO solutions, against 4.5 pH of OP-CO3-OEO-Gly, may result in the breaking down of the cell-walls of the fruit via acid hydrolysis (Marshall et al., 2000). The pH of the immersion solution may coincide with the product coated, in fruits and vegetables the pH varies between 3.5 and 7, with important consequences on color and bioactive molecules preservation (Andrés-Bello et al., 2013). For example, 'Fuji' apple coated with ascorbic acid, and citric acid solutions have shown a severe softening due to the acid hydrolysis of pectin present in the fruit cell wall (Ponting et al., 1971). This result suggested OP-CO3-OEO-Gly as the best material for the coming experiment of food coating. However, further analyzes are required to optimize the experimental conditions to test the preservation properties of coatings on food.

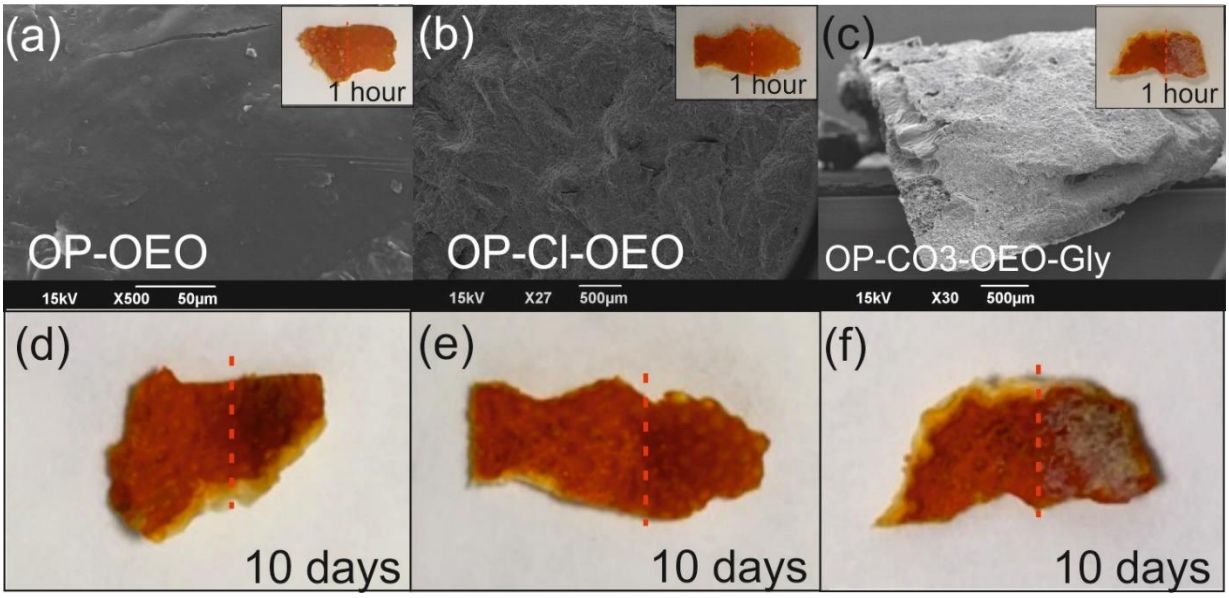

Figure 5.20 The SEM micrographs of the clementine peel coated with **(a)** OP-OEO, **(b)** OP-Cl-OEO, **(c)** OP-CO3-OEO, with the real photograph of clementine slice located inset. The photographs of clementine slice after ten days coated with **(d)** OP-OEO, **(e)** OP-Cl-OEO, **(f)** OP-CO3-OEO.

5.3.10 Inertness test

The inertness was evaluated with the overall migration value test, expressed in terms of (mg/dm^2) using Tenax®. Samples with the best features to be applied as an edible film (OP-Cl-OEO-Gly), and as an edible coating (OP-CO3-OEO-Gly) were measured and represented in **Table 5.1**. The great mechanical properties and no-significant differences in water sensitivity with respect to OP-Cl and OP-Cl-OEO suggested that OP-Cl-OEO-Gly was the best candidate to be applied as an edible film. Among OP-CO3 films, OP-CO3-OEO-Gly was the easiest water-removal and showed the lowest water vapor permeability. OP-Cl-OEO-Gly and OP-CO3-OEO-Gly obtained migration values of 28 ± 5 mg/dm^2 and 13 ± 3 mg/dm^2, respectively. Interestingly, the migration of OP-CO3-OEO-Gly films was half the OP-Cl-OEO-Gly values, probably caused by a higher degree of cross-linking of OP-CO3-OEO-Gly, which hampered the migration. These values were above the overall migration limits established by the European Commission, 10 mg/dm^2 (Silano et al., 2020). Nevertheless, these materials were formed by 100% natural compounds, and all substances can be considered innocuous for the health.

Table 5.1. Overall migration values of OP-Cl-OEO-Gly and OP-CO3-OEO-Gly measured with Tenax®.

Sample	Overall migration (mg/dm^2)
OP-Cl-OEO-Gly	28 ± 5
OP-CO3-OEO-Gly	13 ± 3

5.4 Conclusion

In the current study, materials entirely composed of a vegetable-waste matrix, orange peel, have been developed with a promising application as edible packaging materials. The modification of the arrangement of the pectin-chains inside the orange peel matrix resulted in the development of different bio-based materials with a wide spectrum of applications. Orange peel formed a homogeneous and elastic matrix with excellent antioxidant and UV-blocking properties, depending on the concentration of additives, orange essential oils, and glycerol. In future experiments, the

food preservation properties of these samples, in form of edible films and coatings, will be tested directly in foods.

Chapter 6: Conclusions

6.1 Thesis contribution

This dissertation has contributed to developing new eco-friendly biocomposites using a wide range of techniques and starting materials, with potential application as food-packaging materials, but also in other fields. Moreover, it has evidenced the excellent capability of naturally occurring derivatives to activate and improve the functionalities of bioplastics, reducing the environmental impact, and enhancing food preservation.

Transparent PECA-PPC films exhibited excellent UV-light protection properties, preserving the good optical features. Contrary to most blends loaded with natural molecules, which undergoes a loss of transparency. Finally, active films inhibited 100% of the radical ($DPPH^{\cdot}$) after 2 hours of the ethanolic-solution, indicating the promising antioxidant capacity in fatty foods.

The PVA films blended with two different agro-food wastes exhibited a broad range of properties depending on the concentration and nature of the additive. The incorporation of tea-waste extract reinforced the PVA matrix towards higher values of YM, while discard of balsamic vinegar enhanced the flexibility. In addition, the solvent used for dissolving the tealeaves and PVA reduced the crystallinity of PVA and increased the elongation. The PVA films containing extract of green tea-waste exhibited extraordinary antioxidant properties against two different radicals $ABTS^{+\cdot}$ and DPPH, independently to the content of tea waste. The oxygen barrier features of films loaded with agro-food waste were significantly improved.

Novel and versatile biocomposites (40 wt.% of cellulose and 60 wt.% of petroleum-based bioplastic) were fabricated using free-solvent and industry-scalable methods, extrusion, and hot-press. The content of the petroleum-based polymer, polycaprolactone (PCL), was reduced by incorporating an inorganic filler at high concentrations (10 and 25 wt.%), with no important variations of the polymer performance. These biocomposites were 40 times stronger and absorbed 10 times less liquid water than the neat cellulose paper. In addition, biocomposites were functionalized with two different natural derivatives: aqueous extract of pomegranate peel and curcumin, separately. Pomegranate-based samples showed excellent antioxidant properties and good migration properties in different food simulants, the aqueous food simulant, and the fatty food simulant, suggesting great bioactivity and preservation of foods against oxidation capabilities. Curcumin-based biocomposites exhibited colorimetric changes at different pH environments with a reversible response, when immersed in a buffer solution and basic vapors. Besides, biocomposite

showed a colorimetric-change after some days stored with commercial shrimps, likely to the shrimp spoilage.

Finally, novel edible bioplastics, made up of orange peel and orange essential oil, were fabricated using a water-based approach. The physicochemical properties of films significantly changed with the pH of the gelation solution of the orange peel pectin. Films treated at acidic conditions exhibited good film-forming properties and competitive mechanical properties, while samples fabricated at pH 4.5 were very rigid and opaque, but with a promising application as an edible coating. Future tests on foods may be performed to confirm this hypothesis.

6.2 List of conferences, summer schools, and publications

6.2.1 Conferences

Oral presentation: One-pot Fabrication of Antioxidant Polymeric Films based on Green Tea Waste Extracts. On behalf of the Scientific Committee of the 4th International Conference on Bioinspired and Biobased Chemistry & Materials (N.I.C.E. 2018). Nice, France. October 2018.

Poster session: One-pot Fabrication of Antioxidant Polymeric Films based on Green Tea Waste and Discarded Balsamic Vinegar. Biopol2019. 7th International Conference on Biobased and Biodegradable Polymers. Stockholm, Sweden. June 2019.

6.2.2 Summer schools

Scuola AIM Processing di Materiali Polimerici: XXXIX Convegno-Scuola “Mario Farina” 2018. Bertinoro, Italy. May 2018.

6.2.3 Papers in journals

A. I. Quilez-Molina, J. A. Heredia-Guerrero, A. Armirotti, U. C. Paul, A. Athanassiou, I. S. Bayer. **Comparison of physicochemical, mechanical and antioxidant properties of polyvinyl**

alcohol films containing green tealeaves waste extracts and discarded balsamic vinegar. *Food Packaging and Shelf Life*, 2020, vol. 23, p. 100445.
(DOI: 10.1016/j.fpsl.2019.100445).

A. I. Quilez-Molina, L. Marini, A. Athanassiou, I. S. Bayer. **UV-blocking, Transparent and Antioxidant polycyanoacrylate Films.** *Polymers,* 2020, vol. 12, p. 2011.

(DOI: 10.3390/polym12092011).

6.3 Future prospective

New emerging bioplastics blends may be developed with better economic-feasibility and more adapted to scalable manufacturing processes in order to substitute convectional petroleum-based materials. Improvements in the packaging functionalities, when natural bioactive molecules are incorporated in the polymer matrix, may lead to longer storage times, and rapid biodegradability is expected, reducing the plastic residues. Besides, using agro-food products or solid urban wastes to activate the package offers several advantages in terms of cost and sustainability. However, the tendency may move towards the utilization of the whole vegetal-biomass waste to limit the use of solvents in extractions and to reduce waste surpluses. Another interesting approach consists of using the vegetal residue as a matrix through the use of free-solvent processing like extrusion or hot pressing.

References

Ajay, S. M., Lalit, Y., Dash, M. B. S. K., & Mahanti, N. K. (2019). Application of Biodegradable Polymers in Food Packaging Industry : A Comprehensive Review. *Journal of Packaging Technology and Research*, *3*(1), 77–96. https://doi.org/10.1007/s41783-018-0049-y

Ajitha, A. R., Sabu, T., Mostafapoor, F., Khosravi, A., Fereidoon, A., Khalili, R., Jafari, S. H., Henri, V., Formela, K., & Saeb, M. (2020). *Compatibilization of Polymer Blends Micro and Nano Scale Phase Morphologies, Interphase Characterization and Properties*. Elsevier.

Al Hosni, A. S., Pittman, J. K., & Robson, G. D. (2019). Microbial degradation of four biodegradable polymers in soil and compost demonstrating polycaprolactone as an ideal compostable plastic. *Waste Management*, *97*, 105–114. https://doi.org/10.1016/j.wasman.2019.07.042

Alix, S., Mahieu, A., Terrie, C., Soulestin, J., Gerault, E., Feuilloley, M. G. J., Gattin, R., Edon, V., Ait-Younes, T., & Leblanc, N. (2013). Active pseudo-multilayered films from polycaprolactone and starch based matrix for food-packaging applications. *European Polymer Journal*, *49*(6), 1234–1242. https://doi.org/10.1016/j.eurpolymj.2013.03.016

Almasi, H., Azizi, S., & Amjadi, S. (2020). Development and characterization of pectin films activated by nanoemulsion and Pickering emulsion stabilized marjoram (Origanum majorana L.) essential oil. *Food Hydrocolloids*, *99*(June 2019), 105338. https://doi.org/10.1016/j.foodhyd.2019.105338

Alparslan, Y., & Baygar, T. (2017). Effect of Chitosan Film Coating Combined with Orange Peel Essential Oil on the Shelf Life of Deepwater Pink Shrimp. *Food and Bioprocess Technology*, *10*(5), 842–853. https://doi.org/10.1007/s11947-017-1862-y

Andrés-Bello, A., Barreto-Palacios, V., García-Segovia, P., Mir-Bel, J., & Martínez-Monzó, J. (2013). Effect of pH on Color and Texture of Food Products. *Food Engineering Reviews*, *5*(3), 158–170. https://doi.org/10.1007/s12393-013-9067-2

Armentano, I., Fortunati, E., Burgos, N., Dominici, F., Luzi, F., Fiori, S., Jiménez, A., Yoon, K., Ahn, J., Kang, S., & Kenny, J. M. (2015). Processing and characterization of plasticized

PLA/PHB blends for biodegradable multiphase systems. *Express Polymer Letters*, *9*(7), 583–596. https://doi.org/10.3144/expresspolymlett.2015.55

Arrieta, M. P., Samper, M. D., Aldas, M., & López, J. (2017). On the use of PLA-PHB blends for sustainable food packaging applications. *Materials*, *10*(9), 1–26. https://doi.org/10.3390/ma10091008

Arrua, D., Strumia, M. C., & Nazareno, M. A. (2010). Immobilization of caffeic acid on a polypropylene film: Synthesis and antioxidant properties. *Journal of Agricultural and Food Chemistry*, *58*(16), 9228–9234. https://doi.org/10.1021/jf101651y

Arvanitoyannis, I. S., Bouletis, A. D., Papa, E. A., Gkagtzis, D. C., Hadjichristodoulou, C., & Papaloucas, C. (2011). The effect of addition of olive oil and " Aceto balsamico di Modena" wine vinegar in conjunction with active atmosphere packaging on the microbial and sensory quality of " Lollo Verde" lettuce and rocket salad. *Anaerobe*, *17*(6), 303–306. https://doi.org/10.1016/j.anaerobe.2011.04.010

Asgari, A., Hemmasi, A., Bazyar, B., Talaeipour, M., & Nourbakhsh, A. (2020). Inspecting the properties of polypropylene/ poplar wood flour composites with microcrystalline cellulose and starch powder addition. *BioResources*, *15*(2), 4188–4204. https://doi.org/10.15376/biores.15.2.4188-4204

Assifaoui, A., Loupiac, C., Chambin, O., & Cayot, P. (2010). Structure of calcium and zinc pectinate films investigated by FTIR spectroscopy. *Carbohydrate Research*, *345*(7), 929–933. https://doi.org/10.1016/j.carres.2010.02.015

Bagchi, D., Chaudhuri, S., Sardar, S., Choudhury, S., Polley, N., Lemmens, P., & Pal, S. K. (2015). Modulation of stability and functionality of a phyto-antioxidant by weakly interacting metal ions: Curcumin in aqueous solution. *RSC Advances*, *5*(124), 102516–102524. https://doi.org/10.1039/c5ra21593e

Bastarrachea, L., Dhawan, S., & Sablani, S. S. (2011). Engineering Properties of Polymeric-Based Antimicrobial Films for Food Packaging. *Food Engineering Reviews*, *3*(2), 79–93. https://doi.org/10.1007/s12393-011-9034-8

Battisti, R., Fronza, N., Vargas Júnior, Á., Silveira, S. M. da, Damas, M. S. P., & Quadri, M. G.

N. (2017). Gelatin-coated paper with antimicrobial and antioxidant effect for beef packaging. *Food Packaging and Shelf Life*, *11*, 115–124. https://doi.org/10.1016/j.fpsl.2017.01.009

Bayer, I. S., Guzman-Puyol, S., Heredia-Guerrero, J. A., Ceseracciu, L., Pignatelli, F., Ruffilli, R., Cingolani, R., & Athanassiou, A. (2014). Direct transformation of edible vegetable waste into bioplastics. *Macromolecules*, *47*(15), 5135–5143. https://doi.org/10.1021/ma5008557

Belay, A., Libnedengel, E., Kim, H. K., & Hwang, Y. H. (2016). Effects of solvent polarity on the absorption and fluorescence spectra of chlorogenic acid and caffeic acid compounds: Determination of the dipole moments. *Luminescence*, *31*(1), 118–126. https://doi.org/10.1002/bio.2932

Bellamy, L. (2013). *The infra-red spectra of complex molecules*. Springer Science & Business Media.

Benbettaieb, N., Nyagaya, J., Seuvre, A. M., & Debeaufort, F. (2018). Antioxidant Activity and Release Kinetics of Caffeic and p-Coumaric Acids from Hydrocolloid-Based Active Films for Healthy Packaged Food. *Journal of Agricultural and Food Chemistry*, *66*(26), 6906–6916. https://doi.org/10.1021/acs.jafc.8b01846

Biao, L., Tan, S., Meng, Q., Gao, J., Zhang, X., Liu, Z., & Fu, Y. (2018). Green synthesis, characterization and application of proanthocyanidins-functionalized gold nanoparticles. *Nanomaterials*, *8*(1). https://doi.org/10.3390/nano8010053

Bocco, A., Cuvelier, M. E., Richard, H., & Berset, C. (1998). Antioxidant Activity and Phenolic Composition of Citrus Peel and Seed Extracts. *Journal of Agricultural and Food Chemistry*, *46*(6), 2123–2129. https://doi.org/10.1021/jf9709562

Bonilla, J., & Sobral, P. J. A. (2016). Investigation of the physicochemical, antimicrobial and antioxidant properties of gelatin-chitosan edible film mixed with plant ethanolic extracts. *Food Bioscience*, *16*, 17–25. https://doi.org/10.1016/j.fbio.2016.07.003

Borah, P. P., Das, P., & Badwaik, L. S. (2017). Ultrasound treated potato peel and sweet lime pomace based biopolymer film development. *Ultrasonics Sonochemistry*, *36*, 11–19.

https://doi.org/10.1016/j.ultsonch.2016.11.010

Boudria, A., Hammoui, Y., Adjeroud, N., Djerrada, N., & Madani, K. (2018). Effect of filler load and high-energy ball milling process on properties of plasticized wheat gluten/olive pomace biocomposite. *Advanced Powder Technology*, *29*(5), 1230–1238. https://doi.org/10.1016/j.apt.2018.02.015

Burri, S. C. M., Ekholm, A., Bleive, U., Püssa, T., Jensen, M., Hellström, J., Mäkinen, S., Korpinen, R., Mattila, P. H., Radenkovs, V., Segliņa, D., Håkansson, Å., Rumpunen, K., & Tornberg, E. (2020). Lipid oxidation inhibition capacity of plant extracts and powders in a processed meat model system. *Meat Science*, *162*(December 2019). https://doi.org/10.1016/j.meatsci.2019.108033

Cataldi, P., Heredia-Guerrero, J. A., Guzman-Puyol, S., Ceseracciu, L., La Notte, L., Reale, A., Ren, J., Zhang, Y., Liu, L., Miscuglio, M., Savi, P., Piazza, S., Duocastella, M., Perotto, G., Athanassiou, A., & Bayer, I. S. (2018). Sustainable Electronics Based on Crop Plant Extracts and Graphene: A "Bioadvantaged" Approach. *Advanced Sustainable Systems*, *2*(11), 1800069. https://doi.org/10.1002/adsu.201800069

Caz, P. (2017). *Food Hydrocolloids Polysaccharide-based fi lms and coatings for food packaging : A review*. *68*, 136–148. https://doi.org/10.1016/j.foodhyd.2016.09.009

Celus, M., Kyomugasho, C., Van Loey, A. M., Grauwet, T., & Hendrickx, M. E. (2018). Influence of Pectin Structural Properties on Interactions with Divalent Cations and Its Associated Functionalities. *Comprehensive Reviews in Food Science and Food Safety*, *17*(6), 1576–1594. https://doi.org/10.1111/1541-4337.12394

Cesur, S., Köroğlu, C., & Yalçın, H. T. (2018). Antimicrobial and biodegradable food packaging applications of polycaprolactone/organo nanoclay/chitosan polymeric composite films. *Journal of Vinyl and Additive Technology*, *24*(4), 376–387. https://doi.org/10.1002/vnl.21607

Chandran, M., Tamilkolundu, S., & Murugesan, C. (2020). Conversion of plastic waste to fuel. In *Plastic Waste and Recycling* (Issue January). https://doi.org/10.1016/b978-0-12-817880-5.00014-1

Chen, H. zhi, Zhang, M., Bhandari, B., & Yang, C. hui. (2020). Novel pH-sensitive films containing curcumin and anthocyanins to monitor fish freshness. *Food Hydrocolloids*, *100*(October 2019), 105438. https://doi.org/10.1016/j.foodhyd.2019.105438

Chen, Y. N., Jiao, C., Zhao, Y., Zhang, J., & Wang, H. (2018). Self-Assembled Polyvinyl Alcohol-Tannic Acid Hydrogels with Diverse Microstructures and Good Mechanical Properties [Research-article]. *ACS Omega*, *3*(9), 11788–11795. https://doi.org/10.1021/acsomega.8b02041

Choi, S. B., Kim, N. W., Lee, D. K., & Yu, H. (2013). Growth mechanism of cubic MgO granule via common ion effect. *Journal of Nanoscience and Nanotechnology*, *13*(11), 7577–7580. https://doi.org/10.1166/jnn.2013.7882

Ciolacu, D., Oprea, A. M., Anghel, N., Cazacu, G., & Cazacu, M. (2012). New cellulose–lignin hydrogels and their application in controlled release of polyphenols. *Materials Science and Engineering: C*, *32*(3), 452–463.

Collazo-Bigliardi, S., Ortega-Toro, R., & Chiralt, A. (2019). Improving properties of thermoplastic starch films by incorporating active extracts and cellulose fibres isolated from rice or coffee husk. *Food Packaging and Shelf Life*, *22*(November 2018). https://doi.org/10.1016/j.fpsl.2019.100383

Confente, I., Scarpi, D., & Russo, I. (2020). Marketing a new generation of bio-plastics products for a circular economy : The role of green self-identity , self-congruity , and perceived value. *Journal of Business Research*, *112*(June 2019), 431–439. https://doi.org/10.1016/j.jbusres.2019.10.030

Contardi, M., Heredia-Guerrero, J. A., Perotto, G., Valentini, P., Pompa, P. P., Spanò, R., Goldoni, L., Bertorelli, R., Athanassiou, A., & Bayer, I. S. (2017). Transparent ciprofloxacin-povidone antibiotic films and nanofiber mats as potential skin and wound care dressings. *European Journal of Pharmaceutical Sciences*, *104*(March), 133–144. https://doi.org/10.1016/j.ejps.2017.03.044

Corre, Y. M., Bruzaud, S., & Grohens, Y. (2013). Poly(3-hydroxybutyrate-co-3-hydroxyvalerate) and poly(propylene carbonate) blends: An efficient method to finely adjust properties of

functional materials. *Macromolecular Materials and Engineering*, *298*(11), 1176–1183. https://doi.org/10.1002/mame.201200345

da Costa, L. M., Tronto, J., Constantino, V. R. L., Almeida Fonseca, M. K., Oliveira, A. P., & da Costa, M. R. (2009). Extraction and concentration of biogenic calcium oxalate from plant leaves. *Revista Brasileira de Ciencia Do Solo*, *33*(3), 729–733. https://doi.org/10.1590/s0100-06832009000300025

Dai, H., Ou, S., Huang, Y., & Huang, H. (2018). Utilization of pineapple peel for production of nanocellulose and film application. *Cellulose*, *25*(3), 1743–1756. https://doi.org/10.1007/s10570-018-1671-0

Das, S. (2017). Mechanical properties of waste paper/jute fabric reinforced polyester resin matrix hybrid composites. *Carbohydrate Polymers*, *172*, 60–67. https://doi.org/10.1016/j.carbpol.2017.05.036

Daudt, R. M., Avena-Bustillos, R. J., Williams, T., Wood, D. F., Külkamp-Guerreiro, I. C., Marczak, L. D. F., & McHugh, T. H. (2016). Comparative study on properties of edible films based on pinhão (Araucaria angustifolia) starch and flour. *Food Hydrocolloids*, *60*, 279–287. https://doi.org/10.1016/j.foodhyd.2016.03.040

De Azeredo, H. M. C., Rosa, M. F., De Sá, M., Souza Filho, M., & Waldron, K. (2014). The use of biomass for packaging films and coatings. In *Advances in Biorefineries: Biomass and Waste Supply Chain Exploitation*. https://doi.org/10.1533/9780857097385.2.819

de Moraes Crizel, T., de Oliveira Rios, A., D. Alves, V., Bandarra, N., Moldão-Martins, M., & Hickmann Flôres, S. (2018). Active food packaging prepared with chitosan and olive pomace. *Food Hydrocolloids*, *74*, 139–150. https://doi.org/10.1016/j.foodhyd.2017.08.007

de Moraes Crizel, T., Haas Costa, T. M., de Oliveira Rios, A., & Hickmann Flôres, S. (2016). Valorization of food-grade industrial waste in the obtaining active biodegradable films for packaging. *Industrial Crops and Products*, *87*, 218–228. https://doi.org/10.1016/j.indcrop.2016.04.039

Del Nobile, M. A., & Conte, A. (2013). *Packaging for food preservation*. Springer.

Dilucia, F., Lacivita, V., Conte, A., & Nobile, M. A. Del. (2020). *Enhance Food Packaging*

Performance. https://doi.org/10.3390/foods9070857

Dou, L., Li, B., Zhang, K., Chu, X., & Hou, H. (2018). Physical properties and antioxidant activity of gelatin-sodium alginate edible films with tea polyphenols. *International Journal of Biological Macromolecules*, *118*, 1377–1383. https://doi.org/10.1016/j.ijbiomac.2018.06.121

Du, W. X., Olsen, C. W., Avena-Bustillos, R. J., McHugh, T. H., Levin, C. E., & Friedman, M. (2009). Effects of allspice, cinnamon, and clove bud essential oils in edible apple films on physical properties and antimicrobial activities. *Journal of Food Science*, *74*(7). https://doi.org/10.1111/j.1750-3841.2009.01282.x

Dutta, N., & Maji, T. K. (2020). Synergic effect of montmorillonite and microcrystalline cellulose on the physicochemical properties of rice husk/PVC composite. *SN Applied Sciences*, *2*(3), 1–10. https://doi.org/10.1007/s42452-020-2255-9

Eça, K. S., Machado, M. T. C., Hubinger, M. D., & Menegalli, F. C. (2015). Development of Active Films From Pectin and Fruit Extracts: Light Protection, Antioxidant Capacity, and Compounds Stability. *Journal of Food Science*, *80*(11), C2389–C2396. https://doi.org/10.1111/1750-3841.13074

Embuscado, M. E., & Huber, K. C. (2009). Edible Films and Coatings for Food Applications. In *Edible Films and Coatings for Food Applications* (Issue September 2015). https://doi.org/10.1007/978-0-387-92824-1

Erba, R. D., Groeninckx, G., Maglio, G., Malinconico, M., Erba, R. D., Groeninckx, G., Maglio, G., Malinconico, M., & Im-, A. M. (2019). *Immiscible polymer blends of semicrystalline biocompatible components : thermal properties and phase morphology analysis of PLLA / PCL blends To cite this version : HAL Id : hal-01998591 Italian National Agency for New Technologies , Energy and Sustainabl*.

Esparza, I., Jim, N., Bimbela, F., Ancín-azpilicueta, C., & Gandía, L. M. (2020). *Fruit and vegetable waste management : Conventional and emerging approaches*. *265*(April). https://doi.org/10.1016/j.jenvman.2020.110510

Ezati, P., Tajik, H., Moradi, M., & Molaei, R. (2019). Intelligent pH-sensitive indicator based on

starch-cellulose and alizarin dye to track freshness of rainbow trout fillet. *International Journal of Biological Macromolecules*, *132*, 157–165. https://doi.org/10.1016/j.ijbiomac.2019.03.173

Fei, B., Chen, C., Peng, S., Zhao, X., Wang, X., & Dong, L. (2004). FTIR study of poly(propylene carbonate)/bisphenol A blends. *Polymer International*, *53*(12), 2092–2098. https://doi.org/10.1002/pi.1633

Figueroa-Lopez, K. J., Castro-Mayorga, J. L., Andrade-Mahecha, M. M., Cabedo, L., & Lagaron, J. M. (2018). Antibacterial and barrier properties of gelatin coated by electrospun polycaprolactone ultrathin fibers containing black pepper oleoresin of interest in active food biopackaging applications. *Nanomaterials*, *8*(4). https://doi.org/10.3390/nano8040199

Formela, K., Zedler, Hejna, A., & Tercjak, A. (2018). Reactive extrusion of bio-based polymer blends and composites–current trends and future developments. *Express Polymer Letters*, *12*(1), 24–57. https://doi.org/10.3144/expresspolymlett.2018.4

Fortunati, E., Peltzer, M., Armentano, I., Jiménez, A., & Kenny, J. M. (2013). Combined effects of cellulose nanocrystals and silver nanoparticles on the barrier and migration properties of PLA nano-biocomposites. *Journal of Food Engineering*, *118*(1), 117–124. https://doi.org/10.1016/j.jfoodeng.2013.03.025

Francis, B. R., Watkins, K., & Kubelka, J. (2017). Double hydrogen bonding between side chain carboxyl groups in aqueous solutions of poly (β-L-malic acid): Implication for the evolutionary origin of nucleic acids. *Life*, *7*(3). https://doi.org/10.3390/life7030035

Gaikwad, K. K., Lee, J. Y., & Lee, Y. S. (2016). Development of polyvinyl alcohol and apple pomace bio-composite film with antioxidant properties for active food packaging application. *Journal of Food Science and Technology*, *53*(3), 1608–1619. https://doi.org/10.1007/s13197-015-2104-9

Gaikwad, K. K., Singh, S., & Ajji, A. (2019). Moisture absorbers for food packaging applications. *Environmental Chemistry Letters*, *17*(2), 609–628. https://doi.org/10.1007/s10311-018-0810-z

Gällstedt, B. M., Brottman, A., & Hedenqvist, M. S. (2005). *Packaging-related Properties of*

Protein- and Chitosan-coated Paper and Science. *April*, 161–170.

Gamonpilas, C., Krongsin, J., Methacanon, P., & Goh, S. M. (2015). Gelation of pomelo (Citrus maxima) pectin as induced by divalent ions or acidification. *Journal of Food Engineering*, *152*, 17–23. https://doi.org/10.1016/j.jfoodeng.2014.11.024

Garcia, A. C., Vavrusova, M., & Skibsted, L. H. (2018). Supersaturation of calcium citrate as a mechanism behind enhanced availability of calcium phosphates by presence of citrate. *Food Research International*, *107*(February), 195–205. https://doi.org/10.1016/j.foodres.2018.02.020

Gawkowska, D., Cybulska, J., & Zdunek, A. (2018). Structure-related gelling of pectins and linking with other natural compounds: A review. *Polymers*, *10*(7). https://doi.org/10.3390/polym10070762

Ge, M., Zhao, H., Wang, W., Zhang, Z., Yu, X., & Li, W. (2006). Terahertz time-domain spectroscopy of four hydroxycinnamic acid derivatives. *Journal of Biological Physics*, *32*(5), 403–412. https://doi.org/10.1007/s10867-006-9024-x

Ghasemi, K., Ghasemi, Y., & Ebrahimzadeh, M. A. (2009). Antioxidant activity, phenol and flavonoid contents of 13 citrus species peels and tissues. *Pakistan Journal of Pharmaceutical Sciences*, *22*(3), 277–281.

Gramza, A., Kokczak, J., & Amarowicz, R. (2005). Tea polyphenols - their antioxidant properties and biological activity - : A review. *Polish Journal of Food and Nutrition Sciences*, *14*(3), 219–235.

Güzel, M., & Akpınar, Ö. (2019). Valorisation of fruit by-products: Production characterization of pectins from fruit peels. *Food and Bioproducts Processing*, *115*, 126–133. https://doi.org/10.1016/j.fbp.2019.03.009

Guzman-Puyol, S., Ceseracciu, L., Heredia-Guerrero, J. A., Anyfantis, G. C., Cingolani, R., Athanassiou, A., & Bayer, I. S. (2015). Effect of trifluoroacetic acid on the properties of polyvinyl alcohol and polyvinyl alcohol-cellulose composites. *Chemical Engineering Journal*, *277*, 242–251. https://doi.org/10.1016/j.cej.2015.04.092

Guzman-Puyol, S., Russo, D., Penna, I., Ceseracciu, L., Palazon, F., Scarpellini, A., Cingolani,

R., Bertorelli, R., Bayer, I. S., Heredia-Guerrero, J. A., & Athanassiou, A. (2017). Facile production of seaweed-based biomaterials with antioxidant and anti-inflammatory activities. *Algal Research*, *27*(August), 1–11. https://doi.org/10.1016/j.algal.2017.08.015

Halász, K., & Csóka, L. (2018). Black chokeberry (Aronia melanocarpa) pomace extract immobilized in chitosan for colorimetric pH indicator film application. *Food Packaging and Shelf Life*, *16*(March), 185–193. https://doi.org/10.1016/j.fpsl.2018.03.002

Han, W., Meng, Y., Hu, C., Dong, G., Qu, Y., Deng, H., & Guo, Y. (2017). Mathematical model of Ca2+ concentration, pH, pectin concentration and soluble solids (sucrose) on the gelation of low methoxyl pectin. *Food Hydrocolloids*, *66*(January), 37–48. https://doi.org/10.1016/j.foodhyd.2016.12.011

Hassan, C. M., & Peppas, N. A. (2000). Structure and applications of poly(vinyl alcohol) hydrogels produced by conventional crosslinking or by freezing/thawing methods. *Advances in Polymer Science*, *153*, 37–65. https://doi.org/10.1007/3-540-46414-x_2

He, L., Lan, W., Ahmed, S., Qin, W., & Liu, Y. (2019). Electrospun polyvinyl alcohol film containing pomegranate peel extract and sodium dehydroacetate for use as food packaging. *Food Packaging and Shelf Life*, *22*(August). https://doi.org/10.1016/j.fpsl.2019.100390

Ho, C. W., Lazim, A. M., Fazry, S., Zaki, U. K. H. H., & Lim, S. J. (2017). Varieties, production, composition and health benefits of vinegars: A review. *Food Chemistry*, *221*, 1621–1630. https://doi.org/10.1016/j.foodchem.2016.10.128

Hollingbery, L. A., & Hull, T. R. (2012). The thermal decomposition of natural mixtures of huntite and hydromagnesite. *Thermochimica Acta*, *528*, 45–52. https://doi.org/10.1016/j.tca.2011.11.002

Hornsby, P. R. (1994). The application of magnesium hydroxide as a fire retardant and smoke-suppressing additive for polymers. *Fire and Materials*, *18*(5), 269–276.

Hornsby, P. R. (1996). The application of hydrated mineral fillers as fire retardant and smoke suppressing additives for polymers. *Macromolecular Symposia*, *108*(1), 203–219.

Ilyas, R. A., Sapuan, S. M., Ishak, M. R., & Zainudin, E. S. (2018). Development and characterization of sugar palm nanocrystalline cellulose reinforced sugar palm starch

bionanocomposites. *Carbohydrate Polymers*, *202*(September), 186–202. https://doi.org/10.1016/j.carbpol.2018.09.002

Irache, J. M., Esparza, I., Gamazo, C., Agüeros, M., & Espuelas, S. (2011). Nanomedicine: Novel approaches in human and veterinary therapeutics. *Veterinary Parasitology*, *180*(1–2), 47–71. https://doi.org/10.1016/j.vetpar.2011.05.028

Ishak, W. H. W., Ahmad, I., Ramli, S., & Amin, M. C. I. M. (2018). Gamma irradiation-assisted synthesis of cellulose nanocrystal-reinforced gelatin hydrogels. *Nanomaterials*, *8*(10), 1–13. https://doi.org/10.3390/nano8100749

Jiang, L., Zhang, J., & Wolcott, M. P. (2007). Comparison of polylactide/nano-sized calcium carbonate and polylactide/montmorillonite composites: Reinforcing effects and toughening mechanisms. *Polymer*, *48*(26), 7632–7644. https://doi.org/10.1016/j.polymer.2007.11.001

Jing, X., Mi, H. Y., & Turng, L. S. (2017). Comparison between PCL/hydroxyapatite (HA) and PCL/halloysite nanotube (HNT) composite scaffolds prepared by co-extrusion and gas foaming. *Materials Science and Engineering C*, *72*, 53–61. https://doi.org/10.1016/j.msec.2016.11.049

Jirukkakul, N. (2016). The study of edible film production from unriped banana flour and riped banana puree. *International Food Research Journal*, *23*(1), 95–101.

Johnson, D. R., & Decker, E. A. (2015). The Role of Oxygen in Lipid Oxidation Reactions: A Review. *Annual Review of Food Science and Technology*, *6*(1), 171–190. https://doi.org/10.1146/annurev-food-022814-015532

Kargarzadeh, H., Johar, N., & Ahmad, I. (2017). Starch biocomposite film reinforced by multiscale rice husk fiber. *Composites Science and Technology*, *151*(September), 147–155. https://doi.org/10.1016/j.compscitech.2017.08.018

Kaya, M., Ravikumar, P., Ilk, S., Mujtaba, M., Akyuz, L., Labidi, J., Salaberria, A. M., Cakmak, Y. S., & Erkul, S. K. (2018). Production and characterization of chitosan based edible films from Berberis crataegina's fruit extract and seed oil. *Innovative Food Science and Emerging Technologies*, *45*(April 2017), 287–297. https://doi.org/10.1016/j.ifset.2017.11.013

Khalid, S., Yu, L., Feng, M., Meng, L., Bai, Y., Ali, A., Liu, H., & Chen, L. (2018).

Development and characterization of biodegradable antimicrobial packaging films based on polycaprolactone, starch and pomegranate rind hybrids. *Food Packaging and Shelf Life*, *18*(August), 71–79. https://doi.org/10.1016/j.fpsl.2018.08.008

Khan, B., Bilal Khan Niazi, M., Samin, G., & Jahan, Z. (2017). Thermoplastic Starch: A Possible Biodegradable Food Packaging Material—A Review. *Journal of Food Process Engineering*, *40*(3). https://doi.org/10.1111/jfpe.12447

Khan, S. S., Iqbal, M. A., Malik, A., & Abdul, S. (2016). Effect of crystallization of caffeic acid enhanced stability and dual biological efficacy. *Cogent Biology*, *4*, 1–8. https://doi.org/10.1080/23312025.2016.1243460

Khwaldia, K. (2013). HPMC coating for paper. *BioResources*, *8*(3), 3438–3452.

Kim, H. S., Kim, H. J., Lee, J. W., & Choi, I. G. (2006). Biodegradability of bio-flour filled biodegradable poly(butylene succinate) bio-composites in natural and compost soil. *Polymer Degradation and Stability*, *91*(5), 1117–1127. https://doi.org/10.1016/j.polymdegradstab.2005.07.002

Kim, S., Evans, K., & Biswas, A. (2013). Colloids and Surfaces B : Biointerfaces Production of BSA-poly (ethyl cyanoacrylate) nanoparticles as a coating material that improves wetting property. *Colloids and Surfaces B: Biointerfaces*, *107*, 68–75. https://doi.org/10.1016/j.colsurfb.2013.01.064

Kirwan, M., Brown, H., & Williams, J. (2011). Packaged Product Quality and Shelf Life. *Food and Beverage Packaging Technology: Second Edition*, *1993*, 59–83. https://doi.org/10.1002/9781444392180.ch3

Kumar, R., & Nayak, S. K. (2020). Fabrication of high thermal conductive epoxy composite by adding hybrid of expanded graphite, iron (III) oxide, and silver flakes. *Journal of Materials Science: Materials in Electronics*, *31*(18), 16008–16019. https://doi.org/10.1007/s10854-020-04163-3

Kurek, M., Hlupić, L., Elez Garofulić, I., Descours, E., Ščetar, M., & Galić, K. (2019). Comparison of protective supports and antioxidative capacity of two bio-based films with revalorised fruit pomaces extracted from blueberry and red grape skin. *Food Packaging and*

Shelf Life, *20*(October 2018). https://doi.org/10.1016/j.fpsl.2019.100315

Kuswandi, B., Jayus, Larasati, T. S., Abdullah, A., & Heng, L. Y. (2012). Real-Time Monitoring of Shrimp Spoilage Using On-Package Sticker Sensor Based on Natural Dye of Curcumin. *Food Analytical Methods*, *5*(4), 881–889. https://doi.org/10.1007/s12161-011-9326-x

Lara-Espinoza, C., Carvajal-Millán, E., Balandrán-Quintana, R., López-Franco, Y., & Rascón-Chu, A. (2018). Pectin and pectin-based composite materials: Beyond food texture. *Molecules*, *23*(4). https://doi.org/10.3390/molecules23040942

Lee, J. H., & Yeo, Y. (2015). Controlled drug release from pharmaceutical nanocarriers. *Chemical Engineering Science*, *125*, 75–84. https://doi.org/10.1016/j.ces.2014.08.046

Lee, L. S., Kim, S. H., Kim, Y. B., & Kim, Y. C. (2014). Quantitative analysis of major constituents in green tea with different plucking periods and their antioxidant activity. *Molecules*, *19*(7), 9173–9186. https://doi.org/10.3390/molecules19079173

Lee, W.-H., Loo, C.-Y., Bebawy, M., Luk, F., Mason, R., & Rohanizadeh, R. (2013). Curcumin and its Derivatives: Their Application in Neuropharmacology and Neuroscience in the 21st Century. *Current Neuropharmacology*, *11*(4), 338–378. https://doi.org/10.2174/1570159x11311040002

Liang, J. Z., Zhou, L., Tang, C. Y., & Tsui, C. P. (2013). Crystallization properties of polycaprolactone composites filled with nanometer calcium carbonate. *Journal of Applied Polymer Science*, *128*(5), 2940–2944. https://doi.org/10.1002/app.38359

Licciardello, F., Kharchoufi, S., Muratore, G., & Restuccia, C. (2018). Effect of edible coating combined with pomegranate peel extract on the quality maintenance of white shrimps (Parapenaeus longirostris) during refrigerated storage. *Food Packaging and Shelf Life*, *17*(May), 114–119. https://doi.org/10.1016/j.fpsl.2018.06.009

Liu, J., Wang, H., Guo, M., Li, L., Chen, M., Jiang, S., Li, X., & Jiang, S. (2019). Extract from Lycium ruthenicum Murr. Incorporating κ-carrageenan colorimetric film with a wide pH–sensing range for food freshness monitoring. *Food Hydrocolloids*, *94*(February), 1–10. https://doi.org/10.1016/j.foodhyd.2019.03.008

Liu, J., Wang, H., Wang, P., Guo, M., Jiang, S., Li, X., & Jiang, S. (2018). Films based on κ-

carrageenan incorporated with curcumin for freshness monitoring. *Food Hydrocolloids*, *83*, 134–142. https://doi.org/10.1016/j.foodhyd.2018.05.012

Liu, R., & Mabury, S. A. (2020). *Synthetic Phenolic Antioxidants : A Review of Environmental Occurrence , Fate , Human Exposure , and Toxicity*. https://doi.org/10.1021/acs.est.0c05077

Liu, X., Wang, T., Chow, L. C., Yang, M., & Mitchell, J. W. (2014). Effects of inorganic fillers on the thermal and mechanical properties of poly(lactic acid). *International Journal of Polymer Science*, *2014*. https://doi.org/10.1155/2014/827028

Liu, Y., Wang, S., Lan, W., & Qin, W. (2019). Development of ultrasound treated polyvinyl alcohol/tea polyphenol composite films and their physicochemical properties. *Ultrasonics Sonochemistry*, *51*(July 2018), 386–394. https://doi.org/10.1016/j.ultsonch.2018.07.043

Lopes, J. F. A., & Simoneau, C. (2017). Solubility of Polyvinyl Alcohol in Ethanol. *EFSA Supporting Publications*, *11*(9), 1–20. https://doi.org/10.2903/sp.efsa.2014.en-660

López-De-Dicastillo, C., Alonso, J. M., Catalá, R., Gavara, R., & Hernández-Munoz, P. (2010). Improving the antioxidant protection of packaged food by incorporating natural flavonoids into ethylene-vinyl alcohol copolymer (EVOH) films. *Journal of Agricultural and Food Chemistry*, *58*(20), 10958–10964. https://doi.org/10.1021/jf1022324

Lozano-Navarro, J. I., Díaz-Zavala, N. P., Velasco-Santos, C., Martínez-Hernández, A. L., Tijerina-Ramos, B. I., García-Hernández, M., Rivera-Armenta, J. L., Páramo-García, U., & Reyes-de la Torre, A. I. (2017). Antimicrobial, optical and mechanical properties of Chitosan–Starch films with natural extracts. *International Journal of Molecular Sciences*, *18*(5), 1–18. https://doi.org/10.3390/ijms18050997

Luinstra, G. A., & Borchardt, E. (2012). *Material Properties of Poly (Propylene Carbonates). June 2011*, 29–48. https://doi.org/10.1007/12

Ma, Q., Ren, Y., & Wang, L. (2017). Investigation of antioxidant activity and release kinetics of curcumin from tara gum/ polyvinyl alcohol active film. *Food Hydrocolloids*, *70*, 286–292. https://doi.org/10.1016/j.foodhyd.2017.04.018

Mankidy, P. J., Rajagopalan, R., & Foley, H. C. (2008). *Influence of initiators on the growth of poly (ethyl 2-cyanoacrylate) nanofibers*. *49*, 2235–2242.

https://doi.org/10.1016/j.polymer.2008.03.018

Manrique, G. D., & Lajolo, F. M. (2002). FT-IR spectroscopy as a tool for measuring degree of methyl esterification in pectins isolated from ripening papaya fruit. *Postharvest Biology and Technology*, *25*(1), 99–107. https://doi.org/10.1016/S0925-5214(01)00160-0

Maraveas, C. (2020). Environmental sustainability of plastic in agriculture. *Agriculture (Switzerland)*, *10*(8), 1–15. https://doi.org/10.3390/agriculture10080310

Marshall, M. R., Kim, J., & Wei, C. (2000). Enzymatic browning in fruits, vegetables and seafoods. *Food and Agricultural Organisation*, *41*, 259–312. http://www.fao.org/ag/Ags/agsi/ENZYMEFINAL/Enzymatic Browning.html

Martelli, S. M., Motta, C., Caon, T., Alberton, J., Bellettini, I. C., do Prado, A. C. P., Barreto, P. L. M., & Soldi, V. (2017). Edible carboxymethyl cellulose films containing natural antioxidant and surfactants: α-tocopherol stability, in vitro release and film properties. *LWT - Food Science and Technology*, *77*, 21–29. https://doi.org/10.1016/j.lwt.2016.11.026

Martín-Diana, A. B., Rico, D., Frías, J. M., Barat, J. M., Henehan, G. T. M., & Barry-Ryan, C. (2007). Calcium for extending the shelf life of fresh whole and minimally processed fruits and vegetables: a review. *Trends in Food Science and Technology*, *18*(4), 210–218. https://doi.org/10.1016/j.tifs.2006.11.027

Martin, O., Schwach, E., Avérous, L., & Couturier, Y. (2001). Properties of biodegradable multilayer films based on plasticized wheat starch. *Starch/Staerke*, *53*(8), 372–380. https://doi.org/10.1002/1521-379X(200108)53:8<372::AID-STAR372>3.0.CO;2-F

Masood, M. T., Zahid, M., Goldoni, L., Ceseracciu, L., Athanassiou, A., & Bayer, I. S. (2018). Highly Transparent Polyethylcyanoacrylates from Approved Eco-Friendly Fragrance Materials Demonstrating Excellent Fog-Harvesting and Anti-Wear Properties. *ACS Applied Materials and Interfaces*, *10*(40), 34573–34584. https://doi.org/10.1021/acsami.8b10717

Mazzon, G., Zahid, M., Heredia-Guerrero, J. A., Balliana, E., Zendri, E., Athanassiou, A., & Bayer, I. S. (2019). Hydrophobic treatment of woven cotton fabrics with polyurethane modified aminosilicone emulsions. *Applied Surface Science*, *490*(May), 331–342. https://doi.org/10.1016/j.apsusc.2019.06.069

Mazzon, G., Zanocco, I., Zahid, M., Bayer, I., Athanassiou, A., Falchi, L., Balliana, E., & Zendri, E. (2017). Nanostructured coatings for the protection of textiles and paper. *Ge-Conservacion*, *1*(11), 180–188. https://doi.org/10.37558/gec.v11i0.474

Mi, H. Y., Jing, X., Peng, J., Salick, M. R., Peng, X. F., & Turng, L. S. (2014). Poly(ε-caprolactone) (PCL)/cellulose nano-crystal (CNC) nanocomposites and foams. *Cellulose*, *21*(4), 2727–2741. https://doi.org/10.1007/s10570-014-0327-y

Mishra, R. K., Datt, M., & Banthia, A. K. (2008). Synthesis and characterization of pectin/pvp hydrogel membranes for drug delivery system. *AAPS PharmSciTech*, *9*(2), 395–403. https://doi.org/10.1208/s12249-008-9048-6

Mizrahi, B., Stefanescu, C. F., Yang, C., Lawlor, M. W., Ko, D., Langer, R., & Kohane, D. S. (2011). Acta Biomaterialia Elasticity and safety of alkoxyethyl cyanoacrylate tissue adhesives. *Acta Biomaterialia*, *7*(8), 3150–3157. https://doi.org/10.1016/j.actbio.2011.04.022

Mohanty, A. K., Vivekanandhan, S., Pin, J. M., & Misra, M. (2018). Composites from renewable and sustainable resources: Challenges and innovations. *Science*, *362*(6414), 536–542. https://doi.org/10.1126/science.aat9072

Mondal, S., Ghosh, S., & Moulik, S. P. (2016). Stability of curcumin in different solvent and solution media: UV–visible and steady-state fluorescence spectral study. *Journal of Photochemistry and Photobiology B: Biology*, *158*, 212–218. https://doi.org/10.1016/j.jphotobiol.2016.03.004

Monteiro Espíndola, K. M., Ferreira, R. G., Mosquera Narvaez, L. E., Rocha Silva Rosario, A. C., Machado Da Silva, A. H., Bispo Silva, A. G., Oliveira Vieira, A. P., & Chagas Monteiro, M. (2019). Chemical and pharmacological aspects of caffeic acid and its activity in hepatocarcinoma. *Frontiers in Oncology*, *9*(JUN), 3–5. https://doi.org/10.3389/fonc.2019.00541

Moreira, H. R., Munarin, F., Gentilini, R., Visai, L., Granja, P. L., Cristina, M., & Petrini, P. (2014). Injectable pectin hydrogels produced by internal gelation : pH dependence of gelling and rheological properties. *Carbohydrate Polymers*, *103*, 339–347.

https://doi.org/10.1016/j.carbpol.2013.12.057

Müller-Maatsch, J., Bencivenni, M., Caligiani, A., Tedeschi, T., Bruggeman, G., Bosch, M., Petrusan, J., Van Droogenbroeck, B., Elst, K., & Sforza, S. (2016). Pectin content and composition from different food waste streams in memory of Anna Surribas, scientist and friend. *Food Chemistry*, *201*, 37–45. https://doi.org/10.1016/j.foodchem.2016.01.012

Muller, J., González-Martínez, C., & Chiralt, A. (2017). Combination Of Poly(lactic) acid and starch for biodegradable food packaging. *Materials*, *10*(8), 1–22. https://doi.org/10.3390/ma10080952

Munteanu, S. B., & Vasile, C. (2020). Vegetable additives in food packaging polymeric materials. *Polymers*, *12*(1). https://doi.org/10.3390/polym12010028

Nadagouda, M. N., Iyanna, N., Lalley, J., Han, C., Dionysiou, D. D., & Varma, R. S. (2014). Synthesis of silver and gold nanoparticles using antioxidants from blackberry, blueberry, pomegranate, and turmeric extracts. *ACS Sustainable Chemistry and Engineering*, *2*(7), 1717–1723. https://doi.org/10.1021/sc500237k

Negi, P. S., Jayaprakasha, G. K., & Jena, B. S. (2003). Antioxidant and antimutagenic activities of pomegranate peel extracts. *Food Chemistry*, *80*(3), 393–397. https://doi.org/10.1016/S0308-8146(02)00279-0

Nisar, T., Wang, Z. C., Yang, X., Tian, Y., Iqbal, M., & Guo, Y. (2018). Characterization of citrus pectin films integrated with clove bud essential oil: Physical, thermal, barrier, antioxidant and antibacterial properties. *International Journal of Biological Macromolecules*, *106*, 670–680. https://doi.org/10.1016/j.ijbiomac.2017.08.068

Nogueira, G. F., Soares, C. T., Cavasini, R., Fakhouri, F. M., & de Oliveira, R. A. (2019). Bioactive films of arrowroot starch and blackberry pulp: Physical, mechanical and barrier properties and stability to pH and sterilization. *Food Chemistry*, *275*(April 2018), 417–425. https://doi.org/10.1016/j.foodchem.2018.09.054

Oleyaei, S. A., Almasi, H., Ghanbarzadeh, B., & Moayedi, A. A. (2016). Synergistic reinforcing effect of TiO2 and montmorillonite on potato starch nanocomposite films: Thermal, mechanical and barrier properties. *Carbohydrate Polymers*, *152*(December 2017), 253–262.

https://doi.org/10.1016/j.carbpol.2016.07.040

Otoni, C. G., Avena-Bustillos, R. J., Azeredo, H. M. C., Lorevice, M. V., Moura, M. R., Mattoso, L. H. C., & McHugh, T. H. (2017). Recent Advances on Edible Films Based on Fruits and Vegetables—A Review. *Comprehensive Reviews in Food Science and Food Safety*, *16*(5), 1151–1169. https://doi.org/10.1111/1541-4337.12281

Overy, D. P., Larsen, T. O., Dalsgaard, P. W., Frydenvang, K., Phipps, R., Munro, M. H. G., & Christophersen, C. (2005). Andrastin A and barceloneic acid metabolites, protein farnesyl transferase inhibitors from Penicillium albocoremium: chemotaxonomic significance and pathological implications. *Mycological Research*, *109*(11), 1243–1249.

Pan, H., Hao, Y., Zhao, Y., Lang, X., Zhang, Y., Wang, Z., Zhang, H., & Dong, L. (2017). Improved mechanical properties, barrier properties and degradation behavior of poly(butylenes adipate-co-terephthalate)/poly(propylene carbonate) films. *Korean Journal of Chemical Engineering*, *34*(5), 1294–1304. https://doi.org/10.1007/s11814-017-0066-5

Pan, N., Qin, J., Feng, P., Li, Z., & Song, B. (2019). Color-changing smart fibrous materials for naked eye real-time monitoring of wound pH. *Journal of Materials Chemistry B*, *7*(16), 2626–2633. https://doi.org/10.1039/c9tb00195f

Panrong, T., Karbowiak, T., & Harnkarnsujarit, N. (2019). Thermoplastic starch and green tea blends with LLDPE films for active packaging of meat and oil-based products. *Food Packaging and Shelf Life*, *21*(February), 100331. https://doi.org/10.1016/j.fpsl.2019.100331

Papadopoulou, A., Green, R. J., & Frazier, R. A. (2005). Interaction of flavonoids with bovine serum albumin: A fluorescence quenching study. *Journal of Agricultural and Food Chemistry*, *53*(1), 158–163. https://doi.org/10.1021/jf048693g

Paraskevopoulou, D., Achilias, D. S., & Paraskevopoulou, A. (2012). Migration of styrene from plastic packaging based on polystyrene into food simulants. *Polymer International*, *61*(1), 141–148. https://doi.org/10.1002/pi.3161

Parris, N., Dickey, L. C., Wiles, J. L., Moreau, R. A., & Cooke, P. H. (2000). Enzymatic hydrolysis, grease permeation, and water barrier properties of zein isolate coated paper. *Journal of Agricultural and Food Chemistry*, *48*(3), 890–894.

https://doi.org/10.1021/jf991079y

Pasrija, D., Ezhilarasi, P. N., Indrani, D., & Anandharamakrishnan, C. (2015). Microencapsulation of green tea polyphenols and its effect on incorporated bread quality. *LWT - Food Science and Technology*, *64*(1), 289–296. https://doi.org/10.1016/j.lwt.2015.05.054

Patwa, R., Kumar, A., & Katiyar, V. (2018). Effect of silk nano-disc dispersion on mechanical, thermal, and barrier properties of poly(lactic acid) based bionanocomposites. *Journal of Applied Polymer Science*, *135*(38). https://doi.org/10.1002/app.46671

Paula, M., Diego, I., Dionisio, R., Vinhas, G., & Alves, S. (2019). Gamma irradiation effects on polycaprolactone/zinc oxide nanocomposite films. *Polimeros*, *29*(1), 1–7. https://doi.org/10.1590/0104-1428.04018

Pellegrini, N., Serafini, M., Colombi, B., Del Rio, D., Salvatore, S., Bianchi, M., & Brighenti, F. (2003). Total antioxidant capacity of plant foods, beverages and oils consumed in Italy assessed by three different in vitro assays. *Journal of Nutrition*, *133*(9), 2812–2819. https://doi.org/10.1093/jn/133.9.2812

Peng, Y., Wang, Q., Shi, J., Chen, Y., & Zhang, X. (2020). Optimization and release evaluation for tea polyphenols and chitosan composite films with regulation of glycerol and tween. *Food Science and Technology*, *40*(1), 162–170. https://doi.org/10.1590/fst.34718

Pérez-Jiménez, J., & Saura-Calixto, F. (2006). Effect of solvent and certain food constituents on different antioxidant capacity assays. *Food Research International*, *39*(7), 791–800. https://doi.org/10.1016/j.foodres.2006.02.003

Perez-Pimienta, J. A., Lopez-Ortega, M. G., Chavez-Carvayar, J. A., Varanasi, P., Stavila, V., Cheng, G., Singh, S., & Simmons, B. A. (2015). Characterization of agave bagasse as a function ofionic liquid pretreatment. *Biomass and Bioenergy*, *75*(October 2017), 180–188. https://doi.org/10.1016/j.biombioe.2015.02.026

Perotto, G., Ceseracciu, L., Simonutti, R., Paul, U. C., Guzman-Puyol, S., Tran, T. N., Bayer, I. S., & Athanassiou, A. (2018). Bioplastics from vegetable waste: Via an eco-friendly water-based process. *Green Chemistry*, *20*(4), 894–902. https://doi.org/10.1039/c7gc03368k

Peschel, W., Sánchez-Rabaneda, F., Diekmann, W., Plescher, A., Gartzía, I., Jiménez, D., Lamuela-Raventós, R., Buxaderas, S., & Codina, C. (2006). An industrial approach in the search of natural antioxidants from vegetable and fruit wastes. *Food Chemistry*, *97*(1), 137–150. https://doi.org/10.1016/j.foodchem.2005.03.033

Pettolino, F. A., Walsh, C., Fincher, G. B., & Bacic, A. (2012). Determining the polysaccharide composition of plant cell walls. *Nature Protocols*, *7*(9), 1590–1607. https://doi.org/10.1038/nprot.2012.081

Ponting, J. D., Jackson, R., & Watters, G. (1971). Refrigerated apple slices: effects of pH, sulfites and calcium on texture. *Journal of Food Science*, *36*(2), 349–350.

Priyadarshi, R., Sauraj, Kumar, B., Deeba, F., Kulshreshtha, A., & Negi, Y. S. (2018). Chitosan films incorporated with Apricot (Prunus armeniaca) kernel essential oil as active food packaging material. *Food Hydrocolloids*, *85*(March), 158–166. https://doi.org/10.1016/j.foodhyd.2018.07.003

Priyadarshi, R., Sauraj, Kumar, B., & Negi, Y. S. (2018). Chitosan film incorporated with citric acid and glycerol as an active packaging material for extension of green chilli shelf life. *Carbohydrate Polymers*, *195*(December 2017), 329–338. https://doi.org/10.1016/j.carbpol.2018.04.089

Priyadarsini, K. I. (2014). The chemistry of curcumin: From extraction to therapeutic agent. *Molecules*, *19*(12), 20091–20112. https://doi.org/10.3390/molecules191220091

Rameshkumar, S., Shaiju, P., Connor, K. E. O., & P, R. B. (2020). ScienceDirect Bio-based and biodegradable polymers - State-of-the- art , challenges and emerging trends. *Current Opinion in Green and Sustainable Chemistry*, *21*, 75–81. https://doi.org/10.1016/j.cogsc.2019.12.005

RameshKumar, S., Shaiju, P., O'Connor, K. E., & P, R. B. (2020). Bio-based and biodegradable polymers - State-of-the-art, challenges and emerging trends. *Current Opinion in Green and Sustainable Chemistry*, *21*, 75–81. https://doi.org/10.1016/j.cogsc.2019.12.005

Rastogi, V. K., & Samyn, P. (2015). Bio-based coatings for paper applications. *Coatings*, *5*(4), 887–930. https://doi.org/10.3390/coatings5040887

Rešček, A., Krehula, L. K., Katančić, Z., & Hrnjak-Murgić, Z. (2015). Active bilayer PE/PCL films for food packaging modified with zinc oxide and casein. *Croatica Chemica Acta*, *88*(4), 461–473. https://doi.org/10.5562/cca2768

Rhim, B. J., Lee, J., & Hong, S. (2007). *Increase in Water Resistance of Paperboard by Coating with Poly (lactide) and Science*. *January*, 393–402.

Rhim, J. W., Lee, J. H., & Hong, S. I. (2006). Water resistance and mechanical properties of biopolymer (alginate and soy protein) coated paperboards. *LWT - Food Science and Technology*, *39*(7), 806–813. https://doi.org/10.1016/j.lwt.2005.05.008

Rojas-Graü, M. A., Avena-Bustillos, R. J., Friedman, M., Henika, P. R., Martín-Belloso, O., & Mchugh, T. H. (2006). Mechanical, barrier, and antimicrobial properties of apple puree edible films containing plant essential oils. *Journal of Agricultural and Food Chemistry*, *54*(24), 9262–9267. https://doi.org/10.1021/jf061717u

Salmoria, G. V., Sibilia, F., Henschel, V. G., Fare, S., & Tanzi, M. C. (2017). Structure and properties of polycaprolactone/ibuprofen rods prepared by melt extrusion for implantable drug delivery. *Polymer Bulletin*, *74*(12), 4973–4987. https://doi.org/10.1007/s00289-017-1999-x

Samyn, P. (2013). Wetting and hydrophobic modification of cellulose surfaces for paper applications. *Journal of Materials Science*, *48*(19), 6455–6498. https://doi.org/10.1007/s10853-013-7519-y

Sánchez-González, L., González-Martínez, C., Chiralt, A., & Cháfer, M. (2010). Physical and antimicrobial properties of chitosan-tea tree essential oil composite films. *Journal of Food Engineering*, *98*(4), 443–452. https://doi.org/10.1016/j.jfoodeng.2010.01.026

Sandhya, S., Khamrui, K., Prasad, W., & Kumar, M. C. T. (2018). Preparation of pomegranate peel extract powder and evaluation of its effect on functional properties and shelf life of curd. *Lwt*, *92*(August 2017), 416–421. https://doi.org/10.1016/j.lwt.2018.02.057

Shaghaleh, H., Xu, X., & Wang, S. (2018). Current progress in production of biopolymeric materials based on cellulose, cellulose nanofibers, and cellulose derivatives. *RSC Advances*, *8*(2), 825–842. https://doi.org/10.1039/c7ra11157f

Sharmin, N., Khan, R. A., Salmieri, S., Dussault, D., & Lacroix, M. (2012). Fabrication and Characterization of Biodegradable Composite Films Made of Using Poly(caprolactone) Reinforced with Chitosan. *Journal of Polymers and the Environment*, *20*(3), 698–705. https://doi.org/10.1007/s10924-012-0431-8

Silano, V., Barat Baviera, J. M., Bolognesi, C., Chesson, A., Cocconcelli, P. S., Crebelli, R., Gott, D. M., Grob, K., Lambré, C., Lampi, E., Mengelers, M., Mortensen, A., Steffensen, I. L., Tlustos, C., Van Loveren, H., Vernis, L., Zorn, H., Benfenati, E., Castle, L., … Rivière, G. (2020). Review and priority setting for substances that are listed without a specific migration limit in Table 1 of Annex 1 of Regulation 10/2011 on plastic materials and articles intended to come into contact with food. *EFSA Journal*, *18*(6), 1–104. https://doi.org/10.2903/j.efsa.2020.6124

Siracusa, V. (2012). Food packaging permeability behaviour: A report. *International Journal of Polymer Science*, *2012*(August). https://doi.org/10.1155/2012/302029

Siracusa, V., & Blanco, I. (2020). Bio-polyethylene (Bio-PE), Bio-polypropylene (Bio-PP) and Bio-poly(ethylene terephthalate) (Bio-PET): Recent developments in bio-based polymers analogous to petroleum-derived ones for packaging and engineering applications. *Polymers*, *12*(8). https://doi.org/10.3390/APP10155029

Siracusa, V., Rocculi, P., Romani, S., & Rosa, M. D. (2008). Biodegradable polymers for food packaging: a review. *Trends in Food Science and Technology*, *19*(12), 634–643. https://doi.org/10.1016/j.tifs.2008.07.003

Snitsarev, V., Young, M. N., Miller, R. M. S., & Rotella, D. P. (2013). The spectral properties of (-)-epigallocatechin 3-O-gallate (EGCG) fluorescence in different solvents: Dependence on solvent polarity. *PLoS ONE*, *8*(11), 1–6. https://doi.org/10.1371/journal.pone.0079834

Sriamornsak, P., Sungthongjeen, S., & Puttipipatkhachorn, S. (2007). Use of pectin as a carrier for intragastric floating drug delivery: Carbonate salt contained beads. *Carbohydrate Polymers*, *67*(3), 436–445. https://doi.org/10.1016/j.carbpol.2006.06.013

Surendhiran, D., Li, C., Cui, H., & Lin, L. (2020). Fabrication of high stability active nanofibers encapsulated with pomegranate peel extract using chitosan/PEO for meat preservation. *Food*

Packaging and Shelf Life, *23*(March 2019), 100439. https://doi.org/10.1016/j.fpsl.2019.100439

Synytsya, A., Čopíková, J., Matějka, P., & Machovič, V. (2003). Fourier transform Raman and infrared spectroscopy of pectins. *Carbohydrate Polymers*, *54*(1), 97–106. https://doi.org/10.1016/S0144-8617(03)00158-9

Tagliazucchi, D., Verzelloni, E., & Conte, A. (2008). Antioxidant properties of traditional balsamic vinegar and boiled must model systems. *European Food Research and Technology*, *227*(3), 835–843. https://doi.org/10.1007/s00217-007-0794-6

Tallentire, C. W., & Steubing, B. (2020). The environmental benefits of improving packaging waste collection in Europe. *Waste Management*, *103*, 426–436. https://doi.org/10.1016/j.wasman.2019.12.045

Tedeschi, G., Guzman-Puyol, S., Ceseracciu, L., Paul, U. C., Picone, P., Di Carlo, M., Athanassiou, A., & Heredia-Guerrero, J. A. (2020). Multifunctional Bioplastics Inspired by Wood Composition: Effect of Hydrolyzed Lignin Addition to Xylan-Cellulose Matrices. *Biomacromolecules*, *21*(2), 910–920. https://doi.org/10.1021/acs.biomac.9b01569

Thakur, M., Sharma, A., Ahlawat, V., Bhattacharya, M., & Goswami, S. (2020). Process optimization for the production of cellulose nanocrystals from rice straw derived α-cellulose. *Materials Science for Energy Technologies*, *3*, 328–334. https://doi.org/10.1016/j.mset.2019.12.005

Tian, F., Decker, E. A., & Goddard, J. M. (2013). Controlling lipid oxidation of food by active packaging technologies. *Food and Function*, *4*(5), 669–680. https://doi.org/10.1039/c3fo30360h

Tongnuanchan, P., Benjakul, S., & Prodpran, T. (2012). Properties and antioxidant activity of fish skin gelatin film incorporated with citrus essential oils. *Food Chemistry*, *134*(3), 1571–1579. https://doi.org/10.1016/j.foodchem.2012.03.094

Tønnesen, H. H., Másson, M., & Loftsson, T. (2002). Studies of curcumin and curcuminoids. XXVII. Cyclodextrin complexation: Solubility, chemical and photochemical stability. *International Journal of Pharmaceutics*, *244*(1–2), 127–135. https://doi.org/10.1016/S0378-

5173(02)00323-X

Tripodo, G., Wischke, C., & Lendlein, A. (2011). Highly flexible poly(ethyl-2-cyanoacrylate) based materials obtained by incorporation of oligo(ethylene glycol)diglycidylether. *Macromolecular Symposia*, *309–310*(1), 49–58. https://doi.org/10.1002/masy.201100058

Trnková, L., Boušová, I., Staňková, V., & Dršata, J. (2011). Study on the interaction of catechins with human serum albumin using spectroscopic and electrophoretic techniques. *Journal of Molecular Structure*, *985*(2–3), 243–250. https://doi.org/10.1016/j.molstruc.2010.11.001

Tulamandi, S., Rangarajan, V., Rizvi, S. S. H., Singhal, R. S., Chattopadhyay, S. K., & Saha, N. C. (2016). A biodegradable and edible packaging film based on papaya puree, gelatin, and defatted soy protein. *Food Packaging and Shelf Life*, *10*, 60–71. https://doi.org/10.1016/j.fpsl.2016.10.007

Turner, A. (2018). Black plastics: Linear and circular economies, hazardous additives and marine pollution. *Environment International*, *117*(April), 308–318. https://doi.org/10.1016/j.envint.2018.04.036

Ullah, K., Sohail, M., Buabeid, M. A., Murtaza, G., Ullah, A., Rashid, H., Khan, M. A., & Khan, S. A. (2019). Pectin-based (LA-co-MAA) semi-IPNS as a potential biomaterial for colonic delivery of oxaliplatin. *International Journal of Pharmaceutics*, *569*(December), 118557. https://doi.org/10.1016/j.ijpharm.2019.118557

Ulusoy, B., & Hecer, C. (2018). *Edible Films and Coatings : A Good Idea From Past to Future Technology*. *January*. https://doi.org/10.18488/journal.58.2018.51.28.33

Valdés, A., Burgos, N., Jiménez, A., & Garrigós, M. C. (2015). Natural pectin polysaccharides as edible coatings. *Coatings*, *5*(4), 865–886. https://doi.org/10.3390/coatings5040865

Valdés, A., Ramos, M., Beltrán, A., Jiménez, A., & Garrigós, M. C. (2017). State of the art of antimicrobial edible coatings for food packaging applications. *Coatings*, *7*(4), 1–23. https://doi.org/10.3390/coatings7040056

Varžinskas, V., & Markevičiūtė, Z. (2020). *Sustainable Food Packaging : Materials and Waste Management Solutions*. 154–164. https://doi.org/10.5755/j01.erem.76.3.27511

Vieira, M. G. A., Da Silva, M. A., Dos Santos, L. O., & Beppu, M. M. (2011). Natural-based plasticizers and biopolymer films: A review. *European Polymer Journal*, *47*(3), 254–263. https://doi.org/10.1016/j.eurpolymj.2010.12.011

Villalobos, R., Chanona, J., Hernández, P., Gutiérrez, G., & Chiralt, A. (2005). Gloss and transparency of hydroxypropyl methylcellulose films containing surfactants as affected by their microstructure. *Food Hydrocolloids*, *19*(1), 53–61. https://doi.org/10.1016/j.foodhyd.2004.04.014

Vuoti, S., Laatikainen, E., Heikkinen, H., Johansson, L. S., Saharinen, E., & Retulainen, E. (2013). Chemical modification of cellulosic fibers for better convertibility in packaging applications. *Carbohydrate Polymers*, *96*(2), 549–559. https://doi.org/10.1016/j.carbpol.2012.07.053

Wang, X., Sun, X., Liu, H., Li, M., & Ma, Z. (2011). Barrier and mechanical properties of carrot puree films. *Food and Bioproducts Processing*, *89*(2), 149–156. https://doi.org/10.1016/j.fbp.2010.03.012

Wu, H., Lei, Y., Zhu, R., Zhao, M., Lu, J., Xiao, D., Jiao, C., Zhang, Z., Shen, G., & Li, S. (2019). Preparation and characterization of bioactive edible packaging films based on pomelo peel flours incorporating tea polyphenol. *Food Hydrocolloids*, *90*(October 2018), 41–49. https://doi.org/10.1016/j.foodhyd.2018.12.016

Wyrwa, J., & Barska, A. (2017). Innovations in the food packaging market: active packaging. *European Food Research and Technology*, *243*(10), 1681–1692. https://doi.org/10.1007/s00217-017-2878-2

Xu, Y., Willis, S., Jordan, K., & Sismour, E. (2018). Chitosan nanocomposite films incorporating cellulose nanocrystals and grape pomace extracts. *Packaging Technology and Science*, *31*(9), 631–638. https://doi.org/10.1002/pts.2389

Yang, W., He, X., Luzi, F., Dong, W., Zheng, T., Kenny, J. M., Puglia, D., & Ma, P. (2020). Thermomechanical, antioxidant and moisture behaviour of PVA films in presence of citric acid esterified cellulose nanocrystals. *International Journal of Biological Macromolecules*, *161*, 617–626. https://doi.org/10.1016/j.ijbiomac.2020.06.082

Yao, J., Zhang, P., Fu, Z., Xie, Z., & Bao, G. (2020). *Original article Biocompatible green tea extract-stabilised zinc nanoparticles encapsulated by poly (butyl-2-cyanoacrylate) with control release profile and antioxidative capacity*. 2981–2989. https://doi.org/10.1111/ijfs.14563

Yashin, A. Y., Nemzer, B. V., Combet, E., & Yashin, Y. I. (2015). Determination of the Chemical Composition of Tea by Chromatographic Methods: A Review. *Journal of Food Research*, *4*(3), 56. https://doi.org/10.5539/jfr.v4n3p56

Yin, W. Z., Wang, Y. L., Ji, Q. D., Yao, J., Hou, Y., Wang, L., & Zhong, W. X. (2014). Synthesis and formation mechanism of micro/nano flower-like MgCO3·5H2O. *International Journal of Minerals, Metallurgy and Materials*, *21*(3), 304–310. https://doi.org/10.1007/s12613-014-0909-6

Yousefi, H., Su, H. M., Imani, S. M., Alkhaldi, K., Filipe, C. D., & Didar, T. F. (2019). Intelligent Food Packaging: A Review of Smart Sensing Technologies for Monitoring Food Quality. *ACS Sensors*, *4*(4), 808–821. https://doi.org/10.1021/acssensors.9b00440

Yu, S. H., Hsieh, H. Y., Pang, J. C., Tang, D. W., Shih, C. M., Tsai, M. L., Tsai, Y. C., & Mi, F. L. (2013). Active films from water-soluble chitosan/cellulose composites incorporating releasable caffeic acid for inhibition of lipid oxidation in fish oil emulsions. *Food Hydrocolloids*, *32*(1), 9–19. https://doi.org/10.1016/j.foodhyd.2012.11.036

Zahid, M., Mazzon, G., Athanassiou, A., & Bayer, I. S. (2019). Environmentally benign non-wettable textile treatments: A review of recent state-of-the-art. *Advances in Colloid and Interface Science*, *270*, 216–250. https://doi.org/10.1016/j.cis.2019.06.001

Zebib, B., Mouloungui, Z., & Noirot, V. (2010). Stabilization of curcumin by complexation with divalent cations in glycerol/water system. *Bioinorganic Chemistry and Applications*, *2010*. https://doi.org/10.1155/2010/292760

Zhang, H., He, P., Kang, H., & Li, X. (2018). Antioxidant and antimicrobial effects of edible coating based on chitosan and bamboo vinegar in ready to cook pork chops. *Lwt*, *93*(December 2017), 470–476. https://doi.org/10.1016/j.lwt.2018.04.005

Zhang, S., Sun, X., Ren, Z., Li, H., & Yan, S. (2015). The development of a bilayer structure of

poly(propylene carbonate)/poly(3-hydroxybutyrate) blends from the demixed melt. *Physical Chemistry Chemical Physics*, *17*(48), 32225–32231. https://doi.org/10.1039/c5cp06076a

Zhang, W., Xiao, H., & Qian, L. (2014). Enhanced water vapour barrier and grease resistance of paper bilayer-coated with chitosan and beeswax. *Carbohydrate Polymers*, *101*(1), 401–406. https://doi.org/10.1016/j.carbpol.2013.09.097

Zhao, Q., Tao, J., Yam, R. C. M., Mok, A. C. K., Li, R. K. Y., & Song, C. (2008). Biodegradation behavior of polycaprolactone/rice husk ecocomposites in simulated soil medium. *Polymer Degradation and Stability*, *93*(8), 1571–1576. https://doi.org/10.1016/j.polymdegradstab.2008.05.002

Zhu, G., Xu, Q., Qin, R., Yan, H., & Liang, G. (2005). Effect of γ-radiation on crystallization of polycaprolactone. *Radiation Physics and Chemistry*, *74*(1), 42–50.

Zhuang, S., Li, Y., Jia, S., Hong, H., Liu, Y., & Luo, Y. (2019). Effects of pomegranate peel extract on quality and microbiota composition of bighead carp (Aristichthys nobilis) fillets during chilled storage. *Food Microbiology*, *82*(January), 445–454. https://doi.org/10.1016/j.fm.2019.03.019

Zia, J., Paul, U. C., Heredia-Guerrero, J. A., Athanassiou, A., & Fragouli, D. (2019). Low-density polyethylene/curcumin melt extruded composites with enhanced water vapor barrier and antioxidant properties for active food packaging. *Polymer*, *175*(May), 137–145. https://doi.org/10.1016/j.polymer.2019.05.012

Ziarno, M. (2007). Warsaw Agricultural University SGGW. *Acta Sci. Pol., Tecnologia Alimentarius*, *6*(2), 29–40.